Solvent extraction : a study of the liquid/liquid interface with ligands combining x-ray and neutron reflectivity measurements

Ernesto Scoppola

Collège Doctoral du Languedoc-Roussillon

THÈSE

Pour obtenir le grade de

Docteur

Délivré par **Université de Montpellier**

Préparée au sein de l'école doctorale Sciences Chimiques Balard (ED 459)
Et de l'unité de recherche Institut de Chimie Séparative de Marcoule (ICSM - UMR 5257) et de l'institut Laue Langevin (ILL)

Spécialité : **Chimie séparative, matériaux et procédés**

Présentée par **Ernesto Scoppola**

Extraction par solvant : étude d'une interface liquide/liquide contenant des ligands en associant des mesures de réflectivité de rayons X et de neutrons

Soutenue le 30 Novembre 2015 devant le jury composé de

Dr. Philippe GUILBAUD	Docteur, CEA Marcoule	Rapporteur
Dr. Patrick GUENOUN	Docteur, CEA Saclay	Rapporteur
Dr. Dominique LANGEVIN	Directeur de Recherche, Université Paris Sud	Examinateur
Dr. Ali ZARBAKHSH	MCF, University of London	Examinateur
Pr. Jean-François DUFRÊCHE	Professesur, Université Montpellier	Président
Dr.. Jean-Pierre SIMONIN	Directeur de Recherche, CNRS, UPMC	Examinateur
Dr. Olivier DIAT	Docteur, CEA Marcoule	Directeur de thèse
Dr. Luc GIRARD	MCF, ENSCM	Co-encadrant de thèse
Dr. Giovanna FRAGNETO	Docteur, ILL	Membre Invité

Université Montpellier

Cette thèse a été financée par
le Commissariat à l'Énergie Atomique et aux Énergies Alternatives (CEA)

Et l'institut Laue Langevin

Le travail de thèse s'est déroulé à l'Institut Laue Langevin et à
l'Institut de Chimie Séparative de Marcoule (UMR 5257)

To Margherita

"I don't know anything, but I do know that everything is interesting if you go into it deeply enough."

Richard Feynman (1979)

Each trip begins with people and it ends with new fellow. However, in this coming and going, some fixed points remain. For this, I would like to thank the people who supported me before and during all the challenges I have faced in these three years.

First of all I thank Margherita which has been able to teach me the richness of chaos. She has supported me, quietly but firmly.
I thank my parents for all the discussions and encouragement. Their firmness and rigidity, often difficult to accept, today are an asset. My brother who has learned even more fraternal sense enclosed in the distance.

I thank my supervisors, Giovanna, Olivier and Lionel. Each of them has been able to motivate me, encourage me and question me. The wealth of ideas comes from discussions with other people and my supervisors have been masters of this path. They have been able to teach me and share with me the defeats but also the success of this project.

I thank all the friends in Grenoble for sharing the Italian food, the tresette in the kitchen, skiing and sailing.

I thank Yuri because he has been able to patiently listen to me and teach me the same concepts more than once. His criticality to my ideas has been essential to let me doubt of my ideas. He has taught me that you must always have to be sure that what you claim is the truth.

I thank Richard and Erik who have taught me the meaning of relevance and logic.

I thank my friends in Rome. It is nice to find them every time I need, to share, laugh or just tell stories.

I thank my witnesses that accompany me and Margherita with brotherly affection, because they support us in all the challenge we face.

"Sarebbe tutto più semplice se non ti avessero inculcato questa storia del finire da qualche parte, se solo ti avessero insegnato, piuttosto, a essere felice rimanendo immobile. Tutte quelle storie sulla tua strada. Trovare la tua strada. Andare per la tua strada. Magari invece siamo fatti per vivere in una piazza, o in un giardino pubblico, fermi lì, a far passare la vita, magari siamo un crocicchio, il mondo ha bisogno che stiamo fermi, sarebbe un disastro se solo ce ne andassimo, a un certo punto, per la nostra strada, quale strada? Sono gli altri le strade, io sono una piazza, non porto in nessun posto, io sono un posto."

Alessandro Baricco

Solvent extraction: a study of the liquid/liquid interface with ligands combining x-ray and neutron reflectivity measurements

Abstract: In the frame of the nuclear waste reprocessing and various kinds of critical metals recycling methods, solvent extraction is one of the most used technological processes. The liquid interface between two immiscible fluids is considered as a region where many physical and chemical phenomena take place and can limit or promote the transfer of species between both fluids. The structure of these interfaces has to be known as a function of several thermodynamical parameters to be able to determine the associated energy landscape. X-ray and neutron reflectivity are suitable techniques to probe such kind of fluctuating and buried interfaces at the nanometer scale and at equilibrium. For this study, a new cell has been built and a specific data analysis procedure was established.
We have focused our study on two different biphasic systems (water/dodecane) containing lanthanides salts and two different nonionic ligands or extractant molecules: DMDBTDMA and DMDOHEMA diamides. These ligands are known to have different behaviour in the lanthanides extraction process. Although the amphiphilic chemical structure of both diamides is well known, the structure of the liquid/liquid interface appears to be different as those expected for a classical surfactant molecule. This structure looks more complex, varies as a function of the ligand concentration in the organic phase (below the critical aggregation concentration) and as a function of the proton and salt concentration of the aqueous phase. A monolayer organization does not appear as the main interfacial structuration and a thicker organic layer with an excess of salt has to be considered.
In the case of the DMDBTDMA, this thicker region (approximatively three or four times the length of the ligand) creates an interfacial region where oil and water molecules as well as some salts can mix in. The DMDOHEMA system shows a different structuration where we can roughly observe also a thick layer of the ligand (approximatively two times the length of the ligand) but located more within the oil phase and forming a barrier to the salt distribution.
These different interfacial structures made of DMDBTDMA and DMDOHEMA could allow to explain the diffusive or kinetic regime of ion transfer observed respectively in similar systems by others authors.

Extraction par solvant: étude d'une interface liquide/liquide contenant des ligants en associant des mesures de réflectivité de rayons X et de neutrons

Résumé: Dans le cadre du retraitement des déchets nucléaires et du recyclage de métaux critiques, l'extraction par solvant est l'une des technologies les plus utilisées. L'interface liquide entre deux fluides non miscibles est considérée comme une région où de multiples phénomènes physiques et chimiques sont à prendre en compte et peuvent limiter ou favoriser le transfert d'espèces entre les deux fluides. La structure de ces interfaces doit être connue en fonction de plusieurs paramètres thermodynamiques pour pouvoir déterminer le paysage énergétique associée. La réflectivité de neutrons et de rayons est un des outils appropriés pour sonder ce genre d'interfaces enfouies et fluctuantes à l'échelle nanométrique et à l'équilibre. Pour cette étude, une nouvelle cellule a été construite et un programme spécifique d'analyse de données a été élaboré.
Nous avons également porté notre étude sur deux différents systèmes bi-phasiques (eau / dodécane) contenant des sels de lanthanides et deux différents ligands non ioniques (ou extractants) : une diamide de type DMDBTDMA et de type DMDOHEMA, ces deux extractants étant connus pour avoir des comportements différents dans un processus d'extraction de cations métalliques en phase organique. Bien que la structure amphiphile des deux diamides soit bien connue, la structure de l'interface liquide / liquide semble être différente de celle que l'on pourrait s'attendre avec des tensioactifs classiques. L'organisation de ces ligands à l'interface est en effet plus complexe, varie en fonction de leurs concentrations dans la phase organique (seules des concentrations inférieures à la concentration d'agrégation critique ont été étudiées) et en fonction de la concentration d'acide et de sel dans la phase aqueuse. Une organisation de type monocouche n'est pas l'organisation principale de ces systèmes à l'équilibre mais on observe plutôt une couche épaisse de ligands.
Plus précisément, dans le cas de la DMDBTDMA, cette région plus épaisse (environ trois à quatre fois la longueur du ligand) crée une région interfaciale où les molécules d'huile et d'eau peuvent se mélanger ainsi que les sels. Le système DMDOHEMA, présente une structuration différente avec également une épaisse couche de ligand (environ deux fois la longueur du ligand) mais située plus à l'intérieur de la phase huileuse et distinct de la distribution des sels à l'interface. Ces différentes structures interfaciales de DMDBTDMA et DMDOHEMA peuvent permettre d'expliquer les différents régimes de transfert ionique qualifiés soit de diffusionnel ou de cinétique.

Contents

Introduction

Glenn T. Seaborg, who won the Nobel prize in chemistry for the discovery of transuranium elements, stated in the eighties: *"In the future, chemistry will be called upon to extend our natural resources of copper, lead, zinc, and other non-ferrous metals by making it possible to recover these metals more economically from low-grade ores or to recycle materials now discarded as waste"* [1].
As resources for chemical elements become scarce and the demand is expected to rocket up, recycling becomes crucial. The key point in recycling from waste is separation [2, 3, 4]. For this purpose, liquid/liquid or solvent extraction partitioning methods have been developed to separate compounds based on their different solubilities in immiscible liquids, usually water and an organic solvent ("oil phase"). Among the many solvent extraction technologies [4, 5, 6, 7, 8, 9, 10], those used for metal recovery are quite challenging due to the poor solubility of inorganic ions in oils. Metal extraction thus requires the use of lipophilic extractant molecules to complex the cations and solubilise the complex in the oil phase [11]. In practice, there is a trade-off among selectivity, kinetics and efficiency, in keeping with cost constraints.

However, despite all the attention solvent extraction has received, the molecular structure of the liquid/liquid interface remains quite elusive and, as a result, the mechanisms of complex (ion + extractant molecules + counterions) formation and transfer, all of which influence the kinetics of extraction, are not well understood. Ion-extraction can be referred to as a diffusion-limited or a reaction-limited process depending on the height of the energy barrier at the liquid/liquid interface [12, 13]. To tackle this highly challenging problem, as first step we obtained co-

herent nanometer scale structural information of the interface at equilibrium [14]. We propose in this thesis work to analyze the molecular structure of the buried liquid/liquid interface in such complex systems using for the first time a combination of x-ray and neutron reflectivity and data analysis aided by Fortran code based on Monte-Carlo algorithm.

As described in a recent paper, Schlossman et al. [15, 16] have coupled other techniques such as X-ray reflectivity and X-ray fluorescence measurements in order to gain insight into the ligand and ion distribution at the interface in similar systems but at much lower concentrations. Reflectivity measurements are well suited to the probing of interfacial structures with nm to sub-nm resolution [17]. By combining neutron and X-ray reflectivity measurements it is possible to obtain two fundamentally different scattering contrasts providing complementary scattering length density profiles of the mixture at the liquid/liquid interface [18]. Neutrons provide greater contrast for observing organic species in deuterated environments [19] and the measurements were possible thanks to the unique *reflection down* option of the versatile time-of-flight reflectometer [20], FIGARO, at the Institut Laue-Langevin (Grenoble, France). X-rays on the other hand are more sensitive to the distribution of high Z number ionic species [21, 22]. For this purpose in the three years PhD program we have developed a liquid/liquid cell, as well as the experimental procedures and the method of data analysis. Regarding metal ions, we focused on rare earth Ln^{n+} elements because of their importance in industry. They are considered as critical or strategic elements due to their high values in many applications from catalysis to energy.

CHAPTER 1

Scientific Background

In this chapter we will present the scientific context of this thesis work. On one side the solvent extraction and on the other side the technical developments to study the liquid/liquid interface with scattering techniques.

1.1 Solvent Extraction

Solvent extraction or liquid/liquid extraction is a method to separate compounds based on their relative solubility within two different immiscible liquids. Usually we can consider water and an oil as the two immiscible liquids. So, this process is based on a partitioning method with an ultimate goal for a selective transfer of a substance from one phase toward the other [11]. Without any amphiphilic molecules and under usual conditions (room temperature and atmospheric pressure), oil and water form two phases in equilibrium. Therefore, for a given solute, the polarity will be determined by its solubility in one phase. The more polar solutes dissolve preferentially in the more polar solvent and the less polar solutes in the less polar solvent. The distribution ratio, defined as the ratio between the solute concentration in the organic phase and that in the aqueous phase, depends on thermodynamic properties of the system such as temperature, concentration, pressure. It can be related to the Gibbs free energy ΔG of the extraction process.

Solvent extraction has many applications in various industrial processes ranging

from metal recovery, waste management to pharmacy and cosmetic [4, 5, 9, 10, 23, 24]. Among all the solvent extraction technologies, those used for metal recovery are quite challenging due to the poor solubility of inorganic ions in oils. Metal extraction requires indeed the use of lipophilic extractant molecules to complex the cations and solubilize the complex (extractant + cation + other species) within the oil phase for extraction or within the aqueous phase for desextraction or stripping [25, 26, 27, 28, 29].

There is in practice, a trade-off between selectivity, efficiency and kinetics in keeping the process with some costs constraints [11]. Usually, the simplest device is a contacting tank or column in which an emulsification process is applied to increase the amount of liquid/liquid interface (a higher amount of complexes to be transferred is correlated with a larger specific surface). The process has to be compatible with the settling at both ends via creaming and water coalescence to separate the enriched phase from the impoverished phase and to be fast and efficient for industrial applications. As mentioned previously, the extraction process is operated in the presence of extractant molecules in order to selectively transfer the solute from one phase to the other during extraction and desextraction and also to induce a chemical potentials gradient of the ions (or ion pairs), in favor to one direction of transfer between water and oil. In Figure 1.1 (lefthand side) is schematized the difference of chemical potential for ion 1 to be transferred from water to oil, difference being associated to a ΔG of transfer.

The chemical potential in the aqueous phase can be determined even if the concentration of the different ions is high and the speciation of the multivalent cations can be rather complex. In the oil part this is slightly more complicated because of the aggregation phenomena that exists between the extractant molecules.
Indeed, the self-assembly property of extractant molecules in the organic phase was demonstrated in the 1990s, using small-angle x-ray and neutron scattering techniques (SAXS, SANS) [31]. Usually, extractants form spontaneously small reverse aggregates (with polar parts forming mainly the core of the aggregate around few water molecules or hydrated ions or ion pairs). They are characterized by a low aggregation numbers with less than 10 extractant molecules [32]. The core radius of the aggregate is in general less than 0.5 nm, therefore complexing agents are considering to be in the first or second coordination spheres of the extracted ions. This type of phase behavior can be compared to surfactant system having a packing parameter higher than 1 and dispersed in a oil-rich phase. However, unlike the surfactants, another feature has to be taken into account: the complexation number that relates to the stoichiometry of the complexation reaction

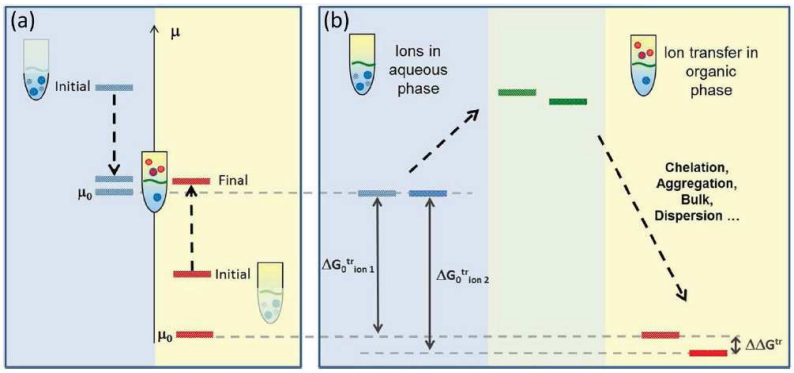

Figure 1.1: (a) Evolution of the chemical potentials of ion pairs during a watersolvent extraction. The reference chemical potential of an ion complexed in water and an ion complexed in reverse aggregates are shown. Initial state is all ions to be extracted in water: In the final state, ions have been extracted and the transfer ends when the chemical potential is equal in coexisting phases. Enrichment of extracted species is understood as differences in the reference potentials in water and solvent, favouring the solvent phase (lower level on the yellow part of diagram. (b) The origin of selectivity ($\Delta\Delta G^{tr}$) between ions 1 and ion 2 (considering common anion). The reference standard chemical potential levels of salt (ion pairs) compared in the water phase (blue background) and in the solvent phase (yellow background). The step in free energy per ion pair extracted from aqueous to solvent phase is $\Delta G_{transfer}$ for ions 1 and 2, respectively. The selectivity between ions 1 and 2 at thermodynamic equilibrium is the double difference between the two steps, i.e. $\Delta\Delta G^{tr}$. The kinetics of ion transfer in transient states may be influenced by an intermediary activated state (green energy level), i.e. when the species to be extracted (or not) interact via dehydration and adsorption with the monolayer at the macroscopic interface [30].

(the average number of ligands participating in the first coordination sphere of a cation within the polar core). This number (between 1 and 4) is different from the aggregation number. The complexation number is important for understanding the short-range interaction [33], whereas the knowledge of aggregation number is important for determining a highly developed surface within the organic solvent that can be considered as a pseudo surface onto which the ions can adsorb (Figure 1.2). This consideration allows then to apply Langmuir type of model to analyse the partitioning data at equilibrium [34]. At this meso-scale, the equilibrium distribution of a hydrophilic solute between an aqueous phase and an organic phase depends on the concentration and the shape of the reverse aggregates. Another difference with surfactant extractant molecules are much less surface-active and show a better solubility in one of the two phases – indeed, the ligands can be more

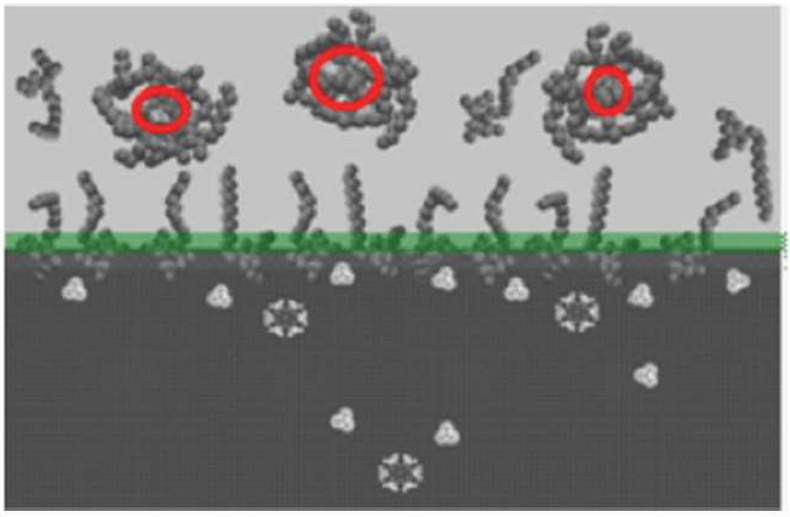

Figure 1.2: Nano-scale artist view of the aqueous solution-solvent macroscopic interface (underlined in green). This macroscopic interface separates the two immiscible phases that are emulsified. The picture is at a primitive level of colloidal chemistry, i.e. "bulk" phases are considered as homogeneous incompressible fluids with scalar properties only. In the solvent (organic) phase, monomers and aggregates coexist. Aggregates have a polar core containing anions, cations and possible water. The polar core is surrounded by the microscopic interface corresponding to a step in dielectric properties (underlined in red). This microscopic picture presents no surface tension between water at equilibrium, when net ion transfer flux is null. Water, salts and cations extracted must be considered in competitive adsorption on the elastic curved microscopic interface, in equilibrium with a reservoir that is the aqueous phase (colour figure online) [30].

liposoluble or more hydrosoluble - a key factor to avoid for the complexes to be stacked at the interface as a usual surfactant, to favor faster extraction kinetics and higher yield rates.

There are different types of extractants that can form different types of complexes and they are classified as follows [35]:

1. By cation exchange: for example, with acidic function like in the Cyanex272 for the Ni/Co separation or Versatic®10, in the HDEHP for rare earth extraction in HCl media or U(VI) in phosphoric acid, in the the neodecanoic acid for the Cu, Ni, and rare earth extraction; any metal transferred in the polar core of the extractant aggregates releases an equivalent quantity of protons.

2. By ”solvation”: for example, with a neutral function like in TBP (tri-n-butyl phosphate) for Th and U extraction in nitric media or Pt and Ir extraction in HCl media, or TOPO; ions are in this case extracted as ion pairs within the polar core of aggregates and there is no detectable release of protons when cations are adsorbed in the solvent phase.

3. By formation of ion pairs: for example, amine salts like Alamine336 for the extraction of Sn, V, Mo, and Cr [36, 37] or TOA; the amine in the oil phase becomes charged by a chemical reaction between the extracted cation. As in case 2, there is no release of protons or hydroxide in the water phase during extraction (or the desextraction).

4. By “synergistic” effects: for example, in enhancing the U(IV) extraction in combining an acidic extractant with a neutral (co)extractant (HDEHP and TOPO) or a LIX63 hydroxyomine with Versatic 10, a carboxylic acid enabling direct separation of Ni, Co, and Zn from Mn, Mg, and Ca [38].

Whatever the type of process, the choice of an efficient extractant depends on the selectivity for the desired metal ion(s) as well as being chemically resistant to the extraction conditions. This is important in order to be able to implement high purification via cascades of coupled devices such as centrifuges, settling tanks, and more specific to nuclear industry, pulsed columns.
Another issue in the extraction process arises from the redox chemistry of the metal ions which, in the case of actinides or lanthanides, can be complex [39] since ions of different valencies coexist. Here, a fine chemical tuning of the extractant molecule by introducing subtle changes in the complex molecular geometry can improve the selectivity in the ion partition.

Surface tension measurement, vapor pressure osmometry, and small-angle x-ray or neutron scattering are the most powerful and standard techniques for characterizing the amphiphilic and aggregation properties of the extractant molecules and some examples on lipophilic systems that we will use in this work will be given in the next part.
It was suggested recently by Dufrêche et al. [40] that the total free energy of transfer should thus take into account several contributions: the supramolecular complexation (or micellisation to keep the common language with surfactant system [41, 42, 43, 44, 45, 46]), the interfacial film bending energy associated to the aggregation, the long-range interactions between these aggregates, the variation in bulk phase cohesion enthalpy and the variation of configuration entropy. Then

the difference of this total ΔG for two different ions 1 and 2, the $\Delta\Delta G$ will determine the selectivity of transfer as sketched in panel (b) of Figure 1.1. However, as mentioned in the legend of Figure 1.1 [30], the kinetics of ion transfer in transient states may be influenced by an intermediary activated state (green energy level), i.e. when the species to be extracted (or not) interact via dehydration and adsorption with the monolayer at the macroscopic interface shown in green in Figure 1.2. This is then one of the objectives of this work. To understand what happens at the interface do we have to consider that the free energy level of this interface is higher, lower or between the initial and final chemistry potential in both fluids? How does it depend on the thermodynamics of the entire system?

It exist several techniques to probe such buried interface. The well-known are, for example, surface tension techniques even if for liquid/liquid interfaces it is sometimes more difficult to handle but this is a technique very sensitive to determine the excess of charged or non-charged species at the interface. The drop profile analysis is one the most used but, for our purpose, to probe ion transfer the large difference in volume between inside and outside the droplet can be a drawback to follow some equilibrium time and we can get only an average information.
Brewster angle and ellipsometry are also relevant optical techniques to probe buried liquid interface, based on the variation of the reflected light polarization and allow to be sensitive to the refractive index variation across and parallel to the interface (interfacial inhomogeneities). However, they are suitable for condensed amphiphiles at the interface and slightly less when the system is disordered. However, diffusion, solvation or transfer, molecular dynamics of active species are inherently complex. A molecular description of the interface as diffuse or rough with lateral and normal diffusion of the interface therefore requires an investigation at the molecular level. Non-linear techniques such as Sum Frequency Generation and more suitable in our case Second Harmonic Generation (SHG) were used and have demonstrated some interest to probe buried liquid interfaces. In the context of ion transfer the group of ICSM have used this technique recently to probe the interface covered with extractant molecules. They have shown that surface tension and SHG measurements can be correlated. Moreover the amplitude of the SHG intensity fluctuations were correlated to some dynamic of transfer with an optimum just below the critical aggregation concentration of extractant in the organic phase. However, the SHG signals are weak and difficult to analyse quantitatively. We can list other techniques such as interfacial rheology, interfacial spectroscopy and electrochemistry, fluorescence microscopy [47, 48, 49, 50, 51, 52, 53, 54, 55, 56] however we have chosen to focus our studies on x-ray and neutron reflectivity mea-

surements whose advantages and drawbacks will be described in the next chapter.

1.2 DMDBTDMA and DMDOHEMA

In nuclear waste management, the americium (Am) and the curium (Cm) elements are the main contributors to the radiotoxicity ("hot" elements) once uranium and plutonium were first extracted (PUREX/COEX processes) to be recycled back to nuclear plants. However these elements that belong to the actinide III family have a similar chemistry with lanthanide III that are also in the fission product but represent only 1-3% of the amount of the fission product and have to be separated from lanthanides.

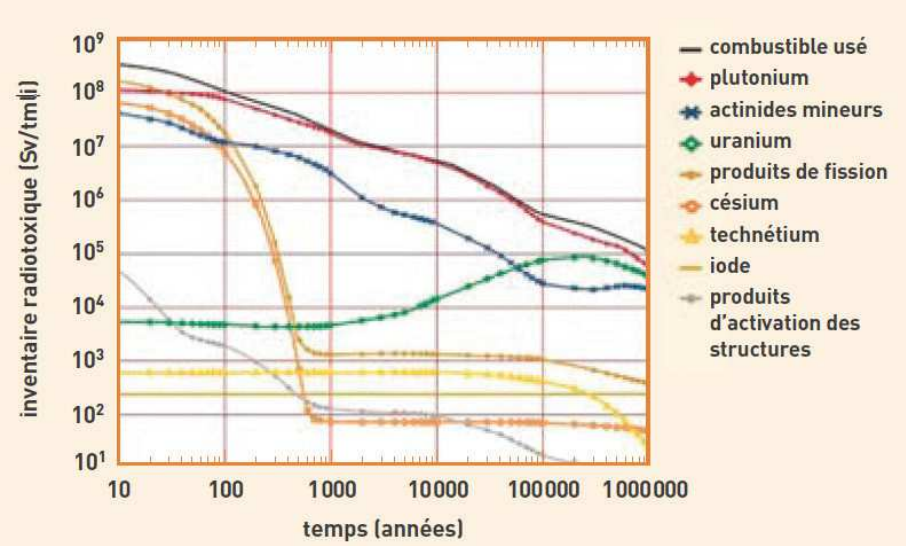

Figure 1.3: Evolution of the radiotoxic inventory, expressed in sieverts per ton of initial heavy metal (uranium) (Sv/tIHM), of spent UOX fuel (based on Uranium OXide) unloaded after burnup of 60 GW·d/t (figure and legend extracted from Clefs CEA n°60).

Ln(III) are considered as hard cations that can be chelated with hard donors groups like oxygen donors such as amide or diamide molecules. An(III) are also hard cation but slightly more soft due roughly to the expansion of their 5f orbitals and then ligands with nitrogen donors groups such as from the pyridine type molecules (BTP or BTBP) can be used but are rather sensitive to radiolysis and selectiveness towards the protons and other elements in the fission products (the transition metals for example).

Nevertheless, the next step after U and Pu extraction proceed with the use of diamide type of molecules to co-extract Ln and An elements. Several options are used to separate Am and Cm from lanthanides not described in this work [57, 58, 59].

In France, the DIAMEX process to extract Ln and An in the oxidation III is using the *N,N'* dimethyl-*N,N'* dioctylhexylethoxy malonamide (DMDOHEMA) as extractant molecules but first studies were focusing on the *N,N'* dimethyl-*N,N'* dibutyltetradecyl malonamide (DMDBTDMA) extractant. This is why also we focused our work on these type of molecules. We can find in literature numerous publication on the subject with results summarized in the following parts. These molecules are considered as neutral and cations are extracted from the aqueous phase as neutral complexes composed by the cation and its counteranions more or less hydrated.
Since these diamide type of molecules (see Figure 1.4) are good extractant towards lanthanides[13, 60, 61, 62, 63], they are also considered as interesting in lanthanide remediation from crude ores or recycling from secondary sources such electronic scrap or catalytic converters for which the exploitation is a challenge for future supply of some of rare metals [2, 64, 65].

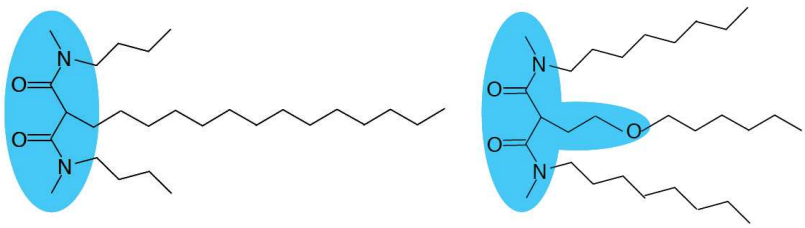

(a) DMDBTDMA (b) DMDOHEMA

Figure 1.4: Structure of (a) DMDBTDMA and (b) DMDOHEMA. The part in blue represents the polar head of ligands, responsible of the amphiphilic properties.

1.2.1 Previous works on DMDBTDMA

Martinet et al. [61, 66] and Bauduin et al. [67] have studied the properties of DMDBTDMA in dodecane and in contact with aqueous phase, like pure water or containing various solute as neodymium nitrate, nitric acid and uranyl nitrate. As shown in Figure 1.5 the decrease of interfacial tension with the increase of

DMDBTDMA bulk concentration, corresponds to general behaviour for classical surfactant making reverse micelles [41, 42, 43, 44, 45, 46].

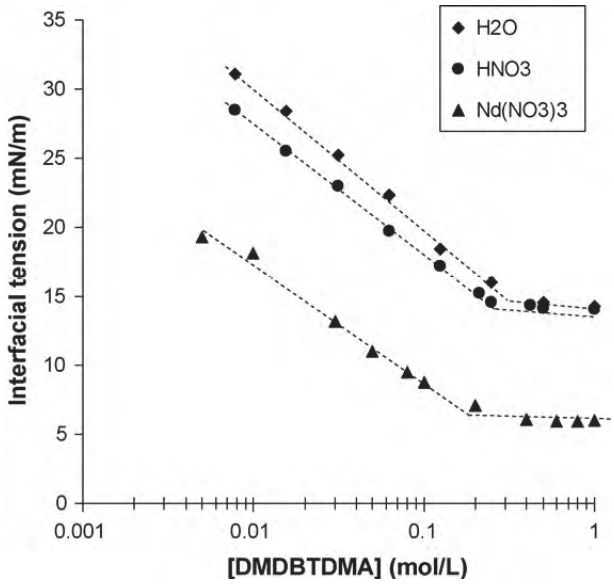

Figure 1.5: Interfacial tension at the aqueous-organic interface for solutions of DMDBTDMA in *n*-dodecane at ambient temperature. H_2O: water aqueous phase; HNO_3: 2 mol/L nitric acid aqueous phase; $Nd(NO_3)_3$: 0.2 mol/L neodymium nitrate, 1 mol/L lithium nitrate, 0.01 mol/L nitric acid aqueous phase [61, 66].

This behaviour is related to the adsorption of extractant due to its amphiphilic character. The change in slope observed for the interfacial tension (see Figure 1.5) at a given extractant concentration, is called Critical Micelle Concentration (CMC) or Critical Aggregate Concentration (CAC) which corresponds to the formation of reverse micelles (or aggregates) in organic phase.
These concentrations are relatively high: 0.25 mol/L for H_2O, 0.23 mol/L for HNO_3 and 0.16 mol/L for the $Nd(NO_3)_3$. Three different values are obtained as function of the aqueous phase which means that the CAC depends on composition and chemical potential of the different phases. The curves reported in Figure 1.5 are obtained at the equilibrium which is achieved with the transfer of some of the solute from the aqueous phase toward the organic phase.
Below the CAC the extractant is mainly in monomeric form. Above the CAC the organic phase contents extractant in monomeric form in equilibrium with aggregates formed around core of hydrated solute.

These interfacial tension measurements are useful to calculate the molecular

area A_0 [m^2/mol] available at the interface at the CAC. By using the Gibbs adsorption equation for neutral species

$$A_0 = -RT\left(\frac{\partial\gamma}{ln(C)}\right)^{-1} \tag{1.1}$$

where R is the universal gas constant, T the temperature in Kelvin, γ the interfacial tension in mN/m and C the bulk concentration of malonamide in the alkane in mol/L.

The biphasic system (extractant in oil contacted with aqueous phase) corresponds in fact to a phase separation called also emulsification failure due to the solute solubilitiy limitation in the organic phase. This phase can be considered as composition point in the triangular phase diagram (extractant/oil/aqueous phase) as shown in Figure 1.6. If solute. such as acid, is added in the system, another

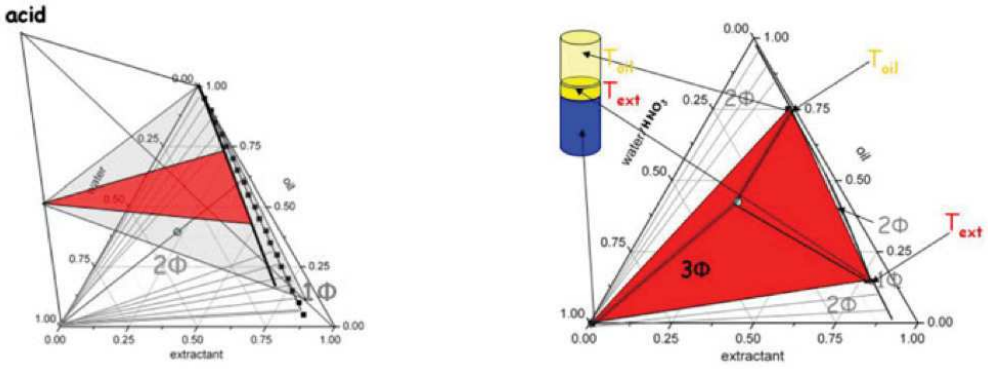

Figure 1.6: Left: 3D representation of the full 4-component phase prism for an extraction system composed of water/HNO_3/oil/extractant, from which one specific cut is shown on the left side. Right: Scheme of a phase diagram for an extraction system composed of water/HNO_3/oil/extractant considered in the case where the acid concentration is high and leads to the "third phase" formation, e.g. [HNO_3]>14.5 M for TBP/dodecane system. The central dot corresponds, for the TBP system with pure water, to a typical extraction composition containing 30% and equal amounts of water and oil (see the tube representation on the left with an oil rich phase in light yellow, an extractant rich phase in dark yellow and an aqueous phase in blue). $T_{ext.}$ and T_{oil} correspond to the demixing third phase and to the excess oil in three-phasic region [68].

phase separation, called third phase, can appear (Third Phase Formation). The third phase formation results in the coexistence of two organic phases, one rich in extractant, the other poor in extractant and still in contact, or in equilibrium, with the aqueous phase.

For the DMDBTDMA system, the third phase formation can be characterized by the LOC (Limit Organic Concentration) which corresponds to the representation of solute concentration in organic phase as function of extractant concentration. The third phase appears at the Liquid/Liquid interface as a jelly phase. Some of the results for DMDBTDMA extracted from the work of Martinet et al [61, 66] are shown in Figure 1.7. If we consider, for example, the biphasic system containing extractant in dodecane contacted with an acidic phase, then, at the demixion limit, we find in the organic phase between 1 and 1.5 nitric acid molecules per DMDBTDMA molecule.

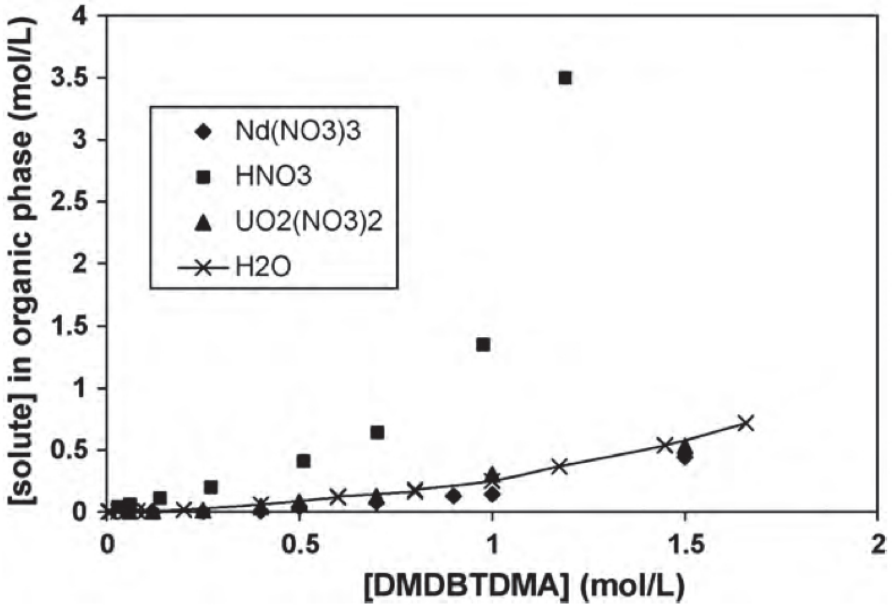

Figure 1.7: LOC of H_2O, $Nd(NO_3)_3$, HNO_3, $UO_2(NO_3)_2$ for DMDBTDMA in solution in *n*-dodecane. The different organic phases are contacted with aquoeus phases containing: (1) $[Nd(NO_3)_3]$ variable, $[LiNO_3]$=1 mol/L, $[HNO_3]$=0.01 mol/L, (2) $[HNO_3]$ variable, (3) $[UO_2(NO_3)_2]$ variable, $[LiNO_3]$=1 mol/L, $[HNO_3]$=0.01mol/L. The curve labelled as H_2O corresponds to the equilibrium between organic phase and pure water; no third phase is observed in this case [61, 66].

Another important point of their work is found in the study of the CAC and the LOC depending on the carbon chain length of the organic solvent or of the extractant. In fact, Martinet et al.[61, 66] have shown that using solvent with shorter carbon chain the CAC decreases. On the contrary, reducing the extractant alkyl chain length, the CAC increases.

On the other hand, it is shown that the extracted amount of acid does not change with the length of the alkyl chain of the solvent or extractant. Their results are shown in Figures 1.8 and 1.9.

Extractant	Diluent	Aqueous phase	CMC (mol/L)	Γ (mol/m^2)	A_0 (Å^2)	ΔG_{mic} (kJ/mol)
DMDBTDMA	*n*-hexane	2 M HNO_3	0.11	$0.7\ 10^{-6}$	227 (±10)	−5.43
DMDBTDMA	*n*-dodecane	2 M HNO_3	0.23	$1.6\ 10^{-6}$	102 (±5)	−3.62
DMDBTDMA	*n*-hexadecane	2 M HNO_3	0.35	$1.6\ 10^{-6}$	102 (±5)	−2.58
DMDBODMA	*n*-dodecane	2 M HNO_3	0.09	$1.8\ 10^{-6}$	93 (±5)	−5.92
DMDBTDMA	*n*-dodecane	H_2O	0.25	$1.7\ 10^{-6}$	96 (±5)	−3.41

Figure 1.8: Critical micelle concentration (CMC), surface excess concentration (Γ) and area per molecule (A_0) obtained from tensiometric measurements at the alkane/water interface for malonamide/alkane solution contacted with H_2O or HNO_3 at room temperature (23 °C) [61, 66].

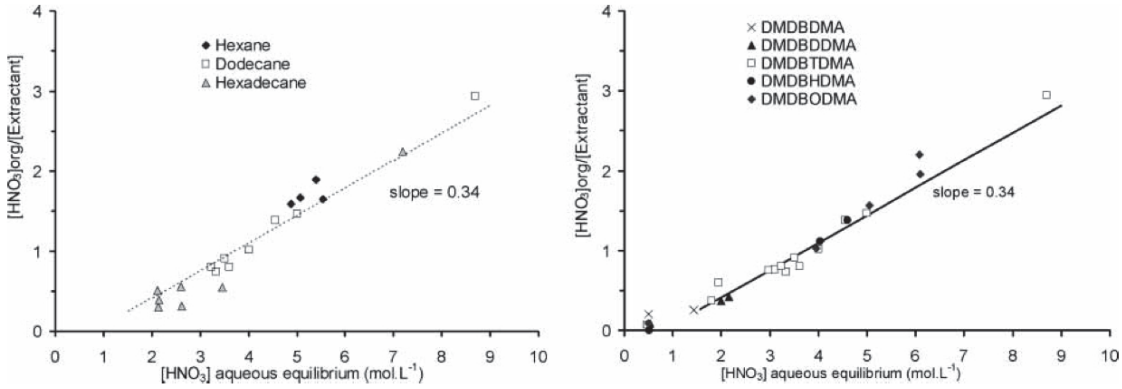

Figure 1.9: $[HNO_3]_{org}/[\text{extractant}]$ ratio *vs.* $[HNO_3]_{aq,eq}$. Temperature: 25 °C. The malonamide concentration varies between 0.2 and 1 mol/L in *n*-alkane. (left) for different chain lengths of *n*-alkane with DMDBTDMA as extractant; (right) for different chain lensgths of extractants in *n*-dodecane as diluent [61, 66].

Others works have focused on the aggregation properties but are not discussed here [69].

1.2.2 Previous works on DMDOHEMA

DMDOHEMA is a diamide extractant slightly different than the DMDBTDMA. The three alkyl chains have the same length and have 8 carbons and the middle chain has an oxygen in position 3 that make the polar head a little bit larger than for the DMDBTDMA.
The molecule is slightly more amphiphilic than the previous one. Indeed, the CAC in dodecane or TPH (a branched dodecane) is below $3 \cdot 10^{-2}$ M depending on the chemical potential of the various species in the aqueous phase in contact with the organic phase. Some examples extracted from the work of Loïc Bosland's [63] or Yannick Meridiano's thesis [62] are as shown in Figures 1.10 and 1.11.

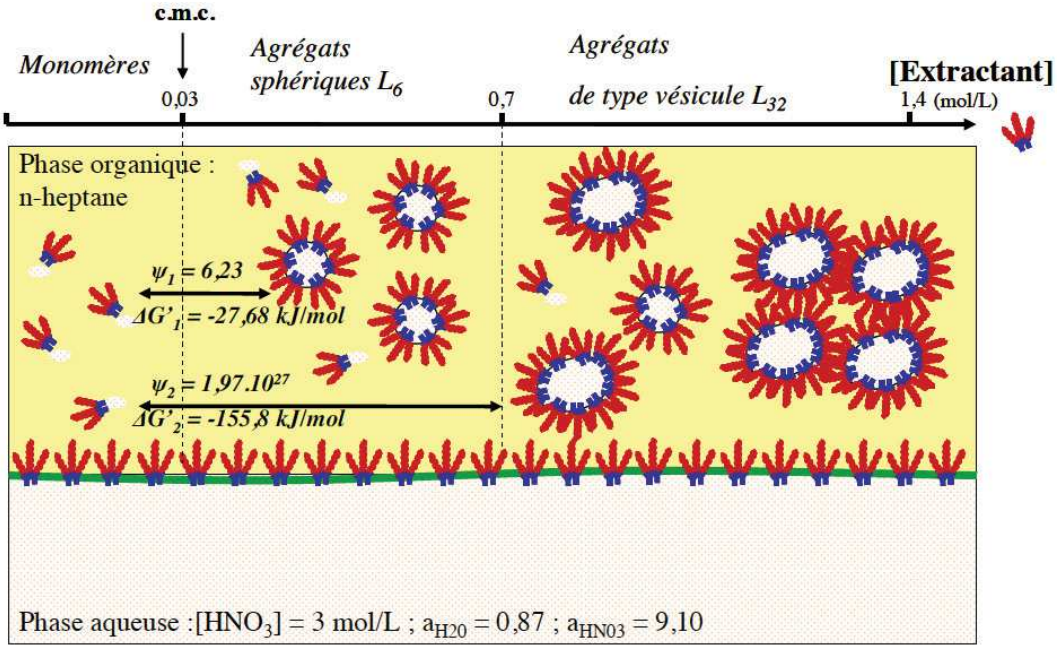

Figure 1.10: Sketch of the aggregation of the DMDOHEMA in heptane contacted with an aqueous phase of nitric acid depending on the extractant concentration. Studied system: DMDOHEMA (0,01 to 1,4 mol/L) in heptane contacted with an aqueous phase of HNO_3 (2.93 mol/L) at 24 °C [62].

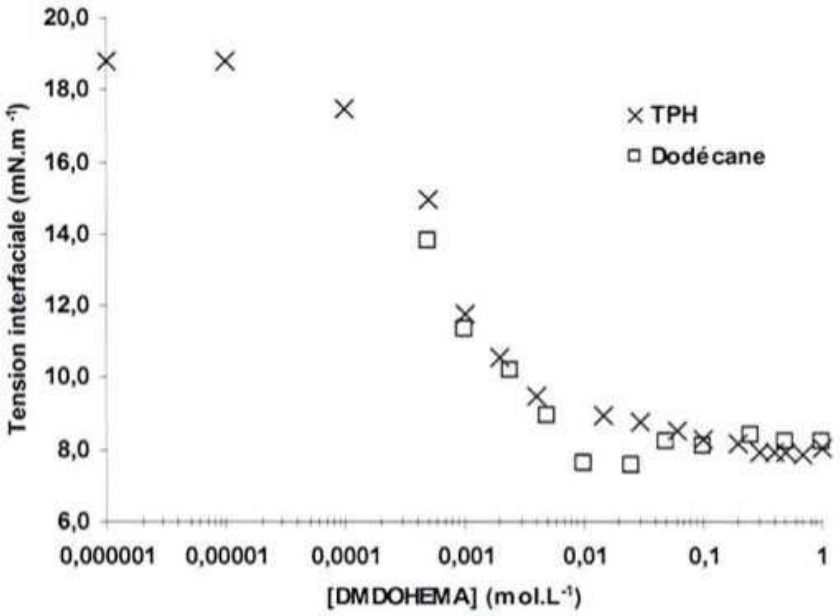

Figure 1.11: Influence of the organic solvent on the interfacial tension. Interfacial tension *vs* DMDOHEMA concentration in TPH or Dodecane (mol/L) contacted with a nitric acid aqueous phase (3 mol/L) [63].

Below the CAC and like the DMDBTDMA system, the extractant in the organic phase is under the form of monomers with the polar head partially hydrated. Above the CAC, aggregates are in equilibrium with the monomers with an aggregation number (>4) depending on the extractant and solute concentration. For the system in contact with pure water, in the analysis of the ratio water/extractant or solute/extractant in the organic phase and as a function of the extractant concentration (see Figure 1.12) then Bosland [63] has determined three regimes summarized as follows:

- 0.01<[DMDOHEMA]<0.04 mol/L: the ratio $[H_2O]$/[DMDOHEMA] decreases,
- 0.04<[DMDOHEMA]<0.1 mol/L: the ratio $[H_2O]$/[DMDOHEMA] is constant,
- 0.1<[DMDOHEMA]<1 mol/L: the ratio $[H_2O]$/[DMDOHEMA] increases and the diamide molecules extract more water.

For the second case with nitric acid (3 mol/L) in water, the results are:

- 0.01<[DMDOHEMA]<0.025 mol/L: the ratio $[H_2O]/[DMDOHEMA]$ decreases, and $[HNO_3]/[DMDOHEMA]$ is constant,
- 0.025<[DMDOHEMA]<0.1 mol/L: the extracting ratio of water and nitric acid are equal and increase. The DMDOHEMA extracts more water and acid,
- 0.01<[DMDOHEMA]<0.025 mol/L: the ratio $[H_2O]/[DMDOHEMA]$ increases faster than $[HNO_3]/[DMDOHEMA]$. The water extraction mechanism changes at 0.1 mol/L.

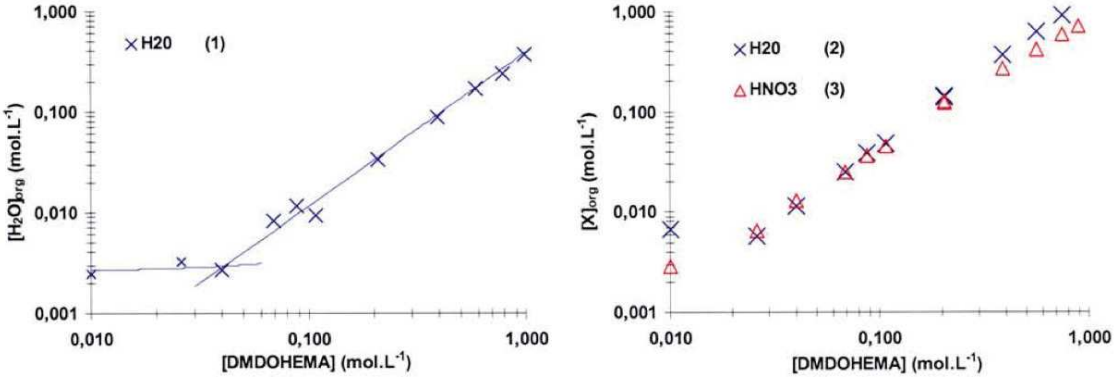

Figure 1.12: (Left) Amount of water extracted (mol/L) *vs* DMDOHEMA concentration in TPH (mol/L) contacted with a water aqueous phase. (Right) Amount of water and nitric acid extracted (mol/L) *vs* DMDOHEMA concentration in TPH (mol/L) contacted with a nitric acid aqueous phase (3 mol/L) [63].

This work was performed in TPH but is was shown that the partitioning of the water or acid is independent on the organic solvent (see Figure 1.13). Only the CAC for the DMDBTDMA varies with the solvent alkyl chain length. Longer carbon chain is, higher the CAC is.

Concerning the partioning of Lanthanide ions, Meridiano has studied the DMDOHEMA in heptane and in contact with various aqueous phase containing Europium nitrate ($Eu(NO_3)_3$) in lithium nitrate or nitric acid aqueous solution [62]. The lithium ions are not complexed by the extractant and they are used only for decreasing the water activity. It was shown by Y. Meridiano that the CAC, as well as the limit of the third phase formation, appears at lower extractant concentration when lanthanide salts are in solution. The reasons are related to the curvature

of the extractant interface within the aggregates for the CAC and to the stronger dipole interaction between the aggregates for the third phase formation. For this type of extracatnt we did not found in the literature the solute/extractant in the organic phase at the appearance of the third phase like for the DMDBTDMA system.

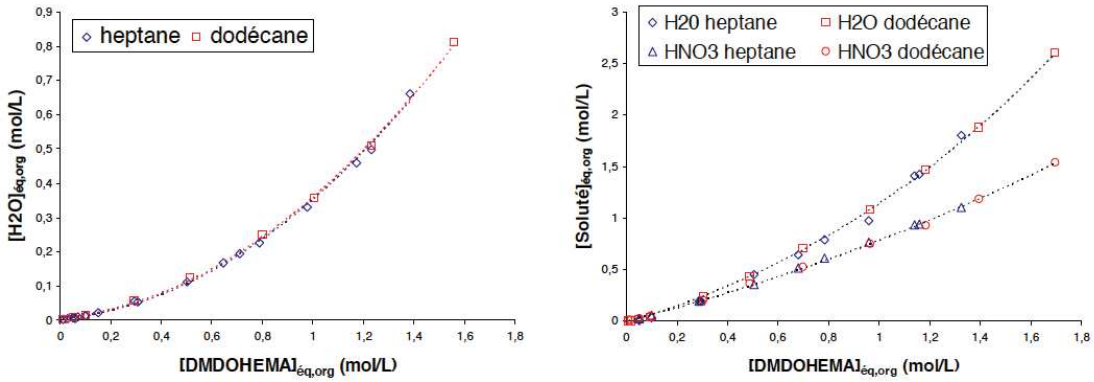

Figure 1.13: Influence of the organic solvent (heptane/dodecane) on the extraction of water and/or nitric acid in the organic phase from a (left) neutral aqueous phase $LiNO_3$ or (right) acid HNO_3 [62].

1.3 Comparison between DMDOHEMA and DMDBTDMA

The studies on two type of malonamide, the DMDBTDMA and the DMDOHEMA have shown that these molecules behave like a surfactant with a packing parameter larger than 1, making inverted aggregates in an organic phase. The nanometric core of these aggregates is neutral and contains some water, some acid or some hydrated pair of ions[1] depending on chemical potential of the water phase in contact with the organic phase.
However some differences exist, such as the value of the CAC which is about ten times lower for the DMDOHEMA than for the DMDBTDMA, the sign of a amphiphilic character more pronounced for the former than for the latter.

Another difference that exists and which was not mentioned in the cited works is related to the kinetic of ion transfer. It has been published in 2014 by Simonin

[1]It exists some debates on the fact that the neutral extractant can form charged aggregates that can fluctuates with the transfer of ions between to individual aggregates.

et al. [13]. By using a specific rotating cell, the authors have studied the extraction kinetics of europium nitrate with these two extractants and their conclusions were: *"The extraction kinetics of Europium(III) cation by DMDBTDMA at 22 °C seems to be very fast and the process seems to be controlled by diffusion. The slow interfacial reaction kinetics reported in the literature using a Lewis-type cell might well have been caused by the effect of a remaining diffusion layer in the organic phase. The kinetics of extraction by DMDOHEMA is found to be slower than by the former extractant at 22°C, but it accelerates rapidly with temperature and becomes fast at 33 °C."*.

Another way to qualify this difference is to consider that the energy barrier, or level at the interface as described in Figure 1.1, can vary as a function of the extractant used due to the conformation and distribution of these molecules at the liquid/liquid interface. This energy level can be higher than the free energy within the aqueous phase and ion transfer that can be only diffusion limited or kinetics limited and so very sensitive to temperature. This is why it is important to be able to describe the extractant structuration at the interface, in equilibrium with those in bulk as well as the distribution of all the other species across the interface. Very few papers exist on this subject [15, 16, 70, 71, 72] and understanding the interfacial structure at water/oil interface, remains from our point of view a key point to understand the extraction process.

In the case of Simonin et al. [13] the questions are: do the DMDBTDMA and DMDOHEMA have a different conformation at liquid/liquid interfaces? How is this structure related to their behaviour in the extraction process? To answer to these questions we focus in this thesis work on the liquid/liquid interface. For the very first time we propose a work combining x-ray and neutron reflectometry experiments. On one side the x-rays allows to determine the distribution of heavy ions across the interface, on the other side neutrons are sensitive to the extractant and solvent distribution. By combining the two, our target is to understand the structuration of extractant and solute at the liquid/liquid interface, trying to explain the different extraction rules found in previous work for DMDBTDMA and DMDOHEMA.

We have focused also our research on systems containing low amount of extractants for two reasons. First performing reflectivity measurement requires to go through a large amount of liquid as we will explained in the next chapter. That means if the concentration of each species are too high the recorded signal will be too low due to a strong radiation absorption and it will be difficult to collect data in a reasonable time. One of the first objectives was to follow the kinetics of

equilibrium related to the ion transfer and so we decided to work around the CAC for each extractant in order to be able to collect data in a minimum of time and as a function of a reasonable time sequences.

Another point is related to previous SHG studies in the group at ICSM. They have indeed shown that the rate of transfer of acid in a system DMDBT-DMA/dodecane/water with nitric acid was increasing when approaching the CAC from the lower concentration side and then becomes low above the CAC even if the amount of protons transferred from water to oil phase is higher increasing the extractant concentration. This means that the "interfacial resistance", in that case, could be considered lower close to the CAC, lower than at very low or at higher concentration of extractants. This results was unexpected and, although this study was unique and has to be repeated in considering other systems, it was necessary to study the interfacial structure of these type of system close to the CAC.

After the first reflectivity tests at the beginning of this thesis work, we realized that kinetics experiments will be difficult to managed and so experiments were performed mainly at equilibrium once the chemical potential of each species are equal in both organic and aqueous phases that means once the transfer (or extraction) of water molecules and ions (when they are used) was established.

1.4 Twenty years of x-ray and neutron reflectivity at liquid/liquid interface

In 1999, Schlossman et al. wrote *"An outstanding problem in the area of interfacial phenomena is the determination of structure at liquid-liquid interfaces, This structure is relevant, for example, to the understanding of electron and molecular transfer across biological membranes and to the partitioning of solvents and metal ions across liquid-liquid interfaces."* [73].

To understand the interfacial structure between two immiscible liquids techniques as interfacial tension [61, 66, 74, 75, 47], second harmonic generation [48] and ellipsometry [76] have been developed or used as mentioned before.

On the other hand, in the past twenty years, many efforts have been made to develop x-ray and neutron scattering techniques to investigate the liquid/liquid interface.

The first neutron reflectivity data at the liquid/liquid interface have been pub-

lished by Lee et al. [77]. The authors write *"We have overcome the problem of neutron absorption in the upper oil phase by using thin oil layers of well controlled thickness"*.. With this setup they report the study of a surfactant at the water-octane interface.

A similar setup has been used in 1993 for the study of β-casein at the hexane-water interface [78]. A sketch of the sample cell used and extracted from Ph.D thesis of Mario Campana [79] is shown in Figure 1.14.

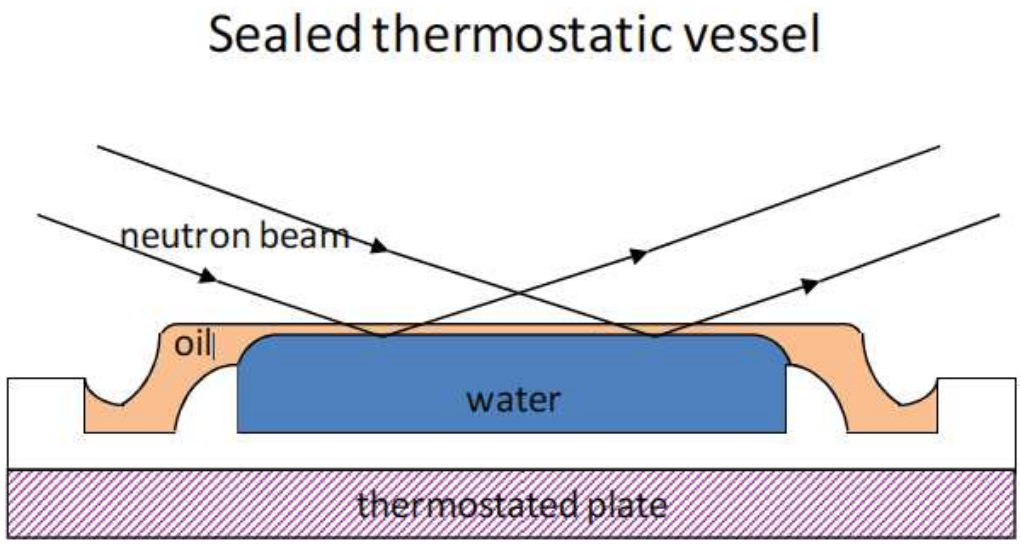

Figure 1.14: Experimental setup for the neutron reflectivity experiment to study β-casein layers at the hexane-water interface [78, 79].

With this type of setting, a layer of 10-20 μm was created on the top of the water surface. In 1999 Zarkakhsh et al. [80] published their technical development to study the liquid/liquid interface. A schematic view of their cell is shown in Figure 1.15.

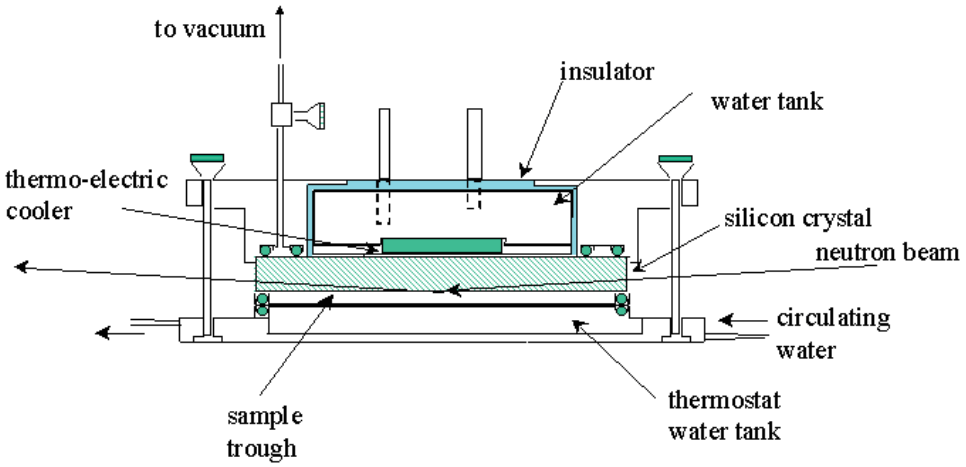

Figure 1.15: A schematic diagram of the experimental cell used to measure the reflectivity from an oil/water interface [80].

In his thesis work, Mario Campana [79] describe the apparatus shown in the Figure above as follows: *"The cell consists of a circular stainless steel trough with an external diameter of 100 mm, which contains the aqueous phase. A circular silicon block, with a diameter of 100 mm and thickness of 10 mm, is used as solid substrate. The block is rendered hydrophobic by means of silane coupling (deposition of C1-layer) prior to use to ensure wettability by the oil phase. After deposition of the oil layer on the silicon block surface, the solid substrate and the stainless steel trough are sandwiched and no leakage is ensured by an o-ring present in the trough. The water phase can be inserted or withdrawn from the cell by syringing it through two greaseless valves. A circulating water bath is connected to two thermostatic water chambers, one above the silicon block and one below the stainless steel trough, insuring a constant and adjustable temperature throughout the whole duration of the measurement. Background scattering arising from the cell is minimised by using a boron external wall that almost fully covers the inner cell, leaving just enough space for the incoming and outgoing neutron beam."*.

This type of cell has been used in several occasions for neutron experiments to study buried interface and adsorption of polymers or surfactants at the hexadecane-water interface [81, 82]. This setting has the great advantage of reducing the neutron attenuation[1] since the beam crosses a silicon block (and a thin deuterated oil

[1]The details of neutron attenuation crossing a liquid are explained in the section 3.4.1.

layer) which has an high transmission coefficient for neutrons.
As Mario Campana refers [79], the oil is deposited on the hydrophobized silicon surface with a spin coater and subsequently freezed. Afterwards, the silicon block with the oil layer (≈ 2.1 μm) is contacted with the water surface.

Despite the advantage in using silicon block to reduce the neutron attenuation, this cell has not been used for our experiments. The purpose of this thesis work is to study the interfacial structure of liquid-liquid interface at various extractant concentrations in oil. For our purpose the possibility of varying the organic phase composition during the experiment is needed. The cell proposed by Zarbakhsh et al. [83] has the limitation that for each extractant concentration a new cell has to be prepared and setup. Moreover, the intial purpose of this thesis was to study the kinetics of extraction which requires the use of ml of oil instead of μl.

A similar cell for neutron reflectivity experiments is presented by Webster et al. [83] to study the interface between water and 1,2-dichloroethane interface. A schematic view of the cell is shown in Figure 1.16.

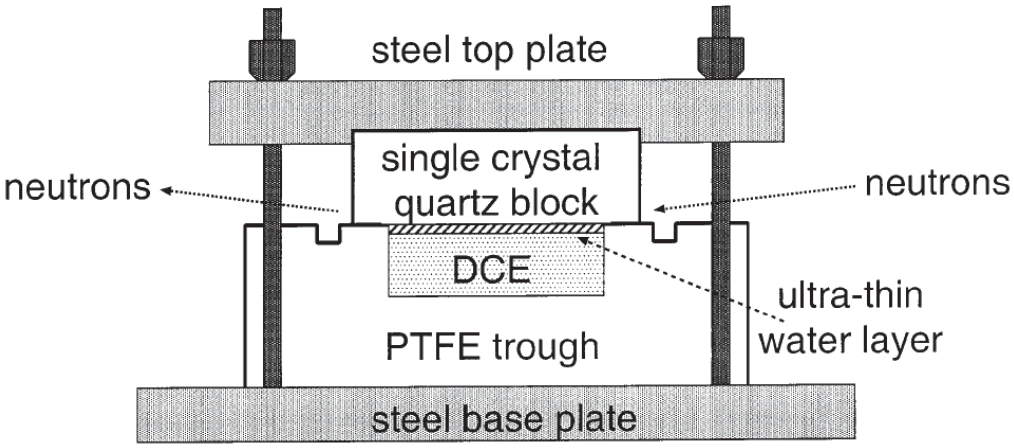

Figure 1.16: A schematic diagram of the experimental cell used to measure the reflectivity from DCE/water interface [83].

In this case, the cell has been designed to study the interface between water and an oil denser than water. As previously written, despite the advantage of a beam crossing a quartz block, this cell has not been used for our experiments due to the reverse geometry of water and oil[1]

[1]For this thesis work an oil ligther than the water, as dodecane, has been used.

Concerning x-ray scattering experiments at liquid/liquid interfaces, we have found two interesting developments in literature.
The first paper, published in 1999 by Schlossman et al. [73], reports a study of the water-hexane interface. Due to the interfacial tension at the alkane/water interface (≈50 mN/m), the authors propose a cell with tilted walls to flatten the liquid-liquid interface. A schematic view of the cell is shown in Figure 1.17.

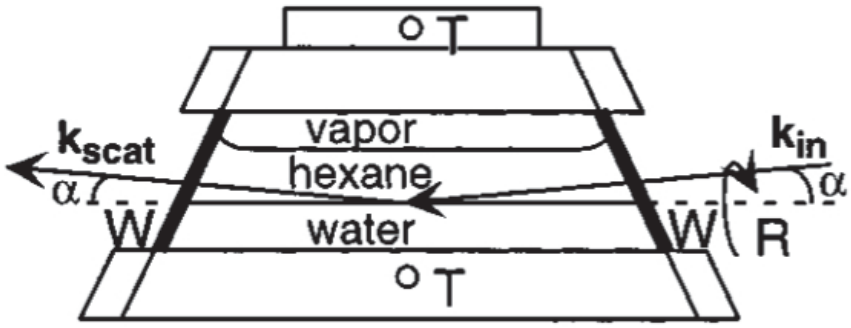

Figure 1.17: A schematic diagram of the experimental cell used to measure the reflectivity from hexane/water interface by x-ray reflectivity experiment [73]. W=mylar windows, T=thermistor to measure temperature, R=rotation about the horizontal used to fine tune the sample flatness. $\mathbf{k}_{in}$ is the incoming x-ray wave vector, $\mathbf{k}_{scat}$ is the scattered wave vector, α is the angle of incidence and reflection.

As the authors claim in their work, *"[..]the mylar windows are slanted 25° from the vertical to reduce the curvature of the interface. This curvature is due to the contact angle of the meniscus where the water-hexane interface is in contact with the windows of the sample cell."* [73]. The flat interface is needed so that the beam is reflected at the same reflection angle for different parts of the interface.
The geometry proposed in this work is interesting to flatten the water/oil interface but has the limitation that it works only for a fixed interfacial tension. It means that if a different oil is substituted to the hexane a different tilting angle for the walls has to be chosen. Moreover, if surfactants or amphiphiles are added to one of the two phases, the contact angle between liquids and walls will change, bending the interface.
As we have written above, this type of geometry has been taken into account for this thesis work but not used because incompatible with the need to work with extractants[1] at different concentrations.

[1]As mentioned before, the extractant have an amphiphile behaviour producing a variation

More recently, in 2014 Schlossman et al. [16] propose a different cell for x-ray reflectivity experiments coupled with fluorescence. A schematic view of the sample cell extracted from their work is shown in Figure 1.18.

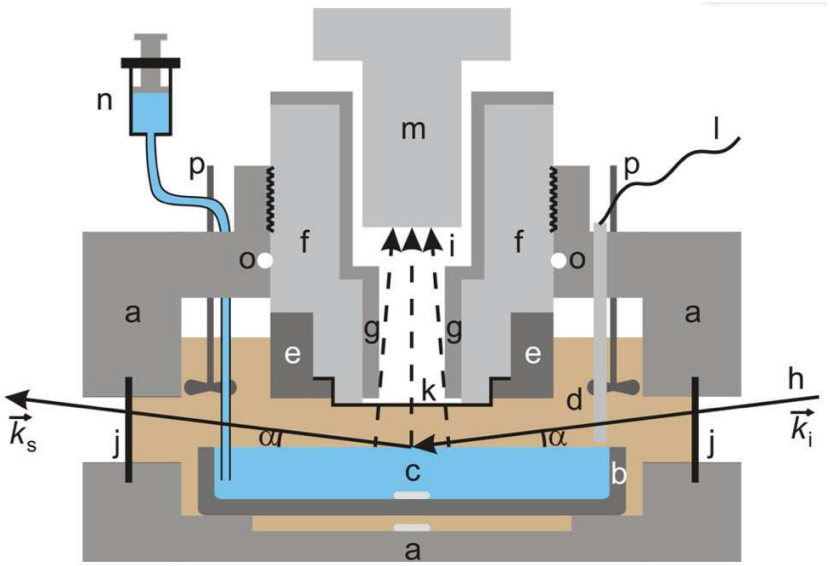

Figure 1.18: Cross-sectional view of the sample cell proposed by Schlossman et al. [16]. Main components of the cell are indicated as (a) Teflon coated aluminum mainframe, (b) glass tray, (c) aqueous phase, (d) organic phase, (e) stainless steel cap, (f) detector well, (g) Teflon collimator, (h) X-ray beam: $\vec{k}_i$, incident X- ray wave vector; $\vec{k}_s$, scattered or reflected wave vector, and angles of incidence and reflection, α, (i) fluorescent X-ray beams from the sample, (j) Mylar windows (150 μm thick), (k) Kapton window (7 μm thick), (l) platinum resistance temperature probe (Omega PT 100), (m) Vortex-60EX energy dispersive detector with 60 mm snout, (n) syringe, (o) Teflon O-ring, and (p) Teflon propellers. Two Teflon coated stir bars are placed in and below the glass tray.

In the previous cell the flat interface was obtained with tilted walls. In the cell shown in Figure 1.18 the water-oil interface is pinned on the rim of the glass tray and the water level is adjusted with a syringe. In this way it is possible to obtain a flat liquid/liquid interface. This is an interesting development, allowing the control of the interfacial curvature for all type of oil with or without surfactants or amphiphiles which was one of the disadvantage of the setup shown in Figure 1.17.

in the interfacial tension at the water-oil interface. This effect would have required one cell for each sample.

As shown in section 3.4.2 this type of geometry has been considered for the liquid/liquid cell built for this thesis work with some differences to reduce the volume of the organic phase.

CHAPTER 2

Reflectivity: Theory and Data Analysis Procedure

2.1 X-ray and Neutron Reflectivity

In the previous chapter we have reminded some of the main studies in bulk phases and at the liquid/liquid interface for understanding the rules governing solvent extraction. The characterization of aggregates in bulk is possible with small angle scattering experiments [32, 40, 62, 67, 68, 84, 85] (x-ray and neutrons) and extractant interfacial properties can be deduced by interfacial tension measurements [47, 61, 66, 74, 75]. In this thesis work we use the x-ray and neutron reflectometry to obtain structural information at the liquid/liquid interface along the normal direction.
The combination of x-rays and neutrons, can be very helpful to understand the structure at the liquid/liquid interface. X-rays allow us to reveal the distribution of aqueous solutes (salts, nitric acid) and neutrons are the perfect tool to understand the structuration of solvents and extractants.
We will explain in this chapter the main principles of x-ray and neutron reflectivity techniques [17, 86] and data analysis procedure followed for this thesis work.

2.1.1 Refraction index

An electromagnetic plane wave described by its electric field $\mathbf{E}(r) = \mathbf{E}_0 exp\,(i\mathbf{k}\cdot\mathbf{r})$, which penetrates into a medium characterized by an index of refraction $n(r)$,

propagates according to Helmoltz equation:

$$\nabla^2_{\mathbf{r}}\mathbf{E}(\mathbf{r}) + k^2 n(\mathbf{r})^2 \mathbf{E}(\mathbf{r}) = 0 \tag{2.1}$$

where $k = 2\pi/\lambda$ is the modulus of the wavevector $\mathbf{k}$ and λ denotes the x-ray wavelength. Treating the N atoms per unit volume as harmonic oscillators with resonance frequencies ω_j, the refraction index is given by

$$n(\mathbf{r}) = 1 + N(\mathbf{r})\frac{e^2}{\varepsilon_0 m}\sum_{j=1}^{N}\frac{f(\omega)}{\omega_j^2 - \omega^2 - 2i\omega\eta_j} \tag{2.2}$$

where ω is the frequency of the incoming wave, e is the charge and m the mass of the electron. η_j is the damping factor and f_j is the forced oscillation strength of atom j. The formfactor f_j is a complex number, $f_j = f_j^0 + f_j^{'}(E) + if_j^{''}(E)$, with the dispersion and absorption corrections, $f_j^{'}(E)$ and $f_j^{''}(E)$ dependent on the radiation energy E[1]. Since for x-rays[2] $\omega > \omega_j$, or far from an adsorption edge, the refraction index can be written as

$$n(\mathbf{r}) = 1 - \delta(\mathbf{r}) + i\beta(\mathbf{r}) \tag{2.3}$$

with the dispersion and absorption terms

$$\delta(\mathbf{r}) = \frac{\lambda^2}{2\pi}\rho(\mathbf{r})\sum_{j=1}^{N}\frac{f_j^0 + f_j^{'}(E)}{Z} \tag{2.4}$$

$$\beta(\mathbf{r}) = \frac{\lambda^2}{2\pi}\rho(\mathbf{r})\sum_{j=1}^{N}\frac{f_j^{''}(E)}{Z} = \frac{\lambda}{4\pi}\mu(\mathbf{r}) \tag{2.5}$$

where we define the x-ray Scattering Length Density[3] (**SLD**) $\rho(\mathbf{r}) = r_e\zeta(\mathbf{r})$ as the product between the classical electron radius $r_e = e^2/4\pi_0 mc^2 \approx 2.81 \cdot 10^{-15}$ m and the elctron density $\zeta(\mathbf{r})$ and $Z = \sum_j Z_j$ is the total number of electrons in the unit cell and $\mu(\mathbf{r})$ is the linear absorption coefficient.. Neglecting $f_j^{'}(E)$ and approximating $f_j^0 \approx Z_j$, we can rewrite the equation 2.2:

$$n(\mathbf{r}) = 1 - \frac{\lambda^2}{2\pi}\rho(\mathbf{r}) + i\frac{\lambda}{4\pi}\mu(\mathbf{r}) \tag{2.6}$$

[1]We can express the form factor in terms of energy (keV) or wavelength (Å) remembering the relation between the two:

$$E(\lambda) = \frac{12.4}{\lambda}.$$

[2]Typic $\omega \approx 10^{19}$ Hz.

[3]The x-ray SLD of water is $\rho(r) = 9.43 \cdot 10^{-6}$ Å^{-2}.

The dispersion $\delta(\mathbf{r})$ is a positive number of the order 10^{-6} for x-rays. The absorption $\beta(\mathbf{r})$ is typically one or two orders of magnitude smaller. Both dispersion and absorption are proportional to the electron density $\zeta(\mathbf{r})$.

2.1.2 Reflectivity in the kinematical approximation

In quantum theory the scattering process can be described by the time-indipendent Schrödinger equation:

$$(\nabla_{\mathbf{r}}^2 + k^2)\psi(\mathbf{r}) = V(\mathbf{r})\psi(\mathbf{r}) \tag{2.7}$$

A comparison with the Helmoltz equation, imposes to connect the scattering potential $V(\mathbf{r})$ to the refraction index as follows:

$$V(\mathbf{r}) = k^2(1 - n^2(\mathbf{r})). \tag{2.8}$$

With the Green's function $G(\mathbf{r} - \mathbf{r}')$ as solution of the equation

$$(\nabla_{\mathbf{r}}^2 + k^2)G(\mathbf{r} - \mathbf{r}') = \delta(\mathbf{r} - \mathbf{r}') \tag{2.9}$$

and $\psi_0(\mathbf{r}) = exp(i\mathbf{k} \cdot \mathbf{r})$ the solution of the associated homogeneous differential equation

$$(\nabla_{\mathbf{r}}^2 + k^2)\psi_0(\mathbf{r}) = 0 \tag{2.10}$$

the solution of the Equation 2.7 satisfies the integral equation:

$$\psi(\mathbf{r}) = \psi_0(\mathbf{r}) + \int G(\mathbf{r} - \mathbf{r}')V(\mathbf{r}')\psi(\mathbf{r}')d^3\mathbf{r}'. \tag{2.11}$$

For an outgoing spherical wave, the Green's function has the form

$$G(\mathbf{r} - \mathbf{r}') = -\frac{1}{4\pi}\frac{exp(ik\left|\mathbf{r} - \mathbf{r}'\right|)}{|\mathbf{r} - \mathbf{r}'|}. \tag{2.12}$$

By identifying ψ_0 with the incoming plane wave $\psi_i = exp(i\mathbf{k} \cdot \mathbf{r})$, Equation 2.11 becomes:

$$\psi(\mathbf{r}) = \psi_i(\mathbf{r}) - \frac{1}{4\pi}\int V(\mathbf{r}')\frac{exp(ik\left|\mathbf{r} - \mathbf{r}'\right|)}{|\mathbf{r} - \mathbf{r}'|}\psi(\mathbf{r}')d^3\mathbf{r}' \tag{2.13}$$

where the second terms describes the scattered wave:

$$\psi_s(\mathbf{r}) = -\frac{1}{4\pi}\int \frac{exp(ikR)}{R}V(\mathbf{r}')\psi(\mathbf{r}')d^3\mathbf{r}' \tag{2.14}$$

where $R = \left|\mathbf{r} - \mathbf{r}^{'}\right|$ is the distance between the source point $\mathbf{r}^{'}$ and the field point $\mathbf{r}$. Substituting $\psi(\mathbf{r}) = \psi_i(\mathbf{r}) + \psi_s(\mathbf{r})$ into the Equation 2.14 we obtain:

$$\begin{aligned}\psi_s(\mathbf{r}) = & -\frac{1}{4\pi}\int \frac{exp(ikR)}{R} V(\mathbf{r}^{'})\psi_i(\mathbf{r}^{'})d^3\mathbf{r}^{'} \\ & -\frac{1}{4\pi}\int \frac{exp(ikR|)}{R} V(\mathbf{r}^{'})\psi_s(\mathbf{r}^{'})d^3\mathbf{r}^{'}.\end{aligned} \tag{2.15}$$

The first term is the first order Born approximation and is due to direct illumination of $V(\mathbf{R})$ by the incident wave $\psi_i(\mathbf{r}^{'})$. The second term is the multiple scattering effect because the source term $V(\mathbf{r}^{'})\psi_s(\mathbf{r}^{'})$ is due to the illumination of the scatterer by the scattered wave $\psi_s(\mathbf{r})$, which itself arises from $V(\mathbf{r}^{'})$. If we assume a stratified medium, changing in perpendicular direction to the interface, the potential $V(\mathbf{r}^{'})$ can be considered constant in the plane. In these hypotesis $V(\mathbf{r}^{'}) = V(z^{'})$ with $z^{'}$ perpendicular to the interface and neglecting multiple scattering effects,replacing $\psi_s(\mathbf{r}) = exp(i\mathbf{k}\cdot\mathbf{r})$ in Equation 2.15 we obtain

$$\psi_s(\mathbf{r}) = -\frac{1}{4\pi}\int \frac{exp(ikR)}{R} V(z^{'})exp(i\mathbf{k}\cdot\mathbf{r}^{'})d^3\mathbf{r}^{'}. \tag{2.16}$$

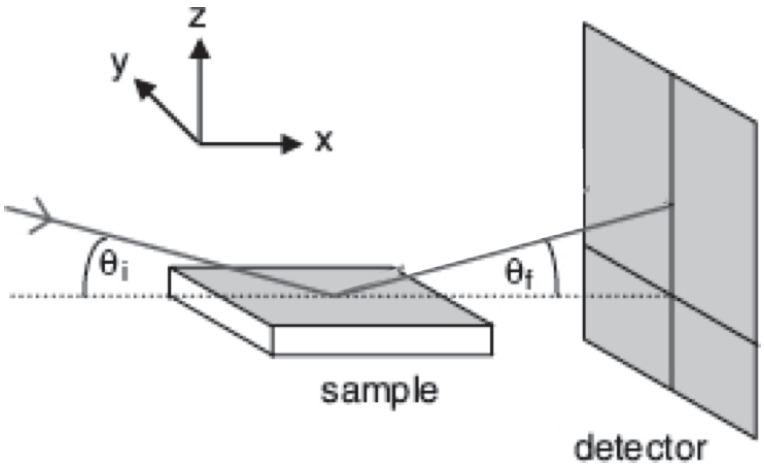

Figure 2.1: Sketch of the specular reflectivity geometry. θ_i and θ_f represent the incoming and outcoming angle (for x-ray and neutron) and they are identical ($\theta_i = \theta_f$). The xy-plane is parallel to the radiation direction and z axes is perpendicular to the surface/interface. Figure taken from [87].

In the specular direction, outgoing scattered wave vector and incident wave vector are at the same angle θ with the $xy-$plane and the scattering plane coincides

with the $yz-$plane. In the far field the distance R can be approximated as

$$R \approx R_0 - y^{'} cos(\theta) + \frac{x^{'2} + y^{'2} sin^2(\theta)}{2R_0} \tag{2.17}$$

and $R_0 \approx r + z^{'} sin^2(\theta)$. By replacing R by R_0 in Equations 2.16 and 2.17 we can integrating with respect to $x^{'}$ and $y^{'}$ over $(-\infty, \infty)$ obtaining:

$$\psi_s(\mathbf{r}) = -\frac{i}{Q_z} exp(i\mathbf{k} \cdot \mathbf{r}) \int V(z^{'}) exp(iQ_z z^{'}) dz^{'} \tag{2.18}$$

where $Q_z = 2ksin(\theta)$. Thus, in the first order Born approximation the reflectance is proportional to the Fourier transform of the potential with respect to the vertical position z

$$r(Q_z) = -\frac{i}{Q_z} \int V(z) exp(iQ_z z) dz = \frac{1}{Q_z^2} \int \frac{dV(z)}{dz} exp(iQ_z z) dz. \tag{2.19}$$

From the Equations 2.3 and 2.8 we can write the complex scattering potential $V(z)$ as

$$V(z) = k^2[1 - n^2(z)] \approx 2k^2[\delta(z) - i\beta(z)]. \tag{2.20}$$

Neglecting absorption ($\beta(z) \ll \delta(z)$)[1] $V(z)$ becomes real and can be approximated by $4\pi\rho(z)$ with $\rho(z)$ defined in equations 2.4 and 2.5. The reflectivity $R(Q_z)$, equal to the modulus square of the reflection coefficient, can be written as:

$$R(Q_z) = |r(Q_z)|^2 = \frac{16\pi^2}{Q_z^4} \left| \int \frac{d\rho(z)}{dz} exp(iQ_z z) dz \right|^2. \tag{2.21}$$

2.1.3 Parratt's Formalism

As shown in Equation 2.21, the reflected intensity is proportional to the Fourier transform of the SLD variation in the direction perpendicular to the surface. This SLD variation is the information we seek by reflectivity experiments. In this section it will be explained how this SLD profiles are related to the reflected and transmitted coefficients in a sample with multiple layers[2].

Let us consider an electromagnetic plane wave hitting a sharp surface and splitting into a reflected and a transmitted wave. The vectors of their electric fields are given by:

$$\mathbf{E_r}(\mathbf{r}) = r_{s,p} \mathbf{E_i}(\mathbf{r}) exp(i\mathbf{Q} \cdot \mathbf{r}) \tag{2.22}$$

[1] This is true for small Z material.

[2] The layers will be indicated with the subscript i.

$$\mathbf{E_t}(\mathbf{r}) = t_{s,p}\mathbf{E_i}(\mathbf{r})exp[i(\mathbf{k_t} - \mathbf{k_i}) \cdot \mathbf{r}] \tag{2.23}$$

where $\mathbf{Q}$ is the wave vector transfer, $r_{s,p}$ and $t_{s,p}$ are the reflection and transmitted coefficient respectively for s and p polarization. Those coefficients can be calculated by the Fresnel formulas from classical optics:

$$r_s = \frac{k_{i,z} - k_{t,z}}{k_{i,z} + k_{t,z}}, \qquad r_p = \frac{n^2 k_{i,z} - k_{t,z}}{n^2 k_{i,z} + k_{t,z}} \tag{2.24}$$

$$t_s = \frac{2k_{i,z}}{k_{i,z} + k_{t,z}}, \qquad t_p = \frac{2k_{i,z}}{n^2 k_{i,z} + k_{t,z}}. \tag{2.25}$$

If α_i is the incidence angle and α_t the transmitted one, we can define:

$$k_{i,z} = ksin(\alpha_i), \qquad k_{t,z} = ksin(\alpha_t) = k\sqrt{n^2 - cos^2(\alpha_i)} \tag{2.26}$$

which are the z-components of the wave vectors of the incoming and transmitted waves.

When n is smaller than unity and this happens in most cases (see Equation 2.6), there exists a critical angle $\alpha_c \approx \sqrt{2\delta}$ below which the real part ok $k_{t,z}$ vanishes and total external reflection ($r \approx 1$) occurs. The intensity of the reflected radiation, the so-called Fresnel reflectivity, $r_F = |r|^2$ is given by:

$$R_F(Q_z) = \left| \frac{Q_z^2 - \sqrt{Q_z^2 - Q_c^2}}{Q_z^2 + \sqrt{Q_z^2 - Q_c^2}} \right|^2 \approx \left(\frac{Q_c}{2Q_z} \right)^4 for Q_z \gg Q_c \tag{2.27}$$

where $Q_z = 2ksin(\alpha_i)$ is the z-component of the wave vector transfer $\mathbf{Q}$ and $Q_c = 2ksin(\alpha_c)$ is the critical wave vector transfer that is related to the SLD by the relation $Q_c = \sqrt{16\pi\rho}$. To give an example, in the case of x-ray reflectivity on free water surface with a beam energy equal to 22 keV the critical edge is $Q_c = 0.022$ Å^{-1}.[1]

Extending this formalism to systems consisting of an arbitrary number of homogeneous layers, *Abeles* [88] connected the transmission and reflection coefficients of two consecutive layers via matrices and *Parratt* [89] developed a recursive formalism providing equivalent results.

[1]The neutron case has not been presented yet but the critical edge for a free D_2O surface is $Q_c = 0.018$ Å^{-1} and in the case of H_2O it does not exist because the neutron SLD of the light water is lower than zero.

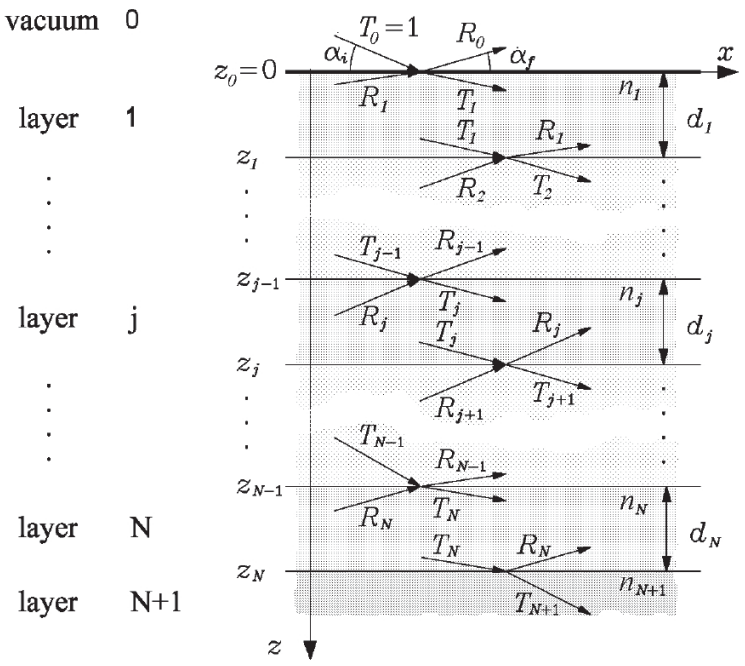

Figure 2.2: Sketch of a system consisting of N layers and $N+1$ interfaces located at z_j. For each interface the amplitude of the reflected and transmitted wave, R_j and T_j is represented. Figure taken from [86].

The ratio $X_j = R_j/T_j$ between the amplitudes of the transmitted and reflected waves at the lower interface j, as shown in Figure 2.2, is given by the recursion formula:

$$X_j = \frac{R_j}{T_j} = exp(2ik_{z,j}z_j)\frac{r_{j,j+1} + X_{j+1}exp(-2ik_{z,j+1}z_j)}{1 + r_{j,j+1}X_{j+1}exp(-2ik_{z,j+1}z_j)} \tag{2.28}$$

with the Fresnel reflection coefficient

$$r_{j,j+1} = \frac{k_{z,j} - k_{z,j+1}}{k_{z,j} + k_{z,j+1}}. \tag{2.29}$$

Since there is no reflection component coming from the bulk of the substrate, the recursion starts with the $R_{N+1} = 0$ and the reflection from the top layer after recursion is:

$$r = |X_0|^2 . \tag{2.30}$$

This approach works for N sharp interfaces. In the presence of roughness or interdiffusion between layers the same method can be used by adding some terms in the calculation of the reflection and transmitted coefficients as shown below.

By starting from the refraction index, in the case of rough layers, for each one of them we can write:

$$n_j(z) = n_j w_j(z) + n_{j+1}[1 - w_j(z)] \tag{2.31}$$

where

$$w_j(z) = \int_{-\infty}^{z} P_j(\zeta - z_j) d\zeta \tag{2.32}$$

is the fraction of material j at the position z. For a Gaussian probability distribution,

$$P_j(z) = \frac{1}{\sqrt{2\pi\sigma_j}} exp\left(-\frac{z^2}{2\sigma_j^2}\right) \tag{2.33}$$

the new Fresnel coefficients are:

$$\tilde{r}_{j,j+1} = r_{j,j+1} exp(-2k_{z,j}k_{z,j+1}\sigma_j^2) \tag{2.34}$$

$$\tilde{t}_{j,j+1} = t_{j,j+1} exp\left[(k_{z,j} - k_{z,j+1})^2 \frac{\sigma_j^2}{2}\right]. \tag{2.35}$$

The new Fresnel coefficients can be used in Equations 2.34 and 2.35 in the Parratt's recursive formula to obtain the reflectivity from N layers with $N + 1$ rough interfaces.

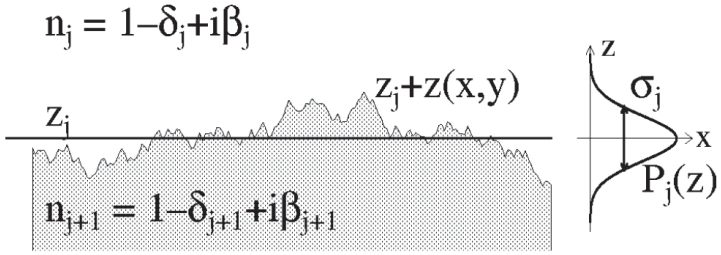

Figure 2.3: Sketch of a rough interface between the layers j and $j + 1$ with mean $z-$coordinate z_j and fluctuations $z(x, y)$. The probability to find the sharp interface at $z_j + z$ is given by the distribution $P_j(z)$ with variance σ_j. In the case of diffuse interfaces, σ_j is the characteristic length of the interdiffusional layer. Figure taken from [90].

2.1.4 X-ray and Neutron: what does it change?

So far we have found all the equations we need to describe the interaction between x-ray radiation and a surface/interface. Of course, due to the duality of

the corpuscolar or wave nature of the neutrons the equations written in the previous paragraphs are still valid for neutron experiments. There is, by the way, a difference in the definition of the quantity $\rho(z)$ defined in equation 2.21, and so the refractive index between the two probes. As shown in Page 28 for x-ray experiments, the refractive index is defined as:

$$n(\mathbf{r}) = 1 - \frac{\lambda^2}{2\pi}\rho(\mathbf{r}) + i\frac{\lambda}{4\pi}\mu(\mathbf{r}) \tag{2.36}$$

where $\rho(\mathbf{r})$ is the x-ray SLD, represented as the product between the electron radius r_e and the electron density $\zeta(\mathbf{r})$. Introducing a complex x-ray SLD[1] $\rho_x(\mathbf{r})$,

$$\rho_x(\mathbf{r}) = r_e\zeta(\mathbf{r}) - i\frac{\mu(\mathbf{r})}{\lambda}, \tag{2.37}$$

the Equation 2.36 can be written as:

$$n_x(\mathbf{r}) = 1 - \frac{\lambda^2}{2\pi}\rho_x(\mathbf{r}). \tag{2.38}$$

In the neutron case, for a system composed by an undefined number of species, we can define the refractive index [91] $n_n(\mathbf{r})$[2]:

$$n_n(\mathbf{r}) = 1 - \frac{\lambda^2}{2\pi}\sum_j \eta_j(\mathbf{r})bj(\mathbf{r}) + i\frac{\lambda^2}{2\pi}\sum_j \eta_j(\mathbf{r})\frac{\sigma_j(\mathbf{r})}{\lambda_0} \tag{2.39}$$

where for the species j at the position $\mathbf{r}$, $\eta_j(\mathbf{r})$ represents the volume fraction, $b_j(\mathbf{r})$ the scattering length and $\sigma_j(\mathbf{r})$ the absoprtion cross section calculated for a wavelength $\lambda_0 \approx 1.80$ Å[92]. By defining a complex neutron scattering lenght density $\rho_n(\mathbf{r})$

$$\rho_n(\mathbf{r}) = \sum_j \eta_j(\mathbf{r})bj(\mathbf{r}) - i\sum_j \eta_j(\mathbf{r})\frac{\sigma_j(\mathbf{r})}{\lambda_0} \tag{2.40}$$

the neutron refractive index can be written as

$$n_n(\mathbf{r}) = 1 - \frac{\lambda^2}{2\pi}\rho_n(\mathbf{r}). \tag{2.41}$$

As defined in Equation 2.21, reflectivity is proportional to the square modulus of the Fourier transform of the **SLD** variation. Using the definition of scattering length density in Equations 2.37 and 2.40 it is possible to write the formula for reflectivity for both neutron and x-ray as follows:

$$R_{x,n}(Q_z) = |r(Q_z)|^2 = \frac{16\pi^2}{Q_z^4}\left|\int \frac{d\rho_{x,n}(z)}{dz} exp(iQ_z z)dz\right|^2. \tag{2.42}$$

[1] To differentiate from the neutron one, we use the subscript x

[2] We denote the neutron refractive index $n_n(\mathbf{r})$ with the subscript n

2.2 Random Sampling for Reflectivity Data

In this thesis work the studied samples are composed by more than one component (water, dodecane, extractant, nitric acid, neodymium and lithium nitrate) and the purpose of the data analysis is to obtain information about the distribution of species across the liquid/liquid interface. To find the exact concentration profile as a function of depth at the interface for each sample, the number of reflectivity curves has to be the same than the unknowns variables in the system. In most cases, for each sample, experiments with x-rays and neutrons were performed, which leads to only two equations related to experimental data. On the other hand, the contrast between x-ray and neutron experiments[1] gives us the opportunity to design data analysis process exploiting the large contrast difference between the two probes.

Equation 2.21 shows that reflectivity is proportional to the modulus square of the SLD variation Fourier transform. In order to determine the distribution profile of each species across the organic/aqueous interface, a Fortran code was developed for Monte Carlo Sampling (**R**andom **M**onte **C**arlo **S**ampling)[2] of the location of the ions and molecules. This approach allowed the analysis of the SLD profiles obtained with the software Motofit[3] [93], refining the distributions fitting x-ray and neutron reflectivity data at the same time.
In this section we will present the mathematics used for the code assuming to have only two experimental curves, one for each probe.

2.2.1 SLD Profile analysis

Let us start from a general case with a system composed by an undefined number Γ of species γ_j with $j = [1, \Gamma]$. For each molecule we define an experimental and theoretical molecular volume $v_{j,exp}$ and $v_{j,theo}$. For a given distance z from the interface, $N_{j,exp}(z)$ and $N_{j,theo}(z)$ represent the experimental and theoretical

[1] With Equations 2.37 and 2.40 we have shown that the x-rays are sensitive to the electron density and the neutrons to the nuclei composition. An example of contrast can be provided for lithium: while in the neutron case the lithium has a negative SLD, in the case of x-ray, by definition, the SLD is positive.

[2] From now on we will refer to the code with the acronym **RMCS**.

[3] We will refer to Motofit as the program use to analyze the x-ray and neutron reflectivity data obtaining a first SLD profile. Motofit represents the first step in the data analysis of this thesis work. The RMCS code, as explained in the text, exploit the SLD profiles found with Motofit as initial guess for a more detailed analysis.

number of molecules for each species and the total number of molecules is given by the sum

$$N(z) = \sum_{j=1}^{\Gamma} N_j(z).$$

For each value of z the experimental and theoretical x-ray SLD can be defined using the equations in paragraph 2.1.4:

$$\rho_{exp,x}(z) = \frac{\sum_{j=1}^{\Gamma} N_{j,exp}(z) Z_j r_e}{\sum_{j=1}^{\Gamma} N_{j,exp}(z) v_{j,exp,x}} - \frac{i}{\lambda} \frac{\sum_{j=1}^{\Gamma} N_{j,exp}(z) \Xi_j}{\sum_{j=1}^{\Gamma} N_{j,exp}(z) v_{j,exp,x}} \tag{2.44}$$

where Z_j is the number of electron and $v_{j,exp,x}$ is the molecular volume for the jth species. Equation 2.44 was obtained by replacing in Equation 2.37

$$\zeta(z) = \frac{\sum_{j=1}^{\Gamma} N_{j,exp}(z) Z_j}{\sum_{j=1}^{\Gamma} N_{j,exp}(z) v_{j,exp,x}} \tag{2.45}$$

$$\mu(z) = \frac{\sum_{j=1}^{\Gamma} N_{j,exp}(z) \Xi_j}{\sum_{j=1}^{\Gamma} N_{j,exp}(z) v_{j,exp,x}} \tag{2.46}$$

proportional to the dispersion and absorption part of the x-ray SLD respectively. The quantity $\rho_{exp,x}(z)$ is obtained via model fitting [93].
On the other hand, the same quantity calculated by the RMCS code can be defined by using the subscript *theo*:

$$\rho_{theo,x}(z) = \frac{\sum_{j=1}^{\Gamma} N_{j,theo}(z) Z_j r_e}{\sum_{j=1}^{\Gamma} N_{j,theo}(z) v_{j,theo,x}} - \frac{i}{\lambda} \frac{\sum_{j=1}^{\Gamma} N_{j,theo}(z) \Xi_j}{\sum_{j=1}^{\Gamma} N_{j,theo}(z) v_{j,theo,x}} \tag{2.47}$$

By keeping the total volume $v_{tot,x}(z)$ constant, we can write:

$$\sum_{j=1}^{\Gamma} N_{j,theo}(z) v_{j,theo,x} = \sum_{j=1}^{\Gamma} N_{j,exp}(z) v_{j,exp,x} = v_{tot,x}(z). \tag{2.48}$$

For the neutron case the same two quantities $\rho_{exp,n}$[1] and $\rho_{theo,n}$ can be defined as follows:

$$\rho_{exp,n}(z) = \frac{\sum_{j=1}^{\Gamma} N_{j,exp}(z) b_j}{\sum_{j=1}^{\Gamma} N_{j,exp}(z) v_{j,exp,n}} - \frac{i}{\lambda_0} \frac{\sum_{j=1}^{\Gamma} N_{j,exp}(z) \sigma_j}{\sum_{j=1}^{\Gamma} N_{j,exp}(z) v_{j,exp,n}} \tag{2.49}$$

[1]Examples of SLD profiles obtained with Motofit are presented in section 2.2.5.

$$\rho_{theo,n}(z) = \frac{\sum_{j=1}^{\Gamma} N_{j,theo}(z) b_j}{\sum_{j=1}^{\Gamma} N_{j,theo}(z) v_{j,theo,n}} - \frac{i}{\lambda_0} \frac{\sum_{j=1}^{\Gamma} N_{j,theo}(z) \sigma_j}{\sum_{j=1}^{\Gamma} N_{j,theo}(z) v_{j,theo,n}} \tag{2.50}$$

obtained replacing the following equation in the Equation 2.40:

$$\sum_j \eta_j(\mathbf{r}) bj(\mathbf{r}) = \frac{\sum_{j=1}^{\Gamma} N_j(z) b_j}{\sum_{j=1}^{\Gamma} N_j(z) v_{j,n}} \tag{2.51}$$

$$\sum_j \eta_j(\mathbf{r}) \sigma_j(\mathbf{r}) = \frac{\sum_{j=1}^{\Gamma} N_{j,exp}(z) \sigma_j}{\sum_{j=1}^{\Gamma} N_{j,exp}(z) v_{j,exp,n}}. \tag{2.52}$$

By fixing the volume

$$\sum_{j=1}^{\Gamma} N_{j,theo}(z) v_{j,theo,n} = \sum_{j=1}^{\Gamma} N_{j,exp}(z) v_{j,exp,n} = v_{tot,n}(z) \tag{2.53}$$

for a given $N_j(z)$, the volume variation due to the substitution of hydrogen with deuterium is taken into account by the formula

$$v_{tot,n}(z) = \frac{\sum_{j=1}^{\Gamma} N_{j,theo}(z) v_{j,theo,n}}{\sum_{j=1}^{\Gamma} N_{j,theo}(z) v_{j,theo,x}} \cdot v_{j,theo,x}(z). \tag{2.54}$$

The two error functions $\epsilon_x(z)$ and $\epsilon_n(z)$ can be introduced:

$$\begin{cases} \epsilon_x(z) = \rho_{exp,x}(z) - \rho_{theo,x}(z) \\ \epsilon_n(z) = \rho_{exp,n}(z) - \rho_{theo,n}(z) \end{cases} \tag{2.55}$$

which are equal to zero if

$$N_{j,theo}(z) = N_{j,exp}(z) \tag{2.56}$$

where $N_{j,exp}(z)$ is the quantity obtained by this data analysis method. By generating for each value of z, a distribution $N_{j,theo}(z)$, trying to minimize the two error functions introduced above, the RMCS code look for the distribution $N_j(z)$ checking the system 2.55 and the equation 2.54.

To start a first analyis of xray and neutron data is performed separately with Motofit to obtain the SLD profile, previously defined as experimental. These SLD profile are provided to the RMCS code[1] who proceeds as follows:

[1]The program needs at least two set of data, one for x-ray and one for neutron.

1. **Set the interface** matching the various profiles to and arbitrary z. This process is called *alignement*;

2. **Create a box** of length $\Delta z = |z_{max} - z_{min}|$ where z_{min} and z_{max} are taken from the SLD profiles at point 1;

3. **Divide the box** in 1 Å thick slices and with a fixed volume;

4. **Fill the slices** with all the species at the initial experimental concentration. For all the $z \in [z_{min}, 0]$ the box is filled with organic components (oil and extractant). For all the $z \in [0, z_{max}]$ the box is filled with aqueous components (water, salts, nitric acid). The initial interface, defined as the separation plane between water and oil, is set at $z = 0$ Å;

5. **Start the random process** from the first slice at $z = z_{min}$:

   (a) A species is randomly chosen;

   (b) For the chosen species with a random process a random amount of molecules is added or removed obtaining a new $N_{j,theo,new}(z)$;

   (c) The SLDs $\rho_{theo,x}(z)$, $\rho_{theo,n}(z)$ and the error functions $\epsilon_x(z)$ and $\epsilon_n(z)$ are calculated;

   (d) If the error functions are both less than or equal a certain value defined as percentage of the $\rho_{x,exp}(z)$ and $\rho_{n,exp}(z)$, the distribution $N_{j,theo,new}(z)$ obtained in (b) is saved as possible solution of the system;

   (e) The program saves the distribution $N_{j,theo,new}(z)$ in $N_{j,theo}(z)$ and starts again from point (a);

   (f) The process is repeated several times[1] for the same slice and then for the next slice until last one;

6. **Repeat the process** at point 4 several times for all the slices and then starting again from point 5 repeating all the process 3000 times.

At the end, all the distributions $N_{j,theo}(z)$ minimizing the error functions defined in Equations 2.55 are saved. Examples are shown in Section 2.2.5.

[1]The number of times is decided from the user. In this thesis work, if not mentioned, this number is fixed to $3 \cdot 10^5$.

2.2.2 The Parratt refinement

After the analysis of the **SLD** profiles the **RMCS** code calculates the average of all the distributions $N_{j,theo}(z)$ which are selected as possible solutions of the system. A second part of the same code starts here, refining the distributions $N_{j,theo}(z)$ to obtain the best fit of experimental reflectivity curves exploiting the Parratt's algorithm. This part of the program is called *Parratt refinement*[1].

For n existing reflectivity curves $R_{l,exp}(Q_z)$ for the same sample, measured with x-rays and/or neutrons, the l^{th} experimental curve can be written as:

$$R_{l,exp}(Q_z) = \frac{16\pi^2}{Q_z^4}\left|\int \frac{d\rho_{l,exp}(z)}{dz} exp(iQ_z z)dz\right|^2 \quad , \quad l = 1, n \tag{2.57}$$

for each of them a theoretical reflectivity curve $R_{l,theo}(Q_z)$, calculated from a theoretical distribution $N_{j,theo}(z)$ exploting the equations 2.47 and 2.50, is defined:

$$R_{l,theo}(Q_z) = \frac{16\pi^2}{Q_z^4}\left|\int \frac{d\rho_{l,theo}(z)}{dz} exp(iQ_z z)dz\right|^2 \quad , \quad l = 1, n \tag{2.58}$$

If the error function for each data is:

$$\chi_l^2 = \frac{1}{N_l - 1}\sum_{Q_z} \frac{\left|R_{l,theo}(Q_z) - R_{l,exp}(Q_z)\right|^2}{\left|\epsilon_l(Q_z)\right|^2} \tag{2.59}$$

where $\epsilon_l(Q_z)$ is the experimental error for the ith curve and each Q_z and N_l the number of experimental points, a global error function can be defined as:

$$\chi_{tot}^2 = \sum_{l=1}^{n} \chi_l^2. \tag{2.60}$$

By minimizing the error function χ_{tot}^2, the distribution $N_{j,exp}(z)$ can be determined. The principle behind this part is the same as before: starting from a given distribution $N_{j,theo}(z)$ the program randomly operates variations minimizing the χ_{tot}^2. In order to do that the program follows the following steps:

1. it averages the distribution $N_{j,theo}(z)$ saved as solution from the **SLD** profile analysis;

[1]The RMCS code and the Parratt refinement are two parts of the same software. We refer to them with different names because the first analyzes the SLD profiles obtained via Motofit[ref motofit] used as initial guess for the RMCS. The second part works directly with the experimental curves collected on the instruments.

2. it choses randomly two numbers z_1 and z_2;

3. for each $z \in [z_1; z_2]$ the program extracts three random numbers: the first one is associated to the species to change, the second to the number of molecule and the third one to select addition or removal of species;

4. following the indications from step 3, the distributions are changed and saved in $N_{j,theo,new}(z)$;

5. the reflectivitiy curve $R_{l,theo}(Q_z)$ for the $N_{j,theo,new}(z)$ are calculated with the Parratt's algorithm[1]

6. the $\chi^2_{tot,new}$ is calculated and:

   (a) if $\chi^2_{tot,new} \leq \chi^2_{tot}$, $N_{j,theo,new}(z)$ is saved in $N_{j,theo}(z)$, $\chi^2_{tot,new}$ is saved in χ^2_{tot} and the program goes back to point 2;

   (b) if $\chi^2_{tot,new} > 2 \cdot \chi^2_{tot}$ the program goes back to point 2;

2.2.3 Error calculation

At the end of the analysis the program has saved all the distributions $N_{j,theo}(z)$ for each minimization step and the best distribution called $N_{j,theo,best}(z)$ with the error function $\chi^2_{tot,best}$. To calculate the errors on the final distribution, the program reads all the previous $N_{j,theo}(z)$ for which:

$$\chi^2_{tot,best} \leq 2\chi^2_{tot} \tag{2.61}$$

and for the jth species the error $\epsilon_j(z)$ at each z is

$$\epsilon_j(z) = MAX\left[|N_{j,theo,best}(z) - N_{j,theo}(z)|\right] \tag{2.62}$$

and the same is done for the error $\epsilon_{R_i}(Q_z)$ associated to the reflectivity curve:

$$\epsilon_{R_l}(Q_z) = MAX\left[|R_{l,theo,best}(Q_z) - R_{l,theo}(Q_z)|\right] \tag{2.63}$$

[1]In the code it is possible to choose the layer thickness and in this thesis work it has been fixed, in the the analysis procedure, to 1 Å. For this reason no roughness has been used.

2.2.4 Special features of the RMCS code

One of the advantage of performing neutron experiment is given by the isotopic substitution. By replacing hydrogen with deuterium, it is possible to collect data on samples with the same structure but with different contrast. By exploiting a co-refining algorithm and analyzing the data together, it is possible to access to structural information difficult to reveal only with one type of data.
The software Motofit [93] allows to co-refine reflectometry data but it remains difficult when data are collected with different radiation source or with instruments with different geometries. The RMCS code[1] has been written to bypass this limitation taking into account all the possible experimental's factors.

As written above, one factor that has to be taken into account is the different geometries of the two instruments exploited for this thesis work. On ID10 at the ESRF, the photon beam pass through the upper phase (dodecane), while on FIGARO at ILL the neutrons cross the lower phase (water). In the RMCS code it is possible to select for each data the type of geometry used in real experiments.

Another advantage of the code is to take into account effects related to the use of monochromatic or polychromatic beam.
On ID10, as shown in section 3.2.1, the energy is fixed to 22 keV (which corresponds to a wavelength $\lambda = 0.5636$ Å) meaning that a monochromatic beam is used. On the contrary on FIGARO, thanks to the time of flight technique, a polychromatic beam is used to investigate the interface/surface affecting the refractive index, as shown in Equation 2.49. Moreover, the imaginary part of the SLD depends on the neutron absorption cross section which is λ-dependent and, for a given wavelength, it is calculated as follows:

$$\sigma(\lambda) = \frac{\lambda}{\lambda_0}\sigma_0 \tag{2.64}$$

where σ_0 is the absorption cross section calculated at $\lambda_0 \approx 1.8$ Å. For example the lithium has a $\sigma_0 = 70.5$ barn[2]. In our experiment a polychromatic beam with wavelength in between 2 Å and 16 Å has been used. From the Equation 2.64 we can see that at the highest wavelength considered in this work, the absorption cross section is eight times larger than at $\lambda = 2$ Å and so the imaginary part of the SLD. More values of σ_0 used for this work can be found in the Neutron Data Booklet [92].
This effect is commonly not taken into account when the imaginary part of the SLD

[1] We refer to RMCS code meaning the entire code including the Parratt refinement.
[2] 1 barn=10^{-24} cm^2.

is negligible or when the beam attenuation is weak enough crossing the sample. In this thesis work, we investigated samples containing lithium and neodymium for which σ_0 is not negligible.

2.2.5 Proof of concept

The RMCS code was first tested on two model systems. An initial distribution was generated and the corresponding SLD profiles and reflectivity curves (x-ray and neutron) were calculated using the formulas shown previously in this chapter[1]. The created data have been analyzed by the RMCS code.

2.2.5.1 Three component system

A first sample system with three components has been created assuming an interface between water and dodecane with an extractant[2] in the organic phase. For the neutron sample we have considered a water phase composed by D_2O and an organic phase composed by the fully protonated extractant and a mixture of H/D dodecane ($C_{12}H_{26}$ and $C_{12}D_{26}$) with a volume ratio 37/63[3]. For the x-ray sample we assume no isotopic substitution and consequently all compounds are fully protonated.
The initial species distribution and the corresponding SLD profiles are plotted in Figure 2.4 while the x-ray and neutron reflectivity curves are shown in Figure 2.5. For all the species the molar volume has been considered constant whatever their position in the bulk or at the interface.

[1]The data used in this section was generated in a Q range similar to the real experimental one.

[2]The molecule chosen is the DMDBTDMA.

[3]For this mixture the corresponding SLD of the dodecane is equal to $4.0 \cdot 10^{-6}$ Å^{-2}.

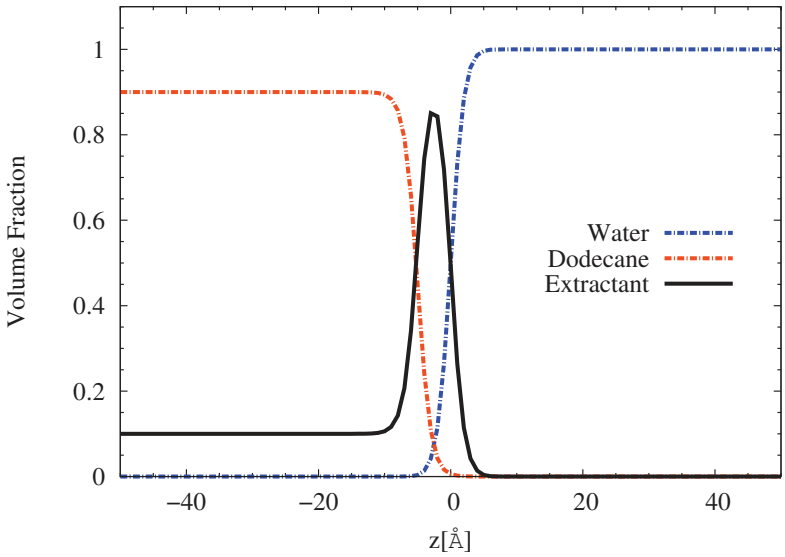

(a) Distribution of Species

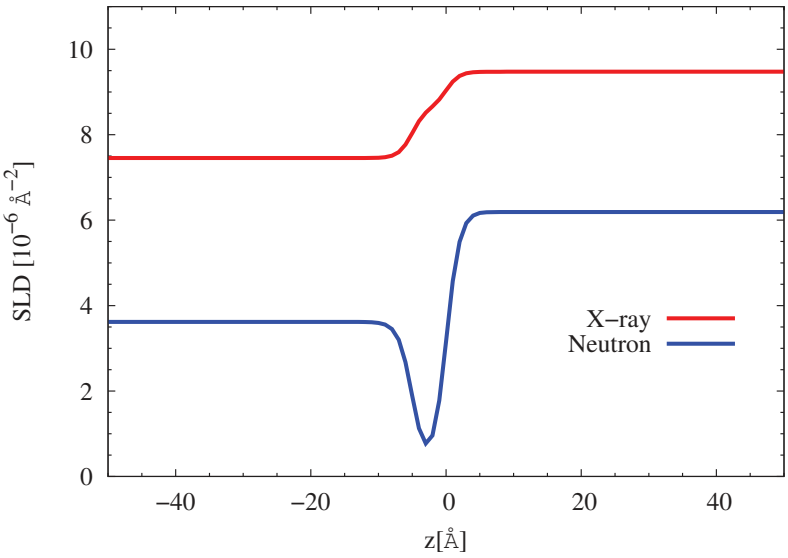

(b) SLD Profiles

Figure 2.4: (a) Distribution of water, dodecane and extractant in volume fraction versus z coordinate. (b) SLD profiles calculated for distribution of species in top panel. The presence of a large amount of fully protonated extractant at the interface produces a deep in the neutron SLD profile and a double shoulder in the x-ray one.

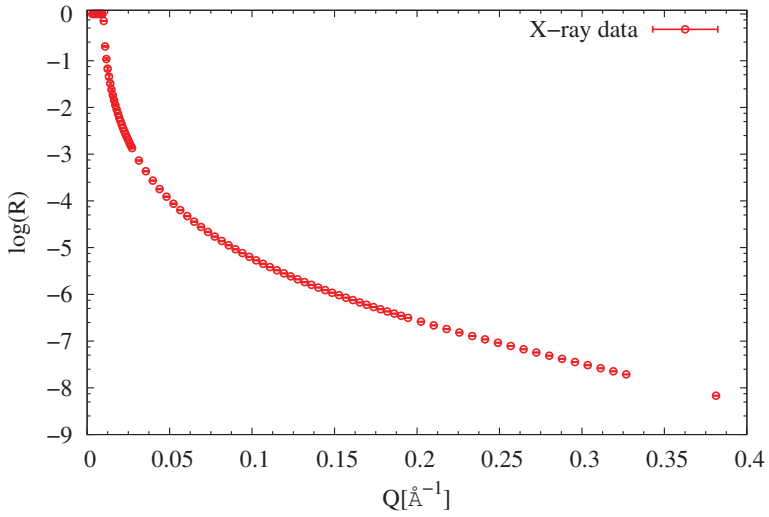

(a) X-ray

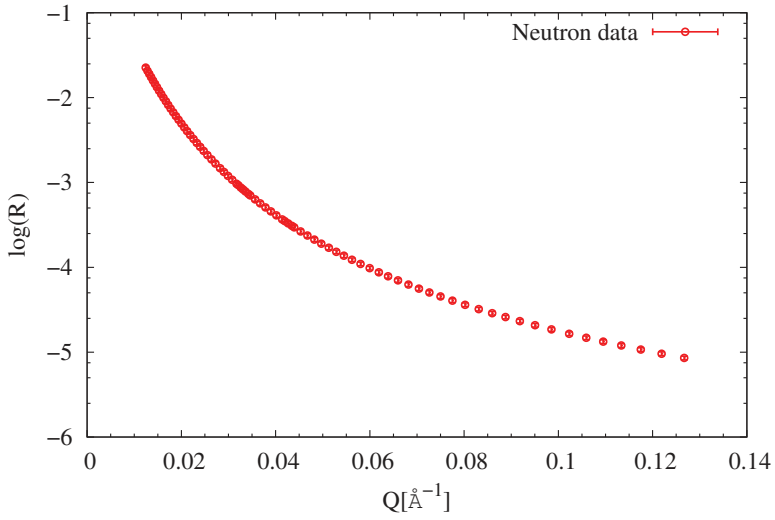

(b) Neutron

Figure 2.5: (a) X-ray and (b) Neutron reflectivity curves calculated, using Parratt's formalism, starting from the SLD profiles shown in panel (b) of Figure 2.4.

The SLD profiles in Figure 2.4 were read by the RMCS code and the possible species distributions have been calculated. Results of the SLD profile analysis are reported in Figures 2.6, 2.7 and 2.8.

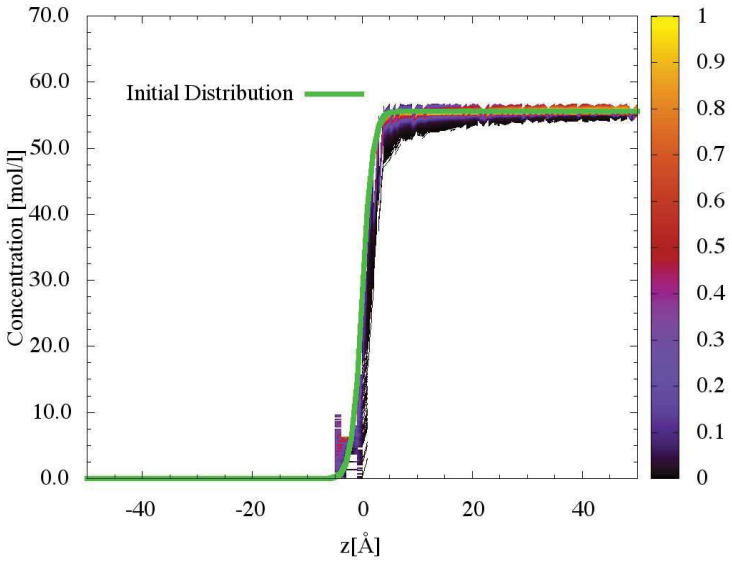

Figure 2.6: Distribution of water. In green the plot of the initial distribution in mol/l. The values calculated by the RMCS code are plotted in three dimensions and the colors represent the probability to find a given amount of water at a each z.

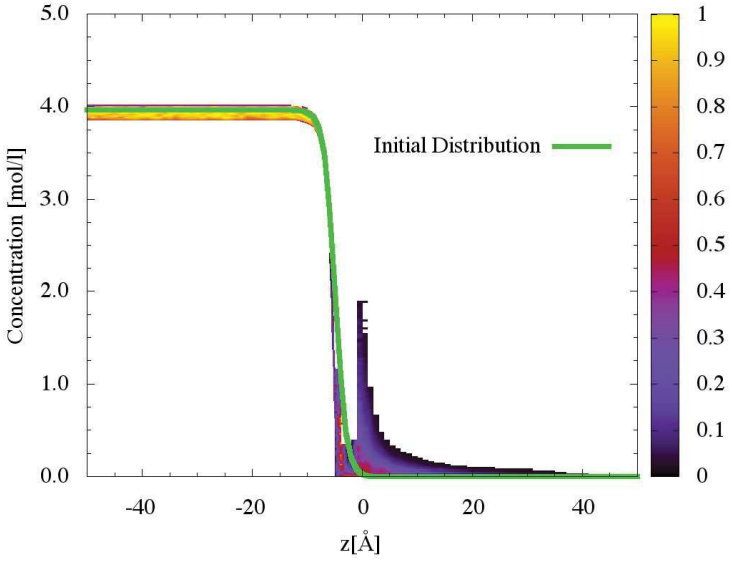

Figure 2.7: Distribution of dodecane. In green the plot of the initial distribution in mol/l. The values calculated by the RMCS code are plotted in three dimensions and the colors represent the probability to find a given amount of dodecane at a each z.

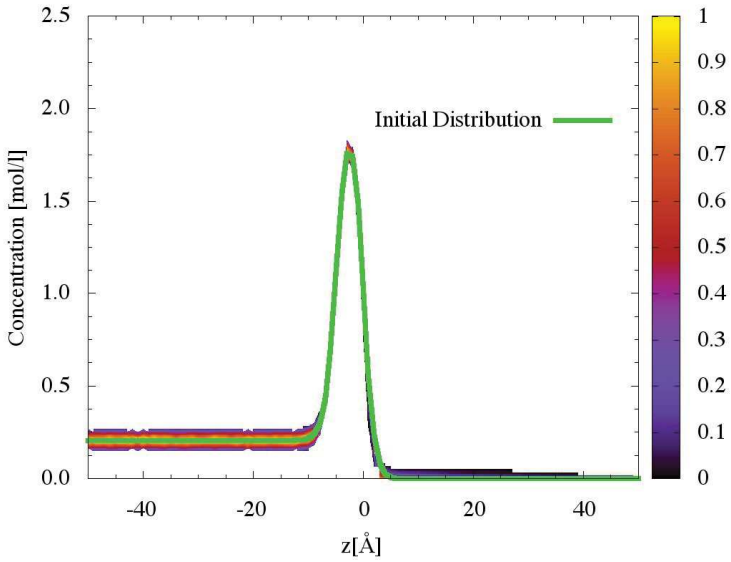

Figure 2.8: Distribution of extractant. In green the plot of the initial distribution in mol/l. The values calculated by the RMCS code are plotted in three dimensions and the colors represent the probability to find a given amount of extractant at a each z.

In Figures 2.6, 2.7 and 2.8 the most probable distribution of species (resulting from the code analysis) is shown in yellow and the real distribution (green line) is superposed to them. Despite the number of unknowns is larger than the number of data sets, the results of the SLD profile analysis shows already a good agreement between the results and the real distribution of species in the samples.
By starting from the average of the possible solutions calculated in the SLD profile analysis, the code uses the Parratt refinement routine to fit the reflectivity data. In the Figure 2.9 are plotted the initial reflectivity curves and the fits while in the Figures 2.10, 2.11 and 2.12 the distribution calculated by the program and compared with the initial one.

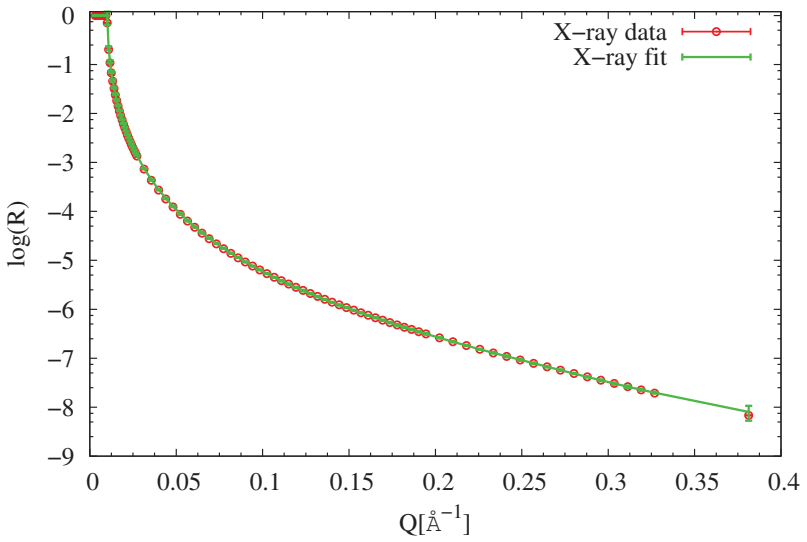

(a) X-ray

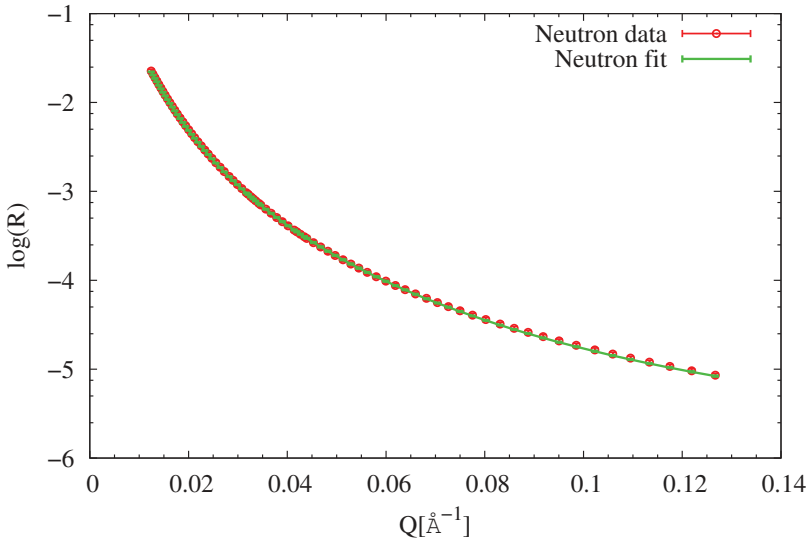

(b) Neutron

Figure 2.9: (a) X-ray Fit in the Parratt Refinement. In red are plotted the initial data with error bars, in green the results of the fitting process. (b) Neutron Fit in the Parratt Refinement. In red are plotted the intiial data with error bars, in green the results of the fitting process.

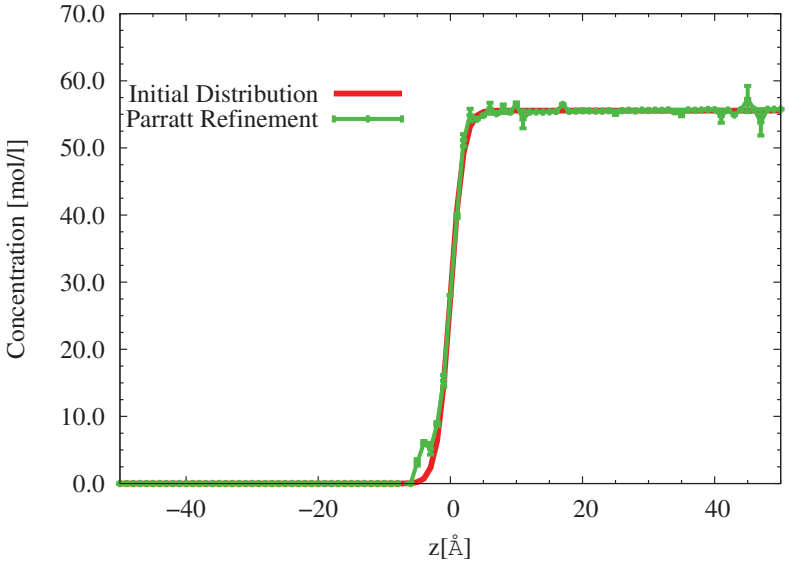

Figure 2.10: Final distribution of water. In light blue the plot of the initial distribution in mol/L, in green the result of the fitting process with error bars.

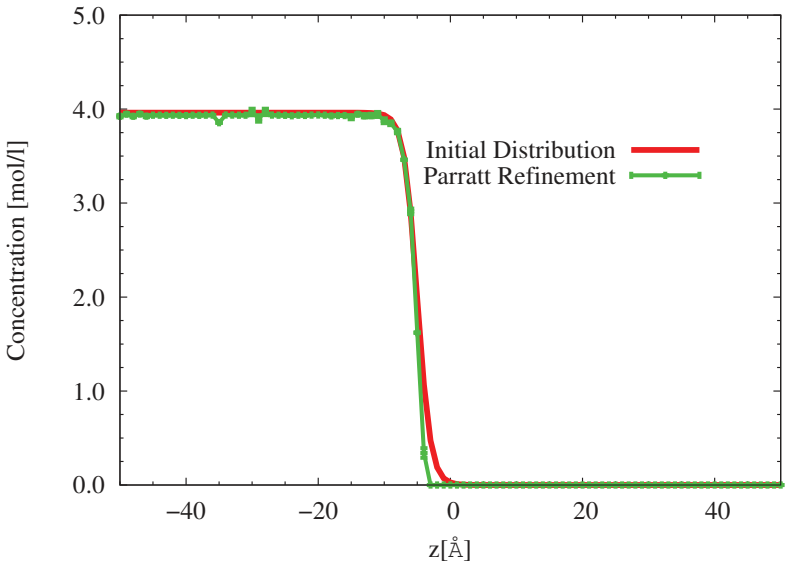

Figure 2.11: Final distribution of dodecane. In light blue the plot of the initial distribution in mol/L, in green the result of the fitting process with error bars.

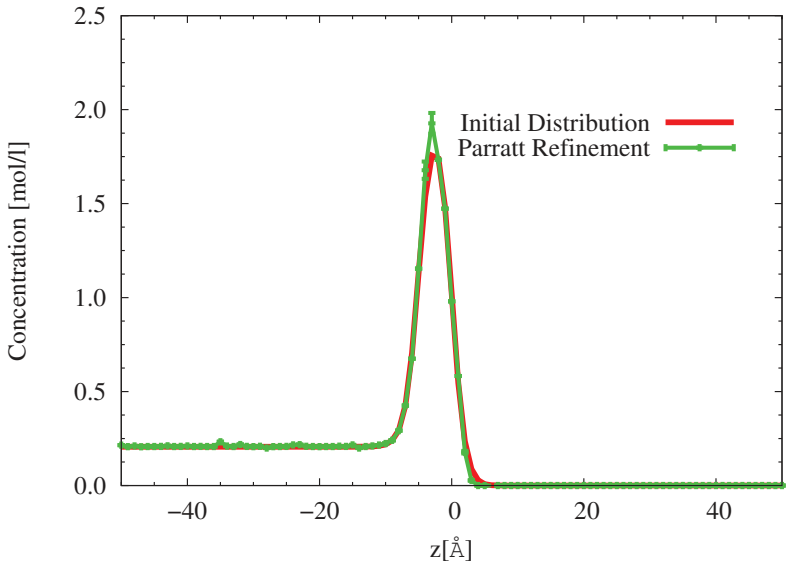

Figure 2.12: Final distribution of extractant. In light blue the plot of the initial distribution in mol/L, in green the result of the fitting process with error bars.

The analysis performed here shows a good agreement between results and real distribution. A small deviation from the real distribution is observed for all the three species in the region -5 Å$\leq z \leq$ 0 Å. This effect is maybe caused by the limited Q range of the neutron reflectivity data , more sensitive to the protonated extractant distribution, limiting the resolution in z. Nevertheless the interfacial structure obtained for the simulated adsorption of extractant is well reproduced despite the number of unknowns (oil,water,extractant) is larger than the number of data sets.

2.2.5.2 Six component system

In a second test the same type of interface was used, with the addition of Lithium and Neodymium Nitrate in the aqueous phase resulting in a six component system[1]. To calculate the neutron SLD profile we have considered the water phase composed by D_2O and the organic phase composed by the fully protonated extractant and a mixture of H/D dodecane ($C_{12}H_{26}$ and $C_{12}D_{26}$) with a volume ratio equal to 37/63[2]. For x-rays we have considered a fully protonated system. The

[1]The salts are considered completely dissociated.

[2]For this mixture the corresponding SLD of the dodecane is equal to $4.0 \cdot 10^{-6}$ Å^{-2}.

arbitrary salt concentration were chosen to be 2 M for Lithum Nitrate and 0.25 M for Neodymium Nitrate. The initial species distribution and corresponding SLD profiles are plotted in Figure 2.13. The reflectivity curves calculated for those distributions are plotted in Figure 2.14.

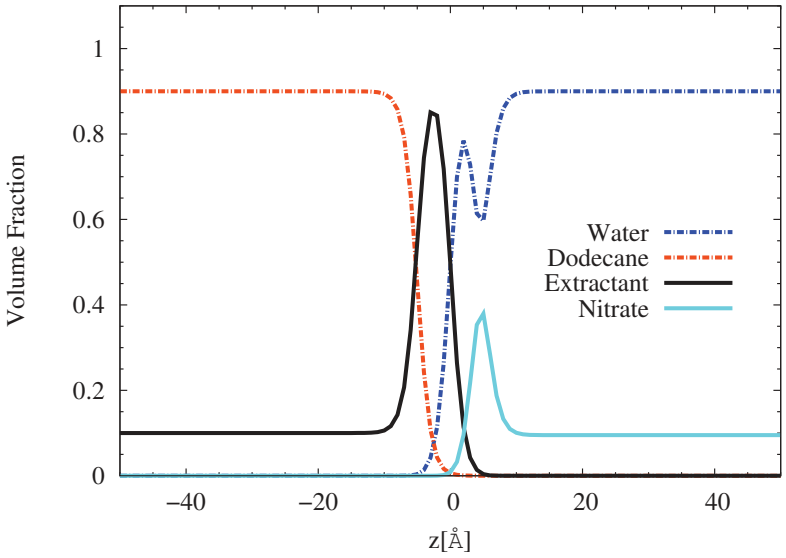

(a) Distribution of Water,Dodecane,Extractant and Nitrate

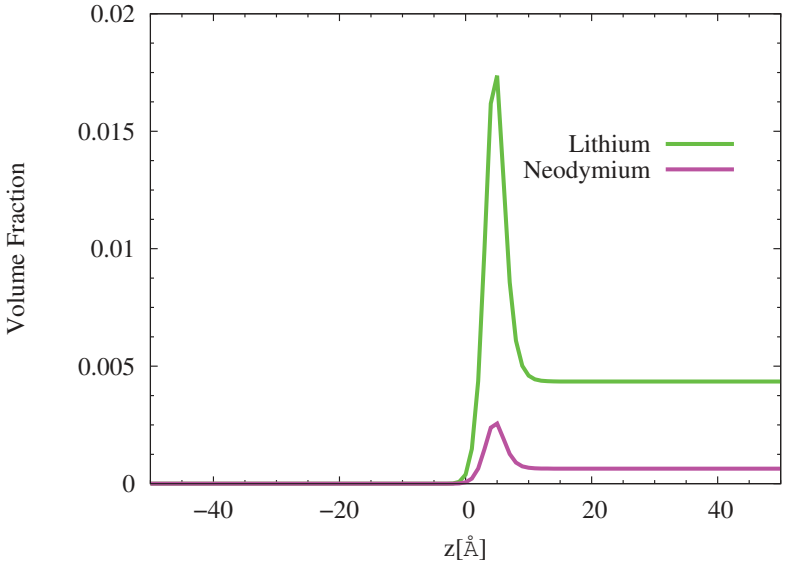

(b) Distribution of Lithium and Neodymium

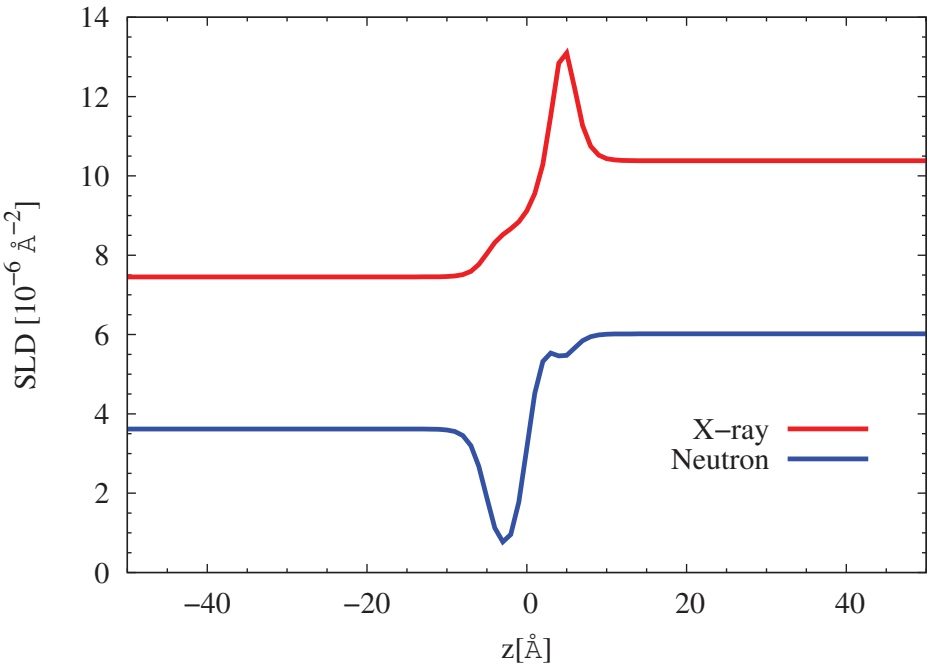

(c) SLD Profiles

Figure 2.13: Distribution of (a) water, dodecane, extractant, nitrate and (b) lithium and neodymium in volume fraction versus z coordinate. (c) SLD profiles calculated for distribution of species in panels (a) and (b). The presence of a large amount of fully protonated extractant at the interface produces a deep in the neutron SLD profil. On the contrary the large amount of ions at the interface produce a peak in the xray SLD profile.

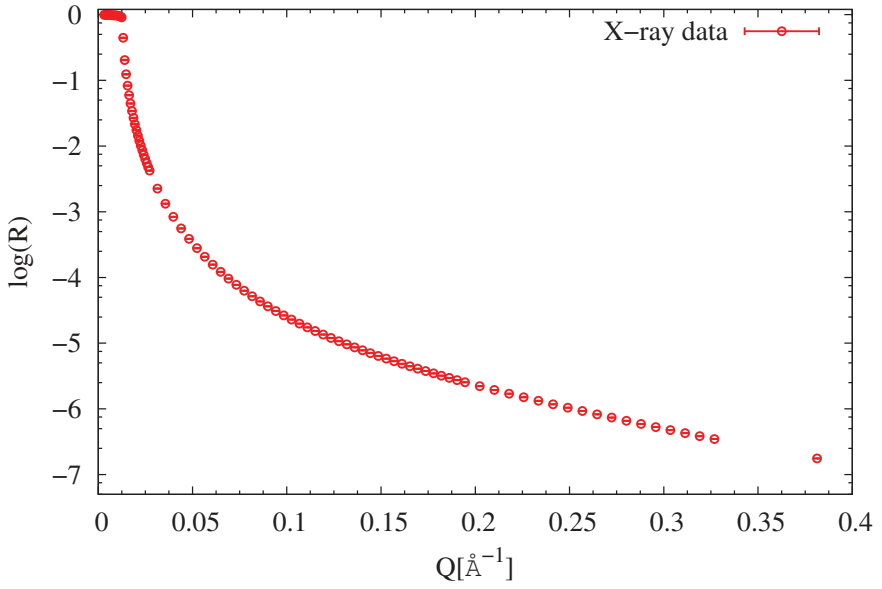

(a) X-ray

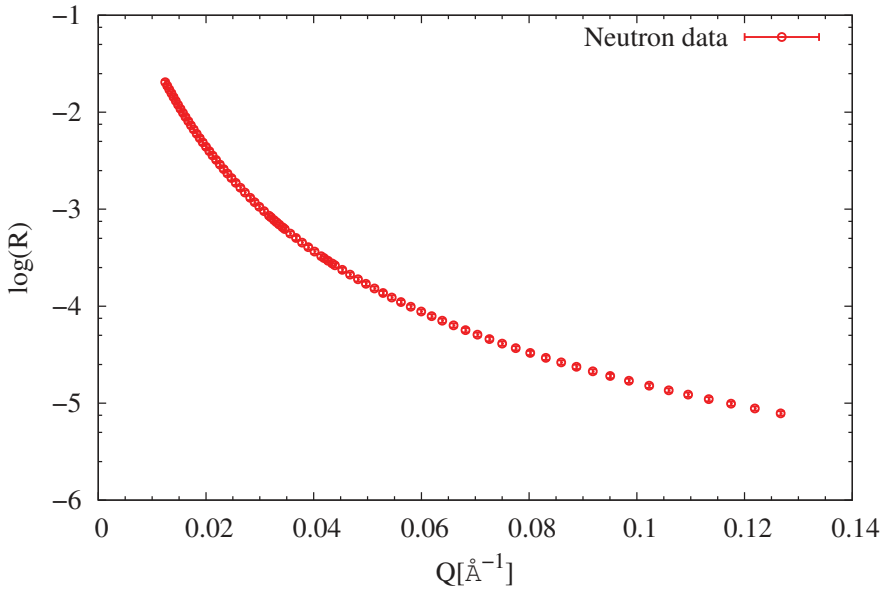

(b) Neutron

Figure 2.14: (a) X-ray (b) Neutron reflectivity curves calculated starting from the SLD profiles shown in panel (c) of Figure 2.13.

SLD profile analysis and Parratt Refinement analysis were performed by the RMCS code. The results of the first step, compared with the original distribution of species, are reported in Figures 2.15, 2.16, 2.17, 2.18, 2.19 and 2.20. We notice a deviation of the ions and extractant distribution from the initial one. The distribution of solvents is well reproduced, especially for water where a small increase of volume fraction has been produced at z=0 Å. The final distributions, calculated using the Parratt refinement, are plotted in the Figures 2.23, 2.24, 2.25, 2.26, 2.27 and 2.28 and reflectivity data and fits are reported in Figures 2.21, 2.22.

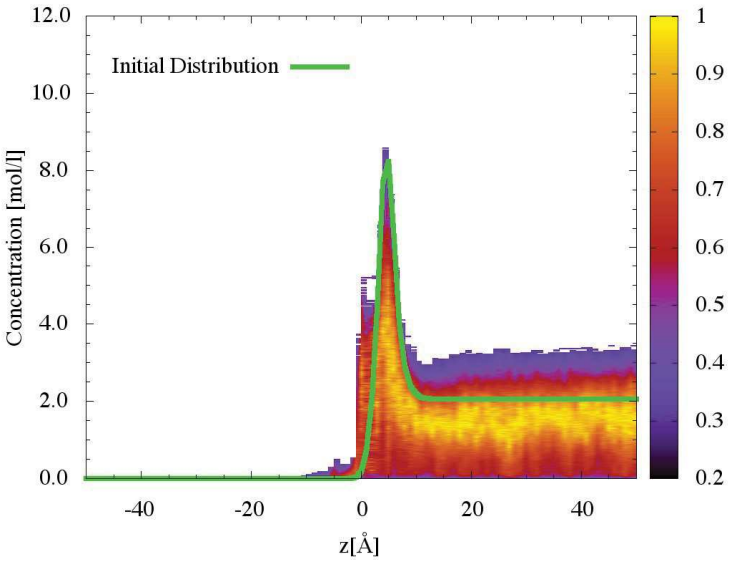

Figure 2.15: Distribution of Lithium. In green the plot of the initial distribution in mol/l. The values calculeted by the RMCS code are plotted in three dimensions and the colors represent the probability for a given amount of Lithium at a each z.

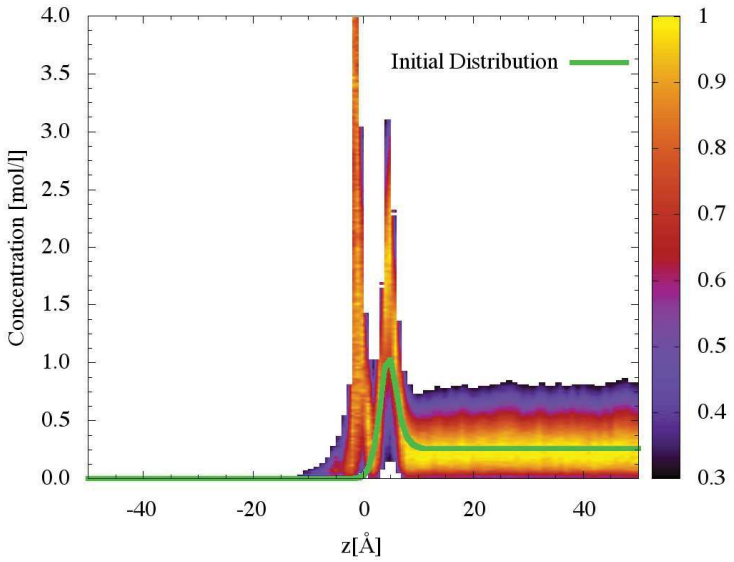

Figure 2.16: Distribution of Neodymium. In green the plot of the initial distribution in mol/l. The values calculeted by the RMCS code are plotted in three dimensions and the colors represent the probability for a given amount of Neodymium at a each z.

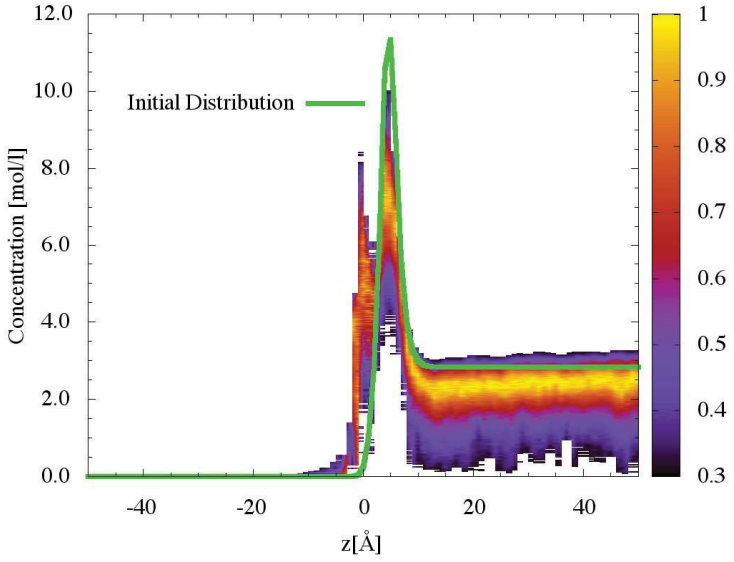

Figure 2.17: Distribution of nitrate. In green the plot of the initial distribution in mol/l. The values calculeted by the RMCS code are plotted in three dimensions and the colors represent the probability for a given amount of nitrate at a each z.

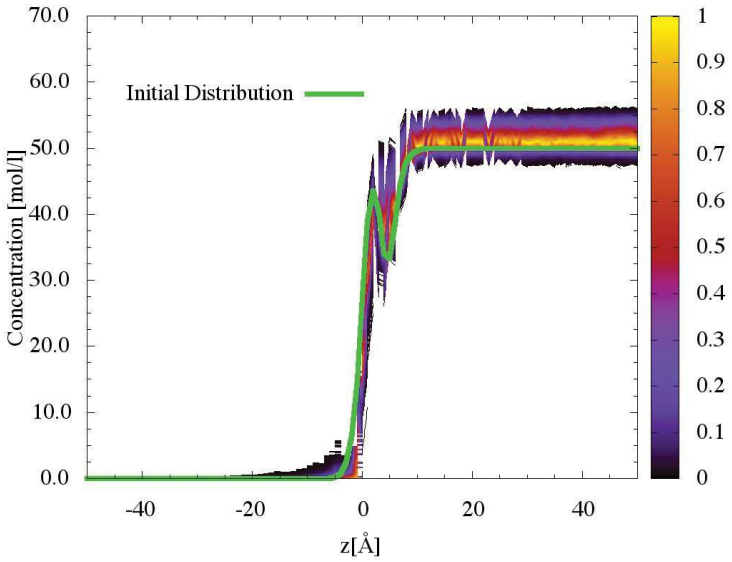

Figure 2.18: Distribution of water. In green the plot of the initial distribution in mol/l. The values calculeted by the RMCS code are plotted in three dimensions and the colors represent the probability for a given amount of water at a each z.

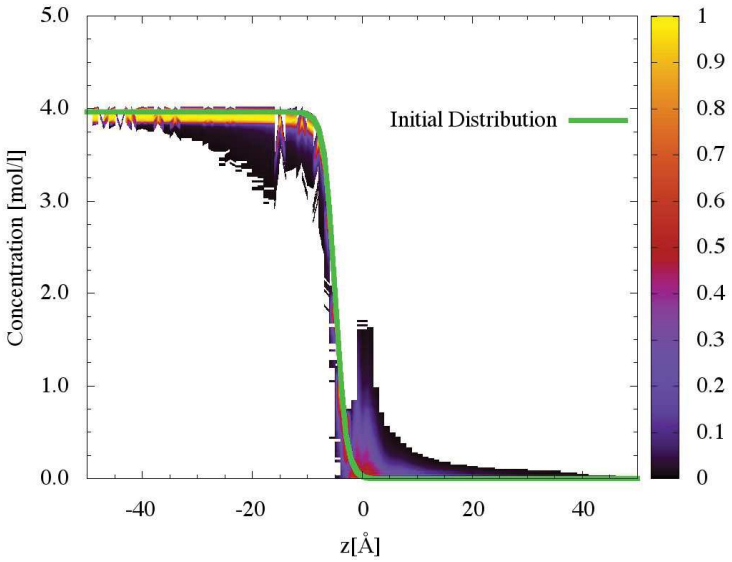

Figure 2.19: Distribution of dodecane. In green the plot of the initial distribution in mol/l. The values calculeted by the RMCS code are plotted in three dimensions and the colors represent the probability for a given amount of dodecane at a each z.

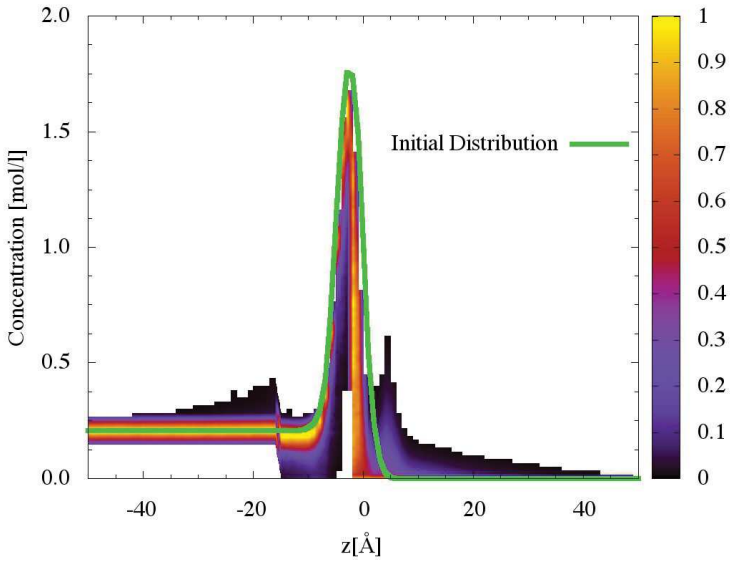

Figure 2.20: Distribution of extractant. In green the plot of the initial distribution in mol/l. The values calculeted by the RMCS code are plotted in three dimensions and the colors represent the probability for a given amount of extractant at a each z.

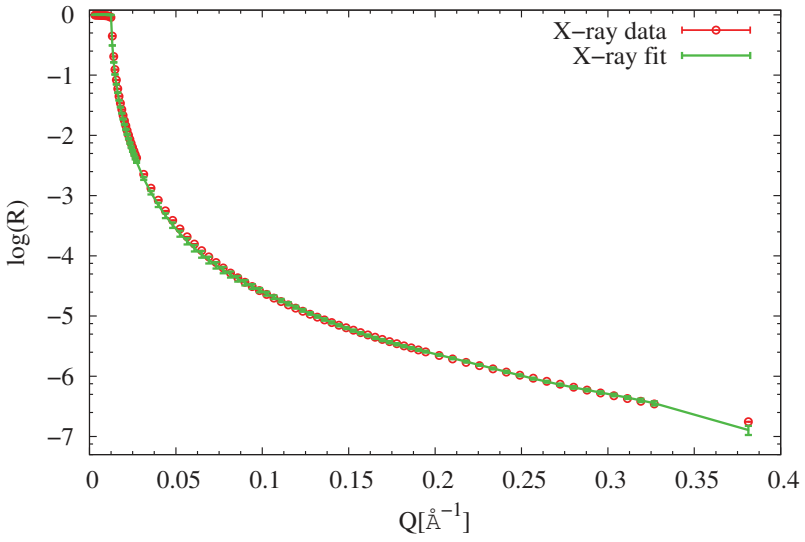

Figure 2.21: X-ray Fit in the Parratt Refinement. In red are plotted the intiial data with error bars, in green the results of the fitting process

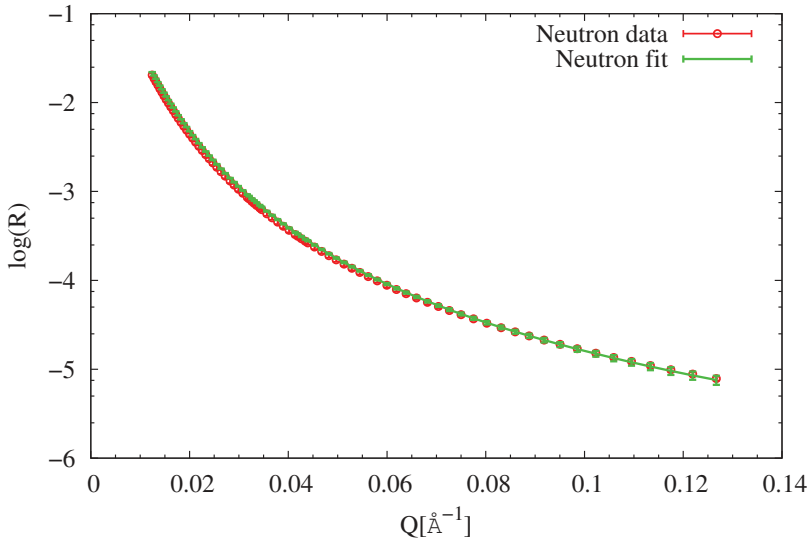

Figure 2.22: Neutron Fit in the Parratt Refinement. In red are plotted the intiial data with error bars, in green the results of the fitting process

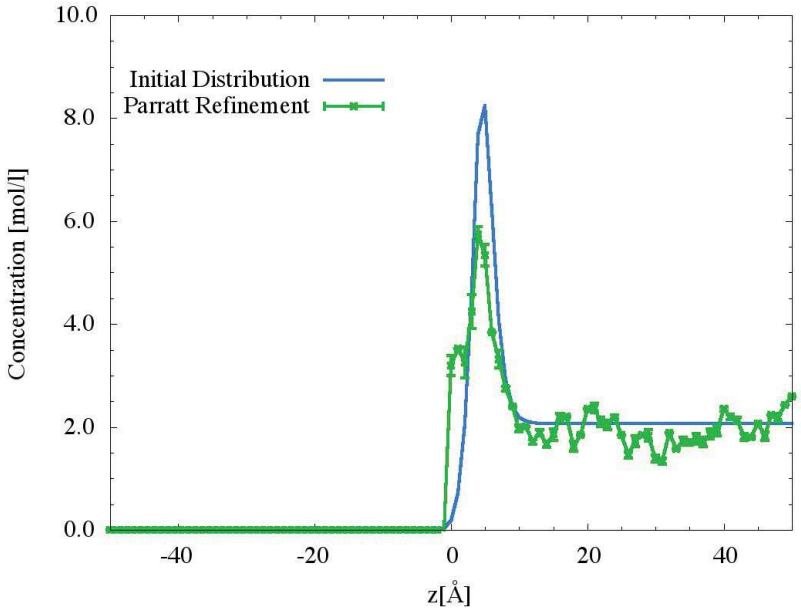

Figure 2.23: Final distribution of Lithium. In light blue the plot of the initial distribution in mol/l, in green the result of the fitting process with error bars.

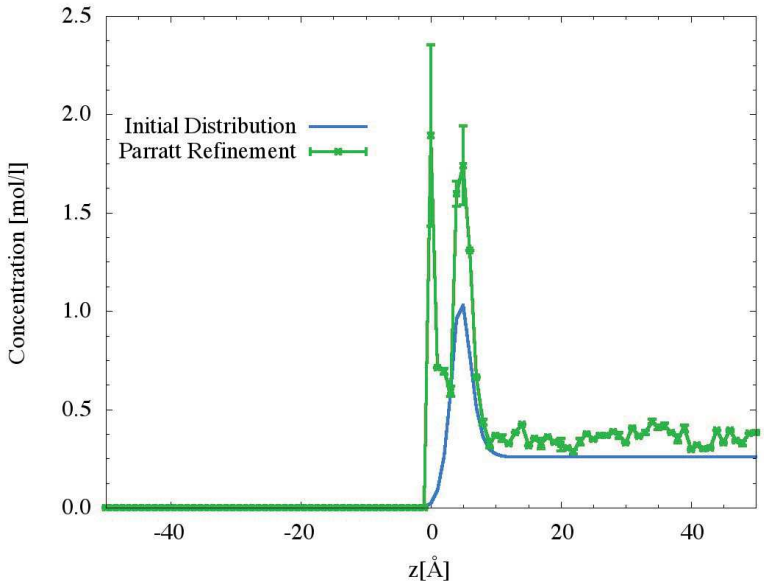

Figure 2.24: Final distribution of Neodymium. In light blue the plot of the initial distribution in mol/l, in green the result of the fitting process with error bars.

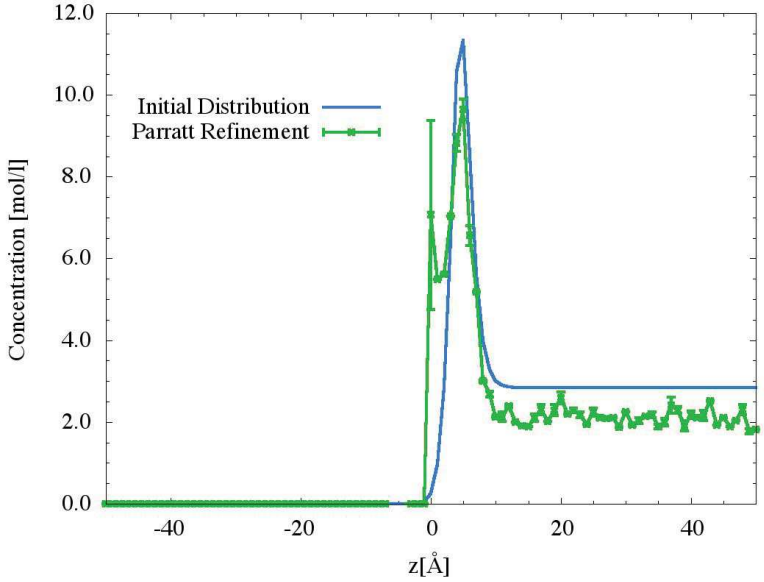

Figure 2.25: Final distribution of nitrate. In light blue the plot of the initial distribution in mol/l, in green the result of the fitting process with error bars.

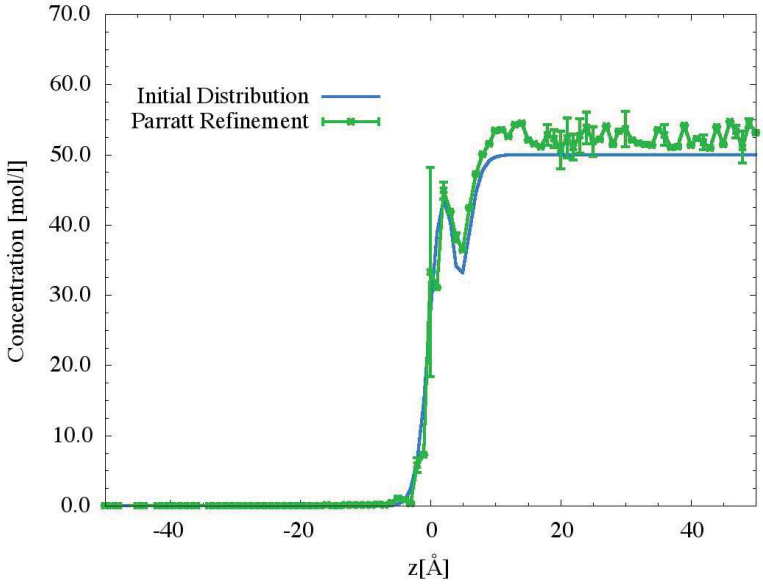

Figure 2.26: Final distribution of water. In light blue the plot of the initial distribution in mol/l, in green the result of the fitting process with error bars.

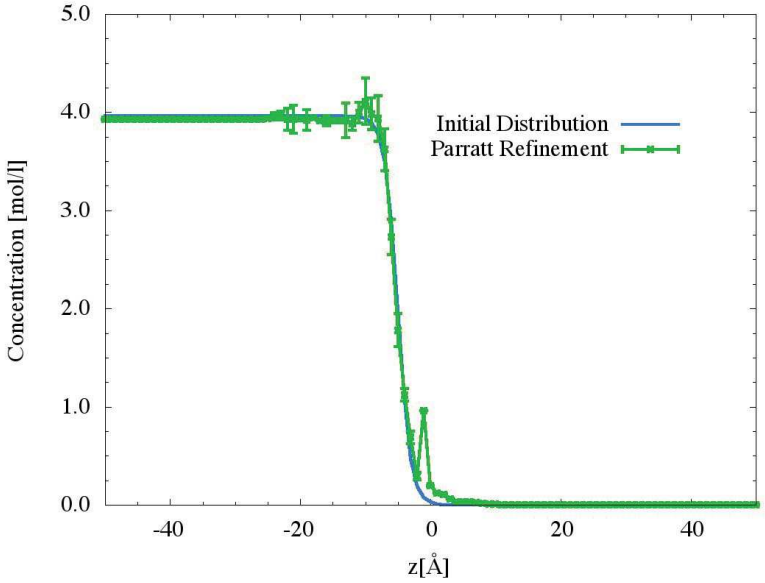

Figure 2.27: Final distribution of dodecane. In light blue the plot of the initial distribution in mol/l, in green the result of the fitting process with error bars.

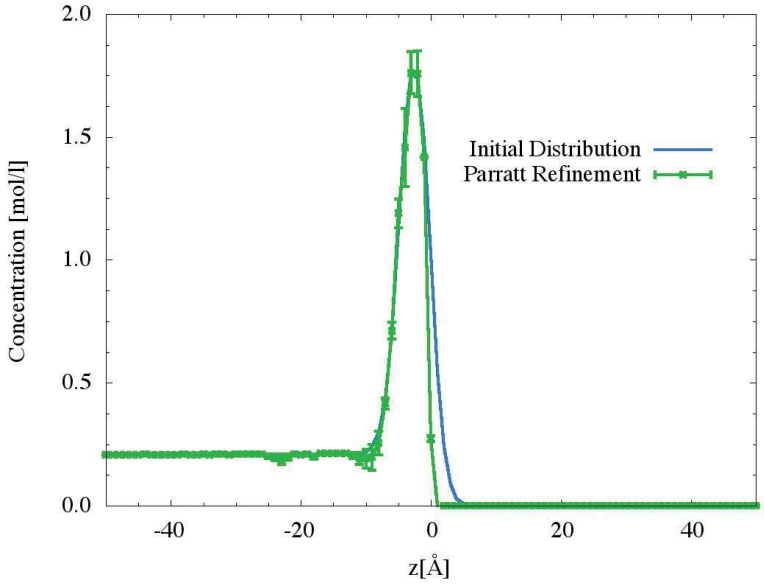

Figure 2.28: Final distribution of extractant. In light blue the plot of the initial distribution in mol/l, in green the result of the fitting process with error bars.

Compared to the system with three components where the final distributions are in agreement with the original ones, in the six component system some deviations occur. In both cases no external constraint as concentration of species or minimization of charge has been imposed.

In the six component system some remarks are necessary:

- looking at the SLD profile analysis, the results provided by the program are not far from the initial distributions;
- two SLD profiles have been used for both cases but, while the first system was created by three components, the second one has six species. Due to the size of the mathematical system, larger deviations are observed as expected;

Taking into account the results of the test we can say that increasing the number of unknown variables in the system, the distribution are in generally reproduced with a loss in the precision. For those cases[1] more reflectivity measurements at different contrasts are needed to provide qualitatively and quantitatively better results.

[1]In this thesis work most samples, only two contrasts have been measured.

CHAPTER 3

Reflectivity Experiments

In the second chapter we have introduced the principles of x-ray and neutron reflectivity and the data analysis procedure established for the investigation of liquid/liquid interface. For the experimental part, we present in this chapter the reflectometers and the liquid/liquid cell developed for this thesis work.

3.1 Principles of reflectivity measurements

A reflectometer is an instrument composed essentialy by four parts: the source, the collimation system, the sample table and the detector.
In the case of x-rays, or synchrotron radiation, the source is the synchrotron, while for neutrons (at ILL) it is a nuclear reactor[1].
The collimation system in the case of x-ray is composed by a vacuum tube and a series of slits and monochromators or mirrors. In the case of neutrons the collimation system is a guide with supermirrors going from the reactor pool (where the neutrons are produced) to the instrument. Slits are used to focus the beam and choppers to select the desired wavelength.
On FIGARO (ILL - Neutron) the sample table is a table that can move to align the sample. In the case of ID10 (ESRF - Synchrotron Radiation) the table is a

[1] In the case of Spallation Sources, as ISIS or J-PARC, the source is the target station.

composed by three parts: a monochromator close to the end of the collimation system deflecting the beam, a sample table and a detector arm. These three parts move together.
Lastly, the detector is a 1D x-ray detector for synchrotron radiation experiments and a series of He^3 tubes for neutron experiments. More detailed information can be found in the works of Smilgies et al. [94] and Campbell et al. [20].
A general experimental procedure is followed to collect data:

- Sample alignment: this procedure is described in the following sections for both x-ray and neutron experiments;
- Transmitted beam recording: the transmitted beam through the sample is necessary to reduce the data and analyze it in absolute scale;
- Reflectivity measurement: it is the measurement of reflectivity curve as described in the following sections;
- Sample change.

This general procedure is valid for both x-ray and neutron experiments with some differences explained in the following sections.

3.2 ID10 beamline at the European Synchrotron Radiation Facility

Synchrotron radiation reflectivity experiments have been perfomed on the beamline ID10 at the ESRF [94] (acronym for **E**uropean **S**ynchrotron **R**adiation **F**acility). This beamline has some technical features, as the high brilliance and vertical scattering plane, which are needed to investigate the liquid/liquid interface. In Figure 3.1 we report the schematich layout of the beamline.

As mentioned above for our experiments at Liquid/Liquid interface an high energy source was needed and this is why we went for a large scale facility instrument instead of a lab instrument. For this work, indeed, experiments have been performed with a beam energy equal to 22 keV corresponding to a photon wavelength $\lambda = 0.5636$ Å.
On this beamline, it is not possible to investigate the interfacial structure shining the sample from the bottom part (water), characteristic that has been taken into account during the development of the liquid/liquid cell used in this work.

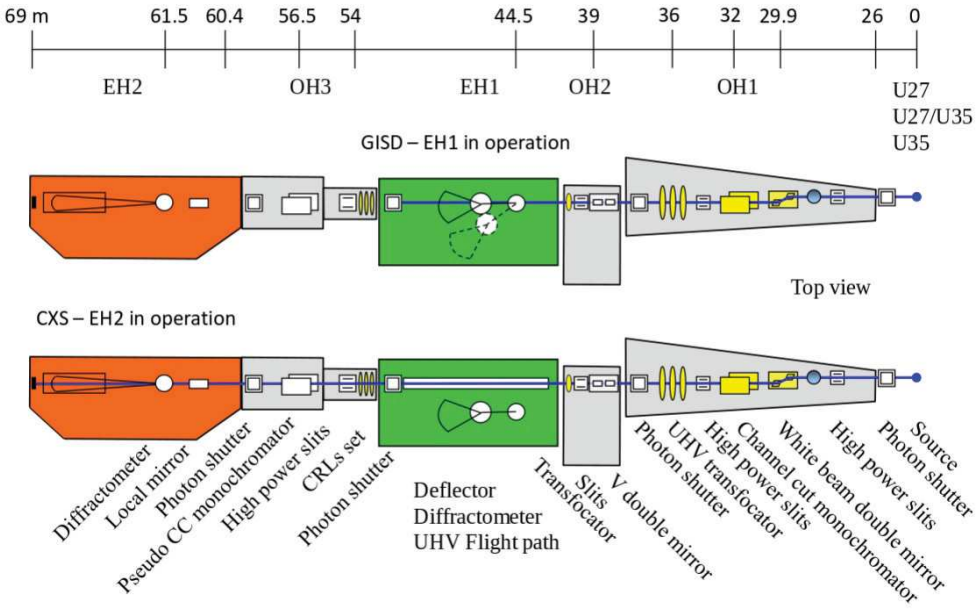

Figure 3.1: Schematic ID10 Beamline layout at Europen Synchrotron Radiation Facility. The experiments of this thesis work have been performed on the EH1 hutch.

3.2.1 X-ray Reflectivity: the experiments

As shown in Equation 2.21 the reflectivity depends on Q_z which can be written as follows:

$$Q_z = \frac{4\pi}{\lambda} sin(\theta). \tag{3.1}$$

The wave vector transfer depends therefore both on the angle (θ) and on the wavelength (λ). With a monochromatic beam, the reflected intensity at different values of the wave transfer vector is obtained by varying the angle between the incoming beam and the surface/interface. On ID10 this is possible thanks to the diffractometer. This part of the instrument, shown as green in Figure 3.1, is positioned just after the beam tube, and is composed by the mirror, the table with the sample on it and the detector.

This type of geometry allows to record the reflectivity at different angles moving the mirror to deflect the beam, moving the sample table to focus the beam on the interface at the chosen angle and, accordingly to that, moving the detector to collect data at the outcoming angle equal to the incoming one.

Due to the level of background at the Liquid/Liquid interface, data were recorded in a Q-range between 0.0 $Å^{-1}$ and 0.3 $Å^{-1}$ which means, as can be verified from equation 3.1, scanning angles between 0.0° and 0.77° with a wavelength $\lambda = 0.5636$ Å corresponding to an energy of 22 keV.
The time needed to record the entire reflectivity curve, considering the measuring time, the time to move the diffractometer and the waiting time to let stabilize the interface, is around 30 minutes. This point is very crucial and has to be kept in mind during experiments: the large time needed to record an entire curve by x-ray reflectivity experiments doesn't allow to do kinetic measurements.
In this thesis work we have been studying the interfacial structure between two immiscible liquids varying the composition in one of the two phases. Every time we changed that composition we have had to wait a given time for each sample, to be sure we were measuring the interfacial structure at the equilibrium. To do that, we followed this procedure:

1. the empty cell is placed on ID10's table;
2. in reflection mode, the table is horizontally tilted measuring the distance between the two reflection peaks of the quartz edges[1] (see Section 3.4);
3. the cell is filled with water (with or without salts/nitric acid);
4. the sample is moved in the vertical direction and the reflectivity for a fixed angle is measured at various table position;
5. the sample table is fixed at the positon value for which a peak is obtained;
6. the organic phase is poured in the cell covering the entire water surface;
7. measurement at a fixed angle $\theta = 0.12°$ every 10 seconds, until constant intensity is observed;
8. the sample is moved in the vertical direction and the reflectivity, for a fixed angle, is measured at various table position;
9. the sample table is fixed at the positon value for which a peak is obtained;
10. the entire reflectivity curve is measured;

[1]The distance between the quartz edges is known and so we can calculate the expected distance between the reflected peak.

11. the concentration of extractant in oil is changed (see Section 3.5) and the procedure is repeated from point 7.

In the Appendix *Sample alignement on ID10 and FIGARO* are reported the macro used during the experiment to align the sample, measure the waiting time and record the reflectivity.

3.3 The reflectometer FIGARO at the Institut Laue Langevin

As previously mentioned, the neutron experiments have been performed on FIGARO at the *Institut Laue Langevin*. This instrument has some features that make it the perfect instrument to investigate the liquid/liquid interface.
While the solid/liquid interface can be studied with a vertical reflectometer[1], free liquid surfaces or liquid/liquid interface require an horizontal geometry[2]. FIGARO, besides being an horizontal reflectometer, owns some unique geometrical features. With a series of mirrors in the neutron guide, the beam can be deflected and two possible geometries are achievable: reflection bottom-up and top-down.
In the first case the incident beam is sent on the sample with a positive angle with respect to the horizontal and the neutrons are reflected in the up-direction. This geometry looks useful to study air/liquid or solid/liquid interfaces crossing with neutrons air or solids.
In the second case the geometry is inverted and the sample is shined from the bottom, reflecting the neutron in the down-direction. On the NG7 reflectometer at NIST this last feature can be found but not combined with the high neutron flux available on FIGARO reason why the latter is the perfect tool to study the Liquid/Liquid interface.
In our samples the water phase is heavier than the organic phase[3] in which hydrogenous extractants are solubilized. While water can be fully deuterated[4] the

[1] An example of vertical reflectometer is D17 at the Institut Laue Langevin.

[2] With vertical/horizontal geometry we mean that the xy-plane of the interface is at 90° or 0° with respect to the ground.

[3] Dodecane is lighter, even if deuterated, than water, even if hydrogenated. Different oils, like fluorinated ones or chloroform, are heavier than water but are not used in this thesis work.

[4] An exception is made when Neodymium Nitrate is solubilized in water. This salt is provided by Sigma in the hexahydrate form. For the concentrations used in this thesis work it means that when dissolved in D_2O the 2% of the total volume is occupied by H_2O.

extractant cannot and, as shown in section 3.4.1, the presence of hydrogen increases the beam attenuation reducing the signal to noise ratio.
Moreover, every time the composition of the phase traversed by neutrons changes, a new transmitted beam has to be recorded because it is needed to reduce and normalize the collected data. Working at different concentrations of extractant but at constant concentration of salts or nitric acid in water allows us to record only one transmitted beam for a defined aqueous phase when the incoming beam crosses this phase. In this way it is possible to save hours during experiments.

In addition to what written above, further characteristics as the high flux nuclear reactor and the ^{3}He detectors makes FIGARO the best instrument to investigate the liquid/liquid interface. More detail about the instruments are explained by *Campbell et al.* [20].

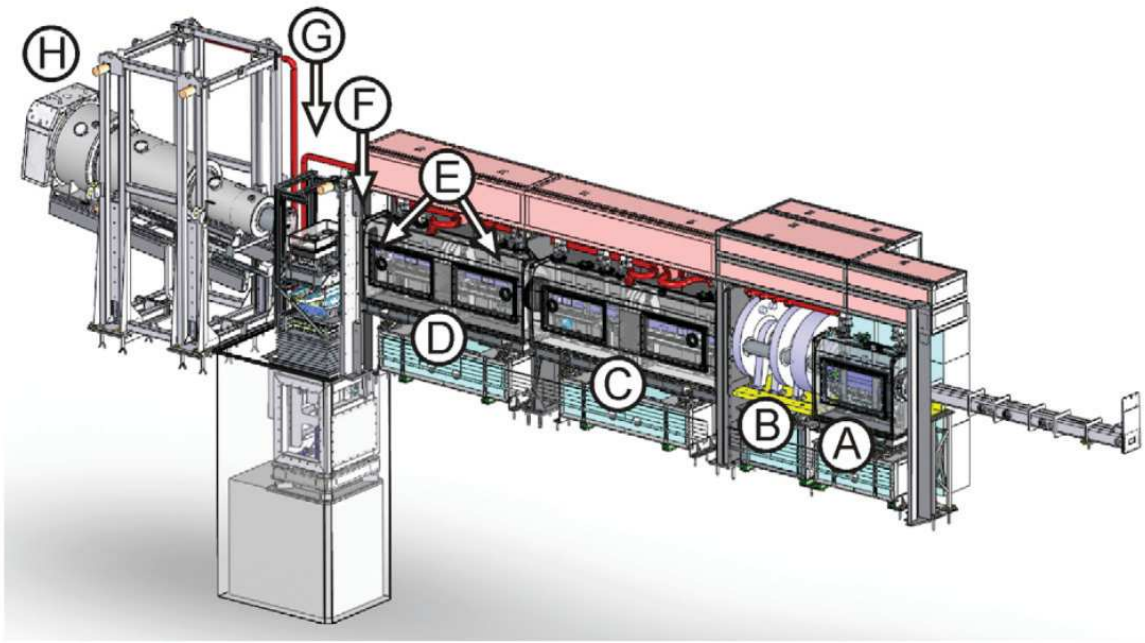

Figure 3.2: Schematic of the instrument highlighting the following primary components: (A) frame overlap mirrors, (B) chopper assembly, (C) deflector mirrors, (D) collimation guide, (E) collimation slits, (F) beam attenuator, (G) sample position and (H) area detector [20].

3.3.1 The neutron advantage: the polychromatic beam

While for x-ray experiments we work with a monochromatic beam, as shown in paragraph 3.2.1, with neutrons we measure the reflectivity exploiting a polychromatic beam. The use of polychromatic beam is often called *Time of Flight* because different wavelengths correspond to different time for neutrons to travel from the neutron guide to the detector, crossing the sample. This means that neutrons detected at different times correspond to different wavelengths and with the knowledge of this time we can reconstruct the distribution in λ of neutrons. This feature as two main advanteges:

1. We do not have to change the angle for each value of the wave transfer vector;
2. Fixing the incidence angle on the sample we can access directly to a Q_z region at the same time;

To explain what is written above, we start again from Equation 3.1:

$$Q_z = \frac{4\pi}{\lambda} sin(\theta)$$

If a polychromatic beam with the wavelength $\lambda \in [\lambda_{min}; \lambda_{max}]$ is considered, the maximum and minimum Q_z values for a fixed θ can be calculated as follows:

$$Q_{z,min} = \frac{4\pi}{\lambda_{max}} sin(\theta) \qquad Q_{z,max} = \frac{4\pi}{\lambda_{min}} sin(\theta). \tag{3.2}$$

For our experiments we used a λ-range between 2 Å and 16 Å and two angles measure the entire reflectivity curve[1]:

$$\theta_1 = 0.623^\circ \qquad \theta_2 = 1.400^\circ \tag{3.3}$$

having access to a Q_z-range $Q_z \in [0.008; 0.154]$ Å^{-1}.

These two angles are used during the experiment and data are collected with the following procedure:

1. the empty cell is placed on FIGARO's table;
2. in reflection bottom-up the table is horizontally tilted measuring the distance between the two reflection peaks of the quartz edges[2] (see Section 3.4);

[1]For higher angles the background would be higher than the reflectivity.

[2]The distance between the quartz edges is known and so we can calculate the expected distance between the reflected peak.

3. the cell is filled with water (with or without salts/nitric acid). By measuring the reflection from the free water surface we adjust the water level to obtain a reflection peak at the center of those obtained for the quartz edges;

4. the geometry is inverted moving to reflection top-down;

5. the organic phase is poured in the cell covering the entire water surface;

6. the detector is masked to measure only in the specular reflection peak and choppers are dephased to increase the flux. A sample alignement procedure starts here moving the sample in the vertical direction and measuring the reflectivity. The sample height is fixed at the value for which a peak is obtained[1]

7. the detector is unmasked and the choppers are rephased and the transmitted beams through the water at $\theta = -0.623°$ and $\theta = -1.4°$ are measured;

8. transmitted beam[2] and reflectivity are recorded;

9. the concentration of extractant in oil is changed (see Section 3.5) and the procedure is repeated from point 6.

In the x-ray experiment procedure we have mentioned the *waiting time*. In the neutron case this step of the experiment is provided exploting more than one cell. In each sample a different aqueous phase is poured. While a sample is measuring (3-6 hours), in another cell the concetration of extractant is changed. In this way while a sample is measuring another one is equilibrating. This means that in between point 9 and 6 (coming back) in the previous list we can insert that the sample table moves to another sample.
This procedure has been developed to ensuring that data are recorded at the equilibrium.

3.4 Liquid-Liquid Cell

The investigation of the liquid/liquid interface has required the development of a specific cell to optimize reflectivity experiments at liquid/liquid interfaces. In

[1]Details for the masks and chopper settings for this step are reported in Appendix *Sample alignement on ID10 and FIGARO*.

[2]The transmission beam at each angle is measured once for each sample. If the aqueous phase does not change the transmitted beam are not measured again.

the first chapter we have shown state-of-art of cells realised for x-ray and neutron experiments [16, 73, 80, 83]. One of the aims of this thesis work is to exploit different types of radiation sources and with this purpose the liquid/liquid cell was developed with the following requirements:

- **Path length minimization:** neutrons are strongly attenuated by liquids, even more when protonated compounds are present. A minimization of the path crossed by neutrons is necessary;
- **Meniscus minimization:** a flat interface is required for reflectivity experiments. A geometry which reduces the meniscus effect at the oil/water interface, indipendent of the surfactant concentration[1], is necessary to perform studies at various extractant concentrations. The choice of materials plays an important role. Working with liquids with different surface wetting properties, an hydrophilic material easy to hydrophobize is convenient and useful to obtain flat liquid/liquid interfaces.
- **Bulk oil and water:** It was necessary to study the interface with the capability to change solute concentration in the two bulk phases. This feature does not allow to use spin coated oil layers[80] or water thin films[83];
- **Same geometry:** having the same geometry for x-ray and neutron experiments is convenient;

Focusing on each one of these points we developed a cell with the best compromise, at the moment, between all of them.

3.4.1 Path length minimization

Depending on absorption and incoherent cross section, a neutron beam can be strongly attenuated and this effect becomes more evident in the case of liquids when passed through material. In the x-ray case this issue is less important for compounds with a low electron density as liquids and viceversa.

In neutron reflectivity experiments it is possible to define the area illuminated by the beam and a compromise between path length and illuminated area can be found. By increasing the sample size, a larger area is available for the neutron

[1] As shown in Chapter 1, the extractant has a surfactant behaviour and at different concentration in organic phase different interfacial tension values are recorded.

beam leading to higher intensity in the reflected beam but the larger the sample the higher the attenuation.

The beam attenuation ca be calculated following the Lambert-Beer Law

$$I(x) = I_0 e^{-\mu x} \tag{3.4}$$

with μ the attenuation coefficient, x the thickness, I_0 the incoming intensity and $I(x)$ the transmitted intensity. Through D_2O the transmission coefficient[1] is $\mu = 1.549 cm^{-1}$. I_0 increases with the illuminated area on the sample.
Finally to avoid recording radiation reflected from the edge of the interface[2] and to avoid the curvature of the meniscus, the illumination area, or footprint, should be 1 cm less than the available area, which means at least 5 mm from each edge. This value has been obtained with test at liquid/liquid interface measuring reflectivity with different footprints. In Figure 3.3 we report the calculation of the transmission normalized to the unit, and the ratio between the footprint and the maximum footprint (5 cm)[3].

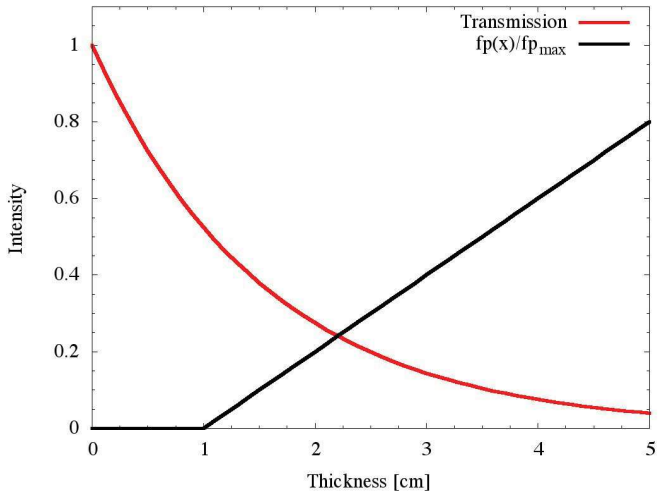

Figure 3.3: The intensity of a neutron beam crossing the D_2O versus the thicknes is plot with red line following Equation 3.4. In black the ratio between the footprint for a given thickness of the sample and the footprint for a thickness of 5 cm is plotted.

[1]The value is taken from the NIST SLD Calculator Applet at http://www.ncnr.nist.gov/resources/activation/

[2]As shown in the section 3.4.2, in our case the interface is in a quartz pool and the reflection from the edges must be avoided.

[3]The footprint max it has been fixed at 5 cm because for higher value the transmission, even if not zero, is too low for reflectivity experiments.

From Equation 3.4 the normalized transmitted beam is given by:

$$T(x) = \frac{I(x)}{I_0} = e^{-\mu x}. \tag{3.5}$$

The product between $T(x)$ and the footprint will provide the best compromise between footprint and transmission.

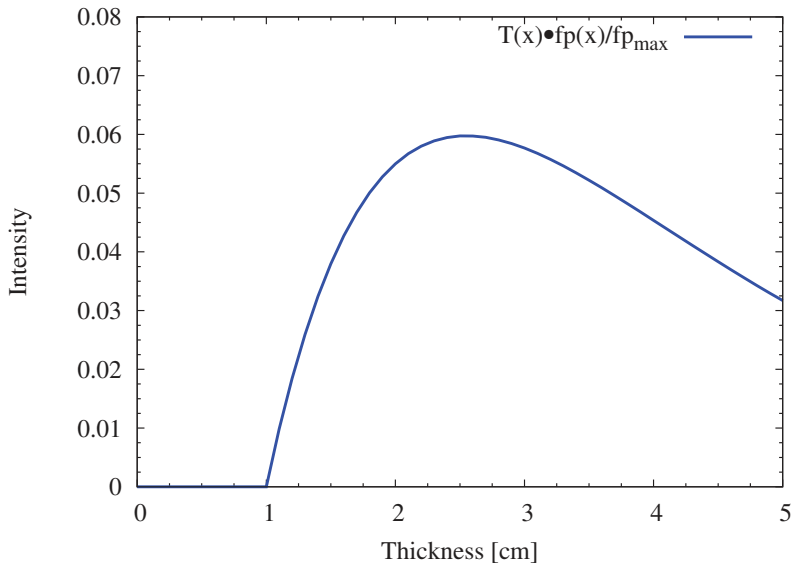

Figure 3.4: Plot of the transmission multiplied by the footprint. The best compromise is obtained at 2 cm.

Figure 3.4 shows clearly that the best compromise between footprint and attenuation is obtained for a sample of two centimeters. However meniscus effects extend over centimeter lengths making the surface curved and this has to be taken into account to optimize the dimensions of a liquid/liquid cell for surface scattering experiments.

3.4.2 The Meniscus minimization

To perform reflectivity experiments a flat surface or interface is required. For experiments at air/liquid interface it is possible to obtain flat surfaces using large cells[1] and at the solid/liquid interface it is possible with polished substrates.

[1]Commonly called through.

At the liquid/liquid interface, because of the beam attenuation discussed in the previous section, it is not possible to use large samples without causing a decrease in the signal over noise ratio. This problem, as discussed above, is more important for neutron experiments while in the synchrotron radiation case the incident flux is much higher and limits the problem of the attenuation in liquid samples from light elements.

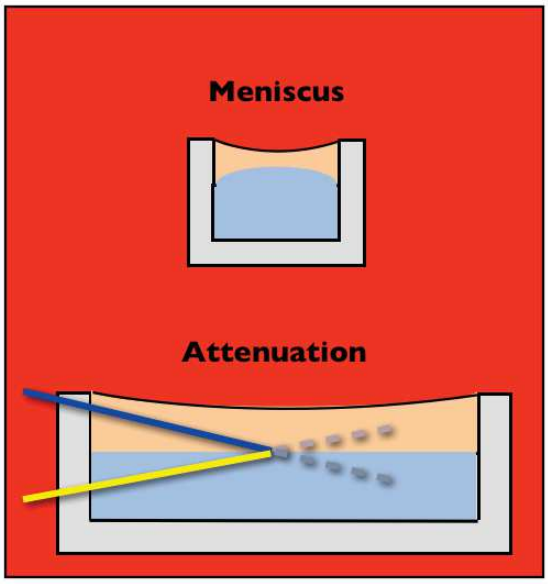

Figure 3.5: Sketch of surface curvature related to sample size. On the top we show the meniscus for small samples, on the bottom the larger size of the cell reduce the effect. In both cases in pink and light blue we represent two liquids.

Schlossman et al. [73] have proposed to use tilted walls to reduce the meniscus depending on the contact angle between water and oil. In this way it is possible to reduce the sample size and the meniscus at the same time. However, when working with amphiphilic molecules, the interfacial tension depends on their concentration which would impose to change then the wall tilt to compensate the variation in the contact angle between liquids and walls making very difficult the sample preparation during an experiment.

A solution to this issue can be the use of vertical walls with an hydrophobic/hydrophilic contrast. Consequently the water and the oil are forced to minimize the contact angle with the surface and consequently at the liquid/liquid interface. This would lead to another experimental issue: a separation line on the

walls between hydrophilic/hydrophobic parts requires an extremely precise control of the amount of water and oil used to avoid crossing that line with one of the two liquids. This issue becomes more evident when an oil is added on the water surface: a pressure is applied and the surface is bent changing the contact pressure and angle with the walls.

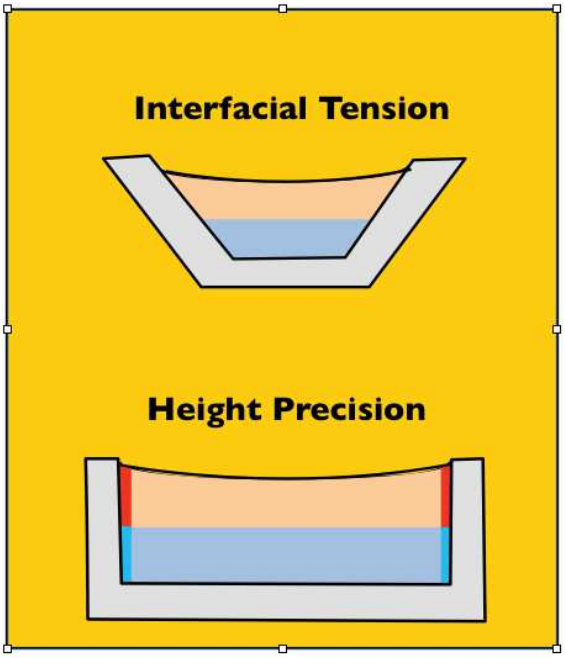

Figure 3.6: Sketch of the contact angle issue. On the top a sketch for a cell with tilted walls, on the bottom flat walls with hydrophobic coating in red and for hydrophylic coating in sky blue. In both cases in pink and light blue we represent two immiscible liquids.

The solution adopted in this work involves the use of a cell with two reservoirs, one for each liquid, with a separation step at the interface height. The hydrophobic/hydrophilic contrast is allowed thanks to the use of hydrophilic quartz on the walls hydrophobized on the oil side. In order to control the amount of liquid injected in the cell and to reduce the curvature, inlets on the bottom part are added. A schematic view of the liquid/liquid cell is shown in Figure 3.7.
This geometry allows to control the meniscus leading to the solution of the beam attenuation issue: control of the meniscus means that we can obtain a flat interface even when reducing the sizes of the cell, which means reducing the pathlength of

the neutrons through the sample and looking for the best compromise between attenuation and footprint.

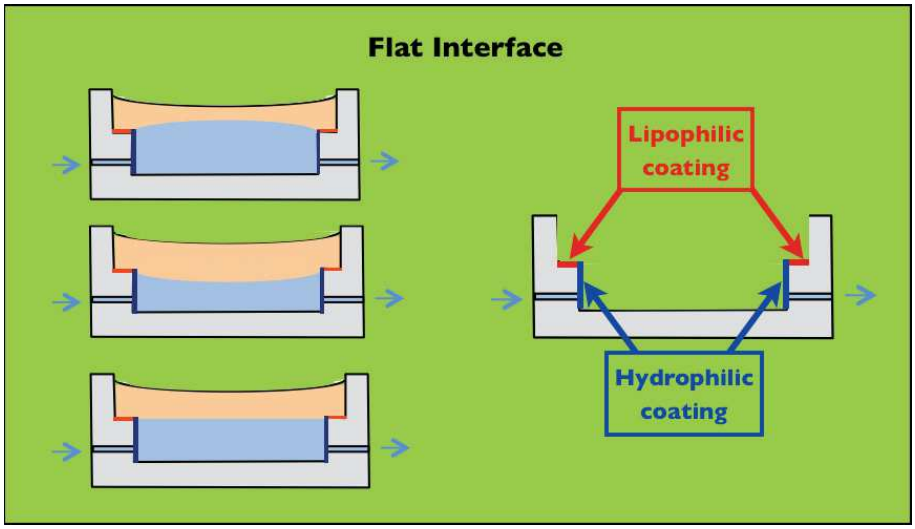

Figure 3.7: Sketch of the geometry of the liquid/liquid cell. Hydrophobic and hydrophilic coating are shown in red and dark blue. In both cases the two liquids are represented in pink and light blue.

3.4.3 Optimisation of sample cell: three years of developments

Focusing on all the details explained above, over the three years of this PhD multiple versions of the cell were developed, working on the dimensions and materials. On the neutron side we have tried to reduce the pathlength with the knowledge of the result shown in Figure 3.4. The version 1.0 is an aluminum cell, with syringes and inlet to adjust the water level and a teflon coating on the edges. The cell is 4 cm wide.

The neutron version 2.0 is a PEEK cell with quartz windows 0.5 cm thick. Other quartz pieces are present on the side of the cell the top of which was made hydrophobic by silanization from OTS. For this version we realized two cells: the first one is 5.0 cm long and used to measure the buried oil/water interface, the second one is 3.5 cm long to measure the liquid/liquid interface in presence of extractant. Due to the lower interfacial tension when adding extractant, the meniscus is reduced and it is possible to use a smaller cell increasing the signal to noise ratio. The same type of cell, but 7.0 cm long, has been made for synchrotron radiation

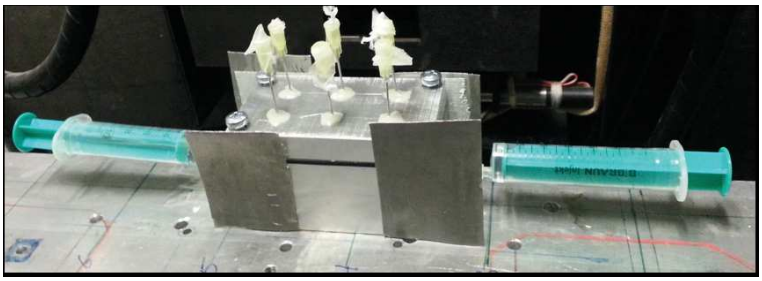

(a) Cell on FIGARO's table.

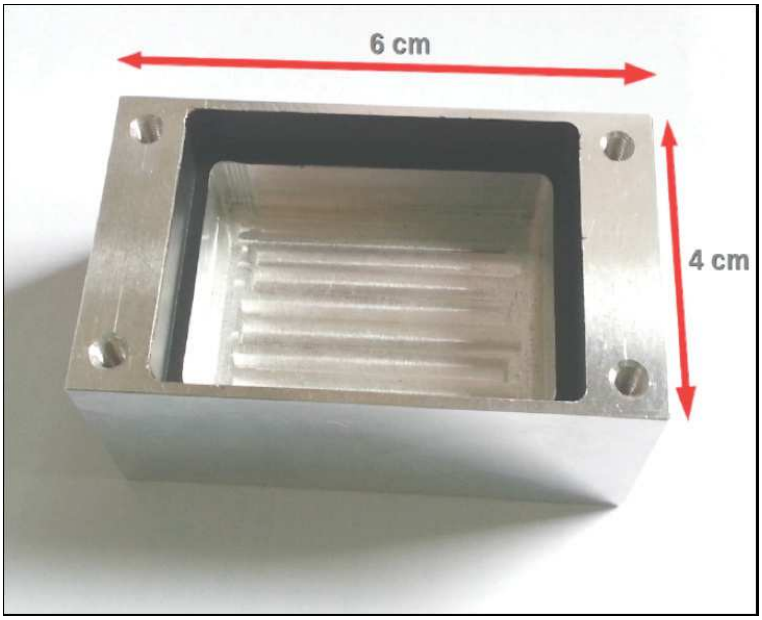

(b) Internal part of the cell.

Figure 3.8: Version 1.0 for the neutron liquid/liquid cell. (a) Picture of the cell during an experiment, with syringes to adjust the water level inside the cell. (b) The internal part of teh cell, with edges and a PTFE coating in black.

experiments. In this case the attenuation is less important and a larger surface allows to obtain flat surface more easily. Moreover, in x-ray experiments the footprint depends on the radiation incident angle which is related to the Q value (Equation 3.1): the lower the incident angle (corresponding to a lower Q value) the larger the footprint[1]. Then, to access to the low Q region a larger length of

[1]For the neutron case the footprint can be changed by changing the slit settings.

the cell is required to avoid over illumation issues[1]. On ID10 a slit opening of 10 μm has been used during experiments which means (at 22 keV) a footprint of approximately 6.5 cm for a Q_z value of 0.05 Å^{-1}. In the case of water/dodecane interface the critical edge is approximately $Q_c \approx 0.01$ Å^{-1} and the choice made for the length of the cell should garantee an illumination of all the sample area for angles higher than critical angle.
Mylar windows, instead of quartz, were used to reduce the absorption.

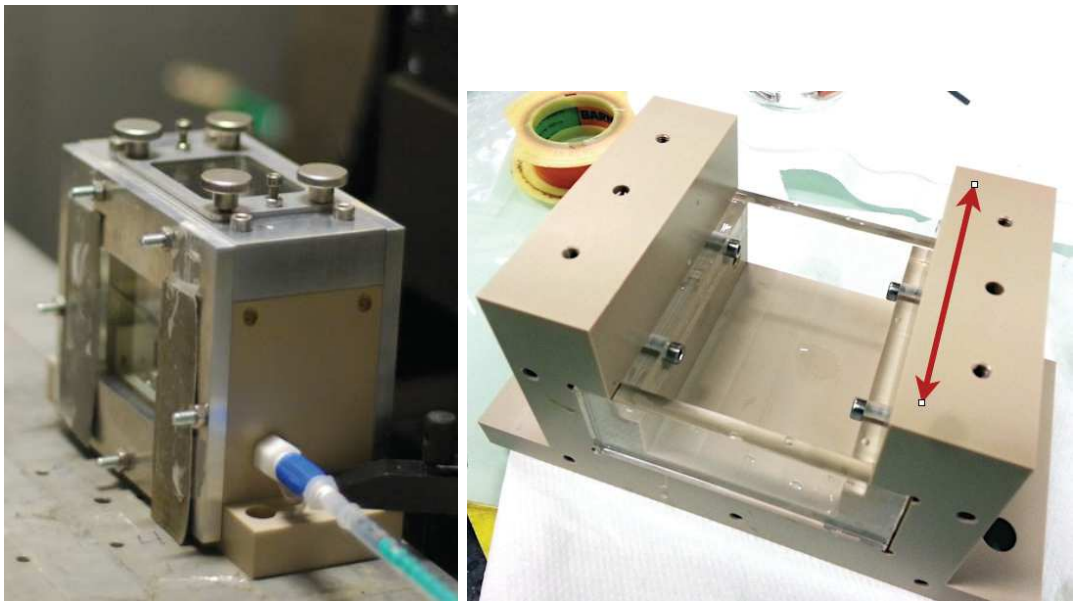

(a) Cell 2.0 on FIGARO's table. (b) Internal part of the cell 2.0.

Figure 3.9: Version 2.0 of the liquid/liquid cell. (a) Picture of the cell during an experiment, with syringes to adjust the water level inside the cell. In the frontal part two cadmium masks have been attached with tape to shield the sides from incident neutrons. (b) The internal part of the cell. We can see quartz windows 0.5 cm thick in the frontal and rear part and small quartz pieces screwed on the side to form the water pool. On the top of the quartz a coating with OTS has been chemically attached. The red arrow indicates the crossing direction for neutrons and x-rays. As mentioned above the cell is (in the arrow's direction) 5.0/3.5 cm for the neutron cell and 7.0 cm for the x-ray cell.

The final version of the cell has been realized all in quartz and it is 3.5 cm long

[1]Over illumination issue means that the sample area is lower than the illuminated area. In our case this would lead to have reflectivity signal from edges. Increasing the angle this effect disappear.

for neutrons, and 7.0 cm long for synchrotron radiation experiments. In the latter case the windows in mylar have been designed with an aluminum ring to avoid leaking issues.
A cell all made by quartz allowed to reduce the number of pieces facilitating cleaning and mounting procedure[1] (see Figure 3.10).

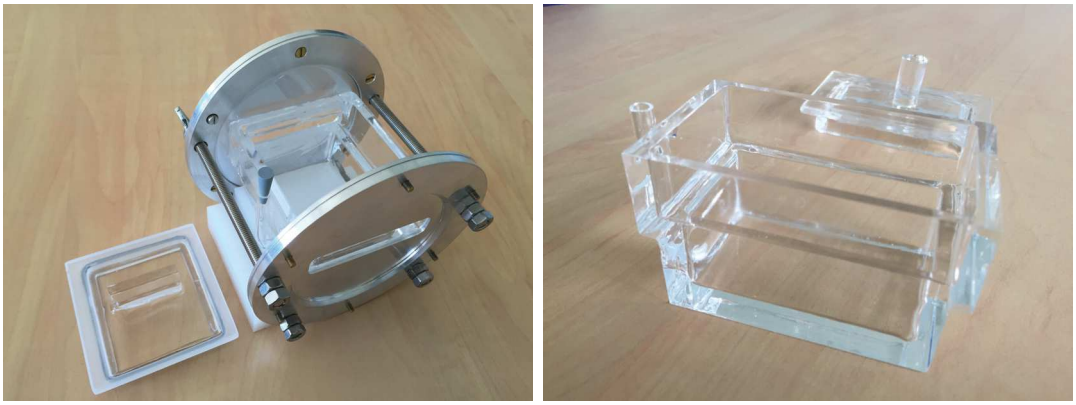

(a) X-ray (b) Neutron

Figure 3.10: Version 3.0 of the liquid/liquid cell. (a) X-ray cell. The inlet for syringes on the side has been replaced by a quartz pipe on the side. The mylar windows are inserted in the aluminum disk in the frontal and rear part of the cell. (b) Neutron cell. As for the x-ray case, the inlet on the side have been replaced by a quart pipe. The cell is all made in quartz (with the same geometry shown in for previous cells) avoiding in this way any possible leaking issue.

3.5 Sample change procedure

The extractants used in this work are denser than dodecane. A sample change, or addition of ligands in organic phase, during experiments requires a particular procedure to avoid the formation of density anisotropies which can lead to local and inhomogeneous formation of third phase. This procedure is described below:

- 2-3 ml of dodecane are withdrawn from the sample;

[1]The cell are cleaned with solvents and Plasma cleaner. This last step is not possible with PEEK cells.

- the dodecane is mixed with the diamide that has to be added in the sample to increase the concentration;
- the solution is added drop by drop in different points of the sample.

For cases as DMDBTDMA in dodecane contacted with nitrate salts aqueous solutions (Section 4.2.3) for which the third phase appears at low extractant concentration, the procedure is repeated two or three times to reduce the amount of ligand added each time.

CHAPTER 4

Experiments and Results

In this chapter collected data, analyzed following the procedure shown in the previous chapter, will be presented. Solutions of DMDBTDMA or DMDOHEMA in dodecane have been studied in contact with an aqueous solution of Nitric Acid (2 M) and with an aqueous solution of $LiNO_3$ (2 M) and $Nd(NO_3)_3$ (0.25 M). In addition, for the second extractant, a series of samples with pure water solutions have been measured.

For the x-ray experiments fully protonated compounds have been used. The $C_{12}H_{26}$ and the extractant have been purified with an Alumina Oxide (basic) column to remove any trace of alcohols or impurities that can contaminate the liquid/liquid interface. For the neutron experiments, H_2O has been replaced with deuterium oxide (D_2O) and the organic phase has been replaced either with $C_{12}D_{26}$ or with a mixture of hydrogenated/deuterated dodecane[1] to obtain an SLD=$4 \cdot 10^{-6}$ Å^{-2}. Moreover, HNO_3 has been replaced by DNO_3.

The data analysis has been carried out initially with Motofit[93] and then with the RMCS code which consists of the SLD profile analysis and the Parratt refinement. For simplicity, the results of the SLD profile analysis have been reported in Appendix *Supporting Material* in comparison with the results of the Parratt refinement presented in this chapter.

[1] A mixture with 37.7% of $C_{12}H_{26}$ and 62.3% of $C_{12}D_{26}$ was used.

4.1 The Water/Dodecane interface

Working with amphiphilic molecules as the malonamide it is important to ensure that no contamination are present in solvents. Hydrogenated dodecane has been purified using an alumina oxide (basic) column to remove any trace of contaminants and interfacial tension at the $D_2O/C_{12}H_{26}$ (purified) interface was measured obtaining a value of 51.0±1.2 mN/m as expected [95].

To prove that no contamination was present in the solvents we have investigated the buried liquid/liquid interface both with x-ray and neutron reflectivity. Unfortunaly, in the first case, the measurements have been unsuccesful because of the high surface tension at the oil/water interface. In fact, the incident angle in the case of x-ray is very small (10 times less than neutrons) and the measurements are very sensitive to the meniscus. We have observed that x-ray reflectivity measurments at liquid/liquid interface require a small amount of surfactant to reduce the interfacial tension flattening the interface.
By neutron reflectivity the interface between fully deuterated water (D_2O) and dodecane either fully deuterated or fully hydrogenated has been measured. The reflectivity curves are plotted in Figure 4.1.

The SLD profile obtained for $D_2O/C_{12}H_{26}$ interface (Figure 4.2a) represents a water/oil interface with an interfacial roughness of 6.8 ± 1.0 Å, as expected [73]. This contrast is not very sensitive to hydrogenated impurities but both SLD profile and interfacial tension measurements provide the same result.

The data collected at $D_2O/C_{12}D_{26}$ interface has not been fitted. Due to the low contrast between the two liquids (see caption Figure 4.1) and the high level of background for experiments at liquid/liquid interface[1], which is comparable to the expected reflectivity, the signal is very noisy. The blue line plotted in the Figure 4.1 is a model reflectivity for a $D_2O/C_{12}D_{26}$ interface with the same roughness parameters obtained fitting the $D_2O/C_{12}H_{26}$ interface and the corresponding SLD profile is shown in Figure 4.2b. This result shows that no contaminations[2] were found in the deuterated dodecane.

[1] In the case of liquid/solid or liquid/air interface the residual background is two order of magnitude lower, between 10^{-7} and 10^{-6} in absolute units.

[2] The contaminants in these type of solvents are usually hydrogenated surfactant or alcohols.

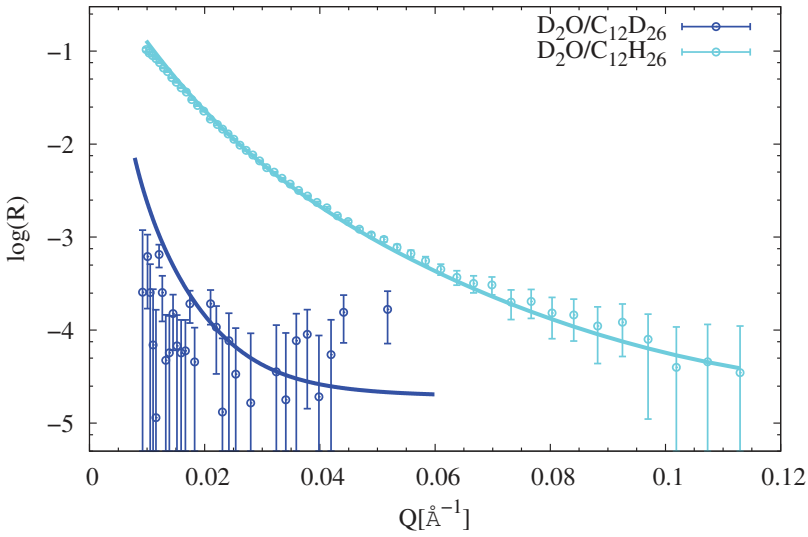

Figure 4.1: Neutron Reflectivity data (circle) and best fits (line) for $D_2O/C_{12}H_{26}$ interface (light blue) and $D_2O/C_{12}D_{26}$ interface (dark blue). The fit for $D_2O/D_{12}D_{26}$ is calculated with a model interface between water and oil and not with fitting procedure. This data is very noisy due to the low contrast between deuterated water (SLD= $6.35 \cdot 10^{-6}$ Å^{-2}) and dodecane (SLD= $6.71 \cdot 10^{-6}$ Å^{-2}).

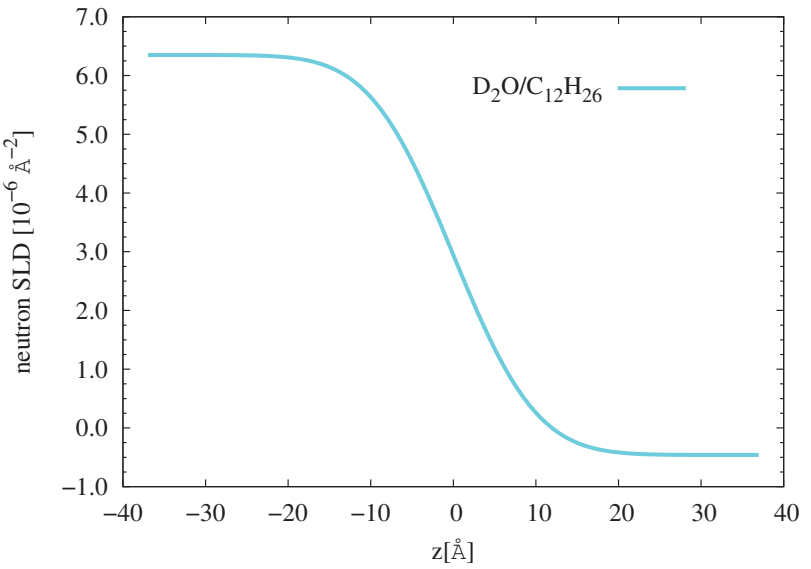

(a) $D_2O/C_{12}H_{26}$ interface

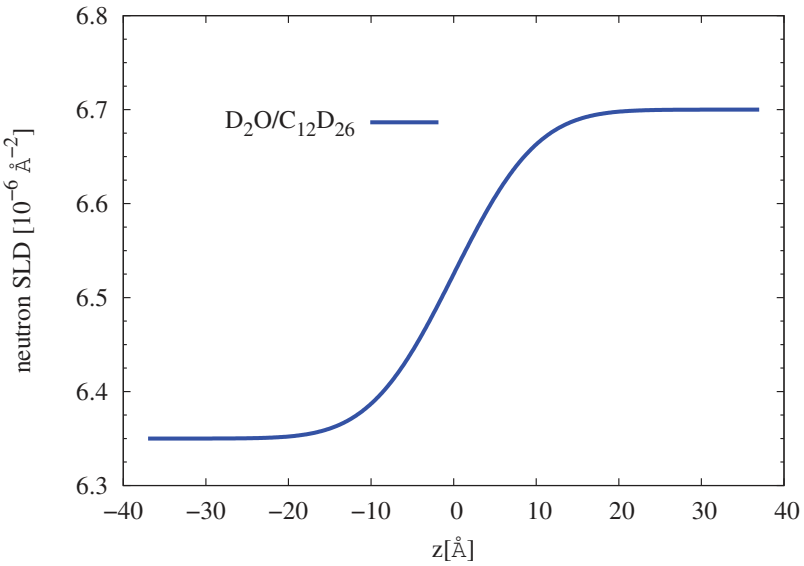

(b) $D_2O/C_{12}D_{26}$ interface

Figure 4.2: Neutron SLD profile for (a) $D_2O/C_{12}H_{26}$ interface and (b) the $D_2O/C_{12}D_{26}$ interface. The SLD for $D_2O/D_{12}D_{26}$ is calculated with a model interface between water and oil and not with fitting procedure. The liquid/liquid interface is placed at z=0 Å (left side, aqueous phase; right side, organic phase).

Afterwards the water/oil interface between fully deuterated water and different mixtures of hydrogenated/deuterated dodecane have been investigated. For these measurements we started from the $D_2O/C_{12}D_{26}$ interface (shown in Figures 4.1 and 4.2b) gradually adding $C_{12}H_{26}$ to increase the contrast. A first attempt of fitting with a model water/oil interface has been done without success. Subsequently, the SLD profiles shown in Figure 4.3b were obtained with a one layer model.

By increasing the contrast the reflected intensity increases, as expected (see Equation 2.27) but an odd result has been found. When $C_{12}H_{26}$ was added to $C_{12}D_{26}$ (curve 5/95 in Figure 4.3) to obtain an SLD of dodecane equal to D_2O ($6.35 \cdot 10^{-6}$ Å^{-2}) no signal was expected[1]. Despite that an increase of signal is observed.

[1]This type of measurement is called Contrast Match because there is no contrast between two bulks.

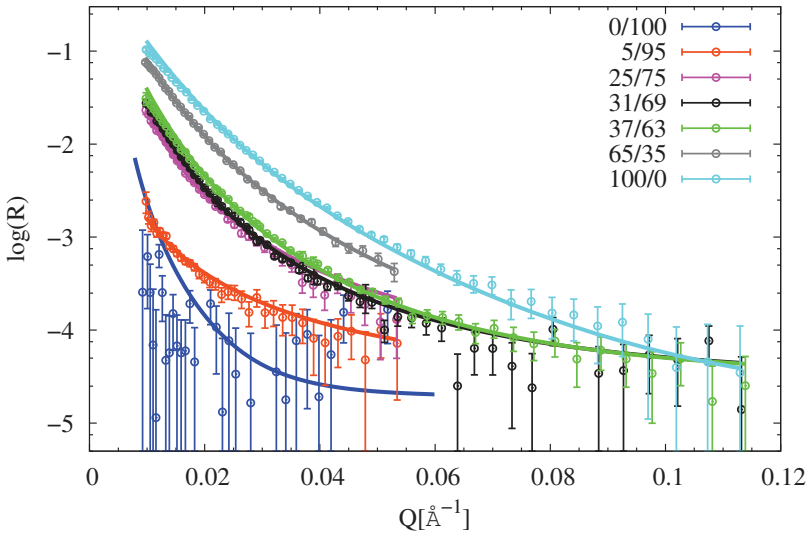

(a) Neutron Data and Fits

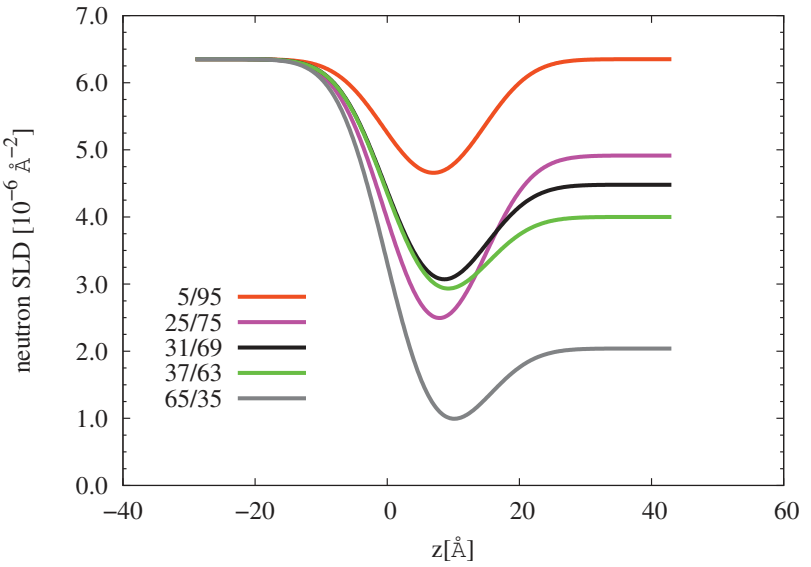

(b) Neutron SLD profiles

Figure 4.3: (a) Neutron Reflectivity data (circle) and best fits (line) at the interface between D_2O and dodecane at different H/D mixtures. The legend reports the volume ratio between hydrogenated and deuterated dodecane. The data 0/100 and 100/0 represent the interface between D_2O and fully hydrogenated or deuterated dodecane, already shown in Figure 4.1. (b) SLD profiles obtained by fitting data in panel (a). The liquid/liquid interface is placed at z=0 Å (left side, aqueous phase; right side, organic phase).

For the fitting process we have fixed for all the data the layer thickness, 14 Å (approximately the length of one dodecane molecule), the roughness σ_1 (water/layer interface) and σ_2 (layer/oil interface), 6 Å, and the interfacial layer SLD, $-0.46 \cdot 10^{-6}$ Å^{-2}, equal to the $C_{12}H_{26}$ SLD. In this way we have calculated the amount of hydrogenous and deuterated dodecane in the interfacial layer, data summarized in Table 4.1.

$C_{12}H_{26}$/ $C_{12}D_{26}$ volume ratio	Amount of $C_{12}H_{26}$	Amount of $C_{12}D_{26}$
5/95	36%	64%
25/75	72%	28%
31/69	60%	40%
37/63	56%	44%
65/35	90%	10%

Table 4.1: Resulting amount of $C_{12}H_{26}$ and $C_{12}D_{26}$ in the interfacial layer at the dodecane/water interface for vaious mixture of $C_{12}H_{26}/C_{12}D_{26}$.

Increasing the amount of $C_{12}H_{26}$ in the organic phase, in the interfacial layer we observe an enrichment of protonated species at the expense of deuterated species except for the sample at 25/75. The question is then, do we have really this type of protonated species enrichment at the interface due to specific van de Waals interactions? Do still exist some hydrogenated impurities in the $C_{12}D_{26}$ which was not purified (because deutarated) and that can adsorb at the liquid/liquid interface such as octanol?

A further test has been conducted with a mixture of deuterated and anhydrous hydrogenous toluene[1] with an SLD equal to $4.0 \cdot 10^{-6}$ Å^{-2}. In Figures 4.4 and 4.5 we show the comparison between reflectivity data and SLD profiles for water/toluene interface and water/dodecane interface at the same contrast.

[1]This mixture has been chosen to easily compare with the mixture of dodecane with same SLD.

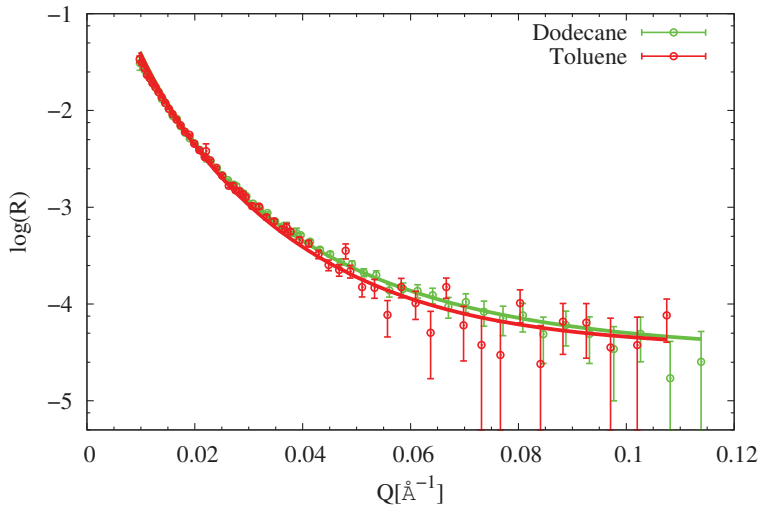

Figure 4.4: Neutron Reflectivity data (circle) and best fits (line) for D_2O/dodecane interface (green) and D_2O/toluene interface (red). In both cases the organic phase has an SLD= $4.0 \cdot 10^{-6}$ Å^{-2}. The ratio between hydrogenated/deuterated species is 25/75 for dodecane and 35/65 for toluene.

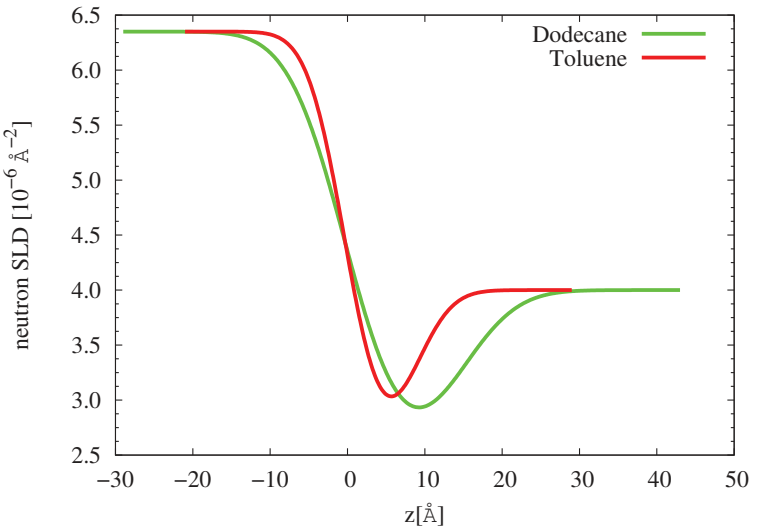

Figure 4.5: SLD profiles for D_2O/dodecane interface (green) and D_2O/toluene interface (red) corresponding to the data in Figure 4.4. In both cases the organic phase has an SLD= $4.0 \cdot 10^{-6}$ Å^{-2}. The liquid/liquid interface is placed at z=0 Å (left side, aqueous phase; right side, organic phase).

The two reflectivity curves in Figure 4.4 are similar, as expected. The small differences in reflectivity curves observed for $Q \geq 0.03$ Å^{-1} result in different SLD profiles for the two organic solvents (Figure 4.5). For the case of water/toluene interface, to fit the data, we have used a one layer model with a fixed layer thickness, 10 Å, fixed layer SLD, $0.95 \cdot 10^{-6}$ Å^{-2} (SLD of hydrogenous toluene) and fixed roughness σ_1 (water/layer interface) and σ_2 (layer/oil interface), 4 Å. In this way we have calculated the ratio between hydrogenous and deuterated oil in the interfacial layer. In Table 4.2 we report the results obtained for water/toluene and water/dodecane (at the same SLD contrast) interface.

Organic Solvent	**Hydrogenous oil volume percentage**	**Deuterated oil volume percentage**
Toluene	34%	66%
Dodecane	56%	44%

Table 4.2: Resulting amount of hydrogenous and deuterated oil in the interfacial layer at the oil/water interface. We compare the results for water/toluene and water/dodecane interface (with the same SLD contrast).

It is interesting to notice that different parameters are obtained for different oils. In the case of water/toluene interface we obtained an interfacial layer with less hydrogenous oil enrichment, compared to the water/dodecane interface. This result could depend on the different size of the two solvent molecules.
Even if the measurement at the $C_{12}H_{26}/D_2O$ interface does not exclude the possibility of residual impurities in the purified oil, the agreement in results with different organic solvents let us suppose a preferential adsorption of hydrogenous oil at the interface, maybe due to the different interaction between water and hydrogen and deuterium at the interface. Future measurements with deuterated organic solvents and mixures of H_2O/D_2O could be helpful for a better understanding of this phenomena. To ensure that samples with malonamides are not affected by this isotopic substitution issue we report in Figure 4.6 the comparison between oil/water interfaces with an without diamide.

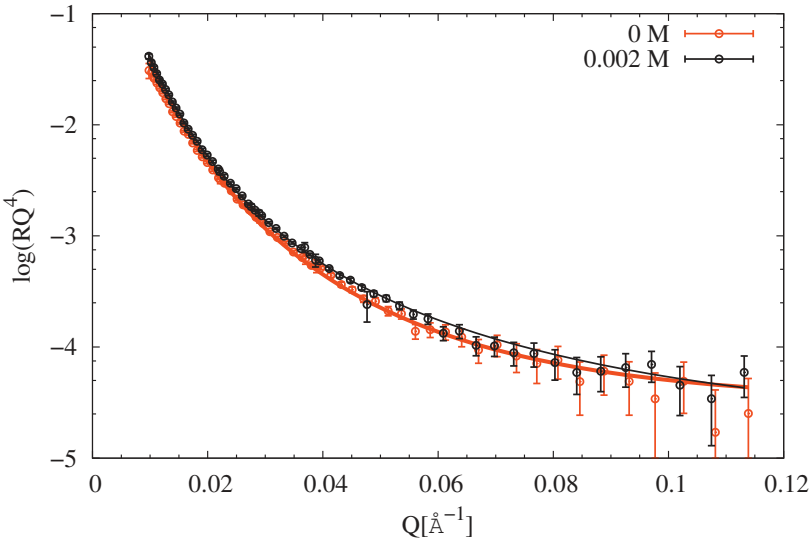

(a) Neutron Data and Fits

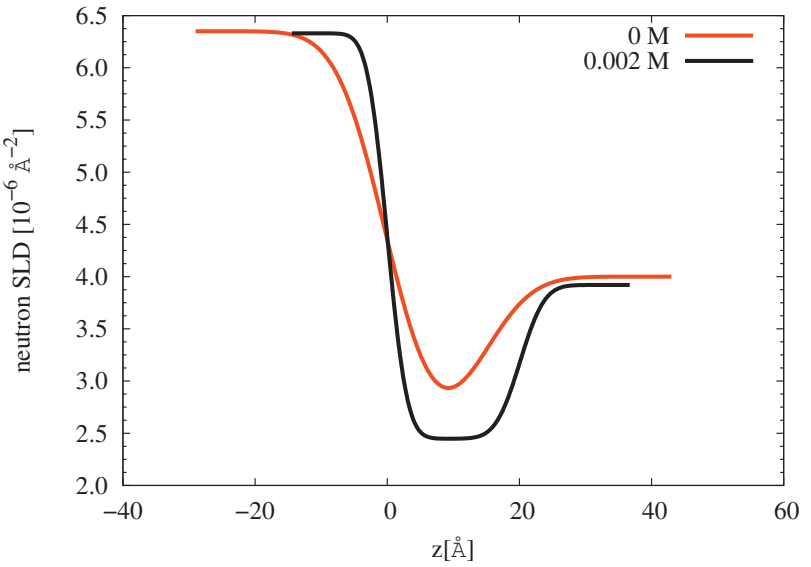

(b) Neutron SLD profiles

Figure 4.6: Comparison between buried oil/water interface with (black) and without (red) malonamide (DMDOHEMA). The aqueous phase was composed by D_2O and the organic phase was a mixture of hydrogenated/deuterated dodecane with an SLD= $4 \cdot 10^{-6}$ Å^{-2} obtained with an H/D ratio of 25/75.

In Figure 4.6a, we observe that even a low amount of extractant produces changes in the the reflected intensity resulting in a different SLD profile (Figure 4.6b). Although this issue of either a selective adsorption of protonated organic species or the presence of impurities at the interface was not fully understood and solved, we can consider in an arbitrary manner that the adsorption of ligand molecules at the interface is not affected by this problem. In other words, we have considered an homogenous (in term of deuteration) organic solvent both in bulk and interface.

4.2 DMDBTDMA at the Liquid-Liquid interface

In this section the results for the study of DMDBTDMA at dodecane/water interface will be reported. In Figure 4.27 the structure of DMDBTDMA is shown.

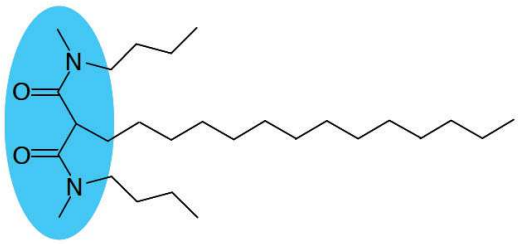

Figure 4.7: Structure of DMDBTDMA. The part in blue represents the polar head of ligand, responsible of the amphiphilic properties.

As explained in the previous chapter, the data analysis process consists of two main parts. In the first, data are analyzed with Motofit [93] to obtain an initial guess for the SLD profiles. The second step is the data analysis with the RMCS code (SLD profile analysis and Parratt refinement) exploiting the SLD profiles obtained via Motofit.
For the latter step a series of parameters has to be provided to the RMCS code, as the scattering lengths[1]. Those values, used for data analysis process for samples with DMDBTDMA, are listed in Table 4.3.

[1]With Equations 2.53 and 2.54 we have explained that the volume for each slice is fixed. In this way the code will calculate the Scattering Length Density as the ratio between the total Scattering Length and the fixed volume. For this reason the information provided to the code is the Scattering Length for each element.

Compound	**X-rays** [10^{-6} Å]		**Neutrons** [10^{-6} Å]	
	Real Part	Imaginary Part	Real Part	Imaginary Part
$C_{12}H_{26}$	2768.200	3.253	-	-
$C_{12}H_{26}/C_{12}D_{26}$	-	-	1512.2	0.019
$C_{12}D_{26}$	-	-	2533.100	0.003
DMDBTDMA	6933.800	1.020	78.282	0.061
H_2O	281.972	0.102	-	-
D_2O	-	-	191.530	0.000
DNO_3	-	-	334.490	0.005
HNO_3	902.371	0.360	-	-
Li	84.534	0.001	-19.000	0.196
Nd	1680.600	58.744	76.900	1.400
NO_3	874.190	0.360	267.750	0.005

Table 4.3: x-ray and neutron scattering lengths used for the RMCS analysis of the samples with DMDBTDMA. For x-rays the values have been calculated at 22 keV, for neutrons at a wavelength $\lambda = 1.8$ Å [92, 96].

4.2.1 Pure water

To understand the behaviour of DMDBTDMA at liquid/liquid interface a first investigation with pure water/dodecane interface has been conducted. During the data analysis process, the data evolution was not coherent and thus we conclude that samples were not equilibrated producing odd models.
In fact, if neutron reflectivity curves are collected on samples out of the equilibrium, it means that the final reflectivity curve is an average of curves corresponding at different structures. Obviously, in these conditions, the final model does not correspond to the real structure at the equilibrium and a final result would be fake.

4.2.2 Water and Nitric Acid

As shown in Chapter 1, Martinet et al. [61, 66] have measured by means of a drop-weight technique, the interfacial tension at the dodecane/water interface for different concentrations of DMDBTDMA and different aqueous phase[1]. For the

[1]The measurements carried out by Martinet et al. have been already shown in chapter 1. For the aqueous phase they selected the pure water, water with nitric acid (2 mol/l) and water with nictric acid (0.01 M), lithium nitrate (1 M) and neodymium nitrate (0.2 M).

three systems investigated (H_2O, HNO_3, $Nd(NO_3)_3$) they recorded three different CAC: 0.25 M for pure water, 0.23 M for nitric acid and 0.16 M for neodymium nitrate. Their results are shown in Figure 4.8.

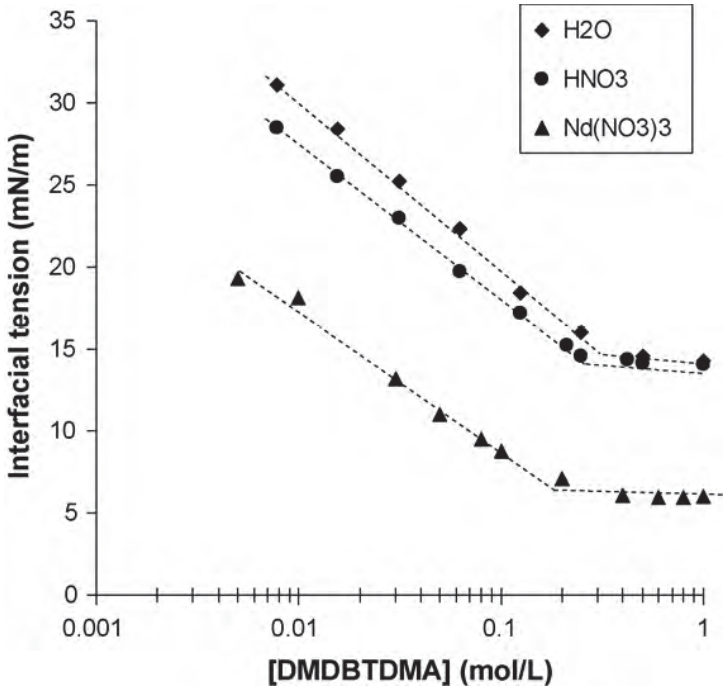

Figure 4.8: Interfacial tension at the aqueous–organic interface for solutions of DMDBTDMA in n-dodecane at ambient temperature. H_2O: water aqueous phase; HNO_3: 2 mol/L nitric acid aqueous phase; $Nd(NO_3)_3$: 0.2 mol/L neodymium nitrate, 1 mol/L lithium nitrate, 0.01 mol/L nitric acid aqueous phase [61, 66]. The change in slope observed in the curve $\gamma = f(lnC)$ (dashed lines), with C the extractant concentration in organic phase, corresponds to the formation of aggregates in the organic phase (CAC) [61, 66]. Figure extracted from reference [66].

Since the CAC for the sample in contact with nitric acid aqueous solution (2 M) is observed for an extractant concentration equal to 0.23 M, samples between 0.02 M and 0.4 M have been investigated in this work. The investigated samples are listed in Table 4.4.

The x-ray data recorded as well as the corresponding fits and SLD profiles obtained with a first analysis with Motofit are plotted in Figure 4.9. The reflectivity curves are plotted in $\log(RQ^4)$ vs Q. Respect to the representation chosen in the previous chapter the one chosen here is preferable to enhance the differences between curves.

Concentration [mol/l]	X-rays	Neutrons
0.02 M	**X**	**X**
0.07 M	**X**	**X**
0.1 M	X	-
0.2 M	**X**	**X**
0.3 M	X	**-**
0.4 M	X	**-**

Table 4.4: List of samples for DMDBTDMA in dodecane contacted with an aqueous phase at 2 M of Nitric Acid. For x-rays experiment HNO_3 in H_2O has been used, replaced by DNO_3 in D_2O for the neutron ones. The X means the sample has been measured, the - it has not, and the bold **X** means the data have been analyzed with the RMCS to investigate the liquid/liquid interfacial structure. The CAC is between 0.2 and 0.3 mol/L.

In Equation 2.21[1] it is shown that the reflectivity is proportional to Q^{-4} and multiplying the intensity for Q^{-4} we can underline the part depending on the Fourier transform of the SLD variation. A more detailed explanation for this representation is reported in Appendix *Reflectivity Data Representation*.

Concerning the data shown in Figure 4.9a, we observe that by increasing the extractant concentration the curves slope increases. This feature can be interpreted either with an increase of interfacial roughness, which is not physical as shown in the example in Appendix *Roughness Analysis*, or with a growth of diffuse layers. Looking at the SLD profiles in panel (b) of the same figure, the presence of a layer (or layers) more and more diffuse seems to be the right interpretation in agreement with the result of the neutron experiment shown in Figure 4.10.
Adsorption of diamide (with a low neutron SLD compared to other compounds) at the interface results in a minimum of the three SLD profiles in Figure 4.10b. Besides, the adsorption of ligand becomes more and more diffuse by increasing the malonamide bulk concentration.

[1]

$$R(Q_z) = |r(Q_z)|^2 = \frac{16\pi^2}{Q_z^4}\left|\int \frac{d\rho(z)}{dz} exp(iQ_z z)dz\right|^2 .$$

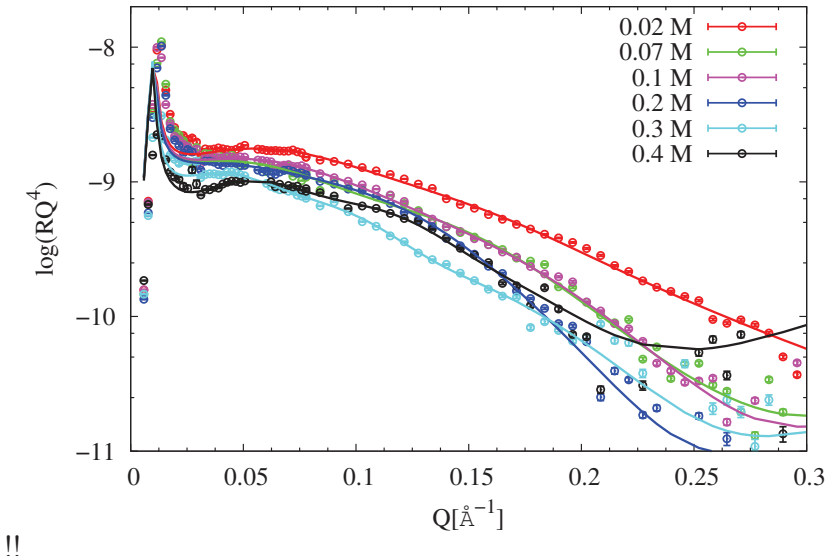

!!

(a) X-ray Data

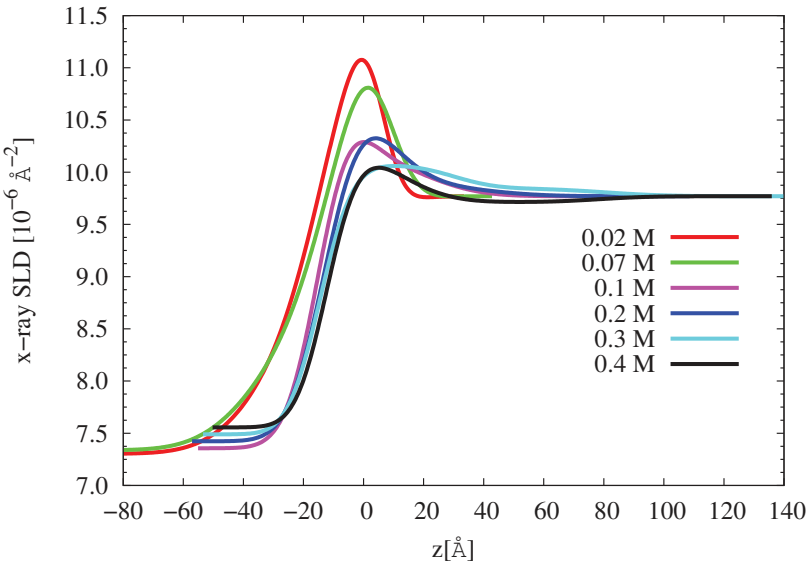

(b) SLD profiles

Figure 4.9: (a) X-ray reflectivity curves and corresponding fits of samples with DMDBTDMA at various concentrations in dodecane contacted with an aqueous solution of nitric acid (2M). In the legend is reported the extractant concentration in organic phase. Data are plotted with circles and error bars, fits with lines. Data have been normalized to the transmitted beam through the oil phase at the measured concentrations ensuring the correct modeling for the fitting process.(b) SLD profiles obtained via fitting process[93] of data shown in panel (a). The liquid/liquid interface is placed at $z = 0$ Å(left side, organic phase; right side aqueous phase).

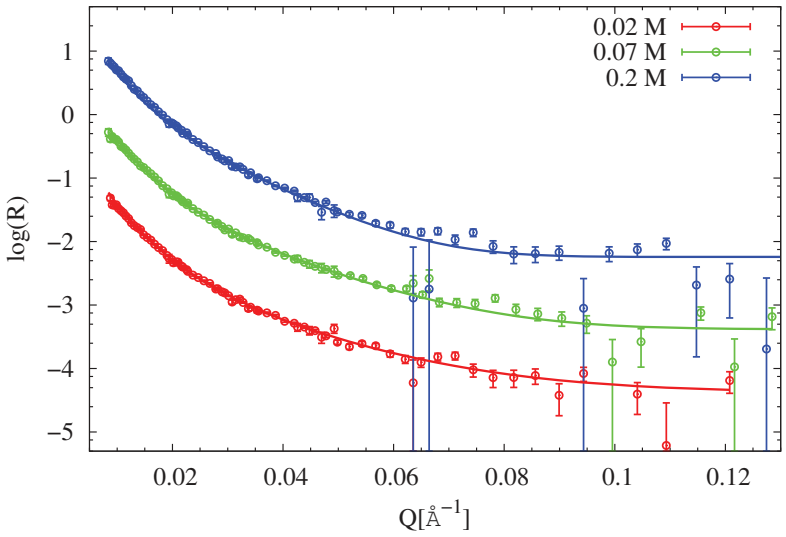

(a) Neutron Data

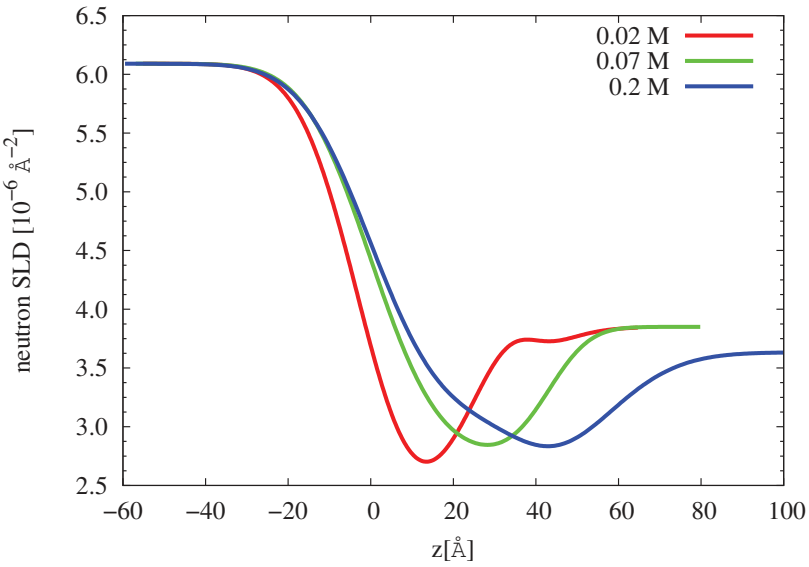

(b) SLD profiles

Figure 4.10: (a) Neutron reflectivity curves and corresponding fits of samples with DMDBTDMA at various concentrations in dodecane contacted with an aqueous solution of nitric acid (2M). The data are shifted for clarity. In the legend is reported the extractant concentration in organic phase. Data are plotted with circles and error bars, fits with lines.(b) SLD profiles obtained via fitting process [93] of data shown in panel (a). The liquid/liquid interface is placed at $z = 0$ Å(left side, water phase; right side organic phase).

At 0.02 M, the x-ray SLD at the interface is higher with respect to the SLD of the two bulk phases. The two compounds in the system with an higher SLD, compared to the oil or water, are the nitric acid and the diamide[1] therefore, the increasing of SLD is in agreement with an adsorption of both compounds at the interface with an excess of nitric acid[2].
The same trend is reproduced for the sample at 0.07 M, even if the maximum value of SLD is lower. At this concentration we observe that the SLD variation around the interface starts broadening. For higher concentrations the SLD maximum in the profiles decreases constantly and the SLD variation across the interface interests a region larger and larger.

A more detailed analysis has been performed with the help of the RMCS code for the samples investigated both with x-rays and neutrons. Data and fits are shown in Figures 4.11 and 4.12[3].

In Figure 4.13 we plot the distribution of dodecane, water and diamide at various extractant concentrations. We observe that the adsorption of DMDBTDMA at the interface does not increase with the bulk concentration. In fact, at 0.02 M and 0.07 M the maximum amount of diamide is found around $z = -20$ Å with an occupied volume between 35% and 40%. At the highest concentration, 0.2 M, the maximum of the diamide distribution is shifted more into the organic phase with a maximum value less than 30%. Moreover, at the highest extractant concentration, the distribution of diamide is broader compared to the first two. The comparison between diamide distributions is plotted in Figure 4.14a.

Nitric acid shows a symmetric behavior approaching to the CAC (Figure 4.14b). At higher extractant bulk concentrations, the nitric acid adsorption interests a larger region with a decrease of its maximum in concentration at the interface. Furthermore, regarding the sample at 0.2 M, the shift of diamide seems leaving space to the nitric acid to penetrate more into the organic phase.

[1] If we divide the diamide in two parts, polar head and tails, the SLDs (in 10^{-6} Å^{-2}) are 9.80 and 7.88 respectively [67].

[2] The x-ray SLD of the nitric acid is equal to $13.2 \cdot 10^{-6}$ Å^{-2}.

[3] To avoid redundance of symbols, the fits have been reported with dashed lines. For each curve, the fitting function for each Q is in the middle point between the two dashed lines. In this way we report the errors on the fitting function calculated as explained in section 2.2.3. From now on data will be presented in $\log(RQ^4)$ for x-rays, $\log(R)$ for neutrons and with confidence region for fits.

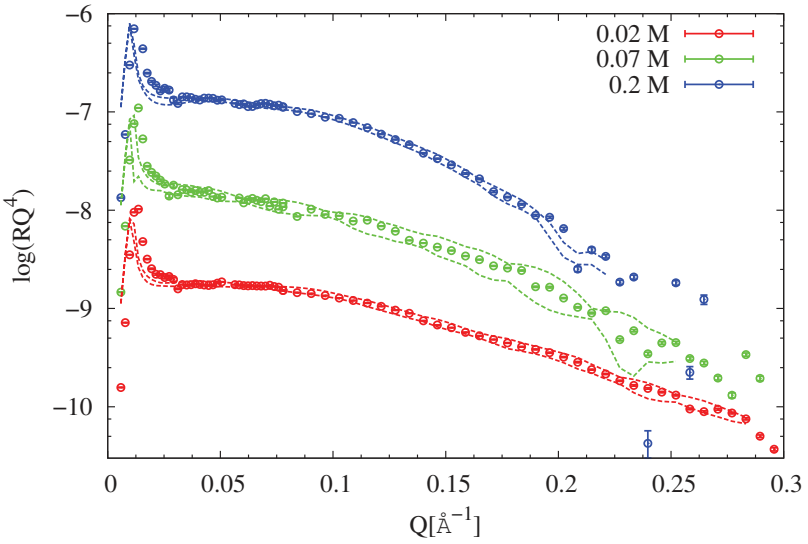

Figure 4.11: X-ray reflectivity data and fits. With circles we report the recorded data with experimental errors, with dashed lines the confidence region for the fitting function. Data have been shifted for clarity.

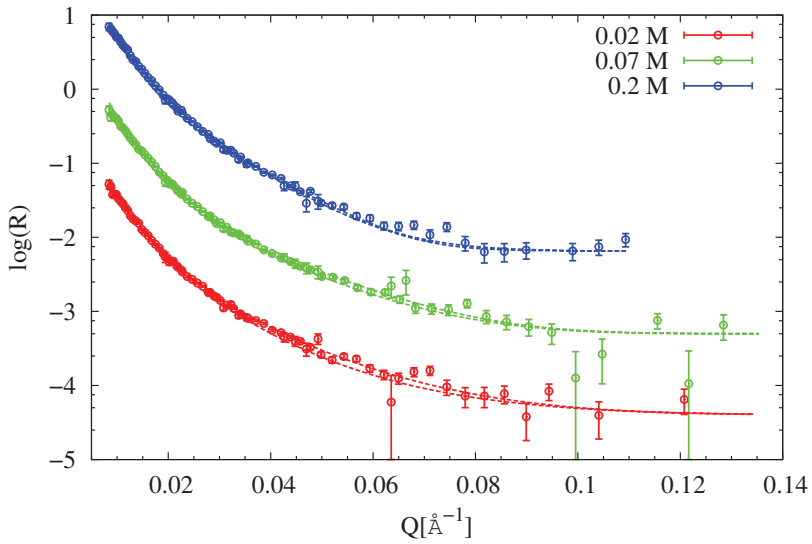

Figure 4.12: Neutron reflectivity data and fits. With circles we report the recorded data with esperimental errors, with dashed lines the confidence region for the fitting function. Sata have been shifted for clarity.

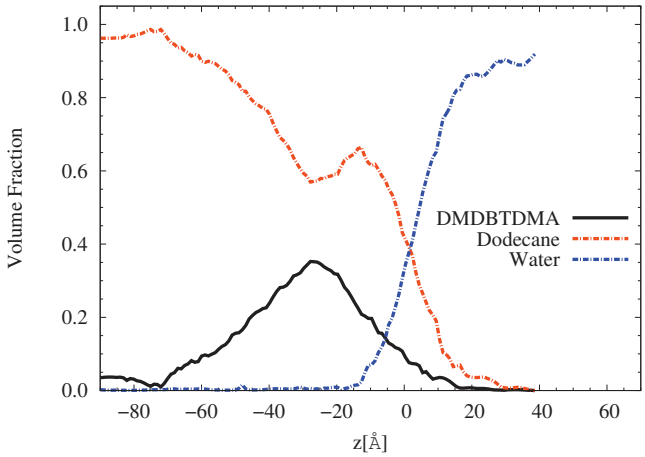

(a) 0.02 M

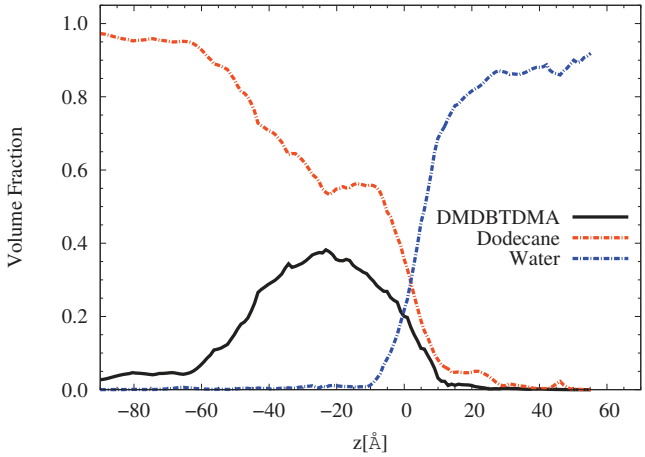

(b) 0.07 M

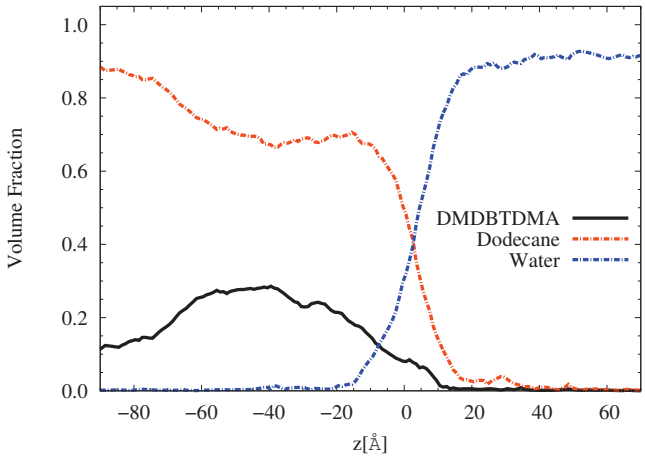

(c) 0.2 M

Figure 4.13: Distribution of DMDBTDMA, water and dodecane for the sample at various concentration of extractant: (a) 0.02 M, (b) 0.07 M, (c) 0.2 M. In the analysis process the initial interface plane is set at $z = 0$ Å.

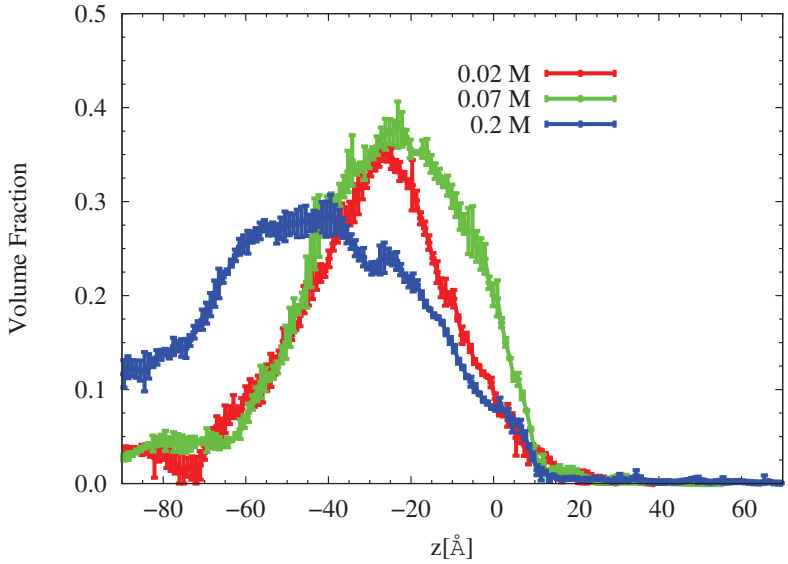

(a) Diamide distributions

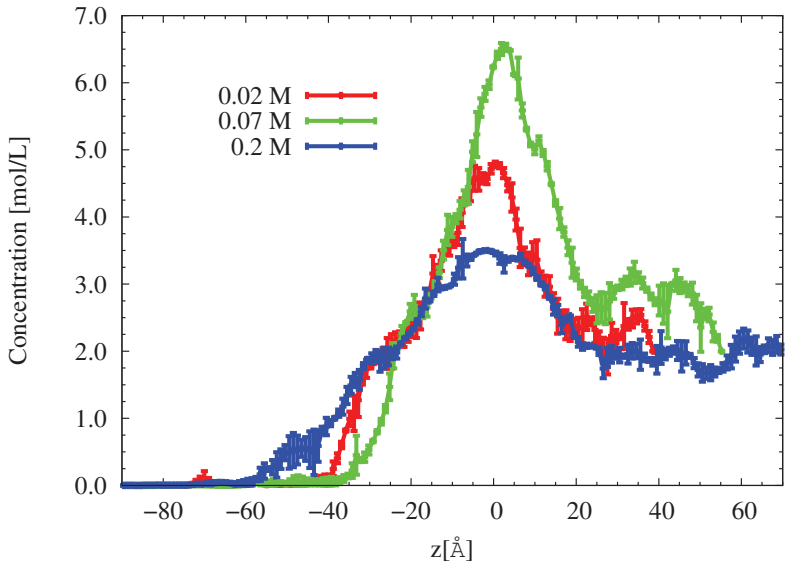

(b) Nitric acid distributions

Figure 4.14: Comparison between distributions of (a) DMDBTDMA and (b) nitric acid, for all the investigated samples. With the vertical bars we report the error in volume fraction calculated as explained in section 2.2.3. In the analysis process the interface is set at $z = 0.0$ Å.

In the Figures 4.15 and 4.16 we compare the distributions of diamide and nitric acid (mol/L *vs* z) for each sample. We observe a strong interpenetration between DMDBTDMA and nitric acid around the interface, increasing with the ligand bulk concentration. At the maximum of extractant distribution the molar ratio between nitric acid and diamide varies between 2.5 and 1.5. We will come back on this at the end of the chapter.

For the highest concentrations, measured only with x-rays, due to the linear model obtained with Motofit, we can suppose that the diamide will distribute on larger volumes and the nitric acid will penetrate even more into the organic phase, allowing the extraction.

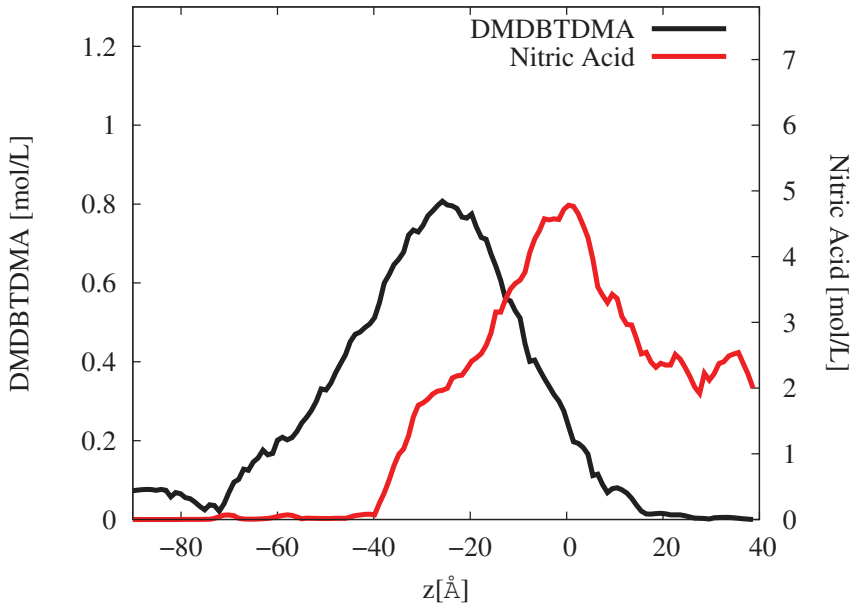

Figure 4.15: Comparison between distributions of DMDBTDMA and nitric acid, for samples with 0.02 M of DMDBTDMA in dodecane. The vertical axes on the left represents the concentration of DMDBTDMA (mol/L) and the right one the concentration of nitric acid (mol/L).

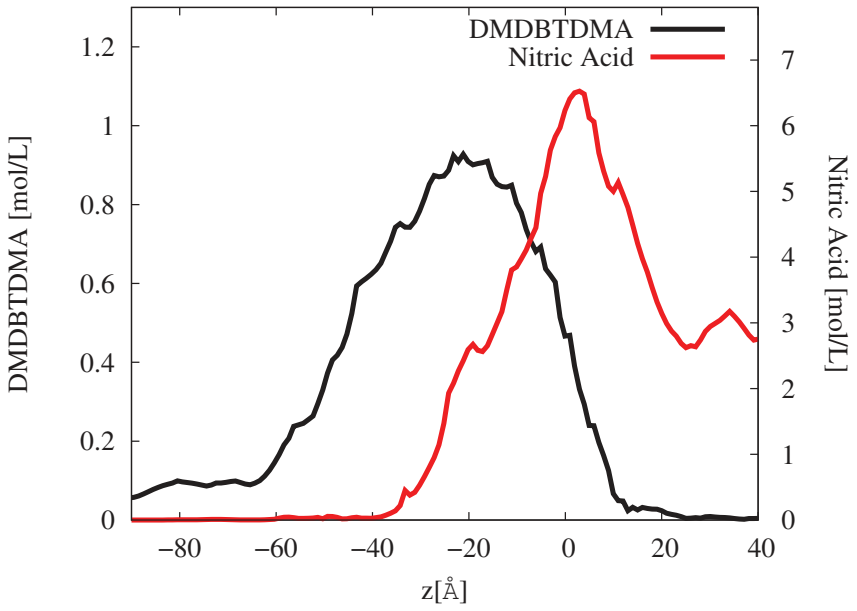

(a) 0.07 M

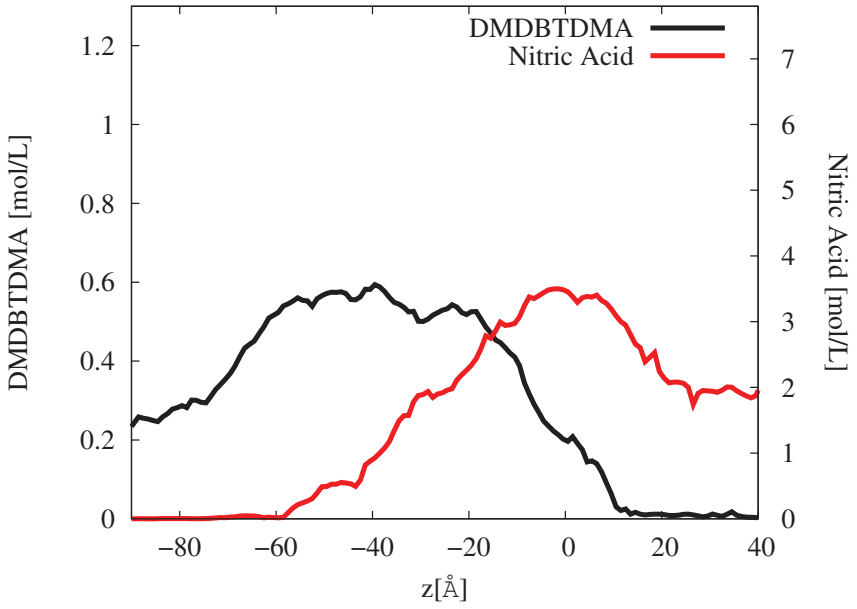

(b) 0.2 M

Figure 4.16: Comparison between distributions of DMDBTDMA and nitric acid, for samples with (a) 0.07 M and (b) 0.2 M of DMDBTDMA in dodecane. The vertical axes on the left represents the concentration of DMDBTDMA (mol/L) and the right one the concentration of nitric acid (mol/L).

4.2.3 Water and Neodymium Nitrate

One of the two most interesting systems of this thesis work is the system containing lanthanide salt which is complexed by DMDBTDMA. In Figure 4.8 we have reported the interfacial tension measurements carried out by Martinet et al. [61, 66] The authors present the values of the interfacial tension at dodecane/water interface at various extractant concentrations, for three different aqueous phases. One of those three is composed by lithium nitrate (1 M), neodymium nitrate (0.2 M) and nitric acid (0.01 M). In this thesis work, in order to study the interface between DMDBTDMA in dodecane contacted with a neodymium nitrate aqueous phase, we have chosen a slightly different system: an aqueous solution of lithium nitrate (2 M) and neodymium nitrate (0.25 M) with no nitric acid.
Measurements of interfacial tension for this system have been carried out with a Kruss drop-shape tensiometer. The recorded values are reported in Table 4.5.

DMDBTDMA [mol/l]	**Interfacial Tension [mN/m]**
Air-Water	76.0 ± 0.2
0.00	49.6 ± 1.4
0.01	15.8 ± 0.2
0.02	13.7 ± 0.4
0.04	11.3 ± 0.7
0.06	8.5 ± 0.2
0.08	7.6 ± 0.2
0.09	7.2 ± 0.4
0.10	6.5 ± 0.4

Table 4.5: Interfacial tension at dodecane/water interface at various DMDBTDMA concentrations. The aqueous phase is an aqueous solution of lithium nitrate (2 M) and neodymium nitrate (0.25 M). On the first column is reported the concentration of extractant in organic phase, on the right one the interfacial tension with the standard deviation. The sample at 0.00 M represents the pure water/dodecane interface.

The measurements at concentrations higher than 0.1 M were not carried out because of experimental difficulties. The measurements have been carried out increasing progressively the concentration of diamide. To do that, an amount of diamide, previously dissolved in dodecane, has been added (as explained in Section 3.5). At concentrations higher than 0.1 M third phase appears destroying the drop. Many attempts have been made and recorded. The interfacial tension at 0.1 M is

very low ($\approx$ 6.5 mN/m). Despite this, the measurements shown in Table 4.5 are in agreement with those presented by Martinet et al. [61, 66]. Further tests with small angle neutron scattering[1] have confirmed the CAC at 0.12 M and formation of a third phase at 0.15 M.
For the reasons explained above samples between 0.02 M and 0.15 M have been investigated in this thesis work, as listed in Table 4.6.

Concentration [mol/l]	X-rays	Neutrons
0.02 M	**X**	**X**
0.04 M	-	X
0.07 M	**X**	**X**
0.08 M	X	-
0.09 M	**X**	**X**
0.1 M	**X**	**X**
0.15 M	-	X

Table 4.6: List of samples for DMDBTDMA in dodecane contacted with an aqueous phase at 2 M $LiNO_3$ and 0.25 M $Nd(NO_3)_3$. The X means that the sample has been measured, the - it has not, and the bold **X** means that data have been analyzed with the RMCS to investigate the liquid/liquid interfacial structure. For neutron experiments an organic phase composed by fully deuterated dodecane, $C_{12}D_{12}$, has been used.

In Figure 4.17a we report data recorded with x-rays and best fits. We observe a more pronounced decrease of the reflected intensity at large Q-values when increasing the diamide concentration. This can be interpreted as an increase of the interface roughness[2] as explained for samples presented in section 4.2.2. Some features, like the weak intensity bump at low Q, however, indicate liquid structuration at larger length scales than those corresponding to a simple monolayer formation.
The SLD profiles obtained with Motofit [93] are plotted in Figure 4.17b.

[1] The data are not presented in this thesis.

[2] From the variation of interfacial tension depending on the extractant concentration and assuming only the adsorption of diamide, we calculated a roughness amplitude variation from 4 to 10 Å[49]. This variation can partially explain the decrease of the reflected intensity at large Q-values and is taken into account within the layer overlapping in the sigma parameters (representing the roughness) during the Motofit modeling.

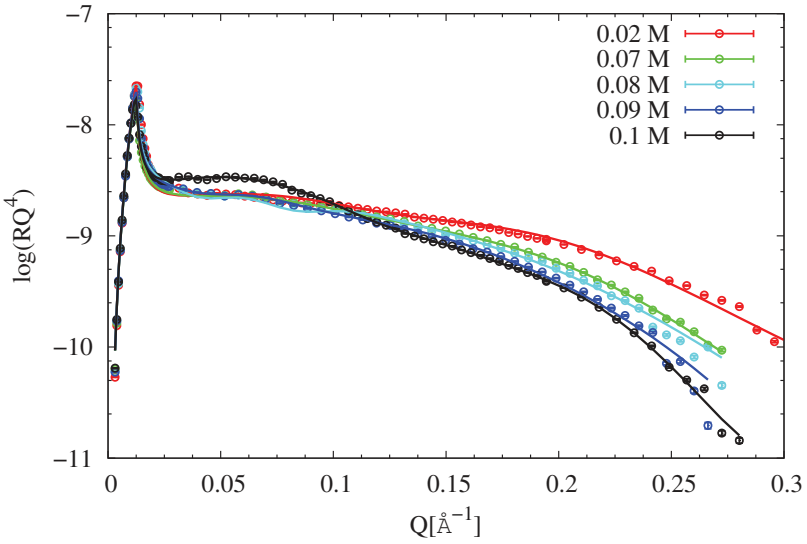

(a) X-ray Data and Fit

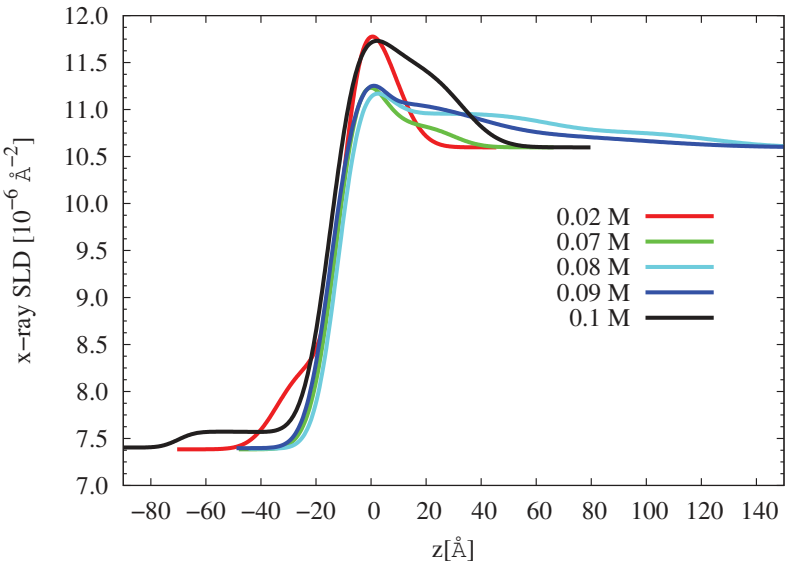

(b) SLD Profiles

Figure 4.17: (a) X-ray reflectivity curves and best fits of samples with DMDBTDMA in dodecane contacted with an aqueous solution of $LiNO_3$ (2M) and $Nd(NO_3)_3$ (0.25 M). Data are plotted with circles with experimental error bars, fits with lines. (b) SLD profiles obtained with best fitting process of data in panel (a).The liquid/liquid interface is placed at $z = 0$ Å (left side, organic phase; right side aqueous phase). In the legend the concentration of diamide in organic bulk phase is reported.

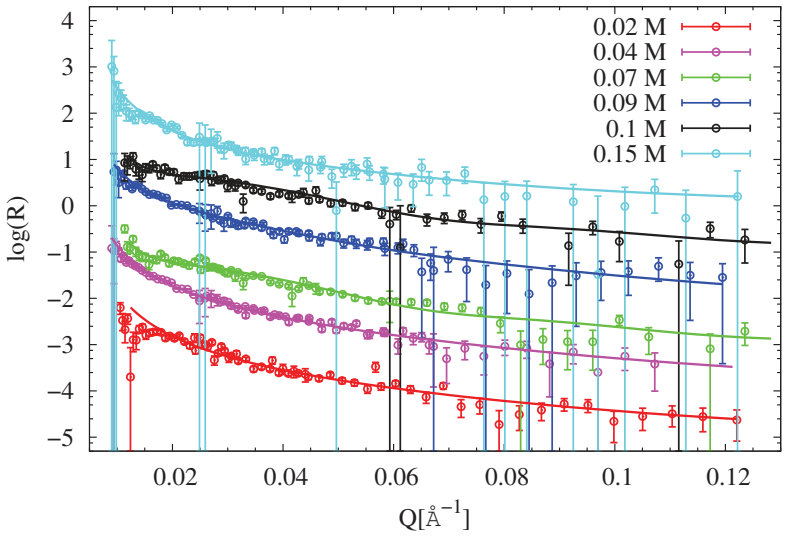

(a) Neutron Data and Fit

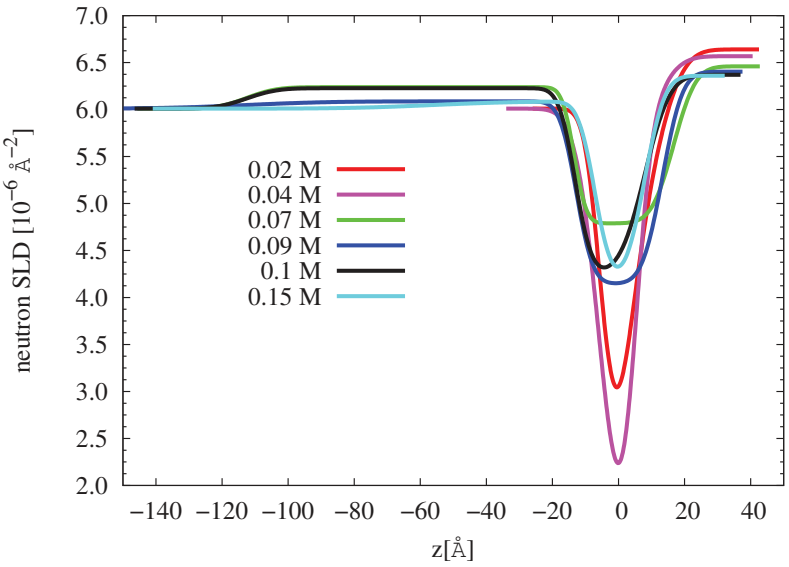

(b) SLD Profiles

Figure 4.18: (a) Neutron reflectivity curves and best fits of samples with DMDBTDMA in dodecane in contact with an aqueous solution of $LiNO_3$ (2M) and $Nd(NO_3)_3$ (0.25 M). Data are plotted with circles and with experimental error bars, fits with lines. The curves have been shifted for clarity. (b) SLD profiles obtained with best fitting process [93] of data in panel (a). The liquid/liquid interface is placed at $z = 0$ Å(left side, aqueous phase; right side organic phase). In the legend the concentration of diamide in organic bulk phase is reported.

Across the liquid/liquid interface, an excess of ions and extractant molecules results in a maximum in the X-ray SLD profiles and a minimum in the neutron SLD profiles (Figure 4.18b), which are inverted due to the different scattering contrasts of the species involved. For X-rays, the electron density (and the SLD, respectively) is the largest in presence of high amounts of ions and data are most sensitive to the concentration of these species at the interface. For neutrons, the diamide is fully protonated (with a low SLD compared to the other deuterated or partially deuterated compounds) and data are most sensitive to the diamide concentration at the interface. At low diamide concentration a dense and sharp distribution of the extractant molecules is observed at the interface which becomes slightly more diffuse as the diamide concentration increases and reaches the CAC. Simultaneously, a wider distribution of ions is observed at the interface. For samples measured with both x-rays and neutrons the RMCS code has been used for the analysis. Data and fits obtained with this procedure are plotted in Figures 4.19 and 4.20.

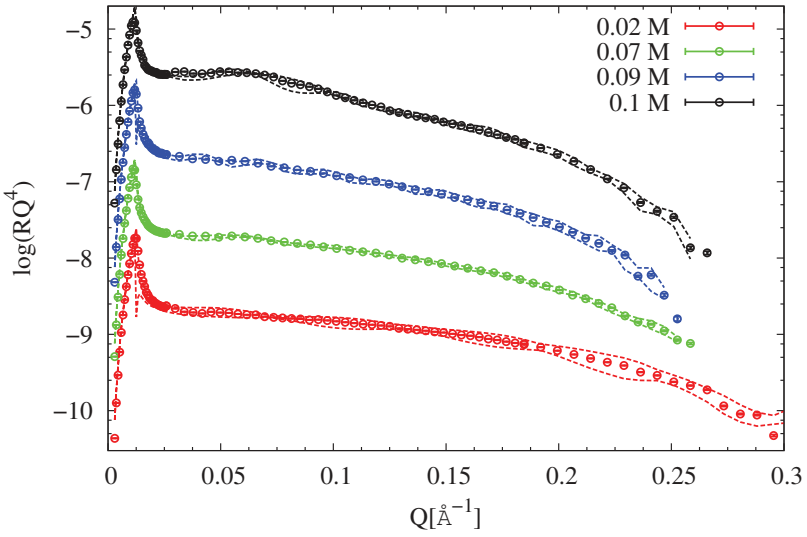

Figure 4.19: X-ray reflectivity data and fits obtained with the RMCS code. With circles we report the recorded data with experimental errors, with dashed lines the confidence region for the fit function. Data have been shifted for clarity.

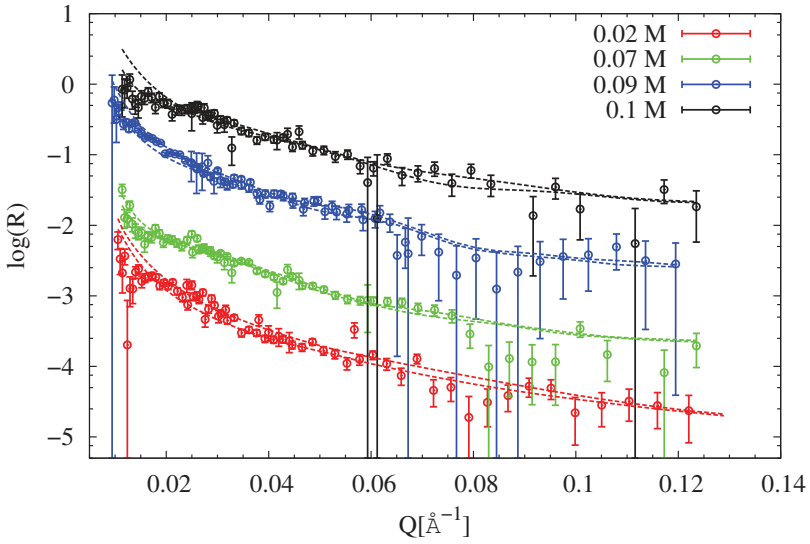

Figure 4.20: Neutron reflectivity data and fits obtained with the RMCS code. With circles we report the recorded data with esperimental errors, with dashed lines the confidence region for the fit function. Data have been shifted for clarity.

The analysis performed with the RMCS code evidences, as for the nitric acid extraction, an unexpected behaviour of extractant and salts. In Figures 4.21 and 4.22 the distributions of diamide, dodecane and water across the interface are plotted.
For the sample at the lowest concentration of DMDBTDMA (Figure 4.21a), a strong adsorption of extractant is observed as expected for a classical surfactant. In fact, close to the xy-plane at $z = 0$ Å, the diamide molecules occupy approximately 60% of the available volume between the water and the dodecane.
For the sample at 0.07 M, shown in panel (b) of the same figure, we observe that the diamide is distributed on a larger volume penetrating more in the water phase and viceversa[1].

For higher concentrations of extractant, this mixing is enhanced. Despite that, the maximum of diamide distribution does not shift[2] and the maximum volume occupied is between 32% and 37%.

[1]The initial interface plane is set at z=0 Å. When we say that one compound penetrates more or less in one phase we assume that for all the $z < 0$ Å we have the organic phase and the aqueous phase for all the $z > 0$ Å.

[2]For the nitric acid extraction we observe that the DMDBTDMA distribution shifts into the organic phase when increasing the concentration in bulk.

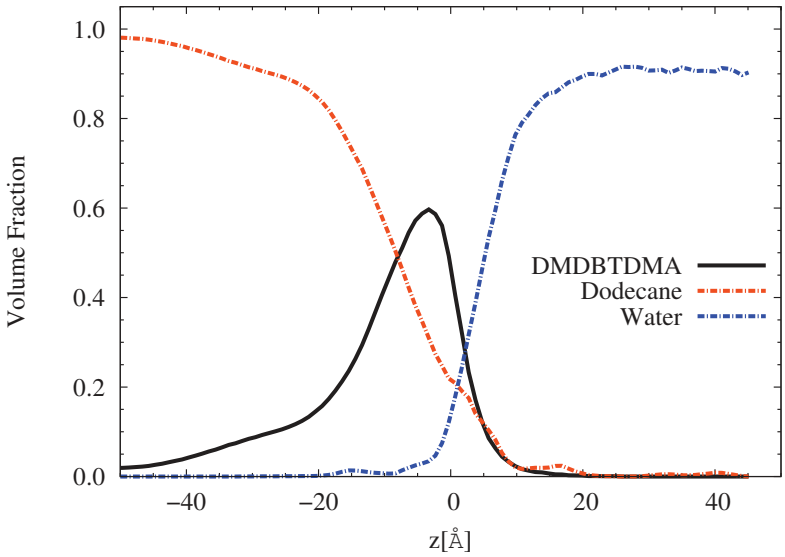

(a) 0.02 M

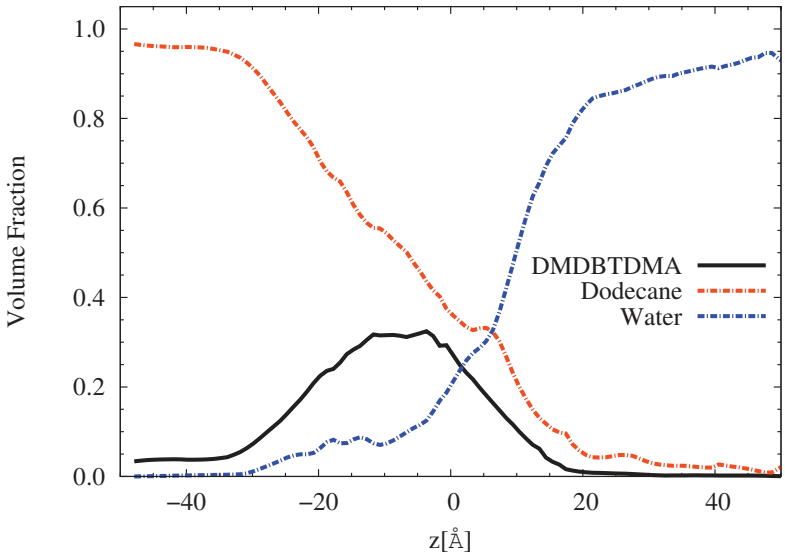

(b) 0.07 M

Figure 4.21: Distribution of DMDBTDMA, water and dodecane for the sample at (a) 0.02 M and (b) 0.07 M. In the analysis process the initial interface xy-plane is set at $z = 0$ Å.

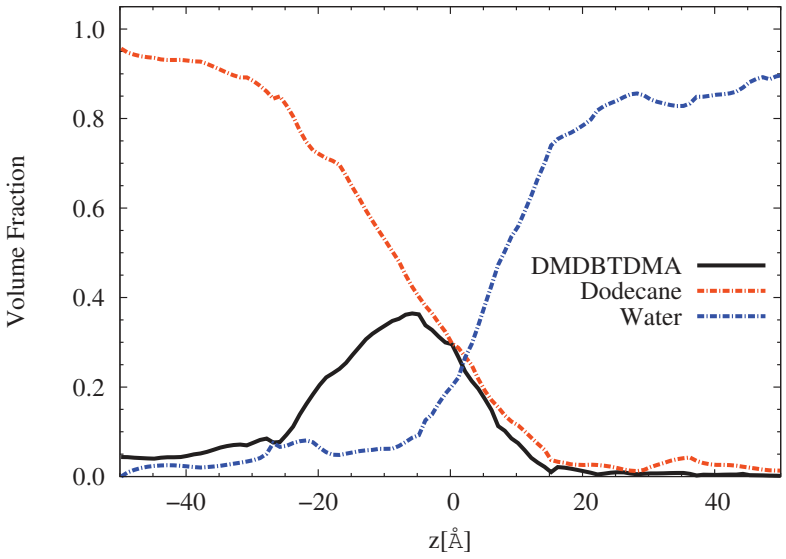

(a) 0.09 M

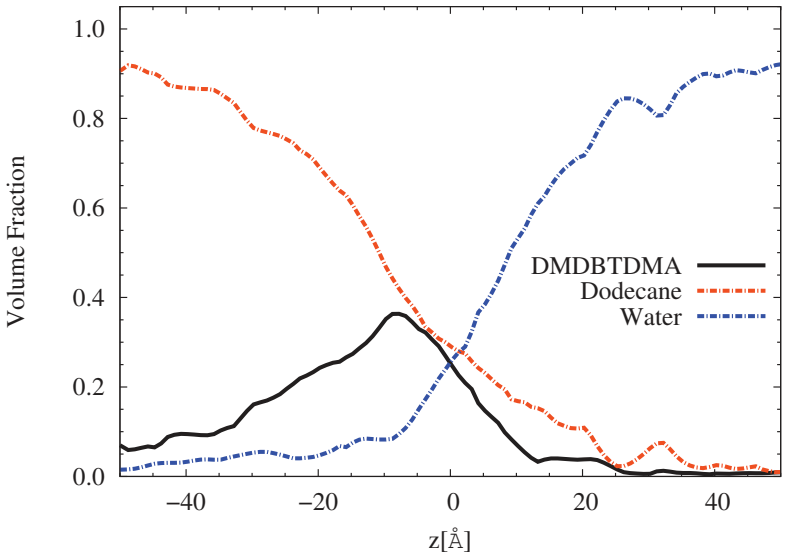

(b) 0.1 M

Figure 4.22: Distribution of DMDBTDMA, water and dodecane for the sample at (a) 0.09 M and (b) 0.1 M. In the analysis process the initial interface xy-plane is set at $z = 0$ Å.

In Figure 4.23 the comparison between diamide distributions for the four in-

vestigated samples is plotted. We observe that the diamide distribution across the liquid/liquid interface becomes larger at higher concentrations of extractant. On the other hand the distribution peak does not shift.

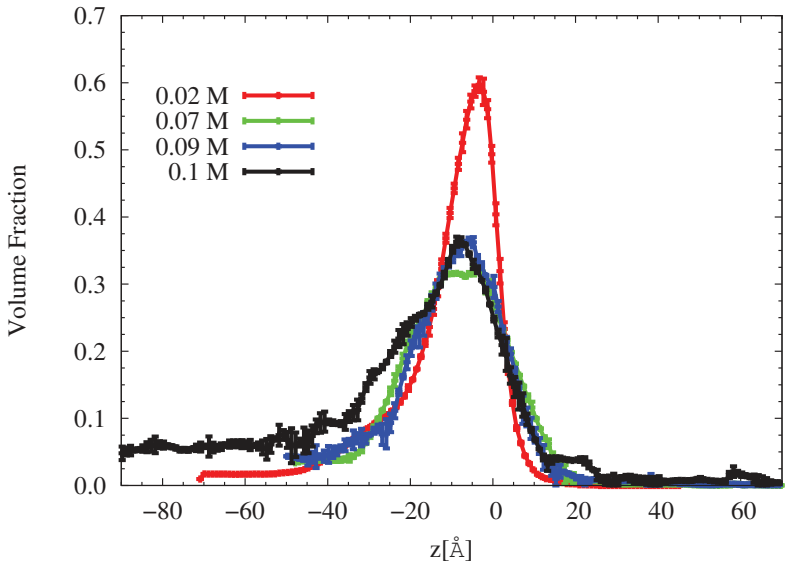

Figure 4.23: Comparison between distributions of DMDBTDMA for all the investigated samples. With the vertical bars we report the error in volume fraction calculated as explained in Section 2.2.3.

In Figure 4.24 the results for lithium, nitrate and neodymium at various extractant concentrations are plotted.
The lithium (panel (a)) shows a symmetric evolution to that of the diamide. At the lowest diamide bulk concentration it is strongly adsorbed, while at higher concentration a weaker adsorption is observed. The interpenetration between diamide and lithium is constant in all the sample.
On the contrary, neodymium and nitrate show a strong adsorption in all samples. Moreover, the penetration of these two ions into the organic phase increases with the ligand bulk concentration.
For all ions the distribution maximum is observed at $z \approx 5$ Å and it does not shift with the extractant concentration.

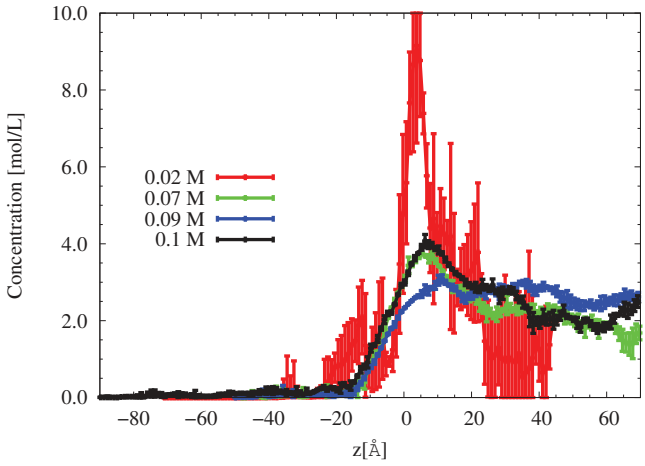

(a) Lithium

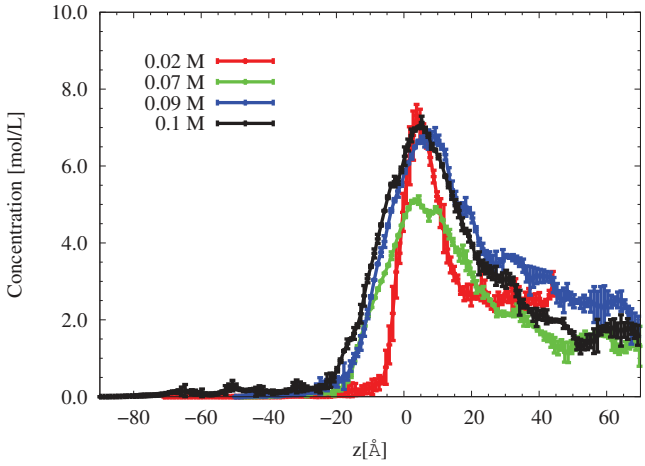

(b) Nitrate (NO_3)

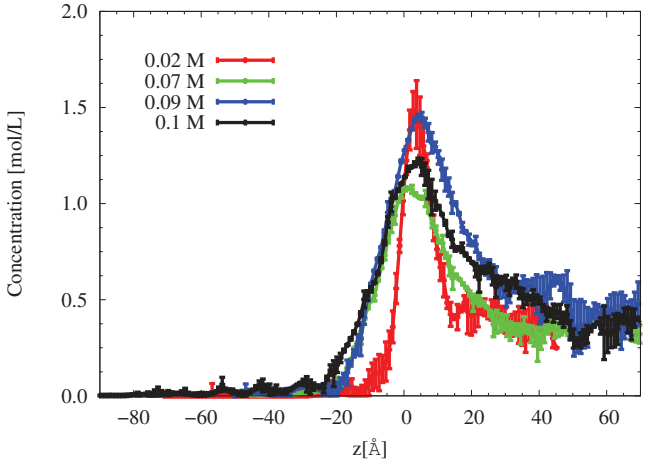

(c) Neodymium

Figure 4.24: Comparison between ion distributions. (a) Lithium, (b) nitrate and (c) neodymium for all the investigated samples. With the vertical bars we report the error in volume fraction calculated as explained in Section 2.2.3. In the analysis process the initial interface xy-plane is set at $z = 0$ Å. The legend shows the concentration of DMDBTDMA in the organic phase.

Since we considered the salts has completely dissociated[1], each ion has a charge. By indicating with j the ion, with q_j the charge, with $N_j(z)$ the number of molecule for a fixed z and with $v_{tot}(z)$ the volume of each slice[2], we can calculate the average charge density Q_{tot} in the simulation box, as

$$Q_{tot} = \frac{\sum_z \sum_{j=1}^{3} q_j N_j(z)}{\sum_z v_{tot}(z)}. \tag{4.1}$$

Q_{tot} was calculated for the four samples shown in this section with Equation 4.1. The average charge density does not go over $(7.0 \pm 5.0) \cdot 10^{-4}$ $e/\text{Å}^3$. Although no minimization of charge has been imposed in the data analysis with the RMCS code, the value of Q_{tot} is very low in agreement the principle of charge conservation[97]. The result shows that the RMCS code finds the distributions, even without any external constraint on the charge, respecting the principles of electrochemistry.

Lastly, in Figures 4.25 and 4.26 the distributions of diamide and neodymium are compared. At 0.02 M the two distributions interpenetrate and their maxima are approximately equal. At higher concentration the interpenetration is stronger, while the maximum of the diamide distribution is much lower, compared to the one at 0.02 M. For the lanthanide it does not go lower than 1.0 mol/L. The interface appears enriched of neodymium ions[3] at all diamide concentrations.
The molar ratio between neodymium and DMDBTDMA at its maximum increases with diamide concentration in dodecane, passing from 0.1 at 0.02 M to 1 at 0.1 M. This result will be discussed in more detail at the end of the chapter.

[1]Our statement does not mean that the salts are completely dissociated in water but for the RMCS code they are considered separately.

[2]In previous chapter we have explained how the volume is calculated. In the simulation settings file the user fixes the volume (in Å^3) for each slice.

[3]For previous considerations, the interface is well enriched of nitrate too.

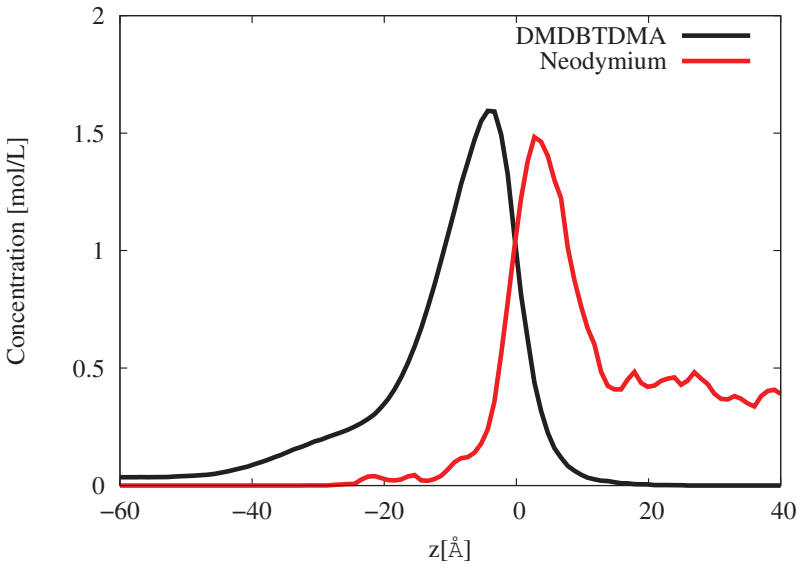

(a) 0.02 M

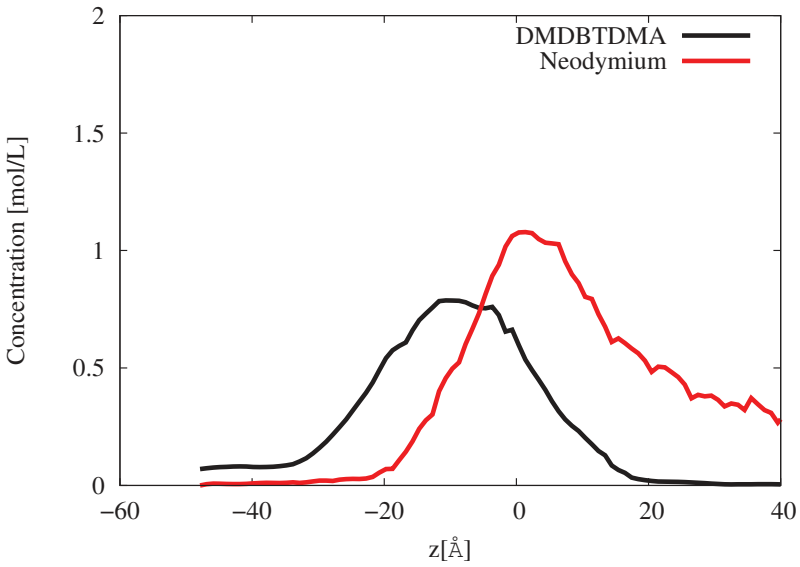

(b) 0.07 M

Figure 4.25: Comparison between neodymium and DMDBTDMA distributions for the sample at (a) 0.02 M and (b) 0.07 M. In the analysis process the initial interface xy-plane is set at $z = 0$ Å. The error bars are not reported for clarity.

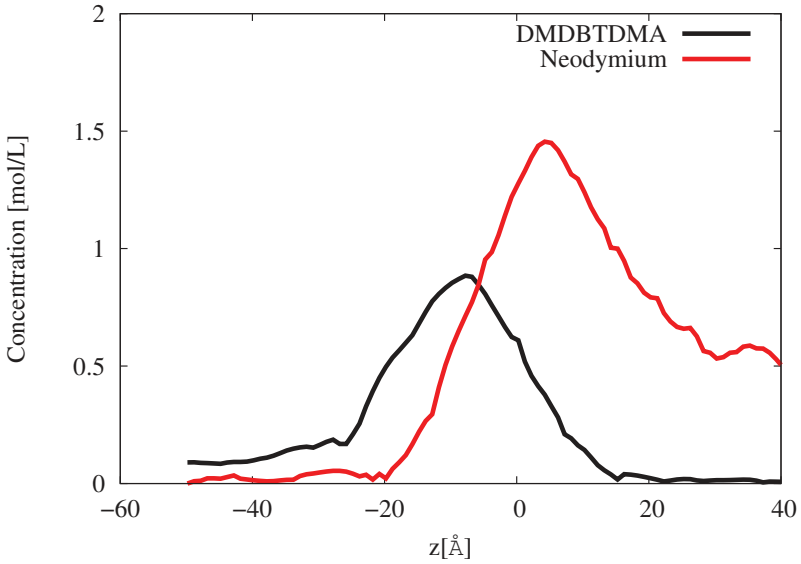

(a) 0.09 M

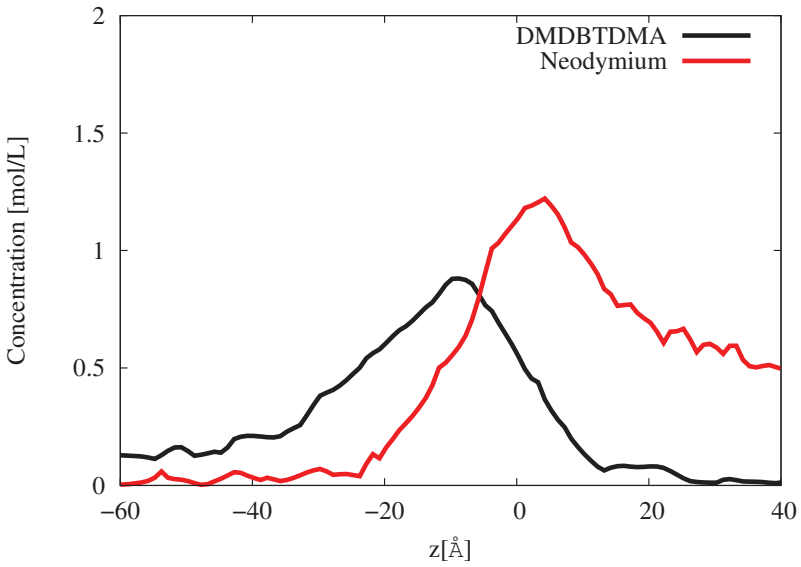

(b) 0.1 M

Figure 4.26: Comparison between neodymium and DMDBTDMA distributions for the sample at (a) 0.02 M and (b) 0.07 M. In the analysis process the initial interface xy-plane is set at $z = 0$ Å. The error bars are not reported for clarity.

4.2.4 DMDBTDMA: Summary

DMDBTDMA has been investigated at the interface between dodecane and aqueous solutions of nitric acid (2 M) or neodymium nitrate (0.25 M). In both cases a diffuse region between water and oil, enriched with extractant and extracted solute, appears approaching to the CAC.

By increasing the concentration of extractant two different evolutions are observed:

- **nitric acid aqueous phase**: the amount of nitric acid at the interface decreases and its distribution is larger penetrating more in the organic phase;
- **neodymium nitrate aqueous phase:** neodymium and nitrate remain well adsorbed at the interface penetrating more and more in the organic phase. Lithium ions adsorption is stronger at the lowest diamide concentration and no shift into the organic phase is observed.

At the beginning of this section in Figure 4.8 we have reported the interfacial tension measurements carried out by Martinet et al. [66, 61].
In their work the authors write: *"The interfacial tension decrease observed with increasing extractant concentration corresponds to the general pattern observed for classical surfactants. The malonamide molecules adsorb to the water/oil interface, and thus decrease the interfacial tension."*. This statement is based on the Gibbs model (see Chapter 1, section 1.2.1) used to calculate the amount of diamide adsorbed at the interface. Nevertheless, their conclusion is in disagreement with our data analysis. In fact, the decrease of the interfacial tension is due to a formation of a larger region in which both diamide and extracted solutes are adsorbed.
The different result depends on the Gibbs model used by Martinet et al. which explains the decrease of interfacial tension by the adsorption of ligand at the interface. On the contrary, in our data analysis we have considered the contribution of all the components adsorbed at the interface

At least for the systems presented in this section, we can consider that our approach using a simple Gibbs model has to be improved taking into account the various interactions between each species at the interface due to the high concentration as well as the polarization effect. Nevertheless this approach remains valid for samples without solutes in the aqueous phase.

Finally, the low value of the interfacial tension can be explained with the formation of a region between two liquids where the separation between aqueous and organic phase is less marked. Since we know that the cation in the organic

phase is solvated within an aggregate of diamide extractant, we can suppose that the transfer of this cation from the aqueous phase toward the organic phase is favoured by the formation of this aggregates in an interfacial region where the concentration and the conformation of the ligand is sufficiently high for the cation to be "encapsulate" without a high energy cost in term of enthalpy and entropy. In the following section let's compare this system with another type of diamide molecule.

4.3 DMDOHEMA at the Liquid-Liquid interface

In this section the results for the study of DMDOHEMA at the dodecane/water interface will be reported. In Figure 4.27 the structure of DMDOHEMA is shown.

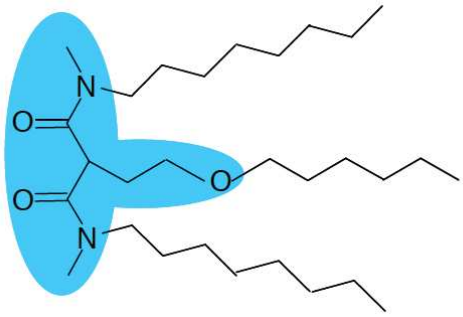

Figure 4.27: Structure of DMDOHEMA. The part in blu represents the polar head of ligand, responsible of the amphiphilic properties.

Previous studies on DMDOHEMA in dodecane in contact with aqueous solution (acid or neutral medium with and without metal salts) report the CAC of DMDOHEMA[1] for concentrations between 0.03 M and 0.1 M [62, 40]. For DMDBTDMA the CAC is approximately ten times higher at 0.25 M. For this reason, in this section, the data shown have been recorded for DMDOHEMA concentrations between 0.002 M and 0.1 M.

As explained in the previous sections, for the data analysis with the RMCS code the scattering lengths of species composing the samples have to be provided to the code. These are reported in Table 4.7 for the samples with DMDOHEMA.

[1]The CAC values at which we refer here depend on the aqueous phase composition. We provide the concentration range observed in literature and in each section we will be more specific depending on the sample presented.

Compound	**X-rays** [10^{-6} Å]		**Neutrons** [10^{-6} Å]	
	Real Part	Imaginary Part	Real Part	Imaginary Part
$C_{12}H_{26}$	2768.200	3.253	-	-
$C_{12}H_{26}/C_{12}D_{26}$	-	-	1512.2	0.019
$C_{12}D_{26}$	-	-	2533.100	0.003
DMDOHEMA	7610.407	1.175	119.664	0.064
H_2O	281.972	0.102	-	-
D_2O	-	-	191.530	0.000
DNO_3	-	-	334.490	0.005
HNO_3	902.371	0.360	-	-
Li	84.534	0.001	-19.000	0.196
Nd	1680.600	58.744	76.900	1.400
NO_3	874.190	0.360	267.750	0.005
DMDBTDMA	6933.800	1.020	78.282	0.061

Table 4.7: x-ray and neutron scattering lengths used for the RMCS analysis of the samples with DMDOHEMA. For x-rays the values have been calculated at 22 keV and at $\lambda = 1.8$ Å for neutrons[92, 96]. In the last line of the table we report x-ray and neutron scattering lengths for DMDBTDMA to easily compare with DMDOHEMA.

4.3.1 Pure Water

To understand the behaviour of DMDOHEMA a first study at the liquid/liquid interface between pure water and pure dodecane as been conducted. For this experiment it has been possible to record data with three different contrasts: the first one by x-ray reflectivity, the other two by neutron reflectivity either with fully deuterated dodecane or with a $C_{12}H_{26}/C_{12}D_{26}$ mixture to obtain an SLD=$4.0 \cdot 10^{-6}$ Å^{-2}. All the three contrasts have been used for the fitting process with a box model in Motofit [93] and for the RMCS code. The list of samples is summarized in Table 4.8.

X-ray data and fits shown in Figure 4.28a show that for higher concentrations of DMDOHEMA in dodecane, the slope of the curve increases, similarly to previous case. Data have been plotted as $\log(RQ^4)$ to enhance the difference between the samples.

The SLD profiles obtained via best fitting process in Motofit [93] (Figure 4.28b) highlight an increase of the SLD intensity at the interface with the diamide concentration in oil. Furthermore the region of interest in the oil phase becomes larger

Concentration [mol/l]	**X-rays**	**Neutrons** (37.7/62.3)	**Neutrons** (0/100)
0.002 M	**X**	**X**	**X**
0.007 M	**X**	**X**	**X**
0.01 M	**X**	**X**	X
0.02 M	X	-	-
0.04 M	**X**	**X**	**X**

Table 4.8: List of samples for DMDOHEMA in dodecane contacted with water. The X means the sample has been measured, the - it has not, and the bold **X** means that data have been analyzed with the RMCS to investigate the liquid/liquid interfacial structure. (37.7/62.3) and (0/100) is the volume ratio between $C_{12}H_{26}/C_{12}D_{26}$ used to vary the contrast. The (37.7/62.3) column represents the samples measured with D_2O and a mixture of hydrogenated/protonated dodecane to obtain an SLD=$4.0 \cdot 10^{-6}$ Å^{-2}. The (0/100) column represents the samples measured with D_2O and $C_{12}D_{26}$. The sample at 0.01 M of DMDOHEMA in fully deuterated dodecane has not been analyzed with the RMCS code. During the data analysis process we have concluded that the measurement has not been performed at the equilibrium.

and the SLD profiles on the oil side become larger and with higher SLD values, consistently with a larger region of adsorption of extractant.
It is important to notice that the value of the SLD profile around $z = 0$ Å is consistent with the scattering length density of the polar head of the DMDOHEMA[1]. Unfotunately the RMCS code it is not capable, at this stage, to separate the head from the tails because a constraint between the number of the two components in different slices would be necessary but difficult to adjust. In the future this is one improvement that has to be done.
Despite this, it is possible to deduce from the first analysis a preferential orientation of the extractant molecules at the interface, with the polar head oriented to the water and the tails sorrounded by dodecane. Unfortunately no more details can be provided with the data collected in this work.

In Figures 4.29 and 4.30 neutron reflectivity data with two different dodecane contrasts are reported. In panel (b) of these figures we observe, as for the x-ray data, a clear adsorption of DMDOHEMA (which has a low SLD compared to dodecane or water) at the interface.

[1]The polar head of DMDOHEMA has an SLD=$9.80 \cdot 10^{-6}$ Å^{-2}.

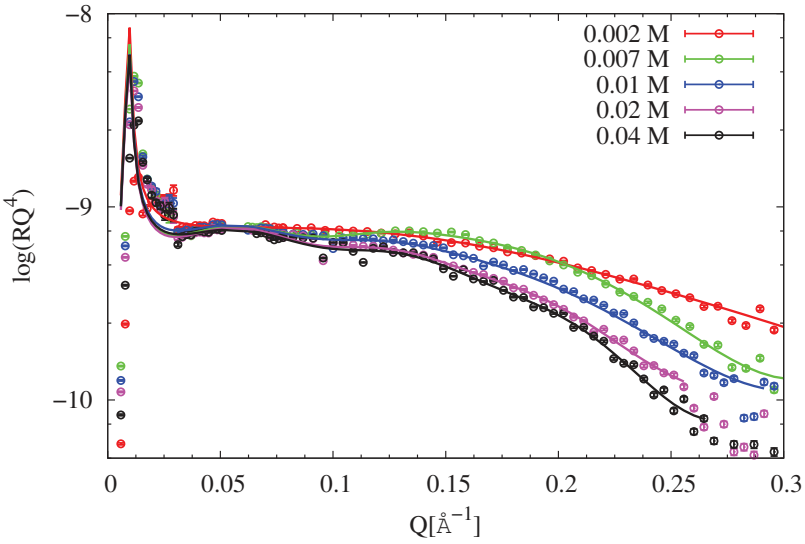

(a) X-ray Data and Fits

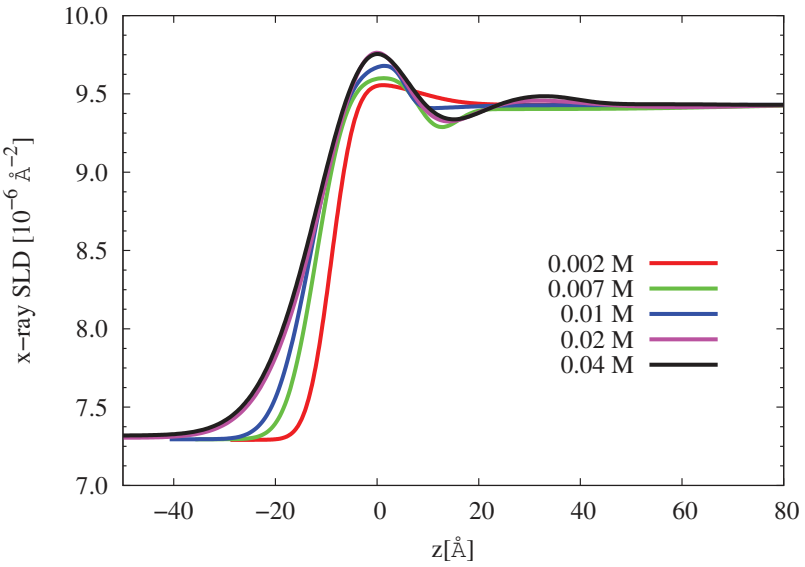

(b) SLD Profiles

Figure 4.28: (a) X-ray reflectivity data and best fits of samples with DMDOHEMA in dodecane contacted with pure water. Data are plotted with circles and error bars, fits with lines. (b) SLD profiles obtained with best fitting process with Motofit [93] for data in panel (a). The liquid/liquid interface is placed at $z = 0$ Å (left side, organic phase; right side aqueous phase).

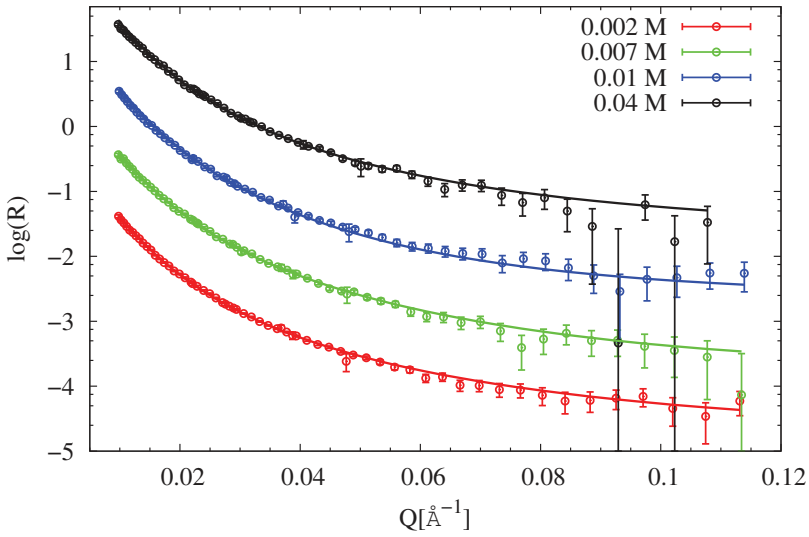

(a) Neutron Data and Fits

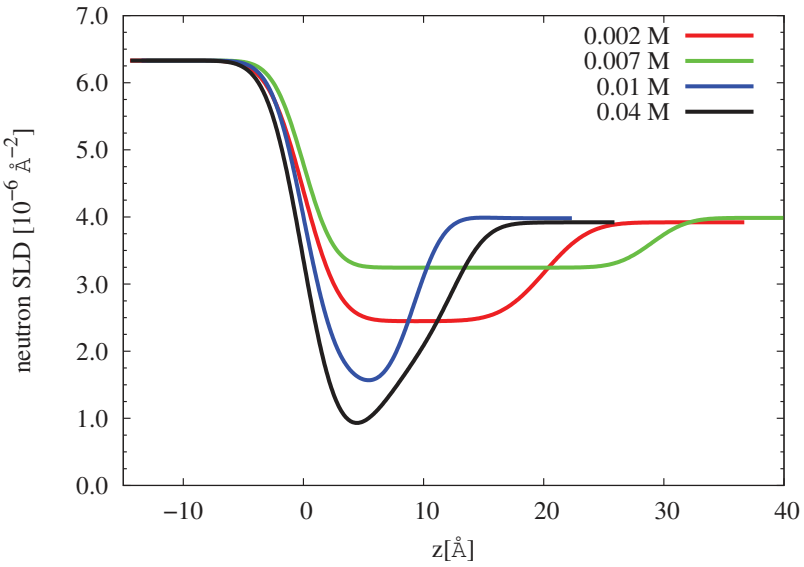

(b) SLD Profiles

Figure 4.29: (a) Neutron reflectivity data and best fits of samples with DMDOHEMA in dodecane contacted with pure water. Data have been shifted for clarity. The water is fully deuterated and the dodecane is a mixture of $C_{12}H_{26}$ and $C_{12}D_{26}$ with a volume ratio of 37/63 and an SLD=$4.0 \cdot 10^{-6}$ Å^{-2}. Data are plotted with circles and error bars, fits with lines. (b) SLD profiles obtained with best fitting process with Motofit[93] for the data in panel (a). The liquid/liquid interface is placed at $z = 0$ Å (left side, water phase; right side organic phase).

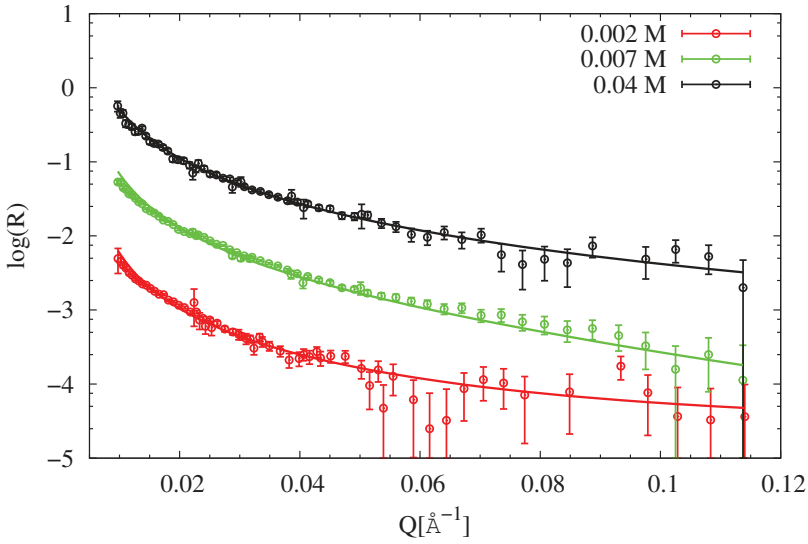

(a) Neutron Data and Fits

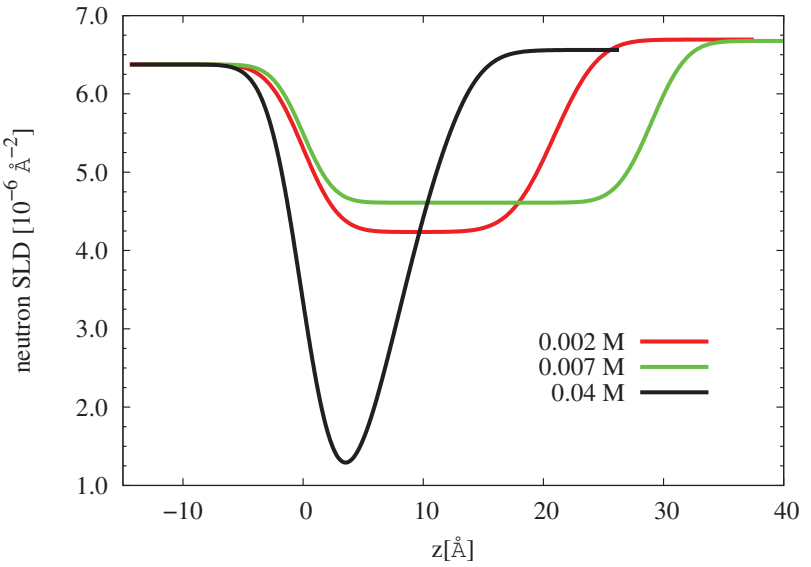

(b) SLD Profiles

Figure 4.30: (a) Neutron reflectivity data and best fits of samples with DMDOHEMA in dodecane contacted with pure water. Data have been shifted for clarity. Both water and dodecane are fully deuterated. Data are plotted with circles and error bars, fits with lines. (b) SLD profiles obtained with best fitting process with Motofit [93] for the data in panel (a). The liquid/liquid interface is placed at $z = 0$ Å (left side, water phase; right side organic phase).

A more detailed analysis has been performed with the RMCS code. Data and fits are shown in Figures 4.31 and 4.32.

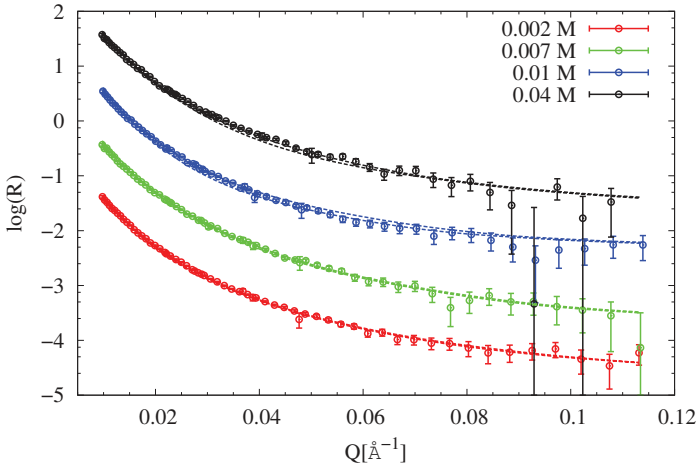

(a) Neutron Data and Fits (Dodecane SLD=$4.0 \cdot 10^{-6}$ Å^{-2})

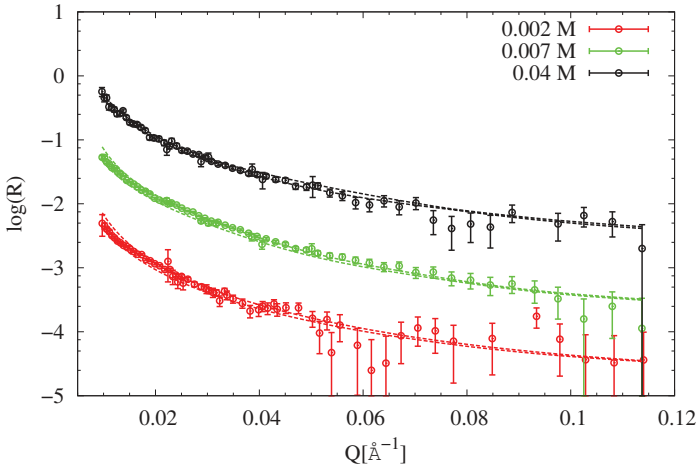

(b) Neutron Data and Fits (Dodecane SLD=$6.7 \cdot 10^{-6}$ Å^{-2})

Figure 4.31: Neutron data and fits for DMDOHEMA at water/dodecane interface. Samples with (b) fully deuterated dodecane and (c) a mixture of $C_{12}H_{26}/C_{12}D_{26}$ at 37.7/62.3. With circles we report the recorded data with experimental errors, with dashed lines the confidence region for the fit function. Data have been shifted for clarity.

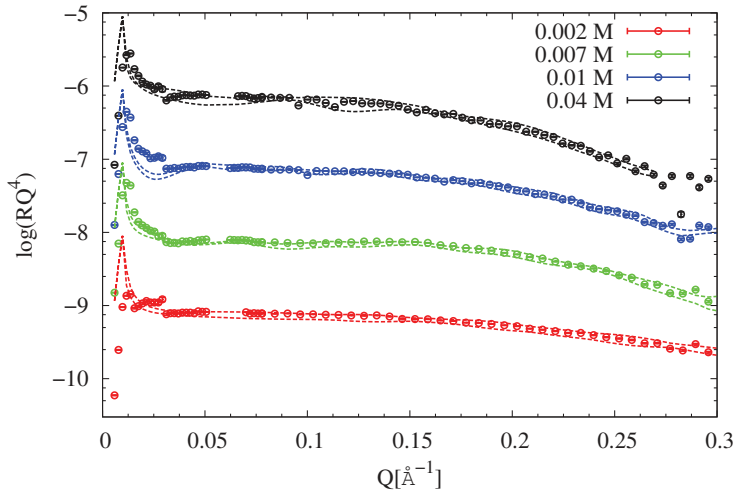

Figure 4.32: X-ray data and fits for DMDOHEMA at water/dodecane interface. With circles we report the recorded data with experimental errors, with dashed lines the confidence region for the fit function. Data have been shifted for clarity.

The distributions of water, dodecane and diamide resulting from the RMCS code are shown in Figures 4.33, 4.34 and 4.35.

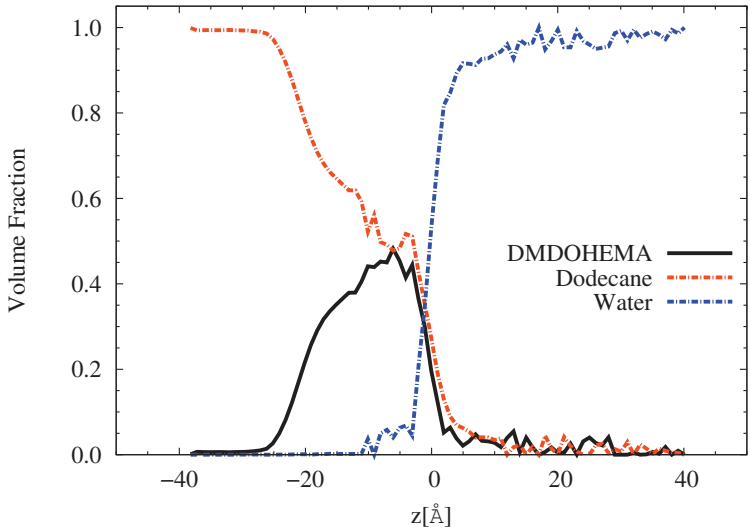

Figure 4.33: Distribution of DMDOHEMA, water and dodecane for the samples at 0.002 M. In the analysis process the initial interface xy-plane is set at $z = 0$ Å.

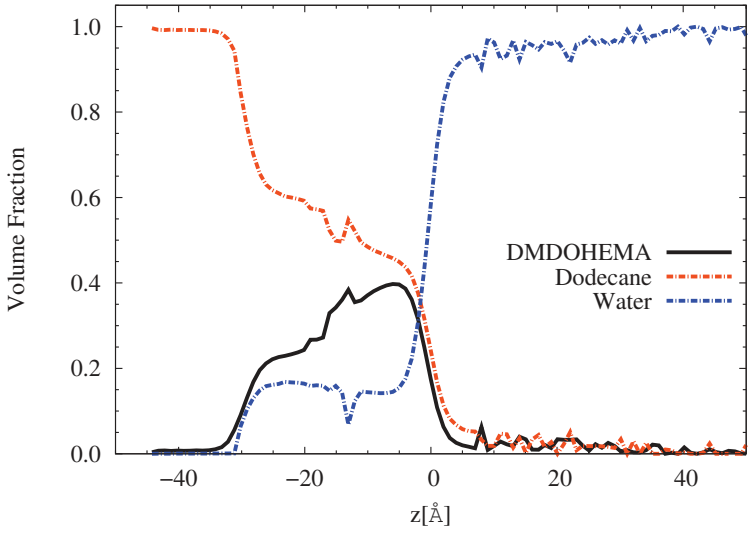

(a) 0.007 M

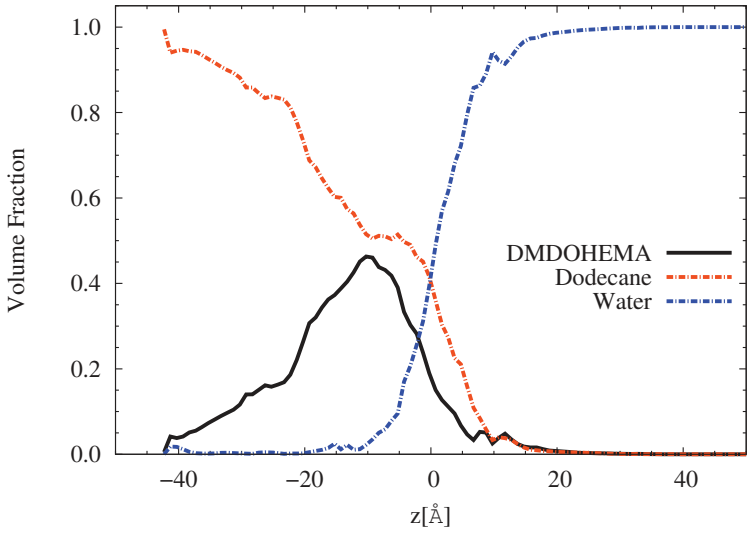

(b) 0.01 M

Figure 4.34: Distribution of DMDOHEMA, water and dodecane for the samples at (a) 0.007 M and (b) 0.01 M. In the analysis process the initial interface xy-plane is set at $z = 0$ Å.

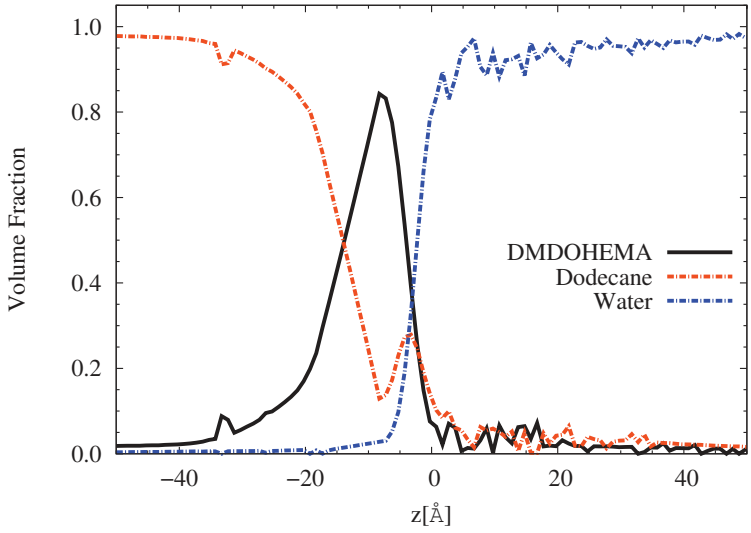

Figure 4.35: Distribution of DMDOHEMA, water and dodecane for the samples at 0.04 M. In the analysis process the initial interface xy-plane is set at $z = 0$ Å.

In the sample at 0.002 M, DMDOHEMA is adsorbed in a region approximately 30 Å thick, with a maximum value of approximately 45% (volume fraction) at $z \approx 5$ Å.

When the extractant concentration increases (0.007 M) we start observing that the diamide spreads over a larger region ($\approx$ 35 Å thick) and the maximum value is lower than the one recorded at 0.002 M. Moreover a not negligible amount of water ($\approx$ 15% of the volume) is observed in the same region. At 0.01 M the diamide distribution appears similar to the one obtained at 0.007 M, with a small increase of the maximum value. We observe also a weak penetration of of water molecules in the z-region in which the diamide is adsorbed. At the highest concentration the adsorption of diamide increases and the distribution becomes more narrow[1] with a maximum volume occupied greater than the 80% of the available volume. In Figure 4.36 the comparison between diamide distributions at various concentrations is plotted to highlight the differences.

[1]The DMDOHEMA starts to increase considerably at $z \approx -20$ Å.

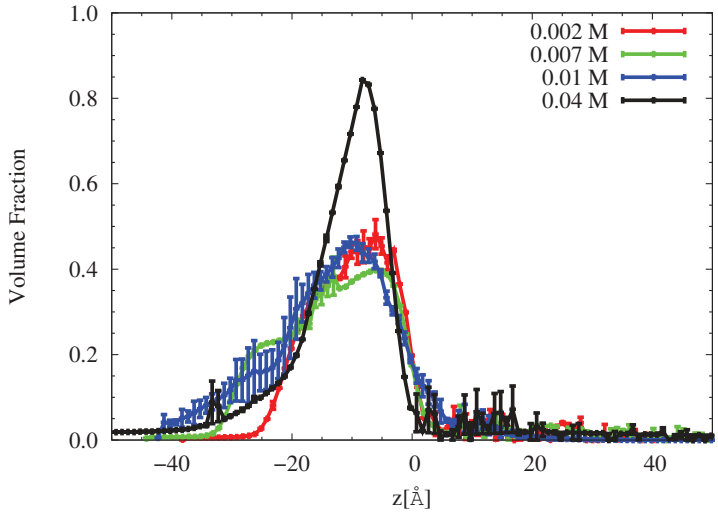

Figure 4.36: Comparison between distributions of DMDOHEMA for all the investigated samples. With the vertical bars we report the error in volume fraction calculated as explaind in Section 2.2.3. In the analysis process the initial interface xy-plane is set at $z = 0$ Å.

A first comparison between the system presented here and the previous with DMDBTDMA, already evidences few differences between the two extractants. While for DMDBTDMA the highest adsorption is observed at the lowest bulk concentration, for DMDOHEMA a behaviour more similar to a classical surfactant is remarked. Moreover, by increasing the ligand bulk concetration, the interpenetration between DMDOHEMA and the aqueous phase is much less pronounced than for DMDBTDMA.

By using the Gibbs adsorption equation (Equation 1.1)

$$A_0 = -RT \left(\frac{\partial \gamma}{\partial ln(C)} \right)^{-1} \tag{4.2}$$

we have calculated the interfacial tension γ at oil/water interface at various extractant bulk concentration C. For each sample we have calculated the z position of the interface as the z-value z_0 for which the volume fraction occupied by organic compounds (oil and extractant) is equal to the water volume fraction. Then, we have calculated the extractant surface excess, $1/A_0$ (see Equation 4.2), at the interface as follows:

$$\frac{1}{A_0} = \int_{-\infty}^{z_0} [\rho(z) - \rho(-\infty)]\, dz + \int_{z_0}^{+\infty} [\rho(z) - \rho(+\infty)]\, dz. \tag{4.3}$$

In Equation 4.3 $\rho(z)$ represents the extractant concentration in mol/L for each z while $\rho(-\infty)$ and $\rho(+\infty)$ represent its concentration in dodecane and water bulk, respectively. By using the Gibbs equation the interfacial tension, in mN/m, is calulated as follows:

$$\gamma = -\frac{RT}{A_0} ln(C) \tag{4.4}$$

The results obtained for the DMDOHEMA at dodecane/water interface are reported in Table 4.9.

Concentration [mol/l]	**Interfacial Tension [mN/m]**	
	Calculated	Experimental
0.002 M	28.30	28
0.007 M	24.63	26
0.01 M	27.12	25
0.04 M	20.64	21

Table 4.9: Interfacial tension for DMDOHEMA at dodecane/water interface. Results reported in 2^{nd} column are obtained by using Equations 4.3 and 4.4. Data in 3^{rd} column are extrapolated from [84].

We observe that the calculated interfacial tension decreases with the extractant concentration in dodecane. These results are in agreement with those obtained, by means of pendant-drop experiments, by Zemb et al. [84]. The same calculation has been performed for the other systems presented in this work, in presence of nitric acid or salts in the aqueous phase. However, the corresponding calculated values do not match the experimental ones. This is certainly related to the fact that the activity of each species within this interfacial region are not taken into account and have to be considered.
In the most simple case of DMDOHEMA at dodecane/water interface the calculation of the surface tension by using a Gibbs model is valid and evidences the surfactant behaviour of the extractant. Moreover, the results show that the density profiles obtained with the RMCS code are in agreement with experimental observations by means of different techniques.

4.3.2 Water and Nitric Acid

The liquid/liquid interface between DMDOHEMA in dodecane in contact with a nitric acid aqueous solution has been studied at different extractant concentrations

in dodecane, as in the previous case. The list of samples investigated by x-ray and neutron reflectivity is reported in Table 4.10.

Concentration [mol/l]	X-rays	Neutrons
0.002 M	**X**	**X**
0.007 M	**X**	**X**
0.01 M	**X**	**X**
0.02 M	X	-
0.04 M	X	X

Table 4.10: List of samples for DMDOHEMA in dodecane contacted with an aqueous phase at 2 M of Nitric Acid. For x-rays experiments HNO_3 in H_2O has been used, replaced by DNO_3 in D_2O for the neutrons case. The X means the sample has been measured, the - it has not, and the bold **X** means that data have been analyzed with the RMCS to investigate the liquid/liquid interfacial structure.

Meridiano et al. [62] have determined by SAXS and SANS measurements that in a system composed by DMDOHEMA in heptane contacted with an aqueous solution of nitric acid (2.93 M), the CAC is at 0.03 M. Replacing heptane with dodecane does not affect the CAC [62]. A sketch with their result is reported in Figure 4.37.

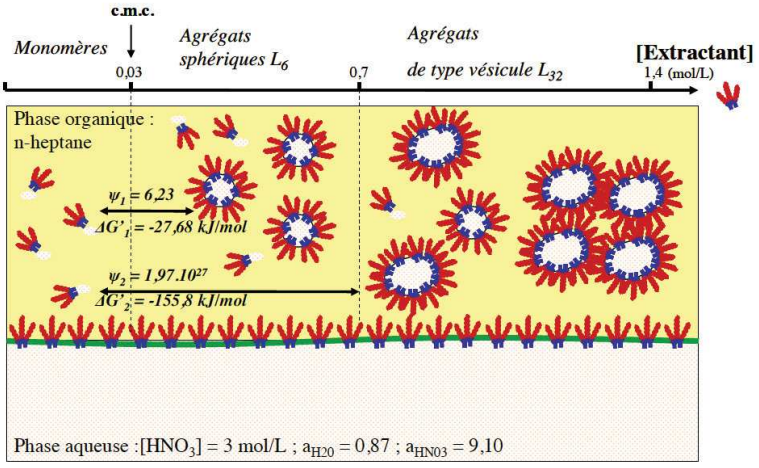

Figure 4.37: Sketch of the aggregation of the DMDOHEMA in heptane contacted with an aqueous phase of nitric acid depending on the extractant concentration. Studied system: DMDOHEMA (0,01 to 1,4 mol/L) in heptane contacted with an aqueous phase of HNO_3 (2.93 mol/L) at 24 °C [62].

In Figure 4.38 the recorded x-ray curves with best fits and SLD profiles obtained with Motofit are plotted. We observe that the reflected intensity *vs* Q decreases faster as the diamide concentration increases. The higher SLD at the interface resulting in the profiles in panel (b) can be correlated with an adsorption of extractant and nitric acid at the interface. This effect increases with ligand bulk concentration.
The same result is pointed out by the neutron data in Figure 4.39. In panel (b), indeed, we observe that compounds with a lower SLD (compared to solvents) adsorb more and more when malonamide is added in bulk.
The analysis of the three samples measured by x-rays and neutrons has been performed with the RMCS code. Reflectivity data and fits are shown in Figure 4.40 and results for the water, dodecane and extractant distributions are plotted in Figure 4.41.

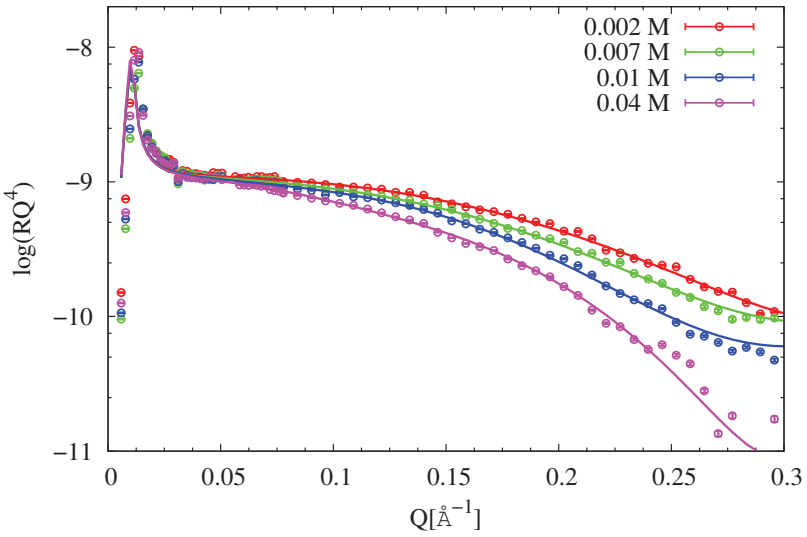

(a) X-ray Data and Fits

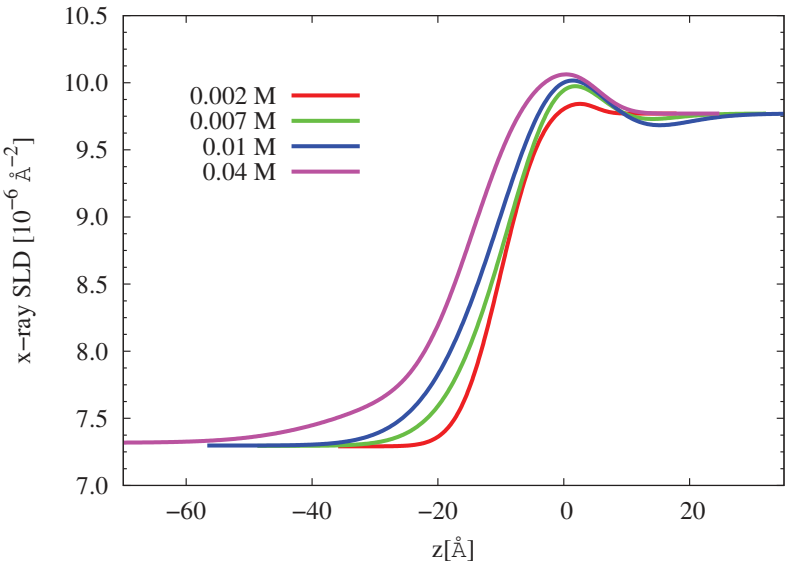

(b) SLD Profiles

Figure 4.38: Samples with DMDOHEMA in dodecane contacted with an aqueous solution of nitric acid (2M).(a) X-ray data and fits. Data are plotted with circles and experimental errors, fits with lines. (b) SLD profiles obtained with the best fitting process with Motofit [93]. The liquid/liquid interface is placed at $z = 0$ Å (left side, organic phase; right side aqueous phase).

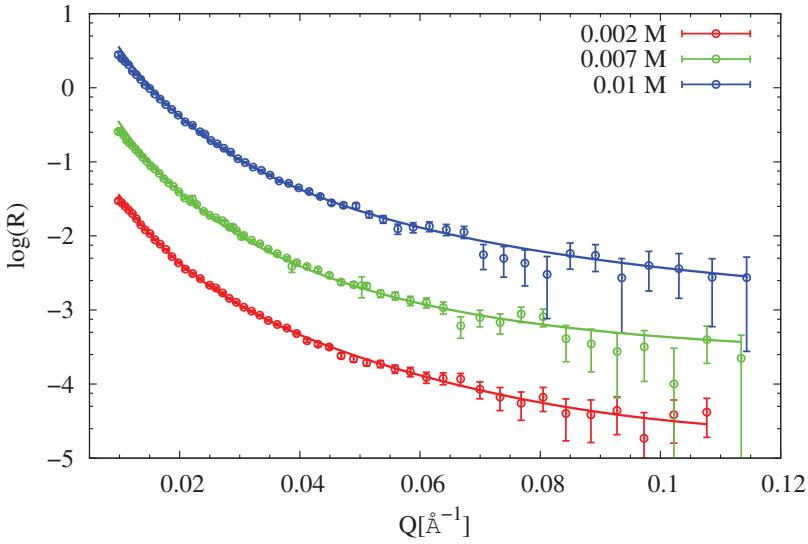

(a) Neutron Data and Fits

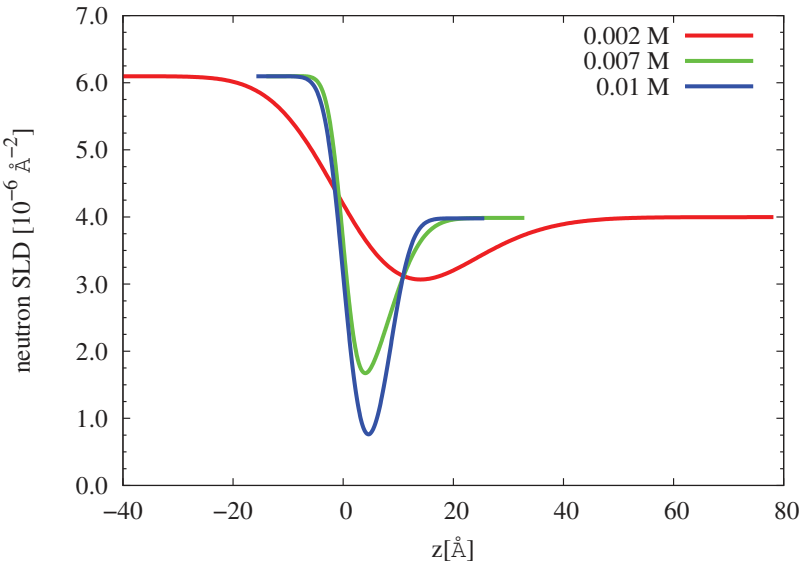

(b) SLD Profiles

Figure 4.39: Samples with DMDOHEMA in dodecane contacted with an aqueous solution of nitric acid (2M).(a) Neutron data and fits. Data are plotted with circles and experimental errors, fits with lines. Data have been shifted for claarity. (b) SLD profiles obtained with the best fitting process with Motofit[93]. The liquid/liquid interface is placed at $z = 0$ Å (left side, aqueous phase; right side, organic phase.

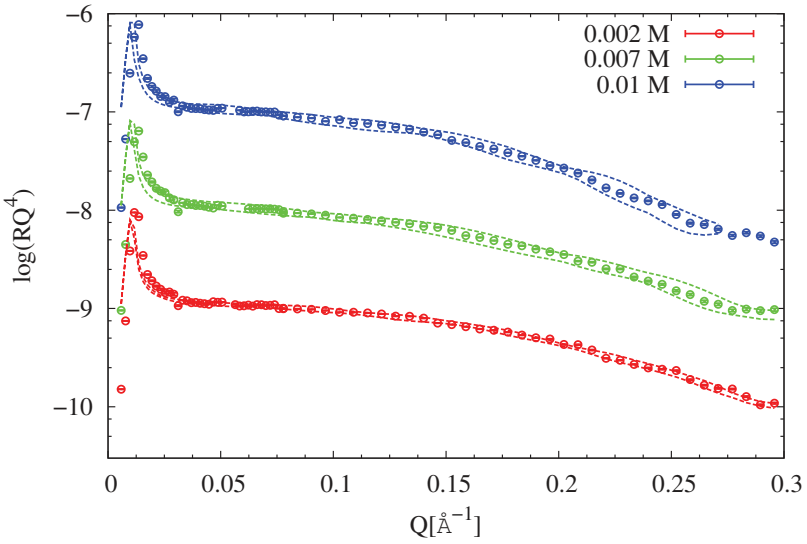

(a) X-ray Data and Fits

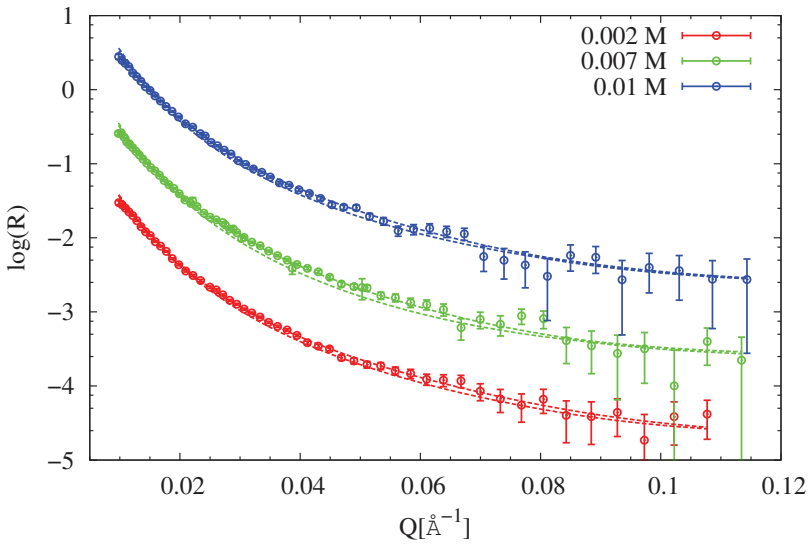

(b) Neutron Data and Fits

Figure 4.40: (a) X-ray and (b) neutron reflectivity data and fits obtained with RMCS code. With circles we report the recorded data with experimental errors, with dashed lines the confidence region for the fitting function. Data have been shifted for clarity.

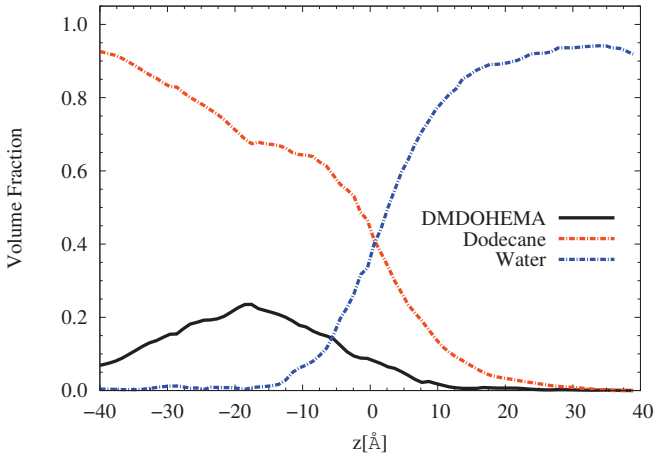

(a) 0.002 M

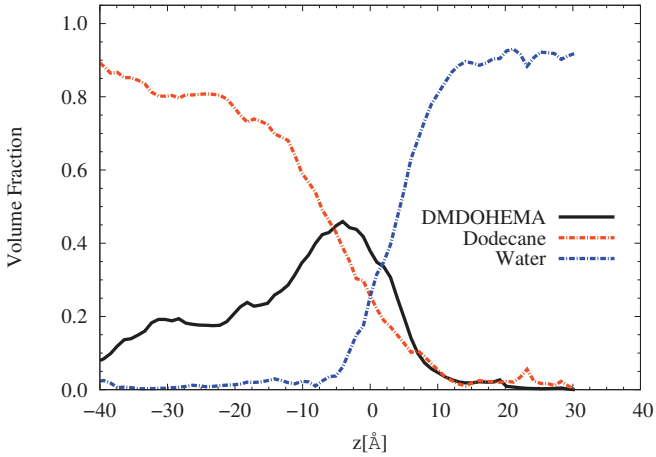

(b) 0.007 M

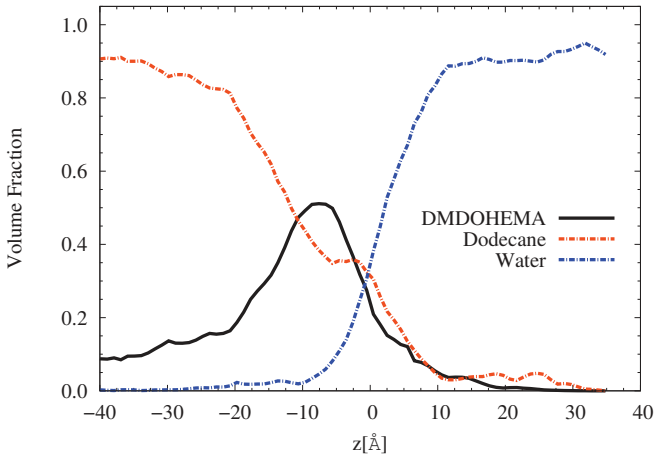

(c) 0.01 M

Figure 4.41: Distribution of DMDOHEMA, water and dodecane. Results for samples at (a) 0.002 M and (b) 0.007 M and (c) 0.01 M. In the analysis process the initial interface xy-plane is set at $z = 0$ Å.

By increasing the concentration of extractant in dodecane we observe that the DMDOHEMA adsorbs more and more at the interface, replacing the oil. At 0.002 M (Figure 4.41a), the interfacial region is formed by water and dodecane, while the malonamide is solvated in oil. At 0.007 M and 0.01 M, the diamide at the interface fills a larger volume compared to the oil.

By comparing the malonamide distribution in different samples, Figure 4.42a, we observe that the amount of diamide adsorbed at the interface increases with the bulk concentration and the distribution center of gravity shifts towards the aqueous phase.
In panel (b) of the same figure, the distributions of nitric acid are plotted. While the diamide adsorbs, the nitric acid desorbs. At the lowest concentration, the maximum of the nitric acid distribution (≈ 3.5 mol/L) is observed at $z \approx -5$ Å. For samples at 0.007 M and 0.01 M the distributions of nitric acid are less broad and shifted towards the aqueous phase[1]. At the highest concentration, the maximum in the distribution (≈ 2.75 mol/L) is found at $z \approx 5$ Å. These observations are opposites to what observed for the DMDBTDMA (see Figure 4.14a).

A comparison between nitric acid and diamide distributions is helpful to have a clear picture of the interface. In Figure 4.42 are plotted both distributions for the three bulk diamide concentrations.
For all samples an interpenetration between diamide and nitric acid is observed (Figure 4.43) but the increasing amount of diamide at the interface produces a desorption of nitric acid. In fact, at the maximum of extractant distribution the molar ratio between nitric acid and diamide varies between 4 and 1.5 with the malonamide bulk concentration. We will come back on this variation at the end of the chapter
Lastly, for the sample at 0.04 M, not analyzed with the RMCS code, we can deduce from the SLD profiles in Figure 4.38b higher adsorption of diamide at the interface and a decrease of the maximum in the nitric acid distribution.

By comparing the results of DMDOHEMA and DMDBTDMA in contact with a nictric acid aqueous solution, differences are observed.
When approaching to the CAC, the DMDOHEMA adsorbs at the interface as expected for a classical surfactant making a barrier to the nitric acid which is pushed out towards bulk water as shown in Figure 4.42. On the contrary DMDBTDMA desorbs and a more diffuse layer, with an increasing amount of nitric acid, is observed (see Figure 4.14).

[1] As previously specified, we consider the aqueous phase the slices for all the $z \geq 0$ Å.

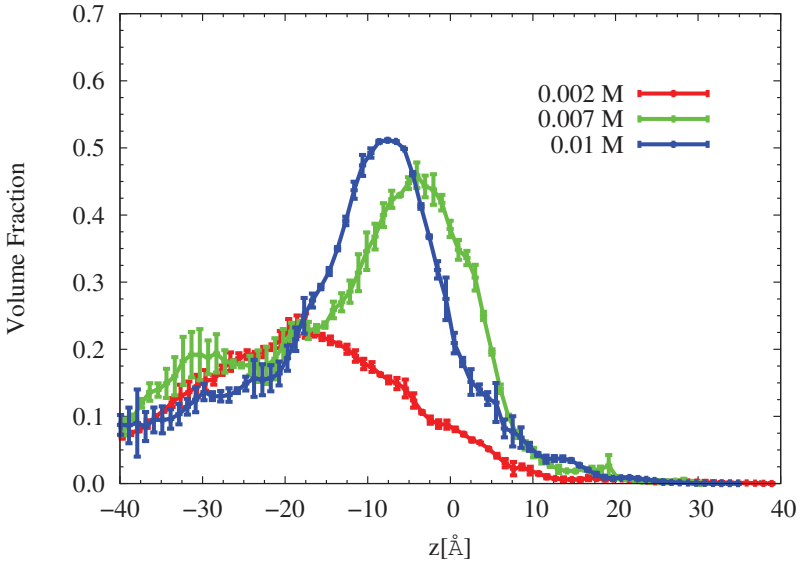

(a) DMDOHEMA

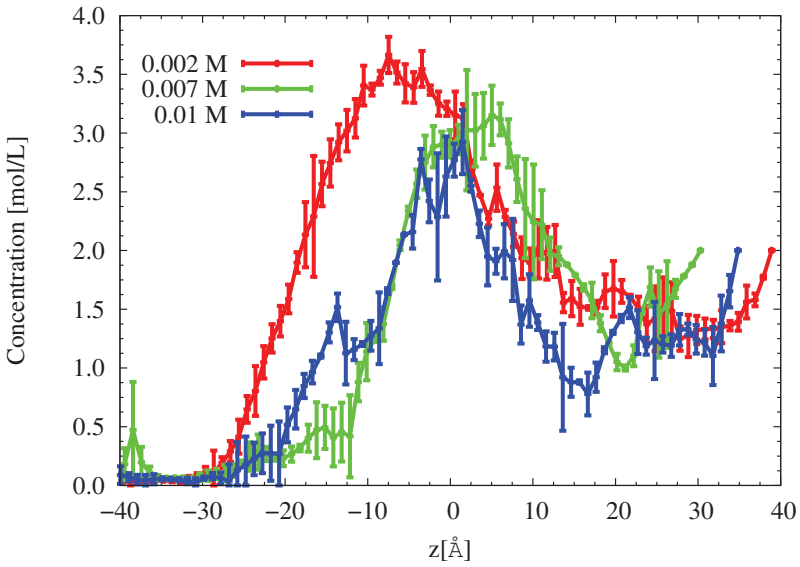

(b) Nitric Acid

Figure 4.42: Comparison between distributions of (a) DMDOHEMA and (b) nitric acid for all the investigated samples. With the vertical bars we report the error in volume fraction calculated as explained in section 2.2.3. In the analysis process the initial interface xy-plane is set at $z = 0$ Å.

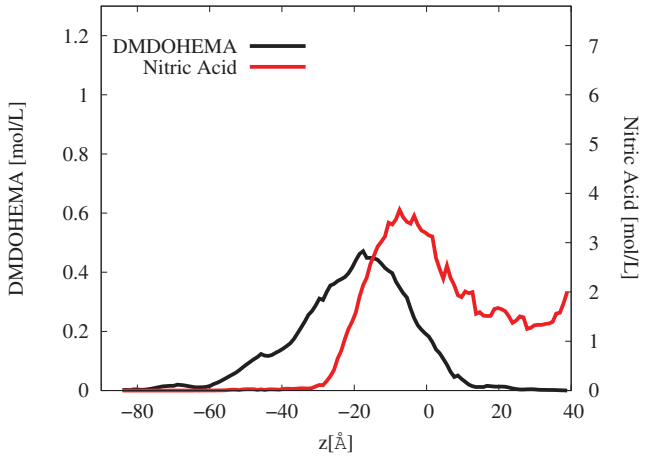

(a) 0.002 M

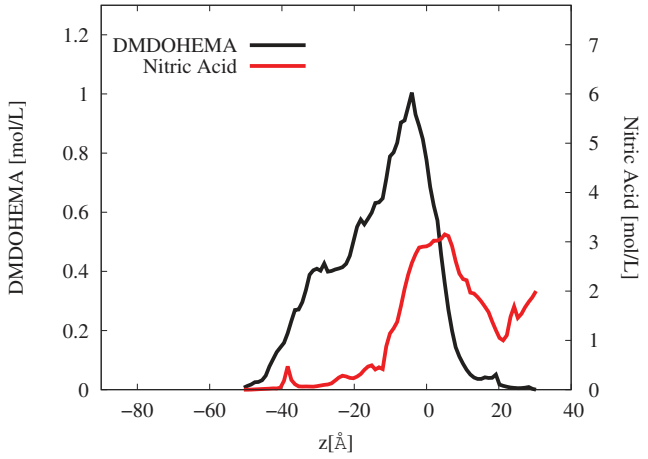

(b) 0.007 M

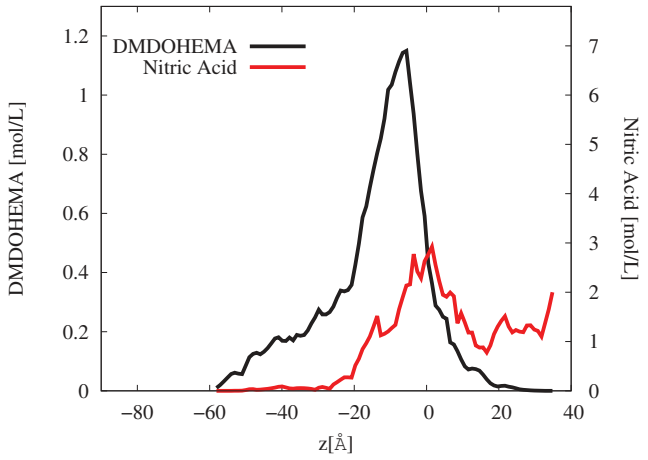

(c) 0.01 M

Figure 4.43: Comparison between distributions of DMDOHEMA and nitric acid, for all the investigated samples. The vertical axis on the left represents the concentration of DMDOHEMA (mol/L) and the right one the concentration of nitric acid (mol/L) allowing the comparison between the two. The z-axes are similar to those of Figure 4.15 to facilitate the comparison.

4.3.3 Water and Neodymium Nitrate

In this work we have studied DMDOHEMA in dodecane in contact with an aqueous solution of $LiNO_3$ (2 M) and $Nd(NO_3)_3$ (0.25 M). For the neutron experiment we have used D_2O for the water phase and a mixture of hydrogenated/deuterated dodecane with a ratio 37.7/62.3[1].
For DMDOHEMA in heptane contacted with an aqueous solution of lithium nitrate (2.93 mol/L), Meridiano [62] shows in his thesis work that the CAC is obtained for an extractant concentration equal to 0.1 mol/L. Furthermore, he shows that the CAC is reduced depending on two contributions: the concentration of metallic salts (europium nitrate in his work) and the organic solvent used. In particular, the longer the alkane chain is, the more efficient the extraction. For these reasons we expect the CAC in between 0.03 M and 0.1 M. Table 4.11 shows the list of samples investigated in this work.

Concentration [mol/l]	X-ray	Neutron
0.002 M	**X**	**X**
0.007 M	**X**	**X**
0.01 M	**X**	**X**
0.02 M	**X**	**X**
0.04 M	**X**	**X**
0.07 M	**X**	**X**
0.1 M	X	-

Table 4.11: List of samples for DMDOHEMA in dodecane contacted with an aqueous phase at 2 M of $LiNO_3$ and 0.25 M of $Nd(NO_3)_3$. The X means the sample has been measured, the - it has not, and the bold **X** means that data have been analyzed with the RMCS to investigate the liquid/liquid interfacial structure.

.

The recorded x-ray data and best fits are reported in Figure 4.44a and in panel (b) the corresponding SLD profiles obtained with Motofit. The first difference to highlight, in comparison with DMDBTDMA, is that for these samples at low Q no modulation of signal or bump appearance is recorded. We can already suppose that the interfacial structure will be different, especially at high concentration.

[1]This mixture has been use to obtain an organic phase with an SLD=4.0 10^{-6} $Å^{-1}$ and the ratio 37.7/62.3 is in volume percentage.

The reflected intensity decreases at high Q with the diamide concentration can be explained as an increase of roughness[1]. Nevertheless the SLD profiles obtained with Motofit [93] show for all samples a layer at the interface with higher SLD compared to the one of the bulk water or to the diamide SLD[2].

In Figure 4.45b the neutron SLD profiles (obtained by fitting the data in panel (a) of the same figure) evidence an adsorption of extractant increasing with the malonamide bulk concentration. From the first results with x-ray and neutron experiments we expect larger variation for DMDOHEMA distribution than for the ions.
The analysis has been performed on x-ray and neutron data with the RMCS code. Data and fits obtained are shown in Figure 4.46. The oil, water and extractant distributions obtained with the RMCS code are plotted in Figures 4.47 and 4.48. At low diamide concentrations (≤ 0.01 M) the amount of DMDOHEMA adsorbed at the interface decreases. At the lowest concentration, the diamide fills at most 40% of the volume, and it decreases progressively to 35% and 30% for samples at 0.007 M and 0.001 M. respectively.
For higher concentration (0.01 M) the malonamide adsorbs as expected for a classical surfactant. The center of gravity of diamide distribution shifts slightly towards the aqueous phase (≈ 5 Å). The comparison between DMDOHEMA distributions is plotted in Figure 4.49.
Finally, at the liquid/liquid interface the most of the volume is filled with dodecane and water, while the diamide is well solvated by the alkane. This has been already observed only for the lowest concentration of DMDOHEMA in contact with nitric acid in Figure 4.41a but never with DMDBTDMA.

[1]This effect has been already discussed for previous samples.

[2]The SLD of the bulk water with salts is $10.59 \cdot 10^{-6}$ Å^{-2} and $8.64 \cdot 10^{-6}$ Å^{-2} for the DMOHEMA.

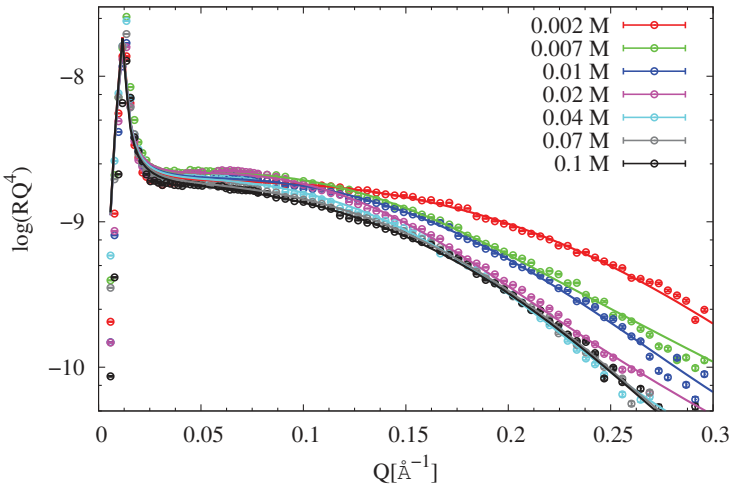

(a) X-ray Data and Fits

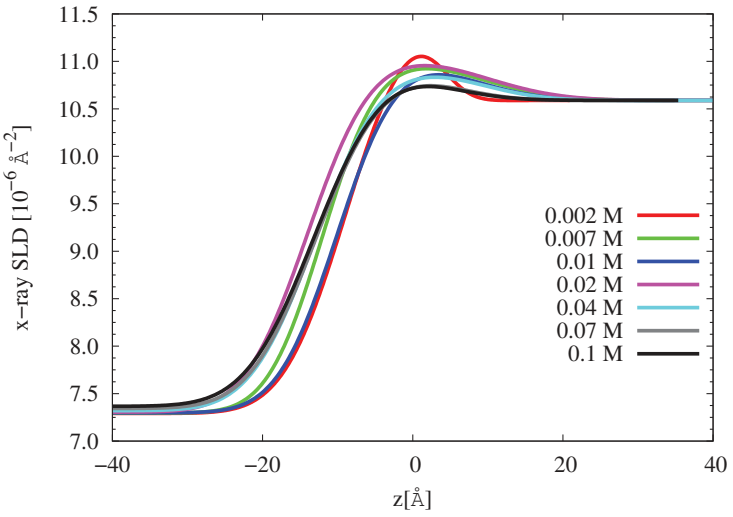

(b) SLD Profiles

Figure 4.44: (a) X-ray data and best fits for DMDOHEMA in dodecane contacted with an aqueous solution of $LiNO_3$ (2M) and $Nd(NO_3)_3$ (0.25 M). (b) SLD Profiles obtained with Motofit[93] with the best fitting process. On the left is represented the SLD of the organic phase, on the right the SLD of water with salts and the liquid/liquid interface xy-plane is placed at $z = 0$ Å.

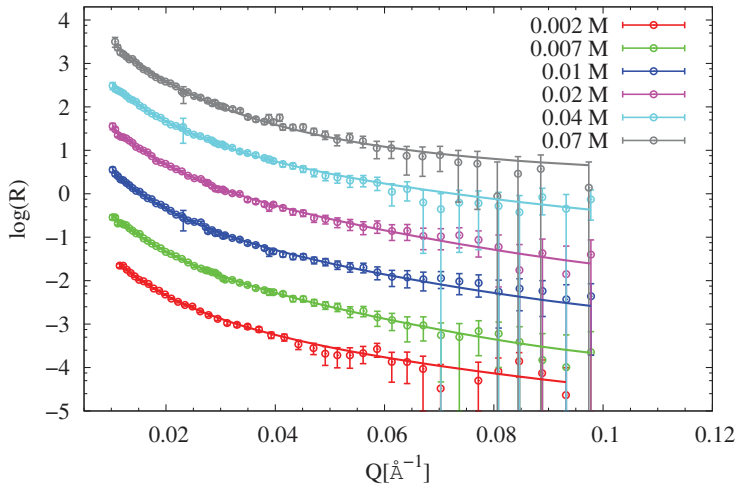

(a) Neutron Data and Fits

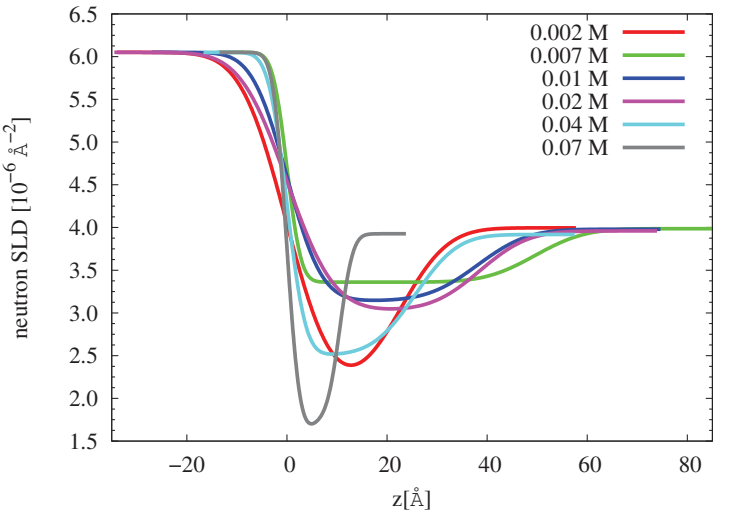

(b) SLD Profiles

Figure 4.45: (a) X-ray data and best fits for DMDOHEMA in dodecane contacted with an aqueous solution of $LiNO_3$ (2M) and $Nd(NO_3)_3$ (0.25 M). Data have been shifted for clarity. (b)Corresponding SLD Profiles obtained with Motofit[93] with the best fitting process. The liquid/liquid interface is placed at $z = 0$ Å (left side, aqueoues phase; right side, organic phase).

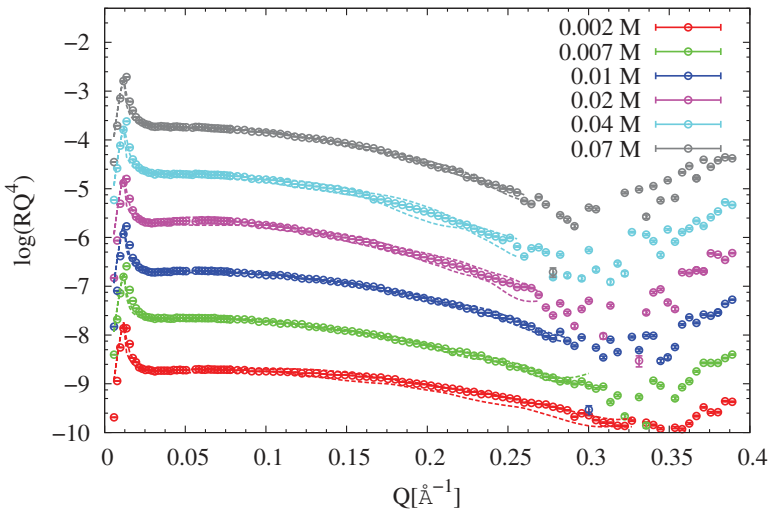

(a) X-ray Data and Fits

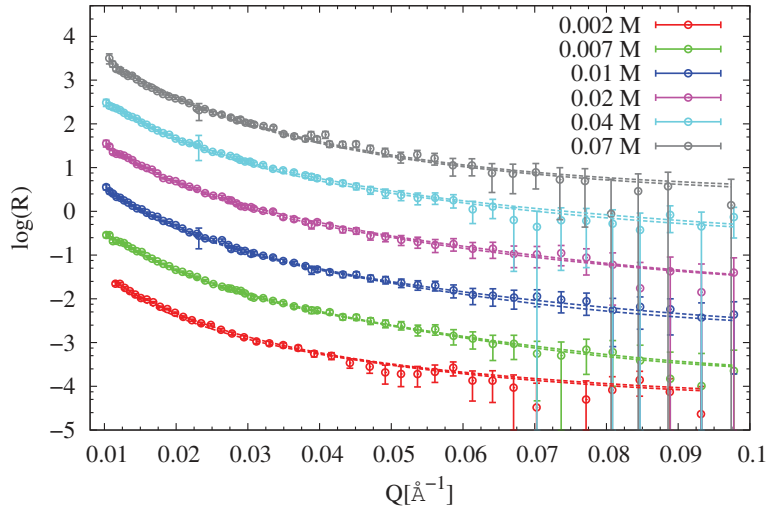

(b) Neutron Data and Fits

Figure 4.46: (a) X-ray and (b) neutron reflectivity data for DMDOHEMA in dodecane contacted with an aqueous solution of $LiNO_3$ (2M) and $Nd(NO_3)_3$ (0.25 M). With circles we report the recorded data with experimental errors, with dashed lines the confidence region for the fitting function obtained with the RMCS code. Data have been shifted for clarity.

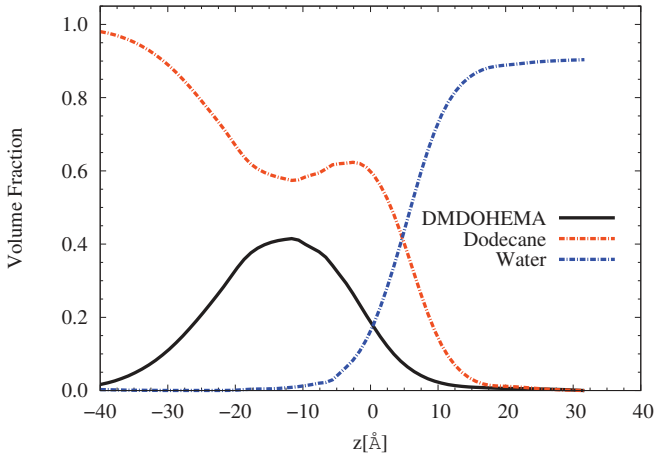

(a) 0.002 M

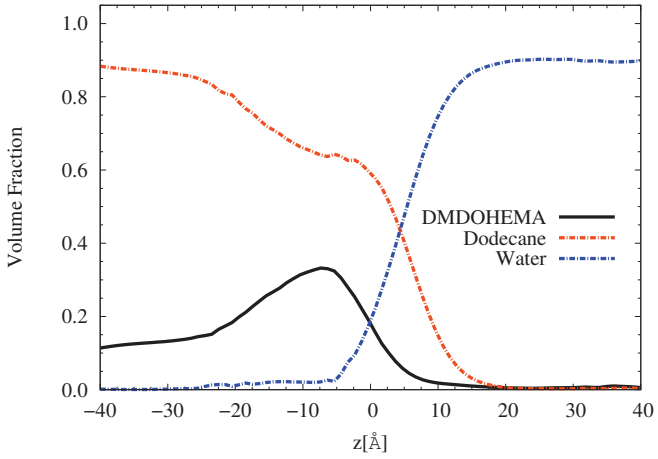

(b) 0.007 M

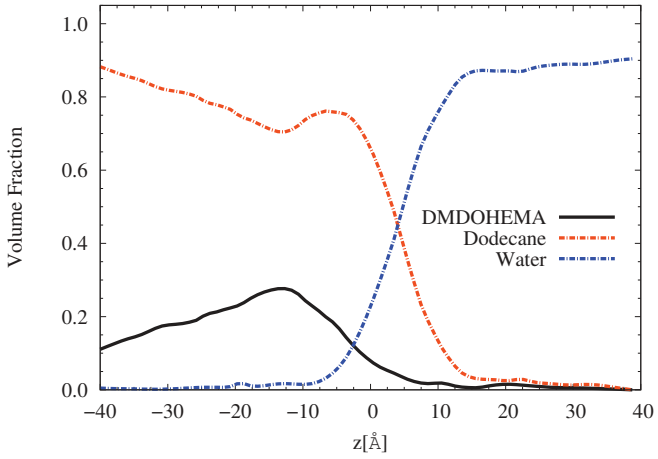

(c) 0.01 M

Figure 4.47: Distribution of DMDOHEMA, water and dodecane at (a) 0.002 M, (b) 0.007 M and (c) 0.01 M extractant concentration. In the analysis process the initial interface xy-plane is set at $z = 0$ Å.

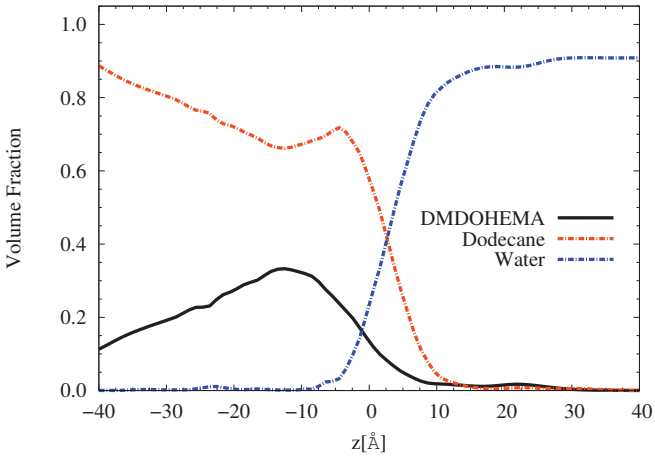

(a) 0.02 M

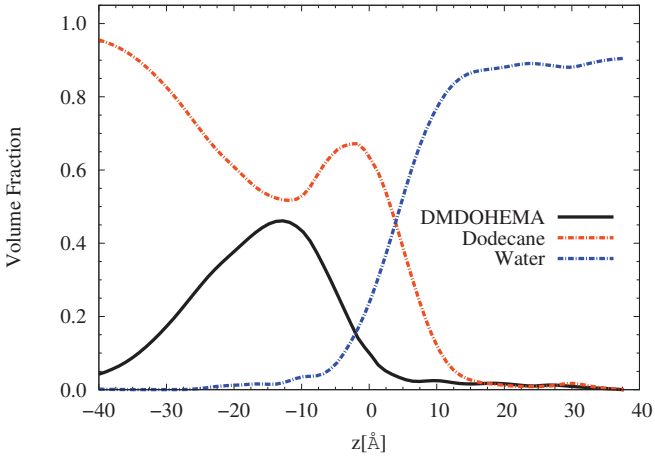

(b) 0.04 M

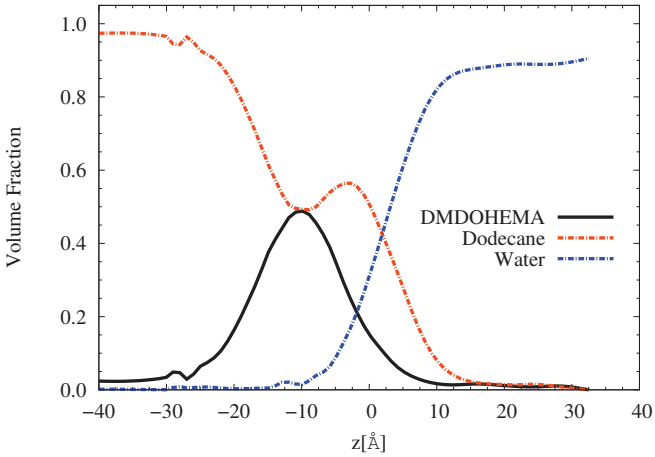

(c) 0.07 M

Figure 4.48: Distribution of DMDOHEMA, water and dodecane at (a) 0.02 M, (b) 0.04 M and (c) 0.07 M extractant concentration. In the analysis process the initial interface xy-plane is set at $z = 0$ Å.

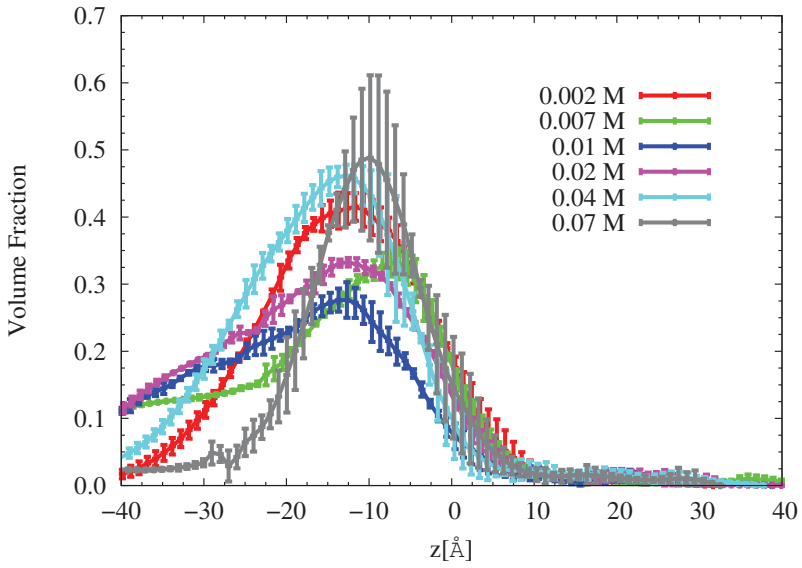

Figure 4.49: Comparison between distributions of DMDOHEMA for all the investigated samples. With the vertical bars we report the error in volume fraction calculated as explained in Section 2.2.3. In the analysis process the initial interface xy-plane is set at $z = 0$ Å.

These results would suggest[1] that DMDOHEMA at the interface exhibits a preferential orientation, with the polar head oriented to the oil phase and the tails facing the water. This type of structure has been already observed, even if for a different type of extractant, by Schlossman et al.[15, 16].

The distribution of ions in Figures 4.50 and 4.51 shows differences between species. For all of them a constant distribution (before approaching to the organic phase) is observed except for the samples at 0.002 M and 0.02 M.
At 0.02 M all three ions are adsorbed at the interface while, at the lowest malonamide bulk concentration only neodymium and nitrate adsorb while lithium distribution remains constant. In the latter case the adsorption of nitrate appears weaker if compared with neodymium[2].

The average charge density for all samples presented here has been calculated with Equation 4.1 and a value of $Q_{tot} \approx (6.0 \pm 7.0) \cdot 10^{-4}\ e/\text{Å}^3$ has been found.

[1]We can not provide experimental measurements as confirmation of what we claim here because such type of information can not be extrapolated from the data we have. Our statement is a suggested interpretation for the DMDOHEMA distributions resulting from the data analysis.

[2]It is important to notice that the oscillations in neodymium distributions looks bigger compared to lithium and nitrate because of the different scale.

This value is consistent, within errors, with an interface with no charge, and no minimization of charge has been used as constraint during the analysis process. For these reasons we can say that the weak adsorption of nitrate in the sample at 0.002 M compensates the excess of charge caused by the adsorption of neodymium, ensuring a conservation of charge.

As we expect, the CAC for concentrations in between 0.03 M and 0.1 M, it is interesting to notice that just before, at 0.02 M, the strongest adsorption is recorded for the lanthanide species and not for lithium.

The most interesting feature is the comparison between extractant and neodymium distributions, shown in Figures 4.52 and 4.53. Compared to the same system with DMDBTDMA, the DMDOHEMA and neodymium distributions exhibit a weak interpenetration. In fact, at the maximum of extractant distribution, the molar ratio between neodymium and diamide remains constantly below 0.01. We will discuss this at the end of the chapter.

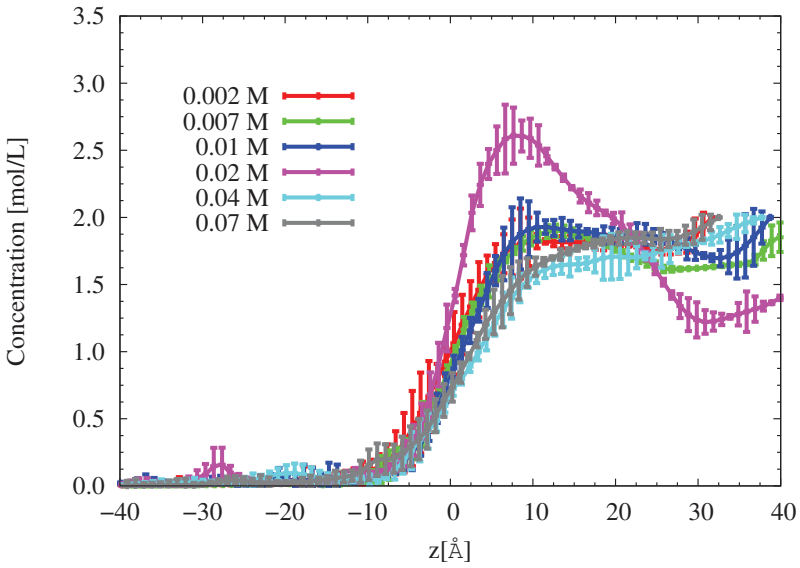

Figure 4.50: Comparison between distributions of lithium for all the investigated samples. With the vertical bars we report the error in volume fraction calculated as explained in section 2.2.3. In the analysis process the initial interface xy-plane is set at $z = 0$ Å.

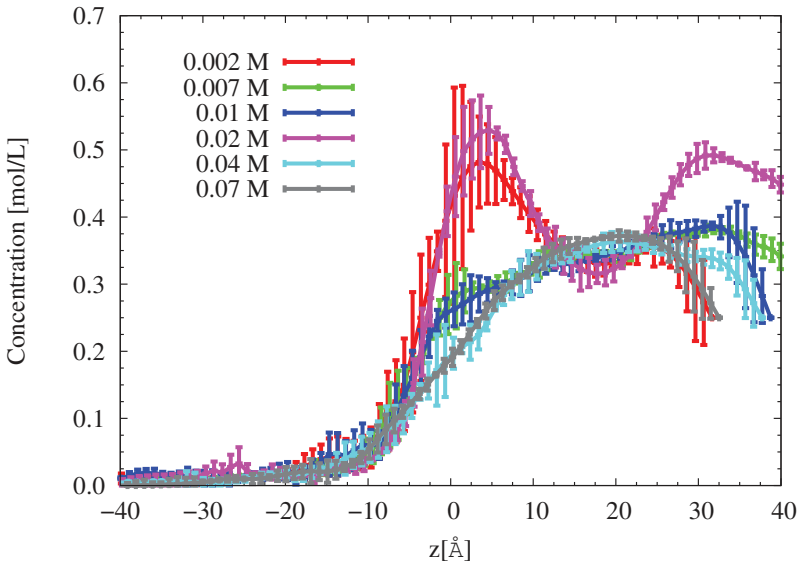

(a) Neodymium

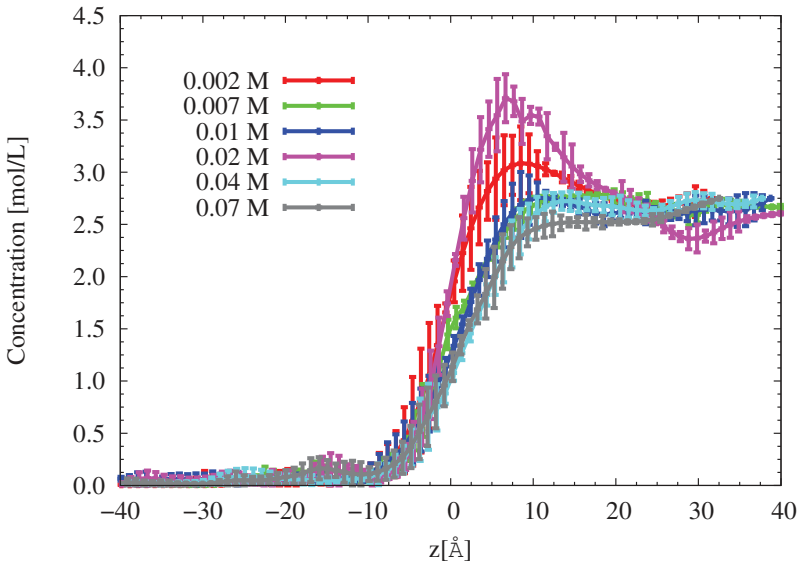

(b) Nitrate

Figure 4.51: Comparison between distributions of (a) neodymium and (b) nitrate for all the investigated samples. With the vertical bars we report the error in volume fraction calculated as explained in section 2.2.3. In the analysis process the initial interface xy-plane is set at $z = 0$ Å.

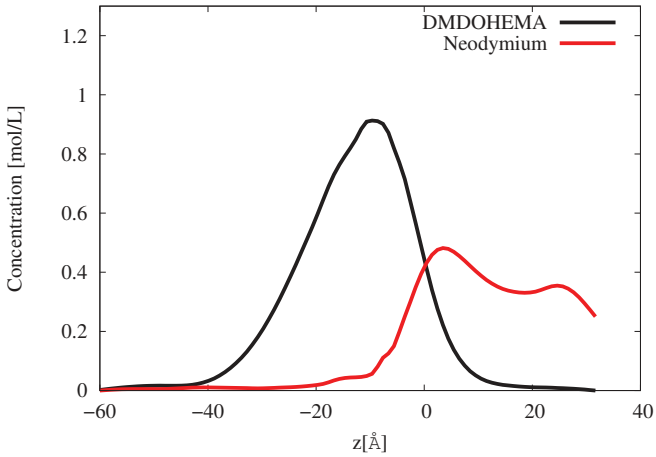

(a) 0.002 M

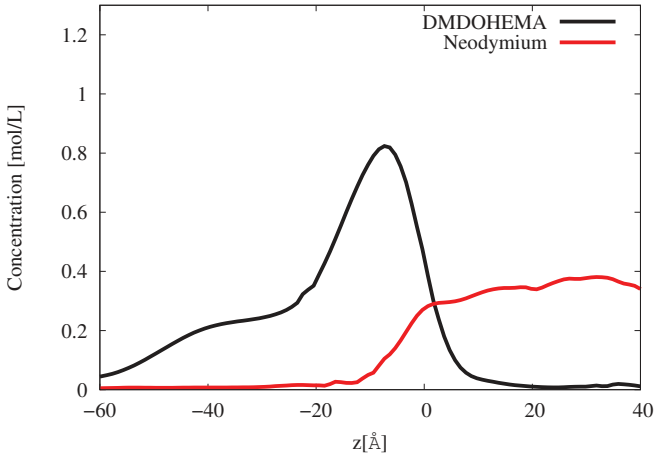

(b) 0.007 M

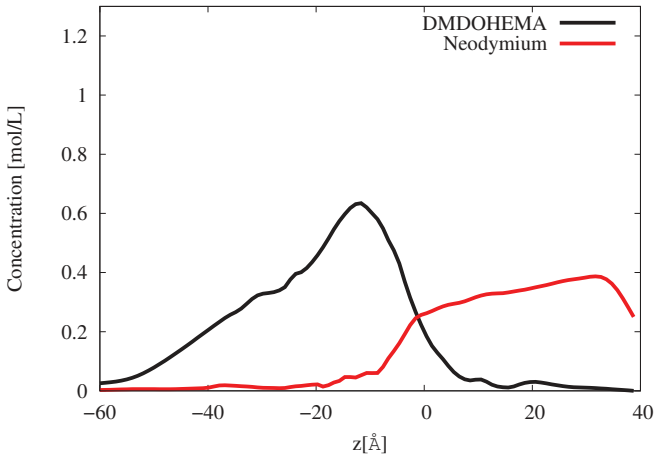

(c) 0.01 M

Figure 4.52: Comparison between neodymium and DMDOHEMA distributions at (a) 0.002 M, (b) 0.007 M and (c) 0.01 M extractant concentration. In the analysis process the initial interface xy-plane is set at $z = 0$ Å. The errorbars are not reported for clarity.

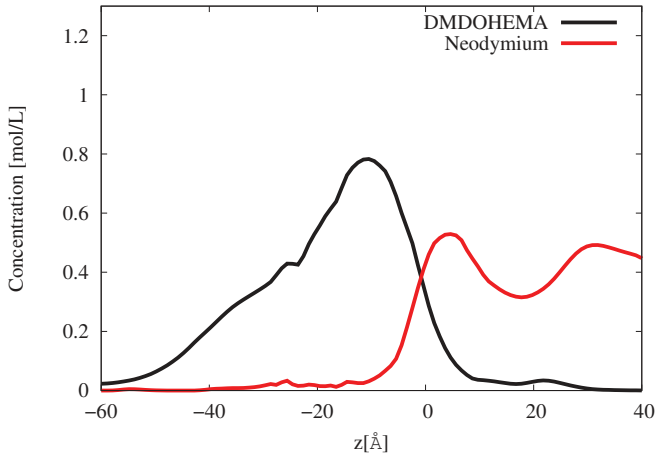

(a) 0.02 M

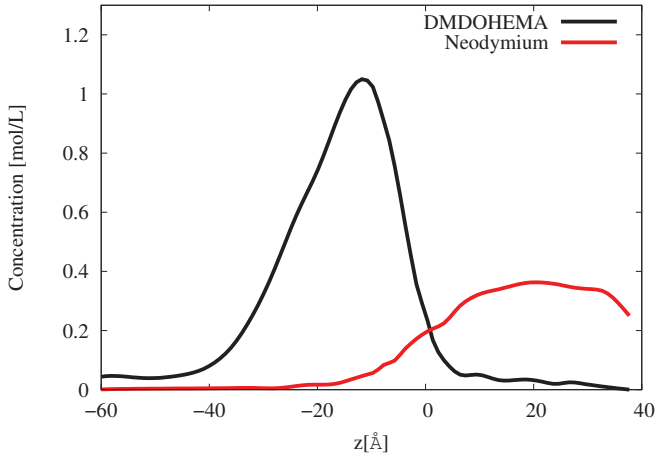

(b) 0.04 M

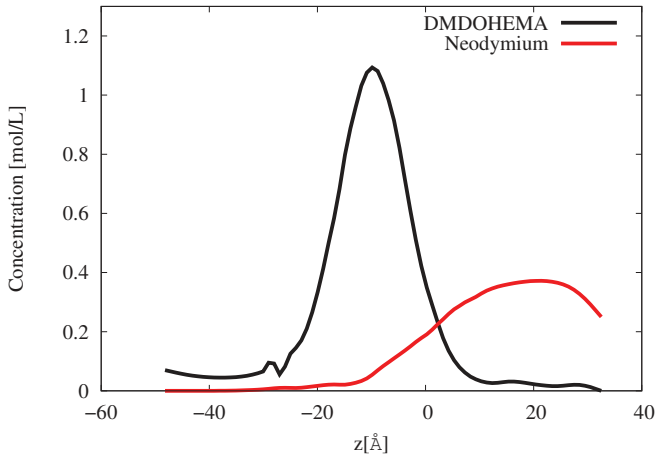

(c) 0.07 M

Figure 4.53: Comparison between neodymium and DMDOHEMA distributions at (a) 0.02 M, (b) 0.04 M and (c) 0.07 M extractant concentration. In the analysis process the initial interface xy-plane is set at $z = 0$ Å. The errorbars are not reported for clarity.

The model obtained with the Motofit analysis for the sample at 0.1 M is equal to the one at 0.07 M (Figure 4.44b). For this reason we can suppose no big difference in diamide or ions distributions between the two samples at the highest concentration.

4.3.4 DMDOHEMA: Summary

The DMDOHEMA in dodecane has been investigated in contact with pure water, nitric acid or neodymium nitrate aqueous phases. In the first two systems a clear adsorption of diamide increasing with the extractant concentration in organic phase is observed. In particular, in the system containing nitric acid, we have observed that the adsorption of diamide produces a desorption of nitric acid.

For the system containing neodymium nitrate, we have observed in average an adsorption of the malonamide with a distribution rather narrow close the interface. However if we look at the organic solvant distribution we can deduce a relative high concentration of oil very close to the aqueous phase. Concerning the distributions of ions, they are rather constant within the aqueous phase and close to the liquid/liquid interface with a weak interpenetration in the extractant-rich interfacial layer.
Concerning the distribution of DMDOHEMA and oils we have suggested a growth of a layer of DMDOHEMA with extractant oriented with tails facing the water and polar heads into the organic phase.

For all the studied systems, by using the Gibbs model and the distributions obtained with the RMCS code we have calculated the interfacial tension at the oil/water interface. Unfortunately, with the only exception of the DMDOHEMA at dodecane/water interface, in the other cases the results are not providing good results. A more complex model considering the activity of species (salts, nitric acid and extractant) at each z-depth is needed but not possible with the only data collected and presented in this work.

4.4 Comparison between DMDBTDMA and DMDOHEMA

The results presented in this work, show a different type of structure of the two ligands at the interface.

In the case of DMDBTDMA we have observed that the interfacial region is

rich in both organic compounds, dodecane and extractant, and water compounds, water and nitric acid or lanthanide salt. Moreover, the distribution of diamide becomes more broader when increasing the extractant concentration in dodecane, unexpected result considering its surfactant behaviour. In addition to that, the density profiles reported in Sections 4.2.2 and 4.2.3 show a strong interpenetration between DMDBTDMA and aqueous solutes.

This type of structure suggests the formation of a diffuse layer with water, organic solvent, extractant and extracted solute, all mixed. The resolution of neutron and x-ray reflectivity does not allows us to say anything about the possible orientation of the diamide molecules that will allow a complexation around the hydrated cations close to the interface. However, above the CAC we know that monomers are in equilibrium with aggregates (see Chapter 1) and the diamide concentration close to the interface is much higher than the CAC. It is then possible to suppose that, in the diffuse region close to the interface, both monomers and aggregates coexist.

This type of interface, which appears more as an *interphase*, is drawn in Figure 4.54.

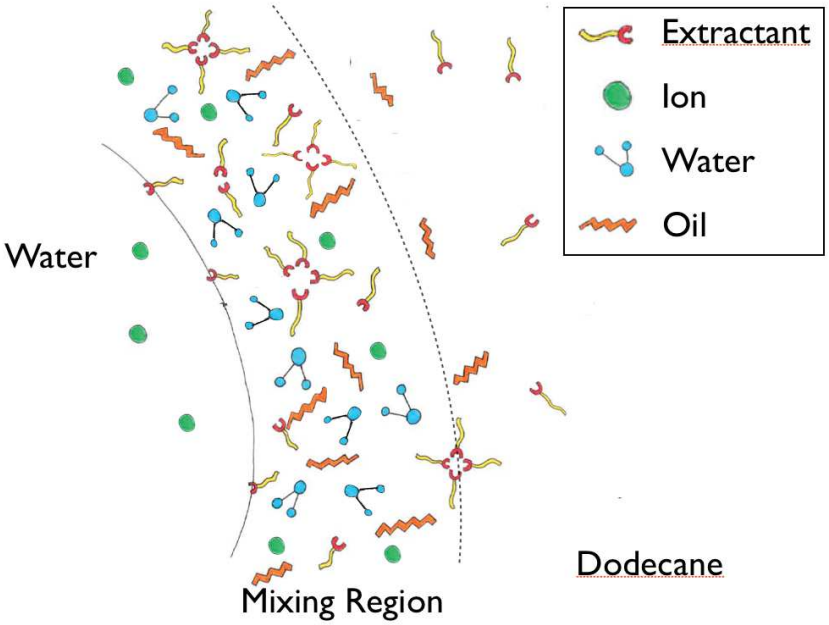

Figure 4.54: Sketch of the structure of DMDBTDMA at the dodecane/water interface. In the region close to the interface we can find extractant (as monomer or aggregates), dodecane, water and extracted solute.

In the case of DMDOHEMA in dodecane contacted with pure water or nitric acid aqueous solution we have observed distributions of extractant becoming more narrow by increasing the extractant concentration in dodecane. In particular, in the case of acid aqueous solution, the adsorption of malonamide causes a desorption of nitric acid. Compared to the DMDBTDMA, the interpenetration between DMDOHEMA and water solutes appears less strong and the latter extractant exhibts a stronger surfactant behaviour. This type of more structured interface can be roughly represented as shown in Figure 4.55.

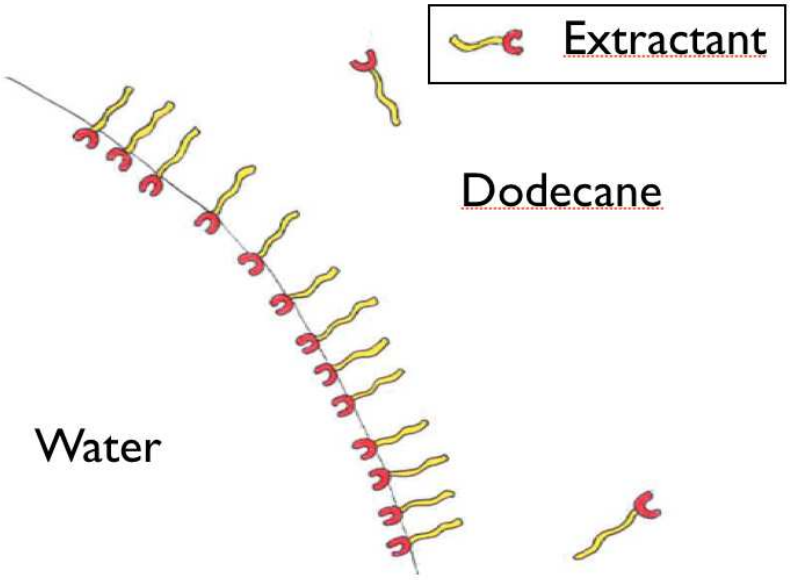

Figure 4.55: Sketch of the interfacial structure of DMDOHEMA in dodecane contacted with pure water or nitric acid aqueous solution.

Lastly, the case of a more structured interface as for DMDOHEMA in dodecane contacted with nitric acid or neodymium nitrate aqueous solution. In this case the extractant exhibits a surfactant behaviour but two points have been highlighted. First, the interpenetration between malonamide and salts appears very low. Second, the interface is very rich in oil and the diamide distributions appear to be shifted more, if compared with other systems, into the organic phase. We have suggested that the DMDOHEMA at the interface could exhibits a preferential orientation, with the polar head oriented to the oil phase and the tails facing the water. The picture that we suggest for these systems with DMDOHEMA is shown in Figure 4.56.

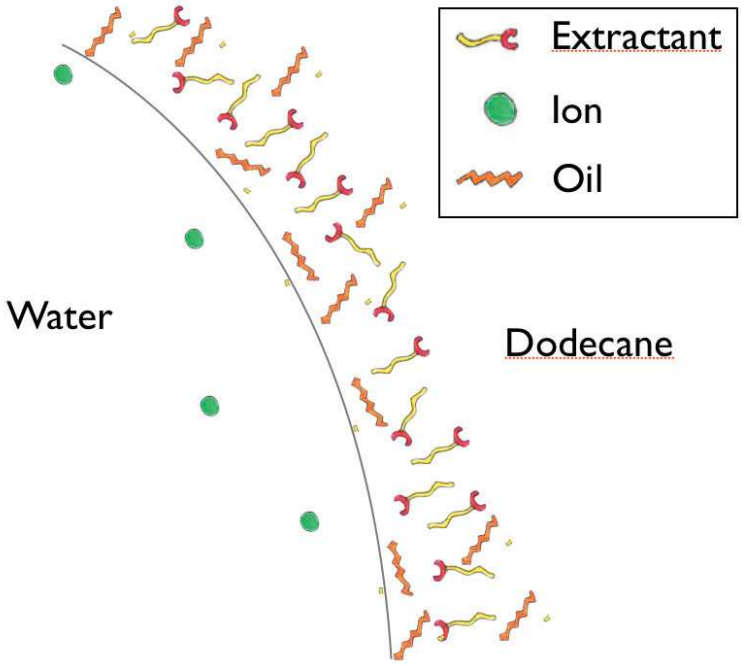

Figure 4.56: Sketch of the structure of DMDOHEMA in dodecane contacted with lanthanide salts aqueous solution. In the region close to the interface we can find extractant with tails facing the water and polar heads into the oil.

In a recent work Mark Schlossman et al.[15, 16] have investigated by x-ray reflectometry and fluorescence the liquid/liquid interface with DHDP extracting erbium ions[1]. In their work the authors say:*"Supramolecular ion-extractant complexes formed at the interface condense into an inverted bilayer when extraction is stopped before completion"*. A picture taken from their work with a sketch of their result is reported in Figure 4.57. In this thesis work no measurements of x-ray fluorescence have been performed, but the resulting distributions of DMDOHEMA, contacted with lanthanide salt aqueous solution, looks compatible with the structure proposed by Schlossman et al. [16].

All these considerations can be summarized in a well defined structure formed by the DMDOHEMA at the interface, versus a more mixed interface, or interphase, formed by the DMDBTDMA. This different structuration could result in a different chemical potential at the interface: higher for the DMDOHEMA and lower for DMDBTDMA. In Chapter 1, Figure 1.1, we have reported a picture extracted

[1]The erbium belongs to the lanthanide series and it is heavier than neodymium.

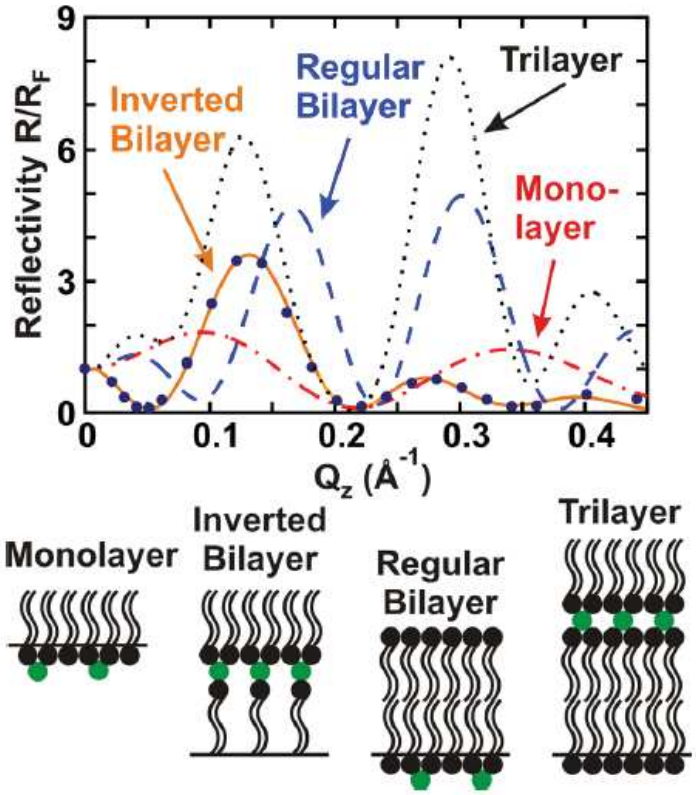

Figure 4.57: (Normalized X-ray reflectivity $R(Q_z)/R_F(Q_z)$ (dark blue dots) from an interface between a 10^{-4} M dodecane solution of DHDP and a $5 \cdot 10^{-7}$ M aqueous solution of $ErBr_3$ (pH = 2.5 adjusted with HBr) at 28 °C. A cartoon of the structures used for the calculations is shown below, where green dots represent Er. Calculations of a typical monolayer (red dash-dotted line), regular bilayer (blue dashed line), trilayer (black dotted line), and the best fit from the inverted bilayer (orange solid line) are also illustrated. A regular bilayer or trilayer has the polar phosphate groups of the lowest leaflet of DHDP in water. It is seen that only the inverted bilayer structure can fit the low Q_z minimum in reflectivity. Interfacial structures with more layers of similar thickness would have shorter-period oscillations that would be inconsistent with the reflectivity data [15].

from a work of Zemb et al. [30] showing the evolution of the chemical potential in a solvent extraction system. By exploiting their diagram, we would like to suggest a schematic view of the different chemical potentials with the two malonamides in Figure 4.58.

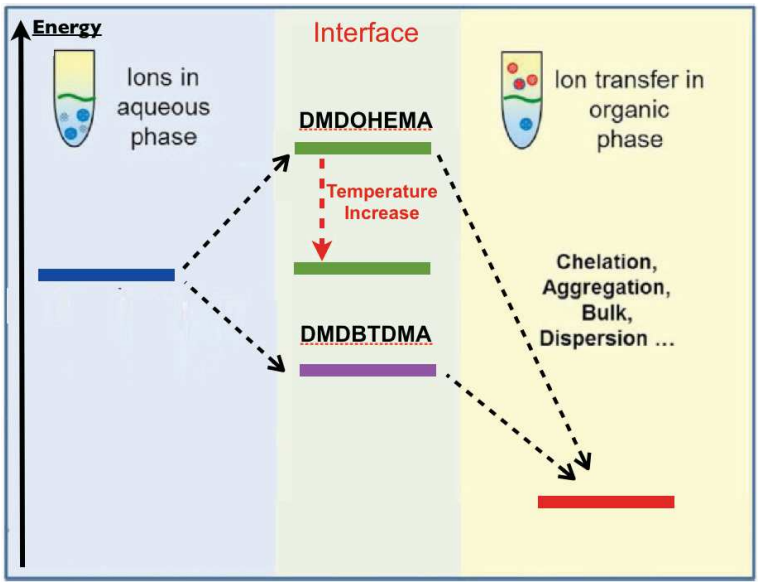

Figure 4.58: Sketch of te difference of chemical potential between bulks and at the liquid/liquid interface for two type of diamide, DMDOHEMA and DMDBTDMA.

4.4.1 The LOC and the liquid/liquid interface

In Chapter 1 we have reported the results obtained by Laurence Martinet [61] on the LOC of DMDBTDMA contacted with different aqueous phases. More detailed results for the nitric acid and neodymium nitrate aqueous phases, extracted from her thesis work, are shown in Figures 4.59, 4.60. We observe that, depending on the aqueous phase, the amount of limit organic concentration (LOC) of extracted solute in organic phase depends on the extractant concentration. For HNO_3 two regimes are found, represented by the two different slopes (*"pente"*) in Figure 4.59:

- For [DMDBTDMA]<0.8 mol/L: in the organic phase for each molecule of diamide, one molecule of nitric acid is found. (Slope=1)
- For [DMDBTDMA]>0.8 mol/L: in the organic phase for each molecule of diamide, ten molecules of nitric acid are found. (Slope=10)

In the case of $Nd(NO_3)_3$ (Figure 4.60) two regimes are found but with different slopes (*"pente"*):

- For 0.4<[DMDBTDMA]<1.25 mol/L: in the organic phase for each molecule of diamide, 0.3 molecules of neodymium nitrate are found. (Slope=0.3)

- For [DMDBTDMA]>1.25 mol/L: in the organic phase for each molecule of diamide, one molecule of neodymium nitrate is found. (Slope=1)

From the distributions shown in Sections 4.2.2 and 4.2.3 we have calculated the ratio between aqueous solute complexed by DMDBTDMA (nitric acid or neodymium ions) in organic phase, as function of the z-depth. The results for the two systems of DMDBTDMA in dodecane contacted with nitric acid or neodymium nitrate aqueous solutions are shown in Figures 4.61 and 4.62.
We observe that close to the interface (z=0 Å) the [Solute]/[DMDBTDMA] ratio increases and it is comparable with the one reported from the work of Martinet [61]. We conclude that the interface is similar to the organic phase at the demixion limit (Third Phase Formation).

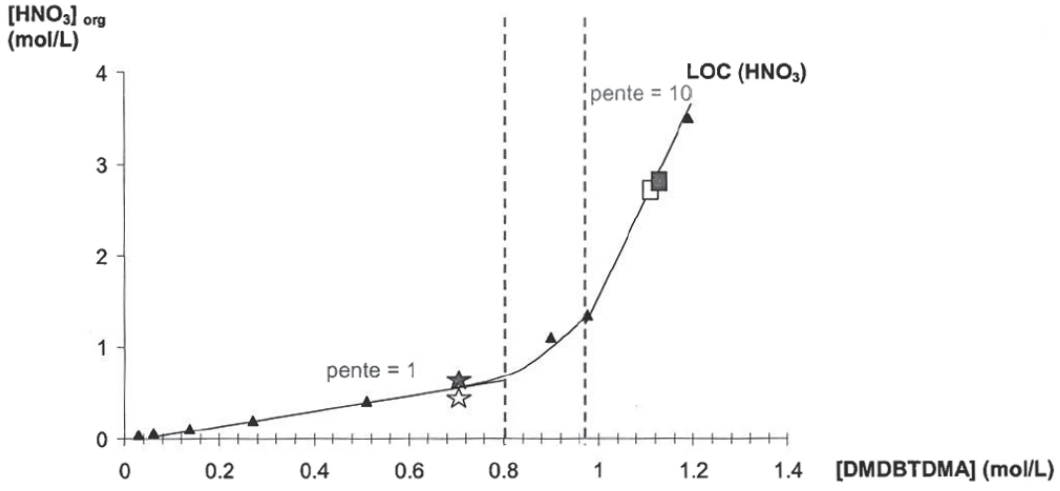

Figure 4.59: Limit Organic Concentration (LOC) of HNO_3 (concentration of HNO_3 in the organic phase just before the third phase formation) as a function of the initial extractant concentration [61]. The "pente" is the value of the ratio between the concentration of nitric acid and malonamide in organic phase at the equilibrium [61].

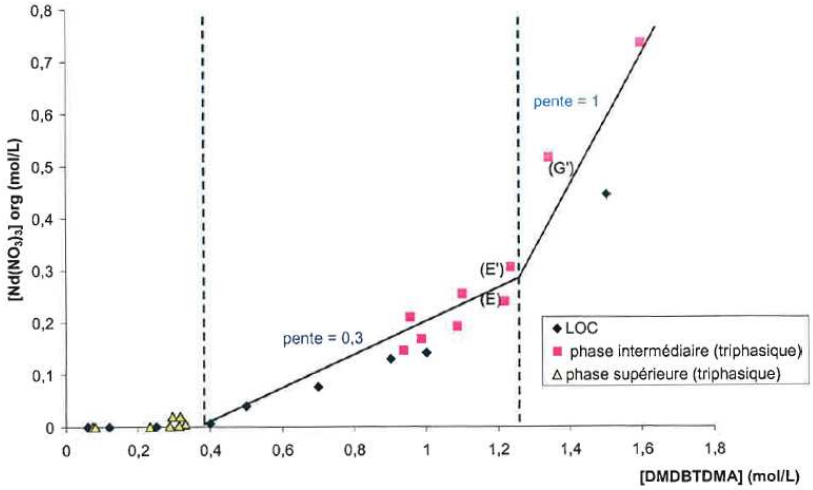

Figure 4.60: LOC of $Nd(NO_3)_3$ (concentration of $Nd(NO_3)_3$ in the organic phase just before the third phase formation) as a function of initial extractant concentration. The "pente" is the value of the ratio between the concentration of neodymium nitrate and malonamide in organic phase at the equilibrium [61].

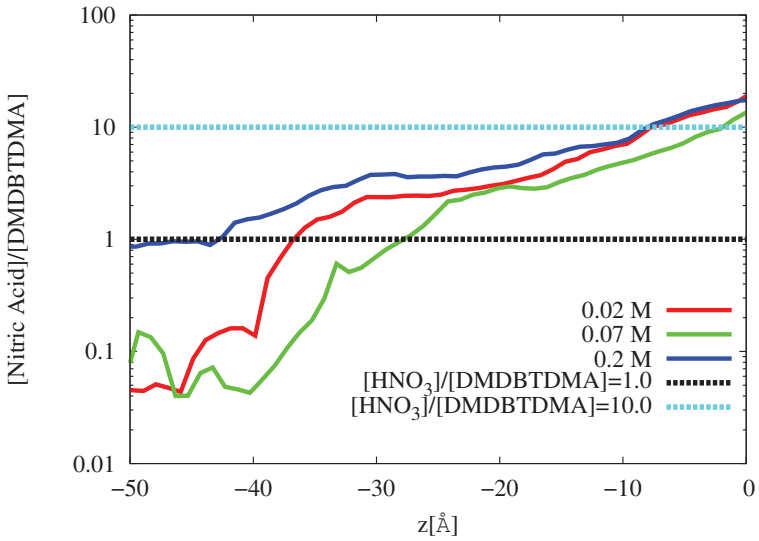

Figure 4.61: Ratio between aqueous solute and DMDBTDMA in organic phase *vs.* z-depth for the samples with DMDBTDMA in dodecane contacted with nitric acid aqueous solution (2 mol/L). With the continuous lines we report the results obtained in this thesis work. With dashed lines we report the slopes found by Martinet [61] shown in Figure 4.59.

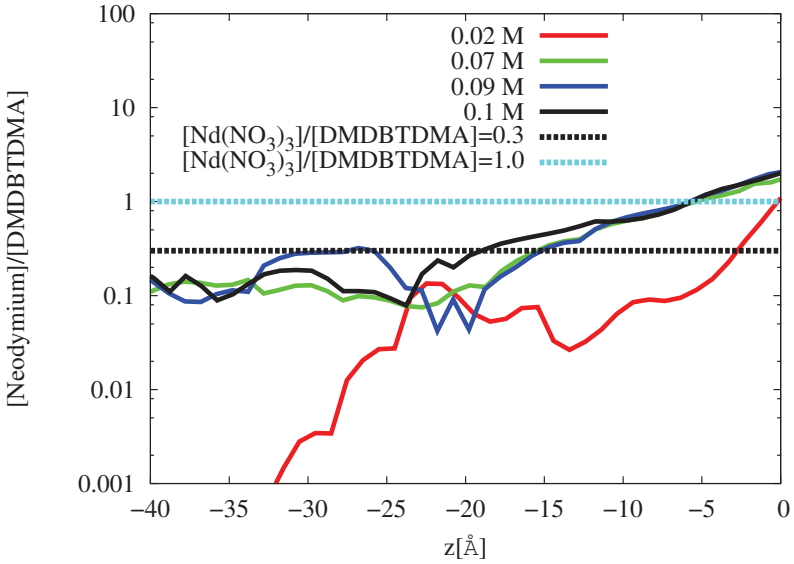

Figure 4.62: Ratio between aqueous solute and DMDBTDMA in organic phase *vs.* z-depth for the samples with DMDBTDMA in dodecane contacted with neodymium nitrate (0.25 mol/L) aqueous solution. With the continuous lines we report the results obtained in this thesis work. With dashed lines we report the slopes found by Martinet [61] shown in Figure 4.60.

For DMDOHEMA systems we have not found in the literature any work reporting the LOC as for DMDBTDMA. With the collaboration of Geoffroy Ferru, we have calculated the LOC for DMDOHEMA in dodecane contacted with nitric acid or neodymium nitrate aqueous solutions. The colected data have been fitted with a linear fit function, as done by Laurence Martinet. Data and fits are shown in Figure 4.63. From the distributions shown in Sections 4.3.2 and 4.3.3 we have calculated the ratio between aqueous solute complexed by DMDOHEMA (nitric acid or neodymium nitrate) in organic phase, as function of the z-depth. The results for the two systems of DMDOHEMA in dodecane contacted with nitric acid or neodymium nitrate aqueous solutions are shown in Figure 4.64.

In both cases shown in Figure 4.64, the increase of the [Solute]/[Extractant] ratio is weaker than the one observe for DMDBTDMA. The [Solute]/[Extractant] ratio, found with the distributions shown in previous sections, becomes comparable to the one obtained with titration measurements only for z-values very close to the interface. The only exception is found for the system with 0.002 M of DMDOHEMA in dodecane contacted with nitric acid aqueous solution (red curve, Figure 4.64a).

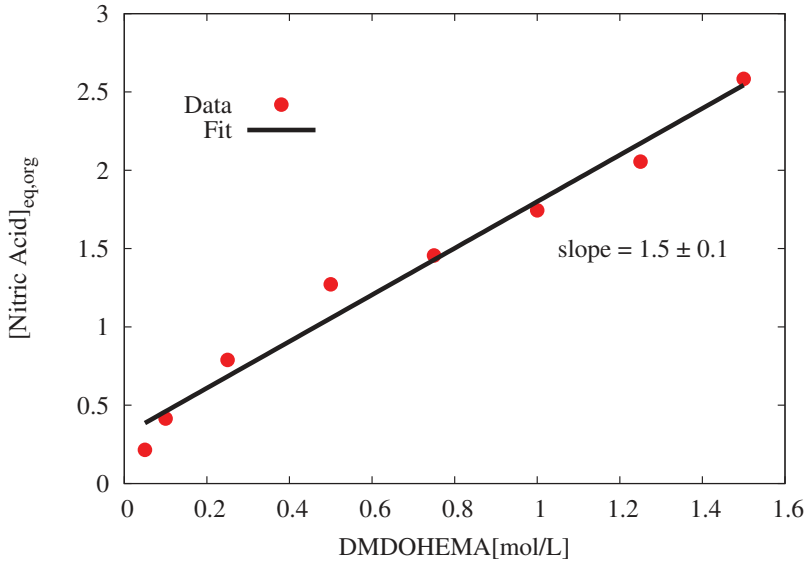

(a) Nitric Acid

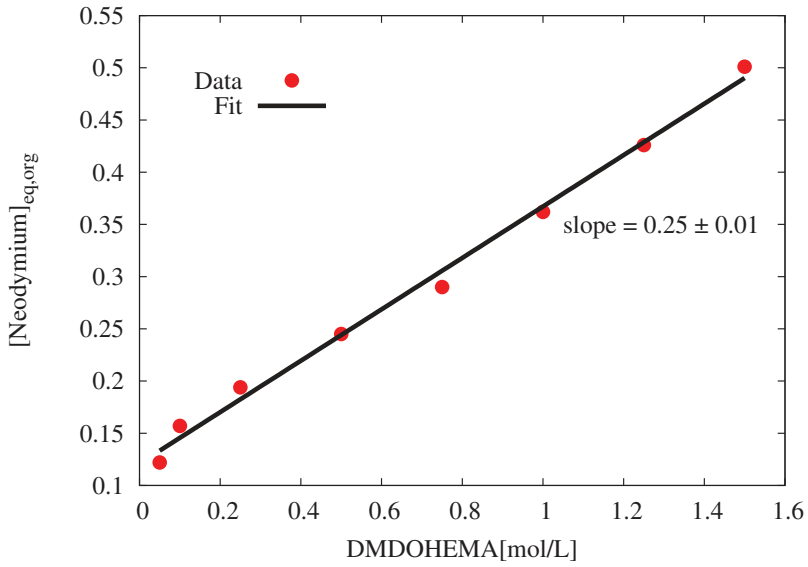

(b) Neodymium Nitrate

Figure 4.63: LOC of DMDOHEMA in dodecane contacted with (a) nitric acid aqueous solution (2 mol/L) or (b) lithium nitrate (2 mol/L) and neodymium nitrate (variable concentration) aqueous solution. Experimental data are reported with red dots, fits with black lines. The slope of the fitting function represents the ratio between extracted solute and extractant molecule in the organic phase at the equilibrium.

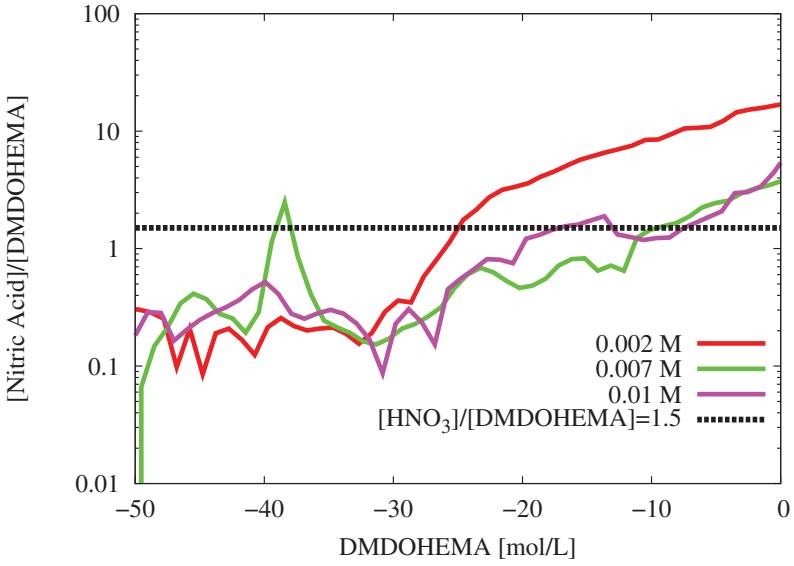

(a) Nitric Acid

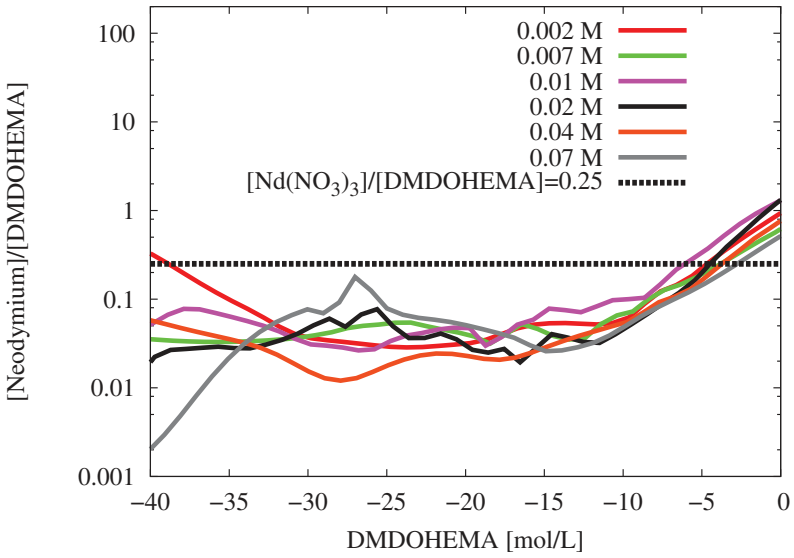

(b) Neodymium Nitrate

Figure 4.64: Ratio between aqueous solute and DMDOHEMA in organic phase *vs.* z-depth for the samples with DMDOHEMA in dodecane contacted with (a) nitric acid aqueous solution (2 mol/L) or (b) neodymium nitrate (0.25 mol/L) aqueous solution. With the continuous lines we report the results obtained in this thesis work. With dashed lines we report the slope calculated by fitting the data reported in Table **??**.

By comparing the results obtained by Martinet [61](Figures 4.59, 4.60) with those obtained for DMDOHEMA by titration experiments (Figure 4.63) we observe that the [Solute]/[Extractant] values obtained for the first ligand are larger than those obtained for DMDOHEMA.

The results shown above are compatible with the pictures of a more diffuse liquid/liquid interface in presence of DMDBTDMA and more structured interface with DMDOHEMA, as shown in Figures 4.55, 4.54 and 4.56. The different structuration of two malonamide and the possible resulting interfacial chemical potential shown in Figure 4.58, could be the explanation for different exctraction regimes. As shown by Simonin et al. [13], extraction by DMDOHEMA is driven by kinetics and by diffusion with DMDBTDMA. Moreover, they have shown that increasing the temperature the extraction with DMDOHEMA becomes more efficient. It is possible that the extractant uses the thermal energy provided to create a more disordered interface in order to approach more to the interface created by the DMDBTDMA, reducing the interfacial chemical potential and allowing the diffusion of aqueous solutes and, consequently, complexation with extractant and aggregates diffusion into the organic phase.

Conclusions

In this thesis work we have studied water/oil interfaces combining x-ray and neutron reflectivity measurements. The particularity of these systems was that the organic fluid contains amphiphilic ligands or extractant molecules used in cation extraction or separation processes.

In literature a lot of fundamental and applied researches were focusing either on bulk properties of these specific ligands or the thermodynamics of the complexation (ion/extractant) or on the kinetics of ion transfer whatever the direction of transfer. However, very few of works are carried out on the interfacial mechanism at the nanometer scale that can help to model in the future with physical parameters the ions transfer and interfacial selectivities. This is understandable because to probe buried and soft interfaces at the nanometer scale is a challenge.
For this purpose we have decided to exploit the high performance of large scale facility instrument such as synchrotron and neutron reactor, using x-ray and neutron surface scattering techniques. Taking care about similar previous experiments described in literature, we have developed and realized a new and suitable liquid/liquid cell with similar characteristic for both types of radiation varying only the scattering contrast of the studied system.

We have focused our research on two different extractants (DMDBTDMA and DMDOHEMA) that nevertheless belong to the same family of neutral extractants, the malonamide type, and already used in solvent extraction (SE) process in industry. Although very similar at the chemical point of view, the kinetics of the lanthanide extraction process is different depending on which extractant is used in a dodecane/water biphasic system (one of the benchmark immiscible fluids for

SE). Usually for applied research, scientists work at relatively high concentration of extractant in oil, however, for our purpose we work at relatively low concentration but close to the critical aggregation concentration for technical reasons (parasitic scattering and signal attenuation).

To analyze quantitatively our reflectivity data, taking into account different scattering contrast for a given system, we were obliged to develop a new Fortran code based on Monte Carlo algorithm to co-refine x-ray and neutron reflectivity data (the RMCS code). Our analysis takes into account various experimental aspects such as imaginary part of the SLD (related to the absorption), different experimental geometries and the fact that we can use monochromatic or polychromatic beam.
Before to apply this technique of data analysis, some proof of quality were provided simulating different model systems composed of various solutes such as extractant molecules and salts, in order to determine concentration profiles at the interface from known distributions. Then, this approach was applied to determine unknown and equilibrated profiles from experimental systems and to compare them as a function of malonamide type of extractant but also as a function of their concentration in the organic phase and for various type of aqueous phases in contact with the organic part.

The first general observation from reflectivity data analysis is that we observed, whatever the thermodynamical conditions, a concentration of the extractant at the aqueous/organic liquid interface. However, the respective distributions of these extractants and the other solutes at the water/oil interface are different, as well as the interpenetration of water and oil via the presence of the extractants. The DMDOHEMA has a surfactant behavior much more pronounced than the DMDBTDMA, with interfacial distribution much more condensed and perhaps with a singularity that is to form an inverted bilayer, as already suggested in recent Schlossman et al. [15] studies on similar systems.
In the case of DMDBTDMA, the interfacial region is much thicker and can be considered as an interphase for which the extractant and solute concentrations are close to those determined at the third phase transition. A schematic view showing these differences in case of the aqueous phase contains a cation that can be complexed by the ligands is presented in Figure 4.65.

With the knowledge of the concentration profiles at the liquid/liquid interface we should be able to recalculate the surface tension in these systems. However, these profiles are averaged and do not inform about how interact each species between them because these interactions as well as the polarization effect generated

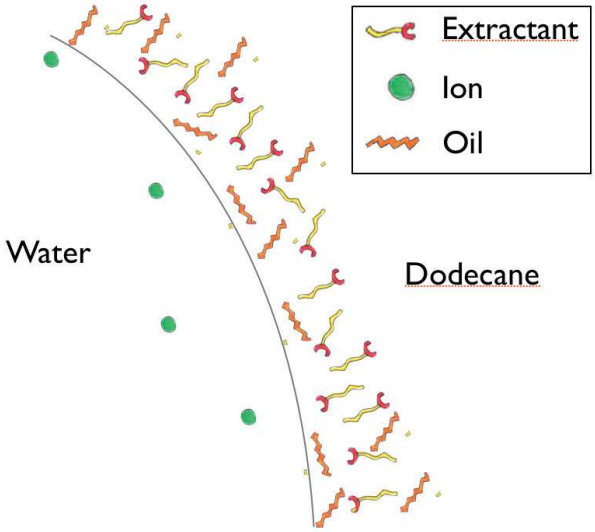

(a) DMDOHEMA

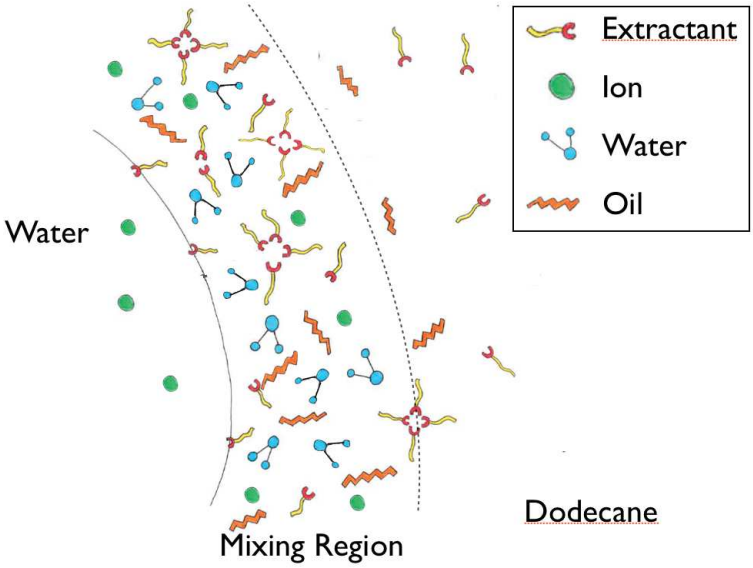

(b) DMDBTDMA

Figure 4.65: Sketch of the interfacial structure of (a) DMDOHEMA or (b) DMDBT-DMA in dodecane in contact with an aqueous solution of lithium nitrate (2 mol/L) and neodymium nitrate (0.25 mol/L).

by the ions adsorptions have to be taken into account in the surface tension. We have shown that a simple Gibbs model can be applied to calculate the LL surface

tension for systems without solutes and are in agreement with the experimental values. The calculation with solutes is another challenge and need to get interfacial spectroscopic information.

Perspectives

The work presented in this thesis represents a step for a better understanding the structure of liquid/liquid interface with or without amphiphilic molecules. The investigation of buried liquid/liquid interface presented in Section 4.1 evidences the necessity of further investigations of the interfacial structure with different mixtures of hydrogenous/deuterated compounds. It is well known that, for example, mixture of hydrogenous/deuterated alkanes demix with a rate depending on their volume ratio [99]. This demixion phenomena, or preferential adsorption of protonated species at liquid/liquid interface, could depends, as we have suggested, on the different intermolecular interaction due to the presence of hydrogen or deuterium.

Concerning the solvent extraction, we have observed that different ligands, with different extraction behaviour (extraction controlled by diffusion or kinetic regime [13]), more or less amphiphilic, show different structuration at the liquid/liquid interface. Studies at the liquid/liquid interface with other extractants with different structure can be helpful to understand physical chemistry properties of extractant at the interface. Examples of different extractant structure are the CMPO (bidendate) for the TRUEX process [100], TODGA (tridendate) [101] and monoamides such as DEHiBA (monodendate) [48].
More complex systems containing co-extractants, such as DMDOHEMA and HDEHP [102], are difficult to study by x-ray and neutron reflectivity due to the high number of unknowns. Despite that it is possible to study these systems by coupling reflectivity with other techniques such as ellipsometry [103], Second Harmonic Generation [47, 48], voltammetry [104], amperometry [50, 53].

On the other hand, studies with different type of aqueous solutes can be interesting to study the structuration of both aqueous solutes and extractant depending on the type of solutes (monovalent, divalent or trivalent) [16, 21].
On the other side, measurements with different aqueous solutes at different concentrations can explain how the interface changes depending on the water activity and/or pH.

Regarding the experimental aspects, few developments can be helpful. First of all the cell should be improved to control the temperature. This is a development very interesting for two main aspects: the first one is the time-saving during the experiments, saving the time needed to change the sample. Moreover it would allow to study the variation of interfacial structure depending on the temperature. Comparison and coupling with experiments with different techniques, such as rotating cell [12, 13], would result easier.
Furthermore, coupling the neutron and x-ray reflectivity with fluorescence measurements [15, 16, 105] can help in reducing the number of unknowns for complex systems, such as extractant in dodecane contacted with lanthanide salt aqeous solutions. In particular, neutron reflectivity measurements can be coupled with neutron fluorescence measurements [105]. This type of measurements exploit the large cross section of elements such as the Gadolinium. In fact, the Gd(III) can be used to model the interaction at liquid/liquid interface between extractant and lanthanide salts ($Gd(NO_3)_3$, $Nd(NO_3)_3$, $Eu(NO_3)_3$).

Lastly, a successful test at liquid/liquid interface with perfluorohexane has been conducted during this thesis work (not reported here). By using fluorinated of oils we have observed a considerable increase in the transmitted and reflected beam counting rate in neutron reflectivity experiments. At the $D_2O/C_{12}H_{26}$ interface at $\theta = -0.617°$, as reported in Appendix *Neutron Reflectivity Experiments Tables*, the counting rate is equal to 115 neutron/second. At the C_6F_{14}/D_2O the counting rate is approximately 600 neutron/second. This intensity increase can be helpful for the study of kinetics of surfactant at the liquid/liquid interface. Furthermore, the neutron SLD of fluorinated oil is lower than D_2O which it means that it is possible to measure the critical edge, not possible for the neutron data presented in this thesis.
Use of fluorinated oils can be helpful for the study of solvent extraction with f-malonamide [106] and neccessary for coupling neutron reflectivity measurements with neutron fluorescence measurements [105] to reduce the amount of hydrogens in the samples.

Due to the large interest for liquid/liquid interface for metal recovery [107, 108]

or biological and pharmaceutical applications [97], all the developments proposed here can be helpful also for the study of systems containing different surfactants [109, 110, 111, 112, 113, 114].

Résumé

Dans le cadre du retraitement des déchets nucléaires et du recyclage de métaux critiques, l'extraction par solvant est l'une des technologies les plus utilisées. L'interface liquide entre deux fluides non miscibles est considérée comme une région où de multiples phénomènes physiques et chimiques sont à prendre en compte et peuvent limiter ou favoriser le transfert d'espèces entre les deux fluides. La structure de ces interfaces doit être connue en fonction de plusieurs paramètres thermodynamiques pour pouvoir déterminer le paysage énergétique associée. La réflectivité de neutrons et de rayons est un des outils appropriés pour sonder ce genre d'interfaces enfouies et fluctuantes à l'échelle nanométrique et à l'équilibre.

Chapitre 1

Au Chapitre 1 nous avons rappelé l'intérêt de l'extraction liquide/liquide dans de nombreux procédés d'extraction minière, de dépollution ou de revalorisation de métaux qualifiés de critique. Déjà G. Seaborg prix Nobel de chimie le rappelait dans une de ses interventions orales en 1980: *"In the future, chemistry will be called upon to extend our natural resources of copper, lead, zinc, and other nonferrous metals by making it possible to recover these metals more economically from low-grade ores or to recycle materials now discarded as waste"*. L'extraction liquide-liquide (LL) ou l'extraction par solvant est un procédé de séparation qui est basé sur le transfert d'un soluté à partir d'une solution 1 en direction d'une phase immiscible 2 dont le contact peut être amélioré par émulsification. En d'autres

termes, c'est un procédé pour séparer des composés en fonction de leurs solubilités relatives dans deux liquides non miscibles, habituellement de l'eau et un solvant organique. L'application ultime est un transfert sélectif à moindre coût et le plus rapide même si un compromis existe toujours entre sélectivité et cinétique. La technologie de séparation LL est un processus d'ingénierie chimique mature et est utilisé dans de nombreuses applications industrielles où la distillation thermique est difficile à mettre en œuvre et est peu sélective. Il est souvent considéré comme une méthode de référence face à des procédés plus récents, tels que la flottation ou la précipitation sélective, qui peuvent parfois réduire le nombre d'étapes et limiter la quantité d'effluents organiques et réduire les coûts.
Cependant, ce processus est lié à la traversée d'espèces hydrophiles au travers d'une interface dont la composition et la structure fluctuent. Dans tous les cas, les espèces solvatées ou hydratées (en fonction de la direction de transfert) doivent explorer diverses configurations de passage, très souvent différentes de celles qui existent dans les solutions bulks et associées à des barrières d'énergie qui déterminent une partie de la cinétique. Plus sélective est le processus, plus lent il est et plus haute est la barrière énergétique.

Dans le cas bien spécifique de la récupération de cations métalliques et en raison de leur faible solubilité dans les huiles qui les rend difficiles à transférer à partir d'une phase aqueuse, le processus d'extraction nécessite l'utilisation de ligands d'extraction dissous dans la phase organique et qui peut interagir avec des cations hydratés afin de solubiliser le un complexe.
Ces ligands ou molécules extractantes doivent être conçus pour améliorer la sélectivité en fonction de la distribution des ions dans la phase aqueuse. Ils ont une grande incidence dans le domaine de la séparation d'ions métalliques, car dans de nombreuses applications des degrés élevés de purification d'ions métalliques provenant de diverses matrices solides ou liquides sont nécessaires comme déjà indiqués ci-dessus: l'isolement de métaux à partir de minerais naturels, la récupération d'un métal à partir de ceux qui sont indésirables et la gestion des déchets liquides en sont des applications pratiques, pour ne citer que certains d'entre eux.
Ensuite, comme mentionné ci-dessus, les propriétés moléculaires qui agissent sur les cinétiques et la sélectivité sont souvent antagonistes et les mécanismes d'extraction, ainsi que leur cinétique à l'échelle moléculaire sont encore mal compris, même si des recherches ont été entreprises, donnant déjà des résultats très intéressants. Les mécanismes de complexations et de spéciations dans chacun des volumes des deux phases sont relativement bien appréhendés quelle que soit la géométrie des procédés ainsi que la caractérisation des couches de diffusion au sein desquelles les

forces de viscosité sont importantes. Les procédés d'extraction sont bien décrits dans les traités de génie chimique, en considérant une suite de trajets de réactions macroscopiques au voisinage d'une interface qui doivent être développées et maintenues dans des décanteurs, des colonnes pulsées ou autres dispositifs émulsifiant ou de cisaillement. Cependant, il reste de nombreuses variables inconnues pour quantifier les barrières d'énergie liées à la sorption et à la désorption d'ions ou de complexes ioniques ou neutres à l'interface eau/huile qualifiée d'active.

Si l'on considère l'épaisseur de cette interface active (quelques nanomètres) comme la distance d'interaction entre les espèces hydratées et solvatées et sur laquelle il existe une discontinuité de polarisabilité et nous pouvons y définir un isotherme d'adsorption, il était permis avant les travaux de cette thèse de diviser cette couche en trois volumes (Figure 5.1): a) le volume de solvant appelé "mouillage" de la monocouche et dans laquelle il est prévu un épuisement des agents complexants, b) la monocouche d'agent d'extraction où l'orientation moléculaire et d'interaction latérale sont essentielles et c) la couche de Stern et de Gouy-Chapman côté face aqueuse. Cela restait bien évidemment une vue très schématique de cette interface ne prenant pas en compte les fluctuations géométriques et de concentration à différentes longueurs d'onde.

Afin d'explorer plus finement cette couche, nous avons centré notre étude sur une investigation utilisant la réflectivité du rayonnement, une technique déjà largement utilisée pour analyser des interfaces liquide/gaz, un peu moins pour des interfaces liquide/liquide.

Le choix des systèmes de ligands choisis a été dicté par des études précédentes au sein de l'équipe du L2IA à l'ICSM mais aussi des collaborations avec d'autres équipes du CEA Marcoule expertes et reconnues au niveau international dans l'extraction liquide/liquide des ions lanthanides et actinides pour des procédés de séparation dans le domaine du retraitement de déchets nucléaires. Il s'agit de ligands de type diamide comme le DMDBTDMA et le DMDOHEMA, sélectifs envers les lanthanides, cations trivalents dans une phase aqueuse plus ou moins acide. De nombreuses études existent et concernent la conformation des complexes diamides/cations en phase organique et en fonction de multiples paramètres thermodynamiques comme la concentration des espèces, l'acidité de la phase aqueuse ou son activité, la température et autres modification chimique sur le ligand lui-même ou le solvant organique. Des études à l'équilibre et hors équilibre ont été réalisées et ces dernières ont montré des différences en particulier sur la nature du transfert ionique qui pouvait être qualifiée de diffusif pour le DMDBTDMA et de cinétique pour le DMDOHEMA, ce dernier étant sensible à la température. Enfin

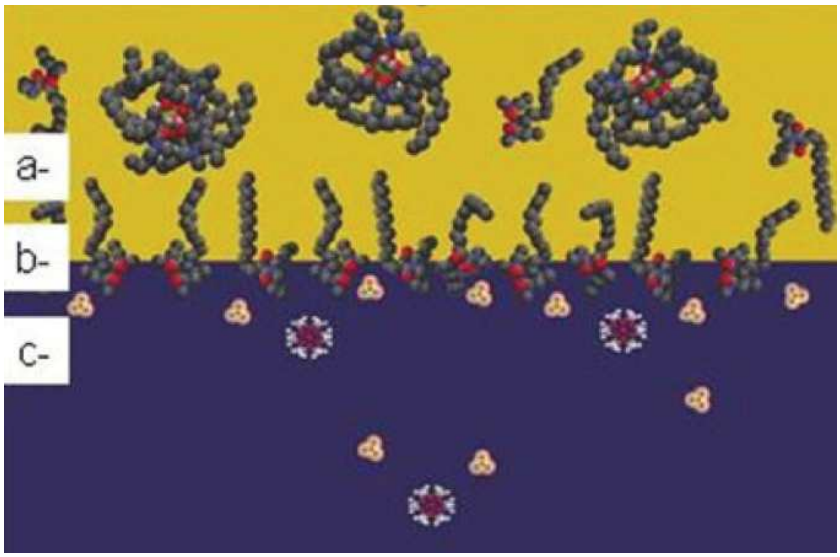

Figure 5.1: Vue de l'artiste à l'échelle de l'interface huile-eau dans une extraction liquide-liquide (P. Guilbaud CEA- Marcoule - collaboration avec ICSM). Les molécules extractantes forment une monocouche à l'interface. Coté phase aqueuse, cette monocouche est en contact avec la double couche formée par des cations adsorbées en équilibre avec les ions en solution. Coté phase organique un fluide complexe entre micelles et des micro-émulsions. Ces agrégats formés par les complexes extractants/ ions hydratés sont des gouttelettes de taille nanométrique en équilibre dynamique. Les interactions entre ces agrégats en bulk ou à l'interface sont des interactions à longue portée. Des instabilités apparaissent lorsque les forces ne sont pas assez répulsives.

des études sur la transition biphasique-triphasique ont été réalisées et ont démontré l'importance des interactions entre agrégats ou complexes ligands/cations en phase organique qui peuvent être appréhendés comme des micelles inverses avec un cœur polaire, un nombre d'agrégation et un nombre de complexation inférieur ou égal au nombre d'agrégation.

Dès lors la question au début de ses travaux de thèse a été : peut-on caractériser à la fois la composition et la structure de l'interface par rapport aux précédentes études réalisées à l'équilibre et hors équilibre et des analyses et résultats qui en avaient été déduits? Pouvait-on en donner une vision au moins schématique cohérente et serait-elle différente de celle imaginée et décrite précédemment? Pouvait-on trouver une différence entre les deux systèmes choisis de diamide sachant que le transfert d'ions europium dans le cadre de travaux de Simonin et al. publiés en 2014 était différent dans chacun des cas.
Donc dans ce Chapitre 1 nous avons décrit la bibliographie utile et succincte autour

des extractants ”diamide” ainsi que ceux qui concernent la réflectivité du rayonnement neutrons et rayons x sur des interfaces enfouies de type liquide/liquide.

Chapitre 2

Le Chapitre 2 est donc consacré à la partie ”théorie de la réflectivité” en y rappelant les concepts et formalisme avec ses approximations utiles pour appréhender les courbes expérimentales obtenues aux cours de ces trois années ainsi que les différences entre réflectivité de neutrons et de rayons x.

Cependant au cours de ces travaux de thèse nous avons développé un programme spécifique d'analyse de données. Ce programme et surtout son concept basé sur une approche Monte Carlo est décrit dans une sous-partie de ce chapitre en y explicitant chacune des étapes de la pré-détermination des distributions générales des densités de longueurs de diffusion à la distribution de chacune des espèces de part et d'autres de l'interface ainsi que la correspondance par un formalisme de Parrat avec les courbes expérimentales. Les erreurs sont prises en compte à chacune des étapes et permettent d'encadrer la solution. Un certain nombre d'exemples test plus ou moins liés aux mesures effectuées sont données à la fin de ce Chapitre 2 afin de valider le concept et la méthode. Bien qu'assez compact il représente un gros travail de programmation.

Chapitre 3

Le Chapitre 3 est quant à lui dédié tout d'abord à la nécessité d'utiliser des sources de rayonnement de type grands instruments tels que le réacteur à neutron à Grenoble, l'Institut Laue Langevin au sein duquel la grande majorité de la thèse a été effectuée ou le synchrotron sur le même site scientifique, l'ESRF.
Géométries et caractéristiques expérimentales et spécifiques y sont rappelées. En particulier l'intérêt d'utiliser un spectromètre unique dans le monde, le spectromètre Figaro à l'ILL qui permet d'attaquer l'interface soit par le haut soit par le bas en fonction de la deutération du milieu et donc du contraste et de la transmission du milieu.

La deuxième partie de ce Chapitre 3 est dédié à la description de la cellule expérimentale qu'il a fallu développer spécifiquement pour cette étude. Il rassemble dans une première partie les développements précédents extraits d'autres études dans le monde sur des interfaces liquide/liquide mettant en exergue les avantages

et inconvénients de chacun de ces développements en fonction des géométries et type de rayonnement utilisés rappelant en même temps les études pertinentes sur le sujet et en particulier des études récentes de Schlossman et al. sur des interfaces d'extractants phosphatés. Ce développement de cellules adaptées s'est déclinée tout au long de la thèse ce qui a parfois engendré des retards dans la collection de données reproductibles et analysables.

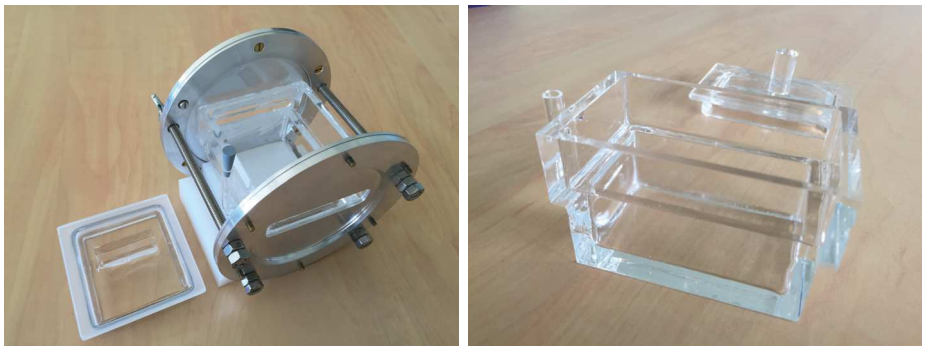

(a) X-ray (b) Neutron

Figure 5.2: Dernière version des cellules expérimentales pour réflectivité neutrons et rayons X.

Chapitre 4

Le Chapitre 4 est enfin la partie qui rassemble l'ensemble des résultats expérimentaux c'est-à-dire courbes de réflectivité x et neutrons jouant ainsi sur différents contrastes d'analyse et ceci sur des interfaces eau/dodécane avec comme ligands le DMDBTDMA ou le DMDOHEMA à différentes concentrations et toujours en dessous de la concentration d'agrégation critique pour des raisons d'absorption et de diffusion des faisceaux x ou neutrons. Le sel de lanthanide choisi a été le nitrate de néodyme dans une phase aqueuse soit acidifiée soit d'activité similaire mais avec un sel de nitrate de lithium, un cation non complexé par les diamides. Nous avons présenté les données en fonction de la complexité du système, composé par l'huile, l'eau et l'extractant, avec et sans les ions. Pour résumer et bien que la structure amphiphile des deux diamides soit bien connue, la structure de l'interface liquide/liquide semble être différente de celle que l'on pourrait s'attendre avec des tensioactifs classiques. L'organisation de ces ligands à l'interface est en effet plus complexe, varie en fonction de leurs concentrations dans la phase organique et en

fonction de la concentration d'acide et de sel dans la phase aqueuse. Une organisation de type monocouche n'est pas l'organisation principale de ces systèmes à l'équilibre mais on observe plutôt une couche épaisse de ligands. Plus précisément, dans le cas de la DMDBTDMA, cette région plus épaisse (environ trois à quatre fois la longueur du ligand) crée une région interfaciale où les molécules d'huile et d'eau peuvent se mélanger ainsi que les sels (Figure 5.3). Le système DM-

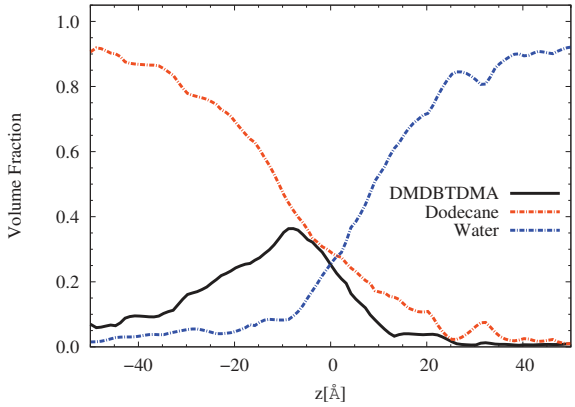

(a) Eau, dodécane, DMDBTDMA

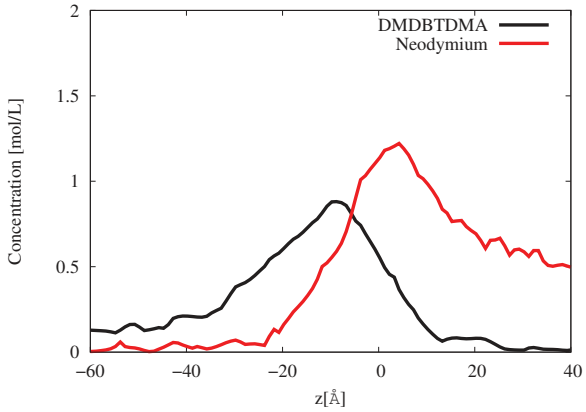

(b) DMDBTDMA et néodyme

Figure 5.3: Exemples de profiles de concentration de différentes espèces de part et d'autre de l'interface liquide/liquide déterminés à partir de l'analyse de courbe de réflectivité neutrons et X pour (a) l'eau/dodécane et l'extractant DMDBTDMA pour une concentration de 0.1 M en présence (b) d'ion néodyme pour 2 M en nitrate de lithium.

DOHEMA, présente quant à lui une structuration différente avec également une

couche de ligand mais plus compact (environ un à deux fois la longueur du ligand) mais située plus à l'intérieur de la phase huileuse et distinct de la distribution des sels à l'interface (Figure 5.4). Ces différentes structures interfaciales de DMDBT-

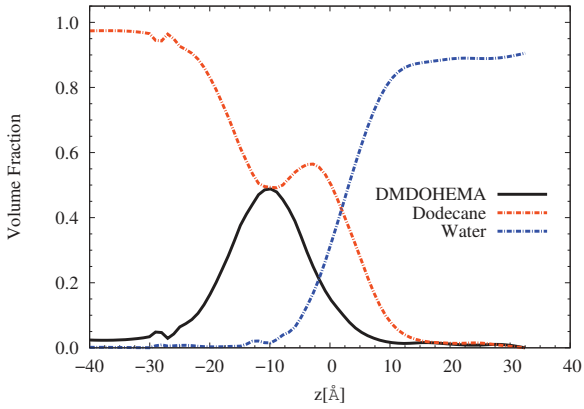

(a) Eau, dodécane, DMDOHEMA

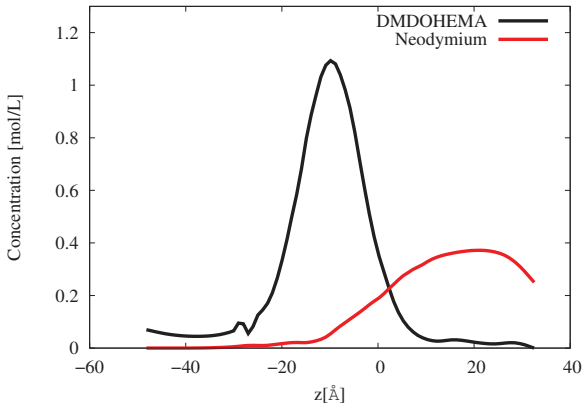

(b) DMDOHEMA et néodyme

Figure 5.4: Exemples de profiles de concentration de différentes espèces de part et d'autre de l'interface liquide/liquide déterminés à partir de l'analyse de courbe de réflectivité neutrons et X pour (a) l'eau/dodécane et l'extractant DMDOHEMA pour une concentration de 0.07M en présence (b) d'ion néodyme pour 2 M en nitrate de lithium.

DMA et DMDOHEMA peuvent permettre d'expliquer les différents régimes de transfert ionique qualifiés soit de diffusionnel ou de cinétique. Ce dernier sans la présence des sels se comporte comme un tensioactif en formant une monocouche à l'interface. Dans ce cas simple une intégration du profil de distribution des es-

pèces à l'interface permet de recalculer la tension de surface en adéquation avec celle déterminée expérimentalement. Il est aussi montré en traitant les rapports de concentration extractant/espèces extraites (cations ou protons) que dans le cas du DMDBTDMA nous nous trouvons avec une interface qui peut être qualifiée d'interphase dont la composition est comparable à celle dans le bulk organique juste avant d'observer la transition vers la troisième phase alors que dans le cas du DMDOHEMA cette concentration n'est pas atteinte. Ceci peut expliquer pourquoi la barrière énergétique pour le système DMDOHEMA est plus élevée et il en découle une expérience à réaliser dans le futur en fonction de la température afin que cette composition et/ou distribution évolue vers une forme plus proche de celle du DMDBTDMA lorsque la température croit (Figure 5.5).

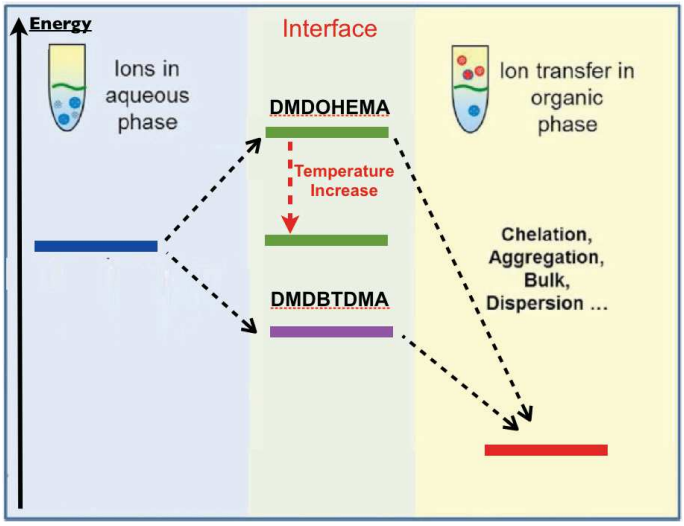

Figure 5.5: Schéma des potentiels chimiques pour les deux type de diamide de part et d'autre de l'interface et à l'interface.

Conclusion

En conclusion, il est possible de donner un schéma représentatif des interfaces complexes dans ces deux systèmes biphasiques en fonction de la composition des phases en contacts. Dans le cas du DMDBTDMA à l'interface eau/dodécane à des concentrations proches de la CAC et une phase aqueuse de faible activité, on observe une surconcentration de l'espèce extractante sur une épaisseur bien supérieure à la longueur moléculaire, comme représenté sur la Figure 5.6. L'interface apparait

dans ce cas comme une interphase riche en extractants qui suggère un transfert facilité du cation extrait de la phase aqueuse vers la phase organique, toutes les conformations et configurations de l'extractant pouvant une complexation du ou des ligants autour du cation partiellement déshydraté. Dans le cas du DMDOHEMA,

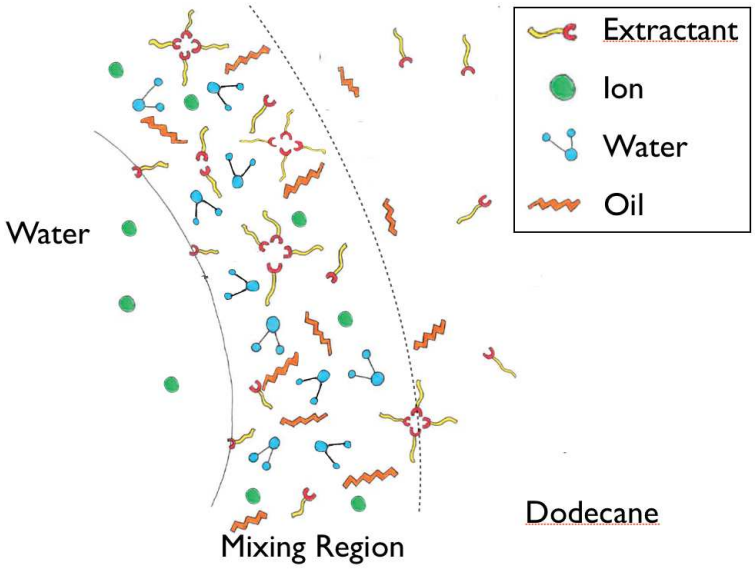

Figure 5.6: Schéma de l'interface eau/dodecane en presence de DMDBTDMA.

cet extractant a un comportant beaucoup plus tensioactif avec une condensation plus marquée à l'interface créant certainement une barrière énergétique au transfert possible d'un cation. Deux types de représentation de l'interface en fonction de la phase aqueuse sont donnés en Figure 5.7 et 5.8. Ces représentations sont en adéquation avec les comportements de transfert d'ions analysés par d'autres équipes de recherche.

Les objectifs de la thèse ont été atteints et permettent de lancer en grands nombre d'autres expériences pour finir de valider l'approche pour sonder ce type d'interfaces enfouies par cette technique de réflectivité. Il était cependant prévu de réaliser des études de cinétique à réaliser mais celles-ci demande encore réflexion pour optimiser la statistique des données. L'alignement des cellules reste une étape cruciale à l'acquisition de données valides et requiert une expertise fine. Le couplage avec d'autres techniques en simultanée demeure une voie à privilégier pour diminuer le nombre de variables dans le système et valider totalement cette approche.

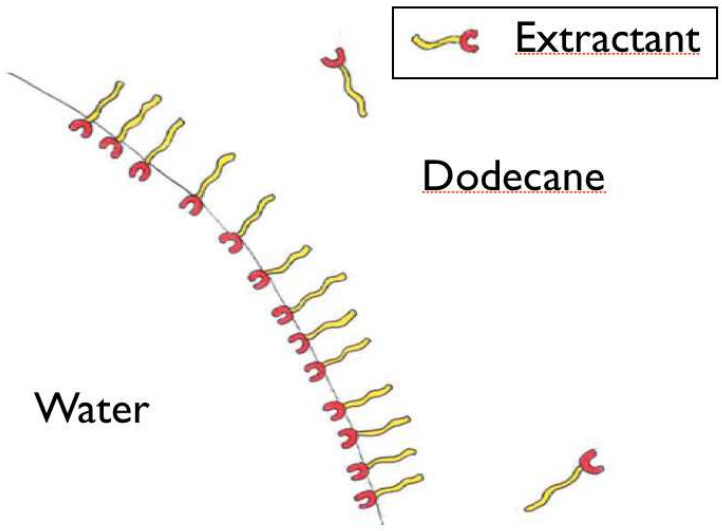

Figure 5.7: Schéma de l'interface eau (avec ou sans acide nitric)/dodecane en presence de DMDOHEMA.

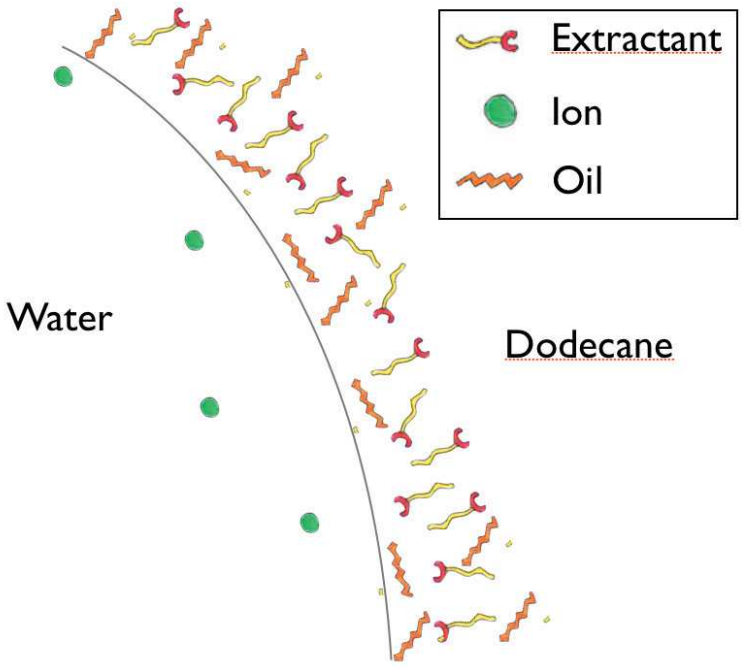

Figure 5.8: Schéma de l'interface eau (avec sel de lanthanide)/dodecane en presence de DMDOHEMA.

Bibliography

[1] G. T. Seaborg, *Our Heritage of the Elements*, Metallurgical Transactions B, 1980, **11B**, 5.

[2] K. Binnemans, P. T. Jones, B. Blanpain, T. Van Gerven, Y. Yang, A. Walton and M. Buchert, *Recycling of rare earths: a critical review*, Journal of Cleaner Production, 2013, **51**, 1.

[3] S. E. Kentish and G. W. Stevens, *Innovations in Separations Technology for the Recycling and Re-Use of Liquid Waste Streams*, Chemical Engineering Journal, 2001, **81**, 149.

[4] H. Shen and E. Forssberg, *An Overview of Recovery of Metals From Slags*, Waste Management, 2003, **23**, 933.

[5] V. Camel, *Extraction Techniques*, Analytical and Bioanalytical Chemistry, 2002, **372**, 39.

[6] F. M. Doyle, *Ion Flotation-Its Potential for Hydrometallurgical Operations*, International Journal of Mineral Processing, 2003, **72**, 387.

[7] M. G. Freire, C. M. S. S. Neves, P. J. Carvalho, R. L. Gardas, A. M. Fernandes, I. M. Marrucho, L. M. N. B. F. Santos and J. A. P. Coutinho, *Mutual Solubilities of Water and Hydrophobic Ionic Liquids*, The Journal of Physical Chemistry B, 2007, **111**, 13082.

[8] J. P. Lamas, L. Sanchez-Prado, C. Garcia-Jares, M. Lores and M. Llompart, *Development of a solid phase dispersion-pressurized liquid extraction method for the analysis of suspected fragrance allergens in leave-on cosmetics*, Journal of Chromatography A, 2010, **1217**, 8087.

[9] F. Valenzuela, C. Fonseca, C. Basualto, O. Correa, C. Tapia and J Sapag, *Removal of Copper Ions From a Waste Mine Water by a Liquid Emulsion Membrane Method*, Minerals Engineering, 2005, **18**, 33.

[10] S. Vitolo, L. Petarca and B. Bresci, *Treatment of Olive Oil Industry Wastes*, Bioresource Technology, 1999, **67**, 129.

[11] J. Rydberg, M. Cox, C. Musikas and G. R. Choppin, *Solvent extraction principles and practice*, Marcel Dekker, New York, 2004.

[12] W. J. Albery, J. F. Burke, E. B. Leffler and J. Hadgraft, *Interfacial Transfer Studied with a Rotating Diffusion Cell*, Journal of the Chemical Society, 1976, **72**, 1618.

[13] J. P. Simonin, L. Perrigaud, K. Perrigaud and T. H. Vu, *Kinetics of Liquid/Liquid Extraction of Europium(III) Cation by Two Malonic Diamides*, Solvent Extraction and Ion Exchange, 2014, **32**, 365.

[14] S. Schöttl, J. Marcus, O. Diat, D. Touraud, W. Kunz, T. Zemb and D. Horinek, *Emergence of Surfactant-Free Micelles From Ternary Solutions*, Chemical Science, 2014, **5**, 2949.

[15] W. Bu, H. Yu, G. Luo, M. K. Bera, B. Hou, A. W. Schuman, B. Lin, M. Meron, I. Kuzmenko, M. R. Antonio, L. Soderholm and M. L. Schlossman, *Observation of a Rare Earth Ion-Extractant Complex Arrested at the Oil-Water Interface During Solvent Extraction*, The Journal of Physical Chemistry B, 2014, **118**, 10662.

[16] W. Bu, M. Mihaylov, D. Amoanu, B. Lin, M. Meron, I. Kuzmenko, L. Soderholm and M. L. Schlossman, *X-Ray Studies of Interfacial Strontium–Extractant Complexes in a Model Solvent Extraction System*, The Journal of Physical Chemistry B, 2014, **118**, 12486.

[17] J. Daillant and A. Gibaud, *X-ray and Neutron Reflectivity, Principles and Applications*, Springer, 2009.

[18] J. S. Pedersen and I. W. Hamley, *Analysis of Neutron and X-Ray Reflectivity Data. II. Constrained Least-Squares Methods*, Journal of Applied Crystallography, 1994, **27**, 36.

[19] J. R. Lu and R. K. Thomas, *Neutron Reflection From Wet Interfaces*, Journal of the Chemical Society, Faraday Transactions, 1998, **94**, 995.

[20] R. Campbell, H. P. Wacklin, I. Sutton, R. Cubitt and G. Fragneto, *FIGARO: the New Horizontal Neutron Reflectometer at the ILL*, The European Physical Journal Plus, 2011, **126**, 107.

[21] G. Luo, S. Malkova, J. Yoon, D. G. Schultz, B. Lin, M. Meron, I. Benjamin, P. Vanýsek and M. L. Schlossman, *Ion Distributions Near a Liquid-Liquid Interface*, Science, 2006, **311**, 216.

[22] M. L. Schlossman, *Liquid–Liquid Interfaces: Studied by X-Ray and Neutron Scattering*, Current Opinion in Colloid & Interface Science, 2002, **7**, 235.

[23] L. Brennan, and P. Owende, *Biofuels from mircoalgae - a review of technologies for production, processing and extraction of biofuels and co-products*, Renewable and Sustainable Energy Reviews, 2010, **14**, 557.

[24] J. P. Lamas, L. Sanchez-Prado, C. Garcia-Jares and M. Llompart, *Determination of fragrance allergens in indoor air by active sampling followed by ultrasound-assisted solvent extraction and gas chromatography-mass spectrometry*, Journal of Chromatography A, 2010, **1217**, 1882.

[25] G. Cote, *Extraction liquide-liquide - Définition du procédé - Réactifs industriels*, Technique de l'Ingénieur, 1998, J2762.

[26] L. Troxler, M. Baden, V. Böhmer and G. Wipff, *Complexation of M^{3+} Lanthanide Cations by Calix[4]arene-CMPO Ligands: A Molecular Dynamics Study in Methanol Solution and at a Water/Chloroform Interface*, Supramolecular Chemistry, 2000, **12**, 27.

[27] J. Vander Linden and R. F. De Ketelaere, Selective recuperation of copper by supported liquid membrane (SLM) extraction, Journal of Membrane Science, 1998, **139**, 125.

[28] W. Zheng, Z. Zhu and C. Y. Cheng, *A literature review of titanium metallurgical processes*, Hydrometallurgy, 2011, **3**, 177.

[29] C. K. Gupta and K. Nagaiyar, *Extractive Metallurgy of Rare Earths*, CRC Press, 2004.

[30] T. Zemb, C. Bauer, P. Bauduin, L. Belloni, C. Dèjugnat, O. Diat, V. Dubois, J. F. Dufrêche, S. Dourdain, M. Davail, C. Larpent, F. Testard, S. Pellet-Rostaing, *Recycling metals by controlled transfer of ionic species between complex fluids: en route to "ienaics"*, Colloid and Polymer Science, 2015, **293**, 1.

[31] K. Osseo-Asare, *Aggregation, reversed micelles and mircoemulsions in liquid-liquidextraction: the tri-n-butyl phosphate-diluent-water-electrolyte system*, Advances in Colloid and Interface Science, 1991, **37**, 123.

[32] S: Nave, C. Mandin, L. Martinet, L. Berthon, F. Testard, C. Madic and T. Zemb, *Supramolecular Organisation of Tri-N-Butyl Phosphate in Organic Diluent on Approaching Third Phase Transition*, Physical Chemistry Chemical Physics, 2004, **6**, 799.

[33] S. Cotton, *Lanthanide and Actinide Chemistry*, Wiley, 2006.

[34] F. Testard, L. Berthon and T. Zemb, *Liquid-Liquid extraction: and adsorption isotherm at divided interface?*, Comptes Rendus Chimie, 2007, **10**, 1034.

[35] P. R. Danesi and R. Chiariza, *The kinetics of metal solvent-extraction*, CRC Critical Reviews in Analytical Chemistry, 1980, **10**, 1.

[36] R. T. Bachmann, D. Wiemken, A. B. Tengkiat, and M. Wilichowski, *Feasibility study on the recovery of hexavalent chromium from a simulated electroplating effluent using Alamine 336 and refined palm oil*, Separation and Purification Technology, 2010, **75**, 303.

[37] J. R. Kumar, J. S. Kim, J. Y. Lee and H. S. Yoon, *Solvent extraction of uranium(VI) and separation of vanadium(V) from sulfate solutions using Alamine 336*, Journal of Radioanalytical and Nuclear Chemistry, 2010 **285**, 301.

[38] K. R. Barnard, N. L. Turner and D. W. Shiers, *LIX®63 stability in the presence of Versatic 10 under proposed commercial extract and strip conditions, part III: Effect of manganese and cobalt loading on oxime stability at 30 °C*, Hydrometallurgy, 2010, **104**, 268.

[39] S. N. Kalmykov and M. A. Denecke, *Actinide Nanoparticle Research*, Springer, 2011.

[40] C. Déjugnat, S. Dourdain, V. Dubois, L. Berthon, S. Pellet-Rostaing, J. F. Dufrêche and T. Zemb, *Reverse Aggregate Nucleation Induced by Acids in Liquid–Liquid Extraction Processes*, Physical Chemistry Chemical Physics, 2014, **16**, 7339.

[41] H. F. Eicke and H. Christen, *Nucleation process of micelle formation in apolar solvents*, Journal of Colloid and Interface Science,1974, **48**, 281.

[42] H. F. Eicke and H. Christen, *Stability of micelles in apolar media*, Journal of Colloid and Interface Science, 1974, **46**, 417.

[43] H. F. Eicke, *Structure and properties of surfactant associates in apolar solvents due to hydrophile-lipophile balance*, Chimia, 1975, **29**, 176.

[44] H. F. Eicke and H. Christen, *Is water critical to formation of micelles in apolar media*, Helvetica Chimica Acta, 1978, **61**, 2258.

[45] H. F. Eicke and A. Denss, *Definition of a micelle revisited*, Journal of Colloid and Interface Science, 1978, **64**, 386.

[46] H. F. Eicke, *Surfactants in nonpolar solvents, aggregation and micellization*, Micelles, 1980, **87**, 85.

[47] G. Martin-Gassin, P. M. Gassin, L. Couston, O. Diat, E. Benichou and P. F. Brevet, *Nitric acid extraction with monoamide and diamide monitored by second harmonic generation at the water/dodecane interface*, Colloids and Surfaces a: Physicochemical and Engineering Aspects, 2012, **413**, 130.

[48] G. Martin-Gassin, P. M. Gassin, L. Couston, O. Diat, E. Benichou and P. F. Brevet, *Second Harmonic Generation Monitoring of Nitric Acid Extraction by a Monoamide at the Water–Dodecane Interface*, Physical Chemistry Chemical Physics, 2011, **13**, 19580.

[49] D. G. A. L. Aarts, M. Schmidt and H. N. W. Lekkerkerker, *Direct Visual Observation of Thermal Capillary Waves*, Science, 2004, **304**, 847.

[50] A. Berduque, A. Sherburn, M. Ghita, R. A. W. Dryfe and D. W. M. Arrigan, *Electrochemically Modulated LiquidLiquid Extraction of Ions*, Analytical Chemistry, 2005, **77**, 7310.

[51] M. M. Knock, G. R. Bell, E. K. Hill, H. J. Turner and C. D. Bain, *Sum-Frequency Spectroscopy of Surfactant Monolayers at the OilWater Interface*, The Journal of Physical Chemistry B, 2003, **107**, 10801.

[52] F. Reymond, D. Fermın, H. J. Lee and H. H. Girault, *Electrochemistry at Liquid/Liquid Interfaces: Methodology and Potential Applications*, Electrochimica Acta, 2000, **45**, 2647.

[53] Z. Samec, E. Samcová, H. H. Girault, *Ion Amperometry at the Interface Between Two Immiscible Electrolyte Solutions in View of Realizing the Amperometric Ion-Selective Electrode*, Talanta, 2004, **63**, 21.

[54] L. J. Sanchez Vallejo, J. M. Ovejero, R. A. Fernández and S. A. Dassie, *Simple Ion Transfer at Liquid/Liquid Interfaces*, International Journal of Electrochemistry, 2012, 1.

[55] S. Ulmeanu, H. J. Lee, D. J. Fermin, H. H. Girault and Y. Shao, *Voltammetry at a Liquid–Liquid Interface Supported on a Metallic Electrode*, Electrochemistry, 2001,**3**, 219.

[56] P. Vanýsek, *Charge Transfer Processes on Liquid/Liquid Interfaces: the First Century*, Electrochimica Acta, 1995, **40**, 2841.

[57] R. Taylor, *Reprocessing and Recycling of Spent Nuclear Fuel*, Woodhead Publishing Series in Energy, 2015.

[58] V. Vanel, L. Berthon, J. Muller, M, Miguirditchain and F. Burdet, *Modelling of americium stripping in the EXAm process*, Procedia Chemistry, 2012, **7**, 404.

[59] J. Chen, S. Wang, C. Xu and X. Feng, *Separation of Americium from Lanthanides by Purified Cyanex 301 Contercurrent Extraction in Miniature Centrifugarl Contactors*, Procedia Chemistry, 2012, **7**, 172.

[60] M. Weigl, A. Geist, K. Gompper and J.I. Kim, *Kinetics of Lanthanide/Actinide Co-Extraction with N,N′-Dimethyl-N,N′-Dibutyltetradecylmalonic Diamide (DMDBTDMA)*, Solvent Extraction and Ion Exchange, 2001, **19**, 215.

[61] L. Martinet, *Organisation Supramoléculaire des phases organiques de malonamides du procédd́ d'extraction diamex*, Rapport CEA-R-6105, 2006.

[62] Y. Meridiano, *Organisation des molécules extractantes de type diamide: lien avec les propriétés extractantes?*, Ph.D. Thesis, 2009.

[63] L. Boslan, *Études Thermodinamique et Cinétique de l'extraction des nitrates e lanthanides par un malonamide (N,N diméthyl-N,N dioctyl hexyléthoxy malonamide ou DMDOHEMA)*, Rapport CEA-R-6099, 2006.

[64] O. Tsydenova and M. Bengtsson, *Chemical hazards associated with treatment of waste electrical and elctronic equipment*, Waste Management, 2011, **31**, 45.

[65] R. Poirot, D. Bourgeois and D. Meyer, *Palladium Extraction by a Malonamide Derivative (DMDOHEMA) from Nitrate Media: Extraction Behaviour and Third Phase Characterization*, Solvent Extraction and Ion Exchange, 2014, **32**, 529.

[66] L. Berthon, F. Testard, L. Martinet, T. Zemb and C. Madic, *Influence of the extracted solute on the aggregation of malonamide extractant in organic phases: Consequences for phase stability*, Comptes Rendus Chimie, 2010, **13**, 1326.

[67] P. Bauduin, F. Testard, L. Berthon and T. Zemb, *Relation Between the Hydrophile/Hydrophobe Ratio of Malonamide Extractants and the Stability of the Organic Phase: Investigation at High Extractant Concentrations*, Physical Chemistry Chemical Physics, 2007, **9**, 3776.

[68] C. Bauer, P Bauduin, J. F. Dufêche, T. Zemb and O Diat, *Liquid/Liquid Metal Extraction: Phase Diagram Topology Resulting From Molecular Interactions Between Extractant, Ion, Oil and Water*, The European Physical Journal Special Topics, 2012, **213**, 225.

[69] L. Berthon, L. Martinet, F. Testard, C. Madic and T. Zemb, *Solvent Penetration and Sterical Stabilization of Reverse Aggregates Based on the DIAMEX Process Extracting Molecules: Consequences for the Third Phase Formation*, Solvent Extraction and Ion Exchange, 2007, **25**, 545.

[70] R. Schurhammer and G. Wipff, *Liquid-Liquid Extraction of Pertechnetic Acid (Tc^{VII}) by Tri-n-butyl Phophate: Where is the Proton? A Molecular Dynamics Investigation*, The Hournal of Pysical Chemistry B, 2011, **115**, 2338.

[71] G. Benay and G. Wipff, *Liquid-Liquid Extraction of Uranyl by TBP: The TBP and Ions Models and Related Interfacial Features Revisited by MD and PMF Simulations*, The Journal of Physical Chemistry B, 2014, **118**, 3133.

[72] C. Gaillard, V. Mazan, S. Georg, O. Klimchuk, M. Sypua, I. Billard, R. Schurhammer and G. Wipff, Acid extraction to a hydrophobic ionic liquid: the role of added tributylphosphate investigated by experiments and simulations, Physical Chemistry Chemical Physics, 2012, **14**, 5187.

[73] D. M. Mitrinović, Z. Zhang, S. M. Williams, Z. Huang and M. L. Schlossman, *X-Ray Reflectivity Study of the WaterHexane Interface*, The Journal of Physical Chemistry B, 1999, **103**, 1779.

[74] N. H. Sagert, W. Lee and M. J. Quinn, *The Adsorption of Tri-N-Butylphosphate at the N-Dodecane-Water Interface*, Canadian Journal of Chemistry, 1979, **57**, 1218.

[75] P. M. Gassin, G. Martin-Gassin, D. Meyer, J. F. Dufrêche and O. Diat, *Kinetics of Triton-X100 Transfer Across the Water/Dodecane Interface: Analysis of the Interfacial Tension Variation*, The Journal of Physical Chemistry C, 2012, **116**, 13152.

[76] J. W. Benjamins, B. Jönsson, K. Thuresson and T. Nylander, *New Experimental Setup To Use Ellipsometry To Study Liquid-Liquid and Liquid-Solid Interfaces*, Langmuir, 2002, **18**, 6437.

[77] L. T. Lee, D. Langevin and B. Farnoux, *Neutron Reflectivity of an Oil-Water Interface*, Physical Review Letters, 1991, **67**, 2678.

[78] E. Dickinson, D. S. Horne, J. S. Phipps and R. M. Richardson, *A Neutron Reflectivity Study of the Adsorption of* $\beta -$ $CaseinatFluidInterfaces, Langmuir$, 1993, ***9***, 242.

[79] M. Campana, *Structural Study of Surfactant at Interfaces*, Ph.D. Thesis, 2012.

[80] A. Zarbakhsh, J. Bowers and J. R. P. Webster, *A New Approach for Measuring Neutron Reflection From a Liquid/Liquid Interface*, Measurement Science and Technology, 1999, **10**, 738.

[81] J. Bowers, A. Zarbakhsh, J. R. P. Webster, L. R. Hutchings and R. W. Richards, *Neutron Reflectivity Studies at Liquid-Liquid Interfaces: Methodology and Analysis*, Langmuir, 2001, **17**, 140.

[82] A. Zarbakhsh, J. R. P. Webster and J. Eames, *Structural Studies of Surfactants at the Oil-Water Interface by Neutron Reflectometery*, Langmuir, 2009, **25**, 3953.

[83] J. Strutwolf, A. L. Barker and M. Gonsalves, D. J. Caruana, P. R. Unwin, D. E. Williams and J. R.P. Webster, *Probing Liquid-Liquid Interfaces Using Neutron Reflection Measurements and Scanning Electrochemical Microscopy*, Journal of Electroanalytical Chemistry, 2000, **483**, 163.

[84] B. Abécassis, F. Testard, T. Zemb, L. Berthon and C Madic, *Effect of n-Octanol on the Structure at the Supramolecular Scale of Concentrated Dimethyldioctylhexylethoxymalonamide Extractant Solutions*, Langmuir, 2003, **19**, 6638.

[85] J. Causse, J. Oberdisse, J. Jestin and S. Lagerge, *Small-Angle Neutron Scattering Study of Solubilization of Tributyl Phosphate in Aqueous Solutions of L64 Pluronic Triblock Copolymers*, Langmuir, 2010, **26**, 15745.

[86] K. M. Zimmermann, *Advanced analysis techniques for x-ray reflectivities: Theory and application*, Ph.D. Thesis, 2005.

[87] J. Kraus, P. Müller-Buschbaum, T. Kuhlmann, D. W. Schubert and M. Stamm, *Confinement effects on the chain conformation in thin polymer films*, Europhysics Letters, 1999, **49**, 210.

[88] F. Abelès, *La théorie générale des couches minces*, Le Journal de Physiqye et le Radium, **11**, 1950, 307.

[89] L. G. Parratt, *Surface Studies of Solids by Total Reflection of X-Rays*, Physical Revies, 1954, **95**, 359.

[90] M. Tolan, *X-Ray Scattering from Soft-Matter Thin Films*, Springer Tracts in Modern Physics, 1999, **48**.

[91] J. B. Hayter and H. A. Mook, *Discrete Thin-Film Multilayer Design for X-ray and Neutron Supermirrors*, Journal of Applied Crystallography, 1989, **22**, 35.

[92] A. J. Dianoux, G. Lander, *Neutron Data Booklet*, Old City Publishing, 2003.

[93] A. Nelson, *Co-Refinement of Multiple-Contrast Neutron/X-Ray Reflectivity Data Using MOTOFIT*, Journal of Applied Crystallography, 2006, **39**, 273.

[94] D. M. Smilgies, B. Boudet, B. Struth and O. Konovalov, *Troika II: a versatile beamline for the study of liquid and solid interfaces*, Journal of Synchrotron Radiation, 2006, **12**, 329.

[95] A. Goebel and K. Lunkenheimer, *Interfacial Tension of the Water/n-Alkane Interface*, Langmuir, 1997, **13**, 369.

[96] Applet from NIST Center for Neutron Research website, *https://www.ncnr.nist.gov/resources/activation/*.

[97] A. G. Volkov and P. F. Brevet, *Liquid interfaces in chemical, biological, and pharmaceutical applications*, 2001

[98] G. Ferru, D. G. Rodrigues, L. Berthon, O. Diat, P. Bauduin and P. Guilbaud, *Elucidation of the Structure of Organic Solutions in Solvent Extraction by Combining Molecular Dynamics and X-Ray Scattering*, Angewandte Chemie International Edition, 2014, **53**, 5346.

[99] R. G. Snyder, V. J. P. Srivatsavoy, D. A. Cates, H. L. Strauss, J. W. White, D. L. Dorset, *Hydrogen/Deuterium Isotope Effects on Microphase Separation in Unstable Crystalline Mixtures of Binary n-Alkanes*, Journal of Physical Chemistry, 1994, **98**, 674.

[100] *Nuclear Wastes: Technologies for Separations and Transmutation*, National Academy Press Washington D.C., 1996.

[101] K. Bella, A. Geist, F. McLachlan, G. Modolo, R. Taylor, A. Wilden, *Nitric acid extraction into TODGA*, Procedia Chemistry, 2012, **7**, 152.

[102] J. Muller, L. Berthon, N. Zorz and J. P. Simonin, *Characterization of Lanthanide and Actinide Complexes in the DIAMEX-SANEX Process*, Proceedings of the First ACSEPT International Workshop, 2010.

[103] J. Meunier, *Optical Reflectivity of Thin Rough Films: Application to Ellipsometric Measurements on Liquid Films*, Physical Review E, 2007, **75**, 061601.

[104] T. Kasahara, N. Nishi, M. Yamamoto and T. Kakiuchi, *Electrochemical Instability in the Transfer of Cationic Surfactant Across the 1,2-Dichloroethane/Water Interface*, Langmuir 20 (3): 875–81.

[105] E. Schneck and B. Demé, *Structural characterization of soft interfaces by standing-wave fluorescence with X-rays and neutrons*, Current Opinion in Colloid & Interface Science, 2015. (In Press)

[106] M. C. Dul, D. Bourgeois, J. Maynadié and D. Meyer, *Synthesis of fluorinated malonamides and use in L/L extraction of f-elements*, Tetrahedron Letters,2013, **54**, 6271.

[107] S. Massari and M. Ruberti, *Rare earth elements as critical raw materials: Focus on international markets and future strategies*, Resources Policy, 2013, **38**, 36–43.

[108] L. Jinxia, M. Hong, X. Yin and J. Liu, *Effects of the Accumulation of the Rare Earth Elements on Soil Macrofauna Community*, Journal of Rare Earths, 2010, **28**, 957.

[109] A. M. Tikhonov, M. Li and M. L. Schlossman, *X-Ray Scattering From N-Alcohol Monolayers at the Water-Hexane Interface*, NSLS Activity Report, 2001.

[110] A. Zarbakhsh, J. R. P. Webster and K. Wojciechowski, *Neutron Reflectivity Study of Alkylated Azacrown Ether at the Air-Liquid and the Liquid-Liquid Interfaces*, Langmuir, 2009, **25**, 11569.

[111] A. Zarbakhsh, A. Querol, J. Bowers and J. R. P. Webster, *Structural Studies of Amphiphiles Adsorbed at Liquid-Liquid Interfaces Using Neutron Reflectometry*, Faraday Discussions, 2005, **129**, 155.

[112] L. Tamam, D. Pontoni, Z. Sapir, S. Yefet, E. Sloutskin, B. M. Ocko, H. Reichert and M. Deutsch, *Modification of Deeply Buried Hydrophobic Interfaces by Ionic Surfactants*, Proceedings of the National Academy of Sciences, 2011, **108**, 5522.

[113] S. V. Pingali, T. Takiue, G. Luo, A. M. Tikhonov, N. Ikeda, M. Aratono and M. L. Schlossman, *X-Ray Reflectivity and Interfacial Tension Study of the Structure and Phase Behavior of the Interface Between Water and Mixed Surfactant Solutions of $CH_3(CH_2)_{19}OH$ and $CF_3(CF_2)_7(CH_2)_2OH$ in Hexane*, The Journal of Physical Chemistry B, 2005, **109**, 1210.

[114] D. M. Mitrinović, S. Williams and M. L. Schlossman, *X-Ray Study of Oil-Microemulsion and Oil-Water Interfaces in Ternary Amphiphilic Systems*, Physical Review E, 2001, **63**, 021601.

6.1 Running Macro on ID10

In this section we report the macro used on ID10 beamline during our experiments on Liquid/Liquid interface.

6.1.1 Sample Alignment

```
airon xt
airshow
fixtable
setfilter 15
autof_setdetector('all2')

ratiosetup ratio mon detcorr
plotselect ratio

shopen
plotselect dir2
setplot 5251
autofoff

umv mu 0.0
umv gam 0.0
_sleep=5
```

```
dscan zgH -0.4 0.4 40 1
diff
invert
cen
undif
where

umv mu 0.04
umv gam 0.04

_sleep=5
dscan zgH -0.05 0.05 20 1
cen
autofon
shclose
```

6.1.2 Equilibration Time

```
airon xt
airshow
fixtable
setfilter 12
autof_setdetector('all2')
ratiosetup ratio mon detcorr
plotselect ratio

shopen
plotselect dir2
setplot 5251

autofoff

umv mu 0.12
umv gam 0.12
slepep(10)

setfilter 8
```

```
_sleep=10
while (1<2){timescan 1}

_sleep=5
setfilter 12

autofon
shclose
```

6.1.3 Recording Reflectivity

```
airon xt
fixtable
_sleep=5
setfilter 15
autof_setdetector('all2')
autofon
ratiosetup ratio mon detcorr
plotselect ratio
setplot 5283

shopen

#AIR-LIQUID
a2scan mu 0 0.2 gam 0 0.2 40 1
a2scan mu 0.2 1 gam 0.2 1 50 1
a2scan mu 0.2 1 gam 0.2 1 70 1
a2scan mu 1 1.4 gam 1 1.4 20 2

#LIQUID-LIQUID
a2scan mu 0.0 0.07 gam 0.0 0.07 35 2
a2scan mu 0.07 0.5 gam 0.07 0.5 40 2
a2scan mu 0.5 1.4 gam 0.5 1.4 25 5

shclose
umv gam 0 mu 0
setfilter 15
```

```
autof_setdetector('all2')
ratiosetup ratio mon detcorr
plotselect ratio
setfilter 12
shopen
plotselect dir2
setplot 5251

autofoff

umv mu 0.0
umv gam 0.0
_sleep=3
dscan zgH -0.4 -0.2 10 1
autofon
setfilter 15
shclose
```

6.2 High Flux Alignment on FIGARO

In this section we report settings for the alignment of samples on the FIGARO reflectometer (ILL). Due to the low counting rate for reflected beam from the liquid/liquid interface, we have optimized a procedure to focalized the beam at the interface.
This procedure requires to put masks on the detector to count only the neutron scattered in the pixel where we expect to measure the reflection peak. To increase the flux the choppers are dephased. In Figure 6.1 we report a screenshot with the NOMAD[1] settings for the sample alignment procedure.

[1]NOMAD is the software controlling FIGARO.

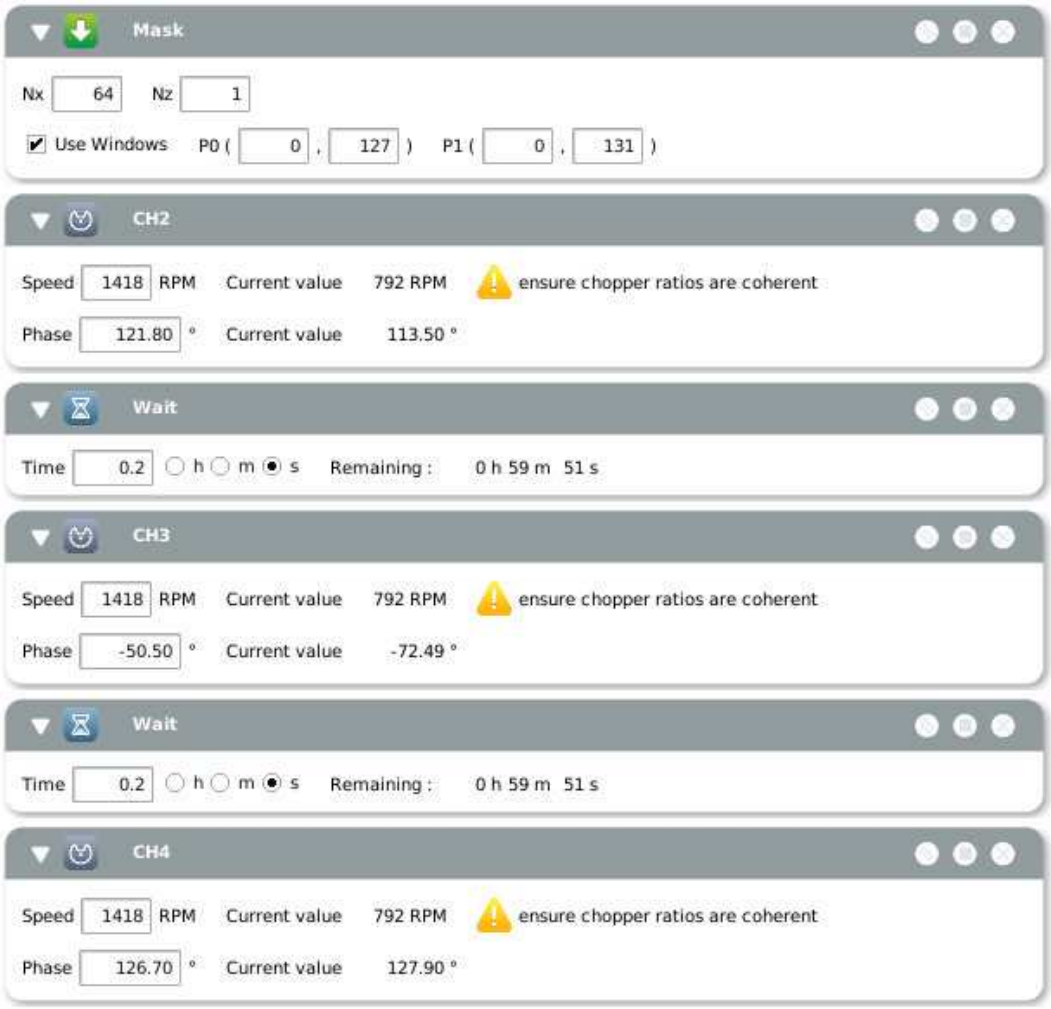

Figure 6.1: NOMAD screenshot of settings for the sample alignment procedure.

Reflectivity Plot and SLD Profiles

In this appendix we show different type of representation for reflectivity data both for x-rays and neutrons. We want to provide some support for reading the data presented in Chapter 4. For this purpose we present models obtained with Motofit software [93] for the buried dodecane/water interface with a without malonamide. In the specific case, we have considered the DMDBTDMA. For each type of interface we present x-ray and neutron reflectivity and SLD profile models,with different roughness value.
The reflectivity data are presented in both log(R) and log(RQ^4) *vs.* Q.

7.1 Oil/Water interface

A simple water/oil interface is presented here. Three reflectivity curves, both with x-rays and neutron, assuming roughness σ equal to 0, 4 and 8 Å are simulated here. In Tables 7.1 and 7.2 we report the parameters used to obtain the x-ray and neutron reflectivity curves in Figures 7.1 and 7.2.

Compound	**Thickness** [Å]	**SLD** [10^{-6} Å^{-2}]	**Roughness** [Å]
Dodecane	∞	7.30	
Water	∞	9.45	0 ; 4 ; 8

Table 7.1: Value of parameters used to calculate model x-ray reflectivity of curves in Figure 7.1. The first compound, dodecane, represents the phase crossed by x-rays. In the last column different roughness value are showed.

Compound	**Thickness** [Å]	**SLD** [10^{-6} Å^{-2}]	**Roughness** [Å]
Heavy Water	∞	6.35	
Dodecane	∞	4.0	0 ; 4 ; 8

Table 7.2: Value of parameters used to calculate model neutron reflectivity of curves in Figure 7.1. The first compound, heavy water, represents the phase crossed by neutrons. In the last column different roughness value are showed. For the organic phase we have assumed a mixtrure of $C_{12}H_{26}$/ $C_{12}D_{26}$ with an SLD= 4.00^{-6} Å^{-2}.

In Figures 7.1 and 7.2 we observe that an increase of roughness produces a large variation of the x-ray reflectivity, larger of the one obtained for neutron reflectivity. These variations are enhanced when $\log(RQ^4)$ *vs.* Q is plotted (panels (b) of the same figures). This effect is even more pronounced when $\log(RQ^4)$ *vs.* Q scale is chosen to represent the data.

In Figure 7.3 we observe that an increase of roughness produces a smoother SLD Profile.

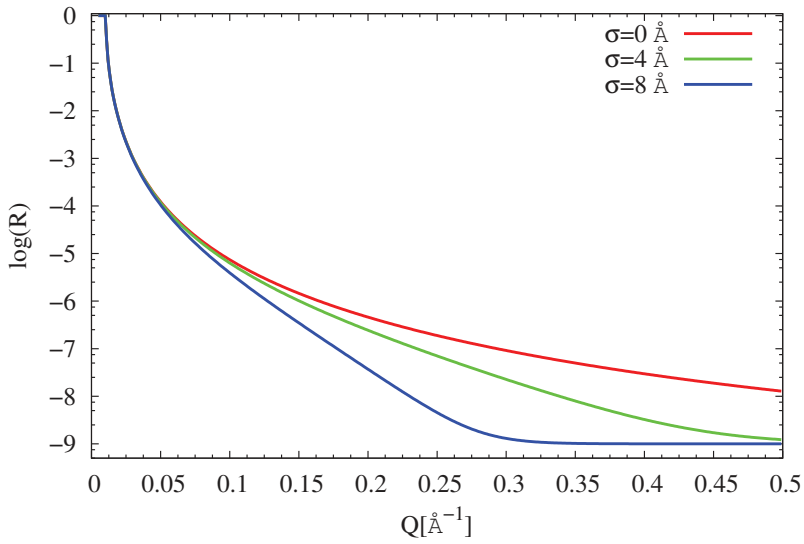

(a) log(R) *vs.* Q

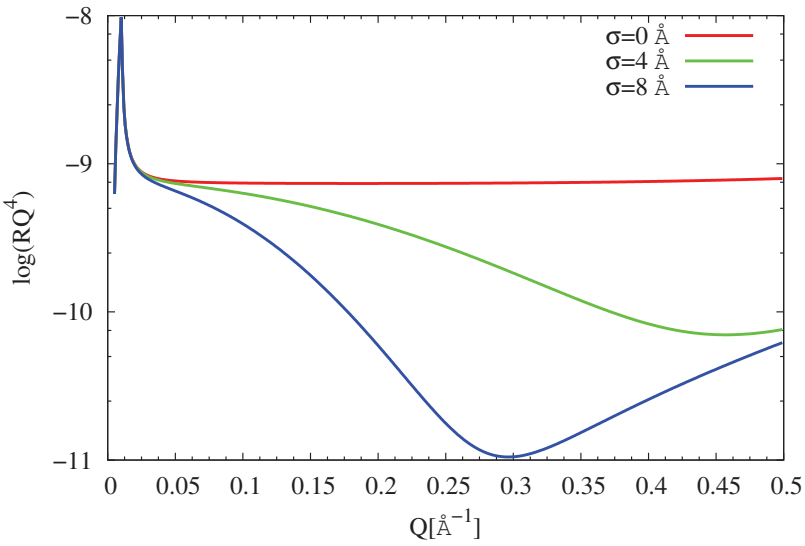

(b) log(RQ^4) *vs.* Q

Figure 7.1: X-ray reflectivity curves in (a) log(R) and (b) log(RQ^4) *vs.* Q calculated with values reported in Table 7.1. The reflectivity is calculated for different interfacial roughness values: (red) $\sigma = 0$ Å, (green) $\sigma = 4$ Åand (blue) $\sigma = 8$ Å.

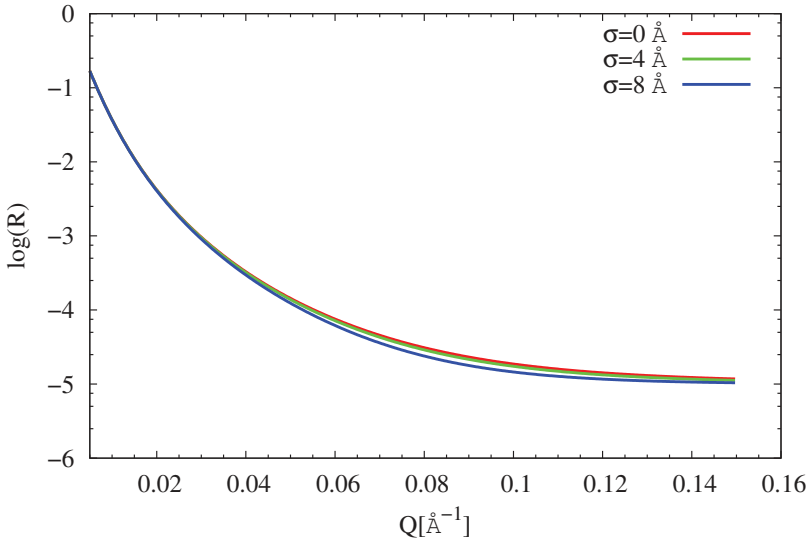

(a) log(R) *vs.* Q

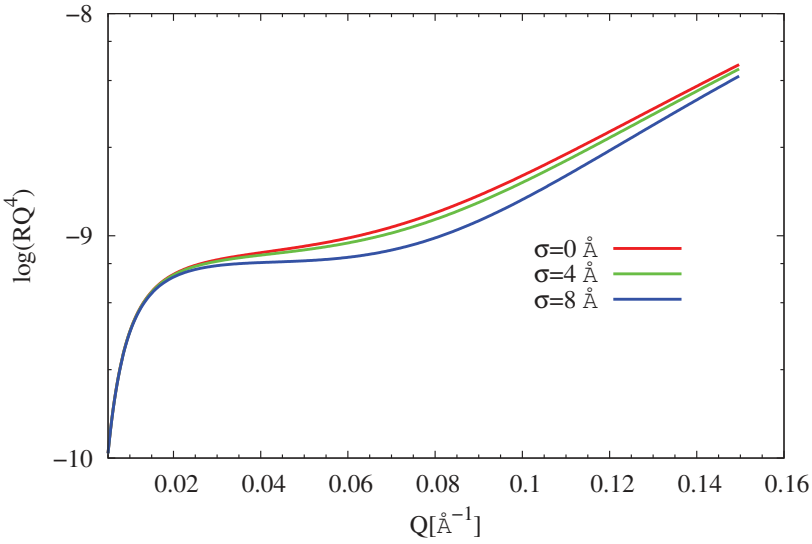

(b) log(RQ^4) *vs.* Q

Figure 7.2: Neutron reflectivity curves in (a) log(R) and (b) log(RQ^4) *vs.* Q calculated with values reported in Table 7.2. The reflectivity is calculated for different interfacial roughness values: (red) $\sigma = 0$ Å, (green) $\sigma = 4$ Åand (blue) $\sigma = 8$ Å.

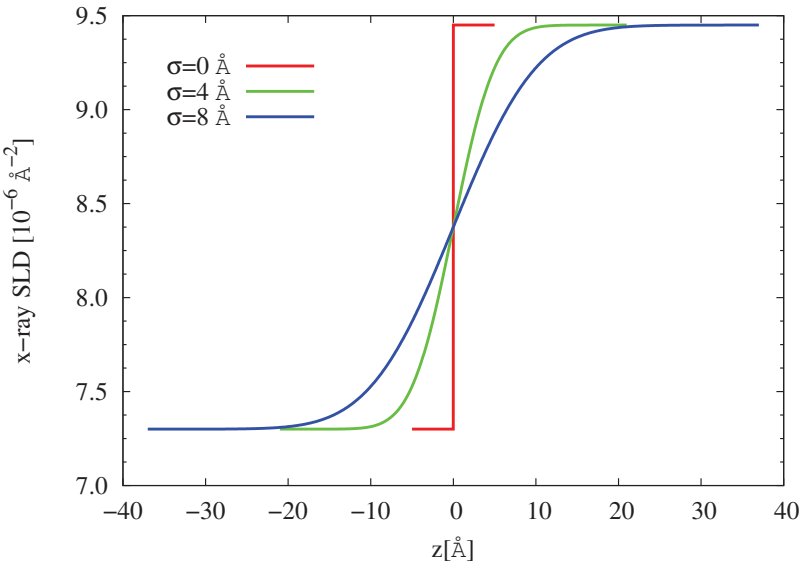

(a) X-ray

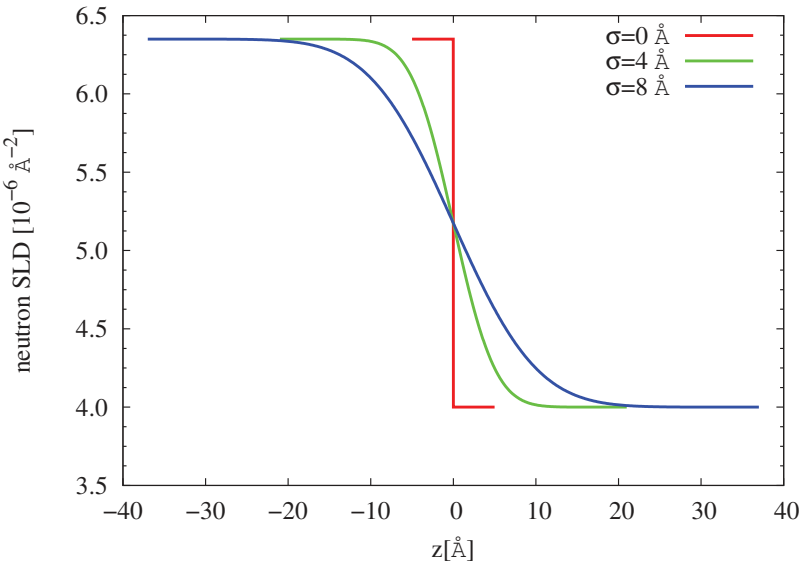

(b) Neutron

Figure 7.3: (a) X-ray and (b) neutron SLD Profiles obtained with parameters in Tables 7.1 and 7.2. The three SLD Profiles correspond to different interfacial roughness: (red) $\sigma = 0$ Å, (green) $\sigma = 4$ Åand (blue) $\sigma = 8$ Å. The liquid/liquid interface is placed at $z = 0$ Å (left side, (a) organic phase, (b) aqueous phase; right side, (a) aqueous phase, (b) organic phase).

7.2 Malonamide at Oil/Water interface

A simple water/oil interface with a DMDBTDMA layer 12 Å thick is presented here. Three reflectivity curves, both with x-rays and neutron, assuming different roughness are calculated. Differently from previous case where only one interface was considered, in the case presented here we have to consider two interfaces (water/diamide and diamide/dodecane) with two roughness, σ_1 and σ_2. Roughness equal to 0, 4 and 8 Å are considered here. In Tables 7.3 and 7.4 we report the parameters used to obtain the x-ray and neutron reflectivity curves in Figures 7.4 and 7.5.

Compound	**Thickness** [Å]	**SLD** [10^{-6} Å^{-2}]	**Roughness** [Å]
Dodecane	∞	7.30	
DMDBTDMA	12	8.64	0 ; 4 ; 8
Water	∞	9.45	0 ; 4 ; 8

Table 7.3: Value of parameters used to calculate model x-ray reflectivity of curves in Figure 7.4. The first compound, dodecane, represents the phase crossed by x-rays. In the last column different roughness value are showed.

Compound	**Thickness** [Å]	**SLD** [10^{-6} Å^{-2}]	**Roughness** [Å]
Heavy Water	∞	6.35	
DMDBTDMA	12	0.0979	0 ; 4 ; 8
Dodecane	∞	4.0	0 ; 4 ; 8

Table 7.4: Value of parameters used to calculate model neutron reflectivity of curves in Figure 7.4. The first compound, heavy water, represents the phase crossed by neutrons. In the last column different roughness value are showed. For the organic phase we have assumed a mixtrure of $C_{12}H_{26}$/ $C_{12}D_{26}$ with an SLD= 4.00^{-6} Å^{-2}.

In Figures 7.4 and 7.5 we observe that an increase of roughness produces a large variation of the x-ray reflectivity, larger of the one obtained for neutron reflectivity. These variations are enhanced when $\log(RQ^4)$ *vs.* Q is plotted (panels (b) of same figures).
It appears clear here that an increase of roughness can be the interpretation[1] for

[1]This interpretation has been highlighted many times in the Chapter 4

decreasing of reflected intensity *vs.* Q. The addition of a DMDBTDMA layer at the interface produces a minimum, less or more defined depending on the roughness, in the x-ray reflectivity curves.

In Figure 7.6a we observe that increasing the roughness $_1$ and σ_2 we pass from a step function to smoother profiles. In panel (b) of same figure, the presence of diamide, which is protonated, produces a deep in the SLD profiles. The deep becomes smoother and less pronounced when roughness increases. This effect can be explained with an interpenetration of layers. In fact, increasing the two roughness we are assuming that some oil and some water are penetrating in the diamide layer reducing the contrast between the two bulks and the interfacial layer.

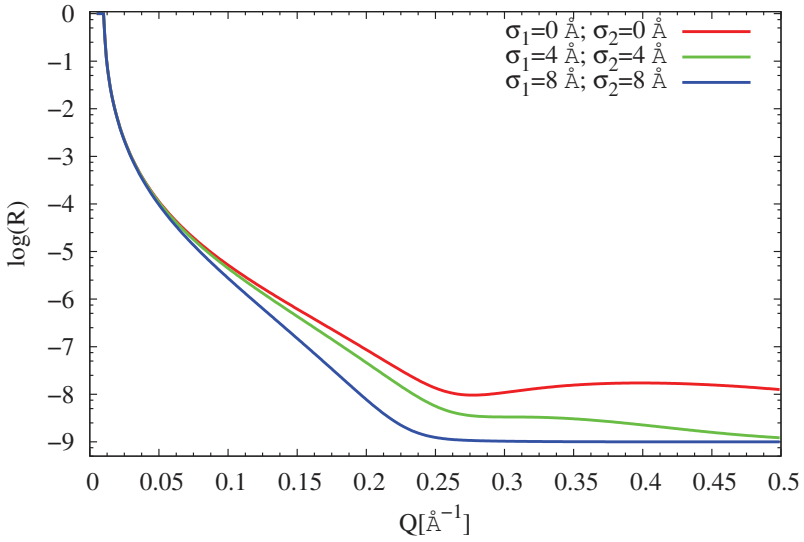

(a) log(R) *vs.* Q

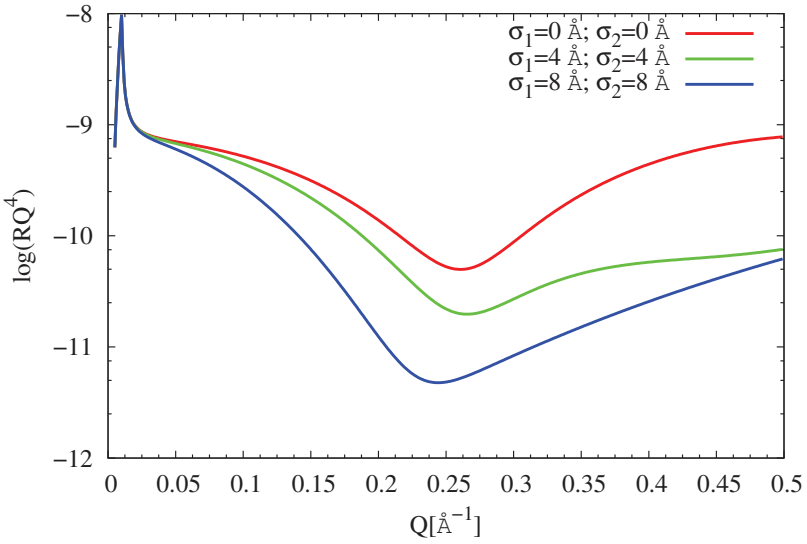

(b) log(RQ^4) *vs.* Q

Figure 7.4: X-ray reflectivity curves in (a) log(R) and (b) log(RQ^4) *vs.* Q calculated with values reported in Table 7.3. The reflectivity is calculated for different interfacial roughness values: (red) $\sigma_1 = 0$ Å, $\sigma_2 = 0$ Å, (green) $\sigma_1 = 4$ Å, $\sigma_2 = 4$ Åand (blue) $\sigma_1 = 8$ Å, $\sigma_2 = 8$ Å.

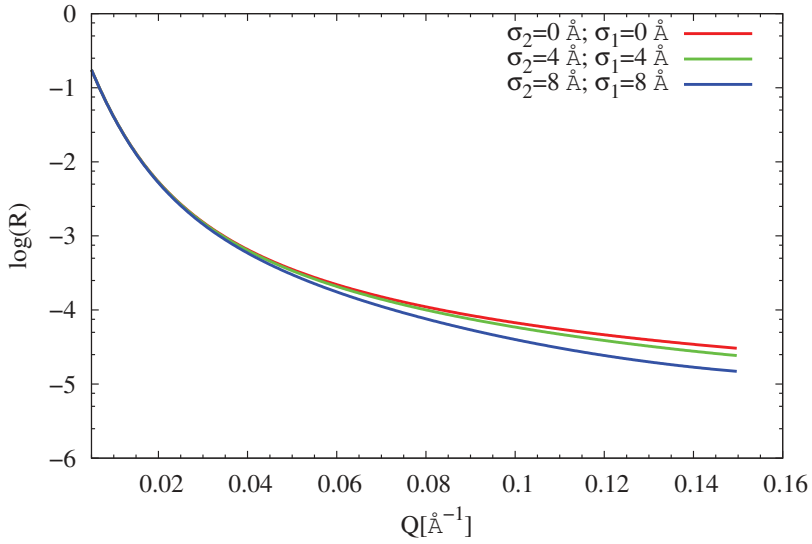

(a) log(R) *vs.* Q

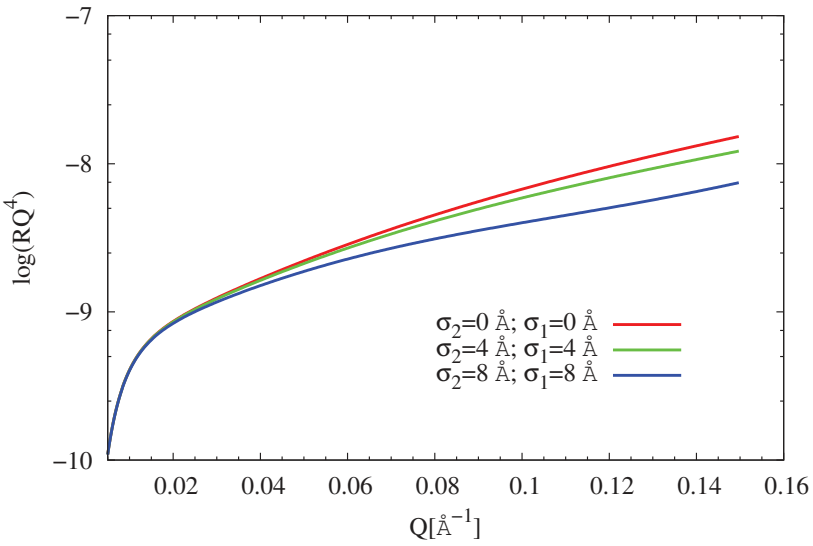

(b) log(RQ^4) *vs.* Q

Figure 7.5: Neutron reflectivity curves in (a) log(R) and (b) log(RQ^4) *vs.* Q calculated with values reported in Table 7.2. The reflectivity is calculated for different interfacial roughness values: (red) $\sigma_1 = 0$ Å, $\sigma_2 = 0$ Å, (green) $\sigma_1 = 4$ Å, $\sigma_2 = 4$ Å and (blue) $\sigma_1 = 8$ Å, $\sigma_2 = 8$ Å.

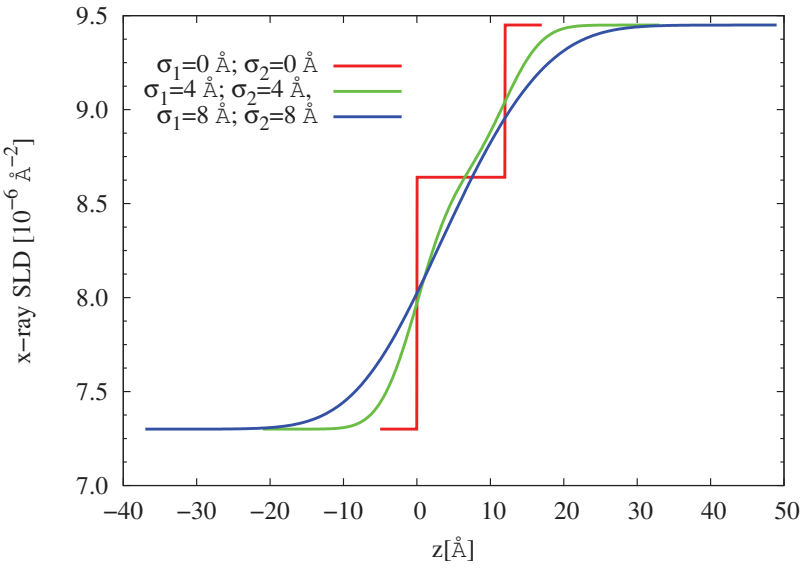

(a) X-ray

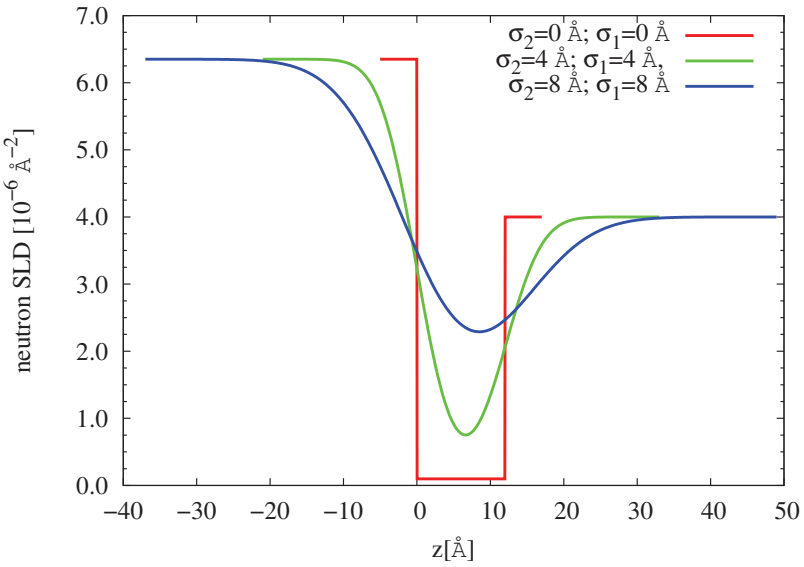

(b) Neutron

Figure 7.6: (a) X-ray and (b) neutron SLD Profiles obtained with parameters in Tables 7.1 and 7.2. The three SLD Profiles correspond to different interfacial roughness: (red) $\sigma_1 = 0$ Å, $\sigma_2 = 0$ Å, (green) $\sigma_1 = 4$ Å, $\sigma_2 = 4$ Åand (blue) $\sigma_1 = 8$ Å, $\sigma_2 = 8$ Å. The liquid/liquid interface is placed at $z = 0$ Å (left side, (a) organic phase, (b) aqueous phase; right side, (a) aqueous phase, (b) organic phase)

Roughness Analysis

In this appendix we report an example showing the convenience of using two layers instead of one for analyzing x-ray reflectivity data for the sample at 0.07 M of DMDBTDMA in dodecane contacted with an aqueous solution of lithium and neodymium nitrate. The purpose is to show that assuming a simple adsorption of diamide on one layer with a large roughness is not sufficient to fit the data.
In Table 8.1 we report the fitting parameters obtained with one layer model. Data, shown in Figure 8.1, have been fitted obtaining a roughness of 7 Å. Subsequently, to improve the fit, we have tried to increase the roughness obtaining a good match for the data at the highest Q for a roughness of 36 Å. However, the increase of roughness does not allow the fitting of points between 0.06 and 0.2 $Å^{-1}$.
In Table 8.2 we report the fitting parameters obtained with a two layers model. As shown in Figure 8.1 with these parameters we are able to obtain a good agreement between data and fit. The different SLD profiles corresponding to parameters reported in Tables 8.1 and 8.2 are plotted in Figure 8.2.

	Thickness [Å]	**SLD** [10^{-6} $Å^{-2}$]	**Roughness** [Å]
Organic Phase	∞	7.39	
$1^{st}layer$	21.1	11.4	6.3
Aqueous Phase	∞	10.6	7.0 ; 36.0

Table 8.1: Fitting parameters in the Motofit procedure for data adjustment plotted in Figure 8.1using a one layer model and varying the roughness.

	Thickness [Å]	**SLD** [10^{-6} Å^{-2}]	**Roughness** [Å]
Organic Phase	∞	7.39	
$1^{st}layer$	6.8	14.3	8.3
$2^{nd}layer$	33.1	10.9	7.9
Aqueous phase	∞	10.6	7.9

Table 8.2: Fitting parameters in the Motofit procedure for data adjustment plotted in Figure 8.1 using a two layers model.

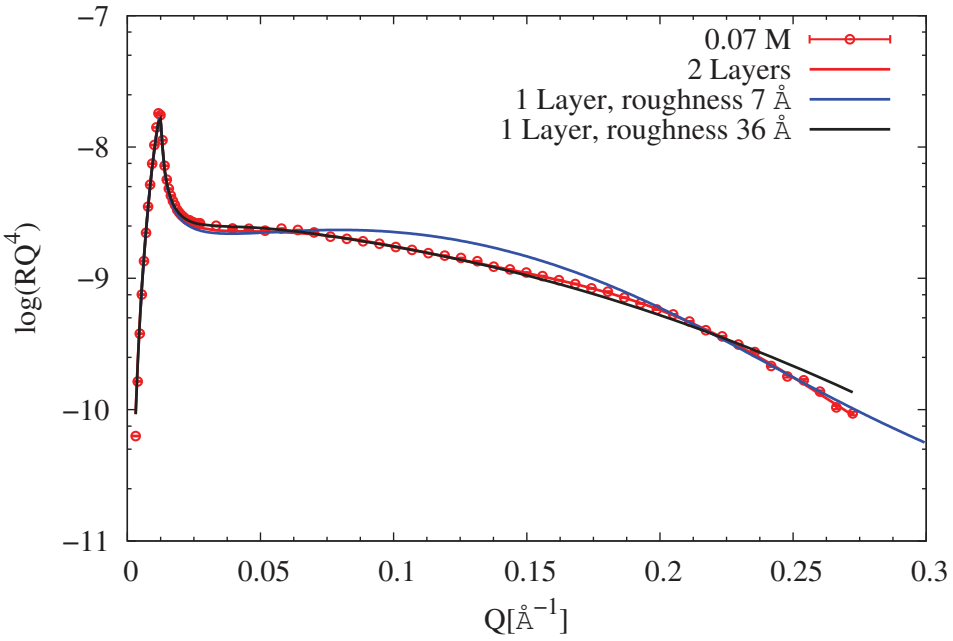

Figure 8.1: X-ray reflectivity data and fits in the log(RQ^4) vs Q representation for the 2 M $LiNO_3$, 0.25 M $Nd(NO_3)_3$ aqueous solution - dodecane interface in presence of 0.07 M DMDBTDMA with the fitting curve using a Parratt procedure. Data are plotted with circles with experimental error bars, fits with lines. Fit obtained with parameters reported in Table 8.1 with a roughness of (blue line) 7 Å and (black line) 36 Å. (Red line) Best fit obtained using a two layers model with parameters reported in Table 8.2.

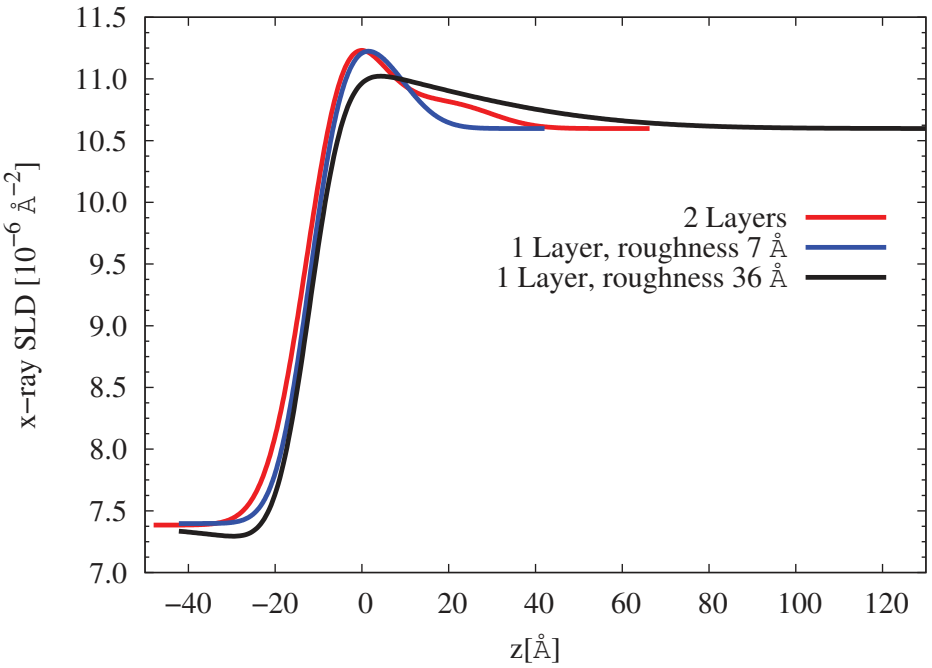

Figure 8.2: SLD profiles for the 2 M $LiNO_3$, 0.25 M $Nd(NO_3)_3$ aqueous solution - dodecane interface in presence of 0.07 M DMDBTDMA corresponding to the fits in Figure 8.1. SLD profiles obtained with parameters reported in Table 8.1 with a roughness of (blue line) 7 Å and (black line) 36 Å. (Red line) SLD profile obtained using a two layers model with parameters reported in Table 8.2. The liquid/liquid interface is placed at $z = 0$ Å (left side, organic phase; right side aqueous phase).

Supporting Material

In this appendix we report the results obtained during the data analysis process. For each sample and each species, the comparison between the results of the SLD Profile analysis and the Parratt Refinement is plot.
As shown in Section 2.2.5 the results of the SLD Profile analysis are plotted with 3D maps: on the x and y axes are reported the concentration and the z-depth respectively. The different colors represent different probability, going from 0% (black) to 100% (yellow).

9.1 DMDBTDMA at Liquid-Liquid interface

9.1.1 Water and Nitric Acid

As shown in Section 4.2.2 we report the list of samples invesitgated and analyzed with the RMCS code in Table 9.1.

Concentration [mol/l]	**X-ray**	**Neutron**
0.02 M	**X**	**X**
0.07 M	**X**	**X**
0.2 M	**X**	**X**

Table 9.1: List of samples for DMDBTDMA in dodecane contacted with an aqueous phase at 2 M of Nitric Acid analyzed with the RMCS code. For x-ray's experiment the HNO_3 in H_2O has been used, replaced by DNO_3 in D_2O for the neutron's one. The X means the sample has been measured, the - it has not, and the bold **X** means the data have been analyzed with the RMCS to investigate the liquid/liquid interfacial structure.

0.02 M of DMDBTDMA in Dodecane

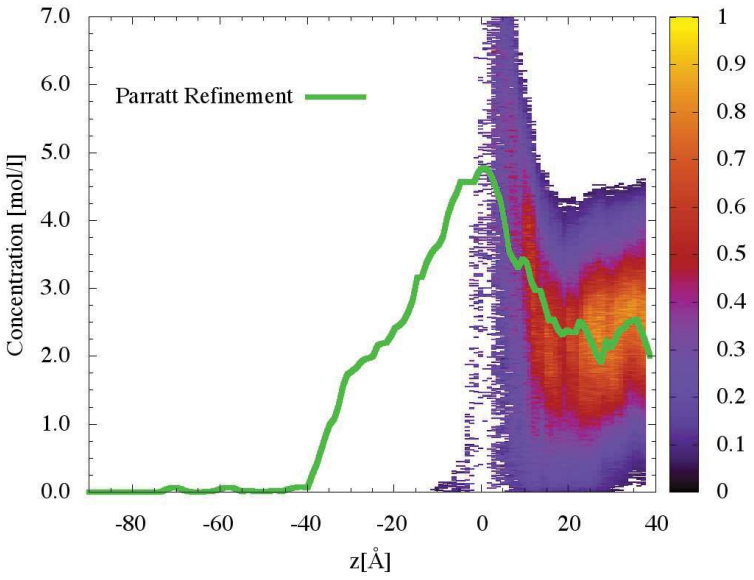

(a) Nitric acid

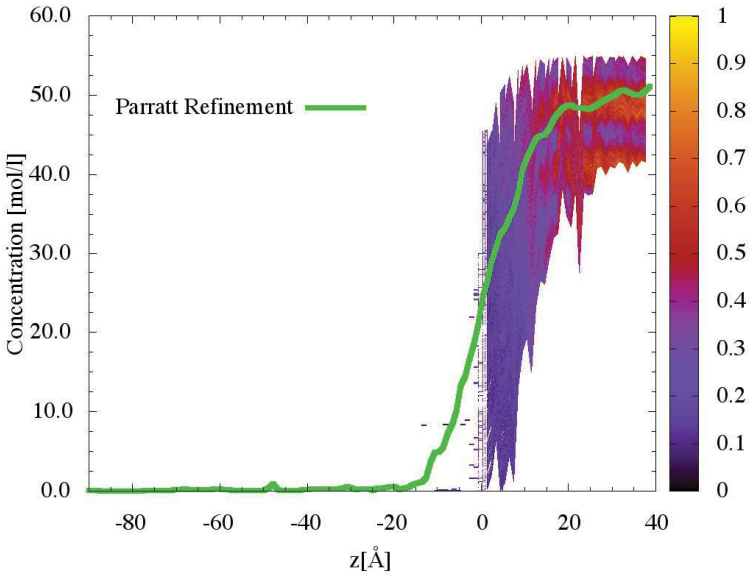

(b) Water

Figure 9.1: Concentration of (a) nitric acid and (b) water (mol/L) versus z-depth. Sample: DMDBTDMA in dodecane (0.02 M) contacted with nitric acid aqueous solution (2 mol/L). The green line represents the result of the Parratt Refinement and the color map the result of the SLD Profile Analysis.

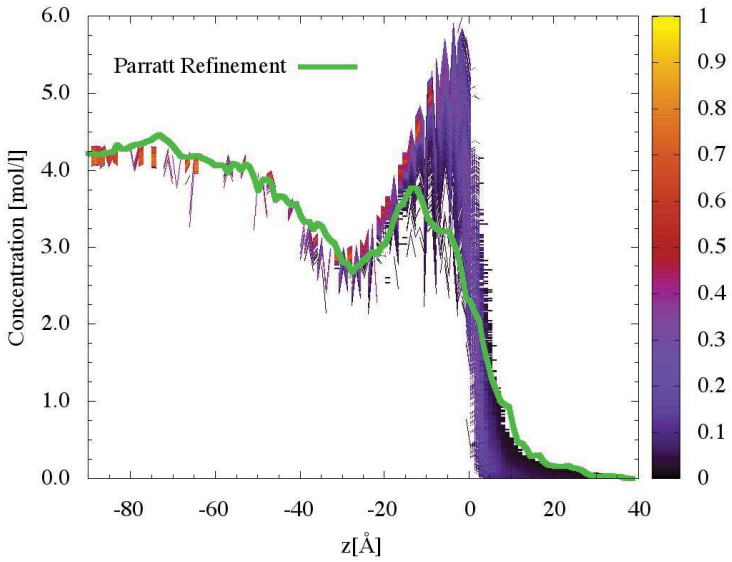

(a) Dodecane

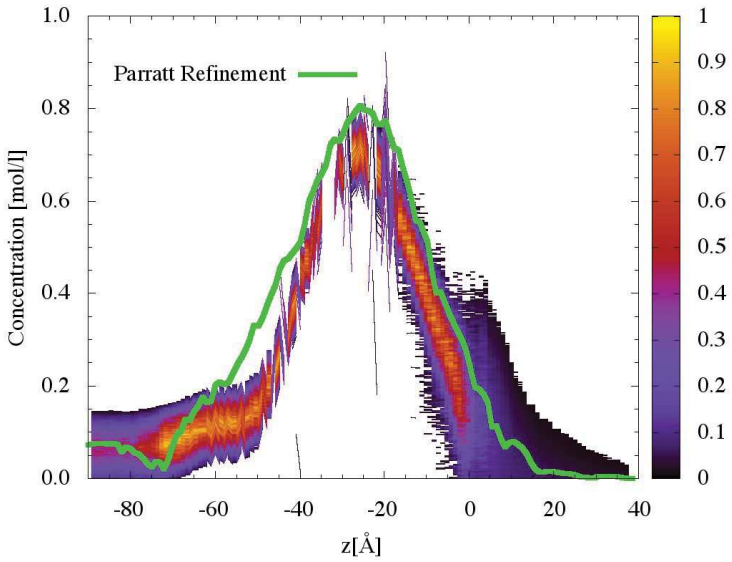

(b) DMDBTDMA

Figure 9.2: Concentration of (a) dodecane and (b) DMDBTDMA (mol/L) versus z-depth. Sample: DMDBTDMA in dodecane (0.02 M) contacted with nitric acid aqueous solution (2 mol/L). The green line represents the result of the Parratt Refinement and the color map the result of the SLD Profile Analysis.

0.07 M of DMDBTDMA in Dodecane

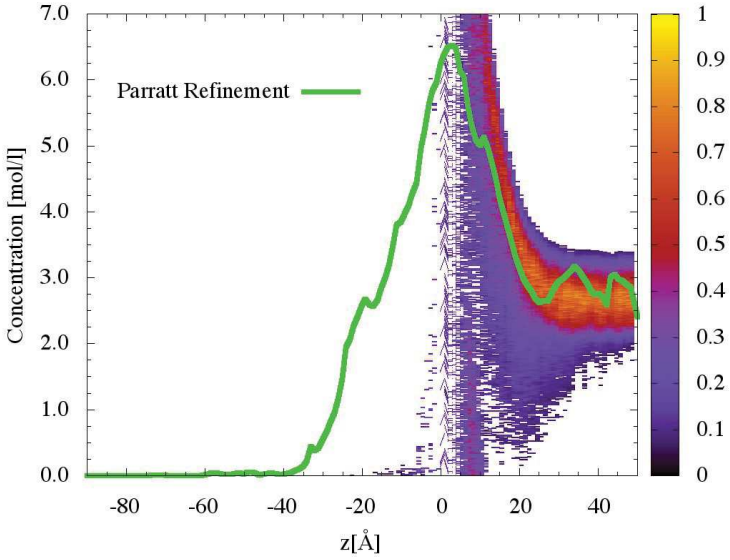

(a) Nitric acid

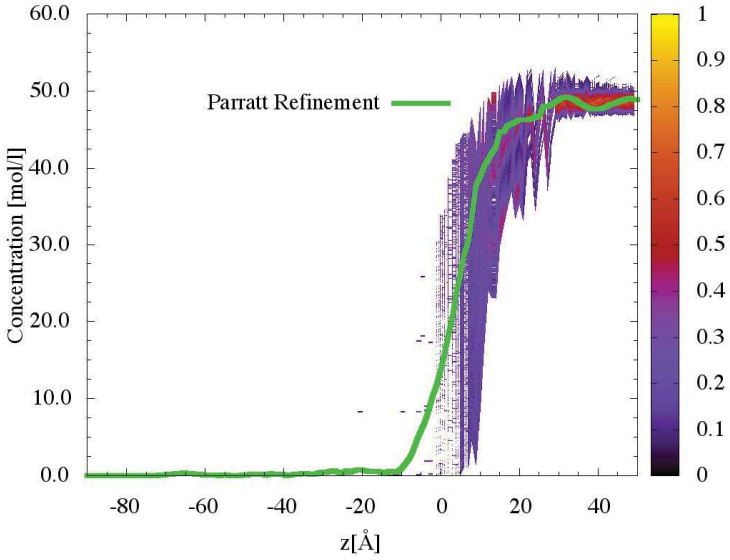

(b) Water

Figure 9.3: Concentration of (a) nitric acid and (b) water (mol/L) versus z-depth. Sample: DMDBTDMA in dodecane (0.07 M) contacted with nitric acid aqueous solution (2 mol/L). The green line represents the result of the Parratt Refinement and the color map the result of the SLD Profile Analysis.

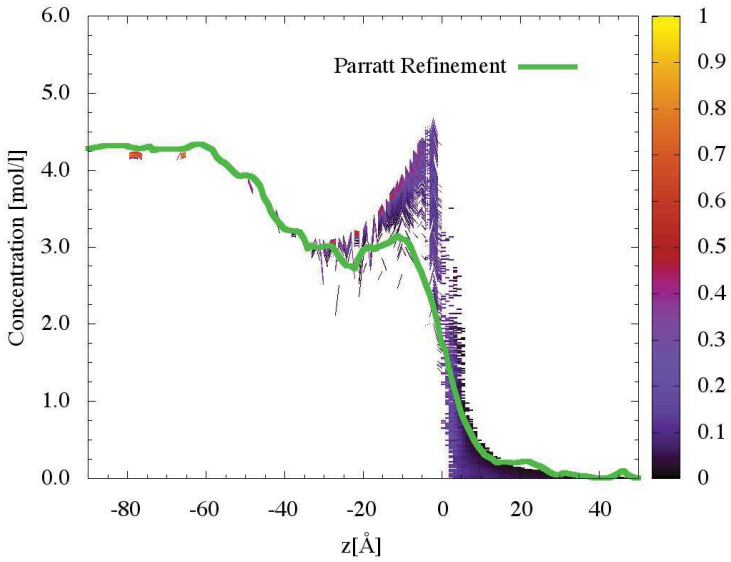

(a) Dodecane

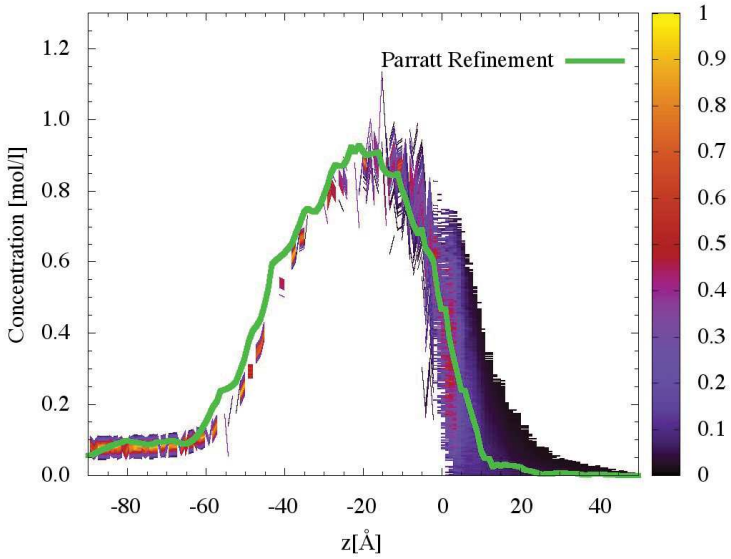

(b) DMDBTDMA

Figure 9.4: Concentration of (a) dodecane and (b) DMDBTDMA (mol/L) versus z-depth. Sample: DMDBTDMA in dodecane (0.07 M) contacted with nitric acid aqueous solution (2 mol/L). The green line represents the result of the Parratt Refinement and the color map the result of the SLD Profile Analysis.

0.2 M of DMDBTDMA in Dodecane

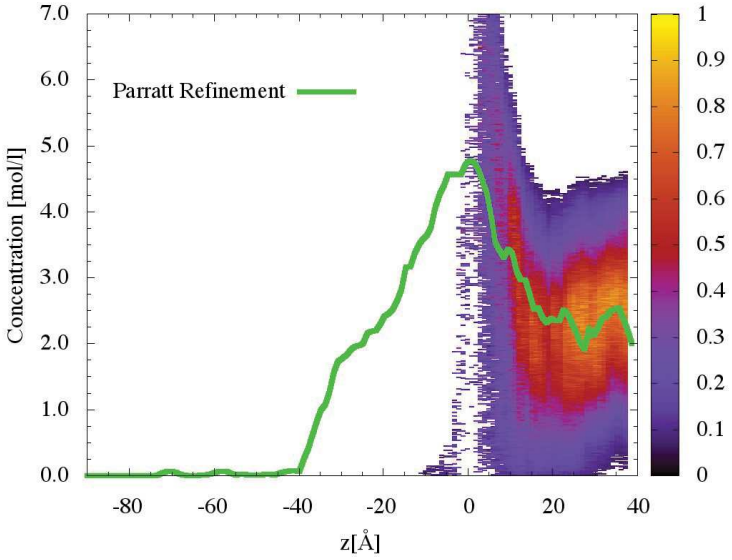

(a) Nitric acid

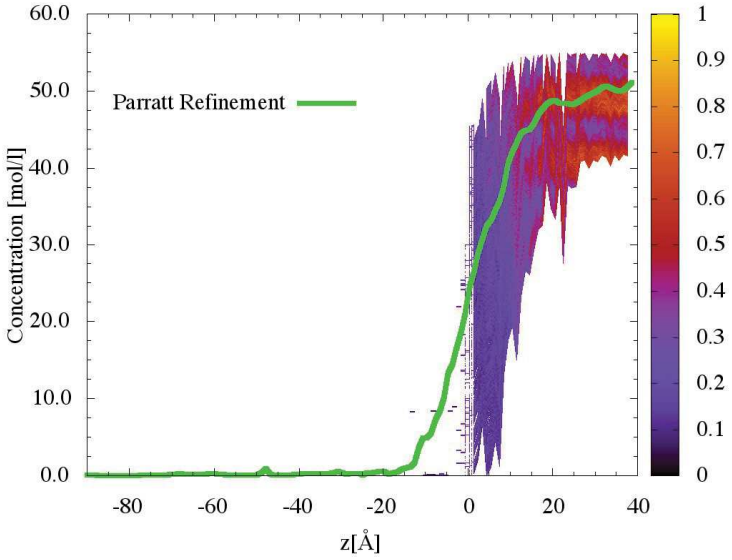

(b) Water

Figure 9.5: Concentration of (a) nitric acid and (b) water (mol/L) versus z-depth. Sample: DMDBTDMA in dodecane (0.2 M) contacted with nitric acid aqueous solution (2 mol/L). The green line represents the result of the Parratt Refinement and the color map the result of the SLD Profile Analysis.

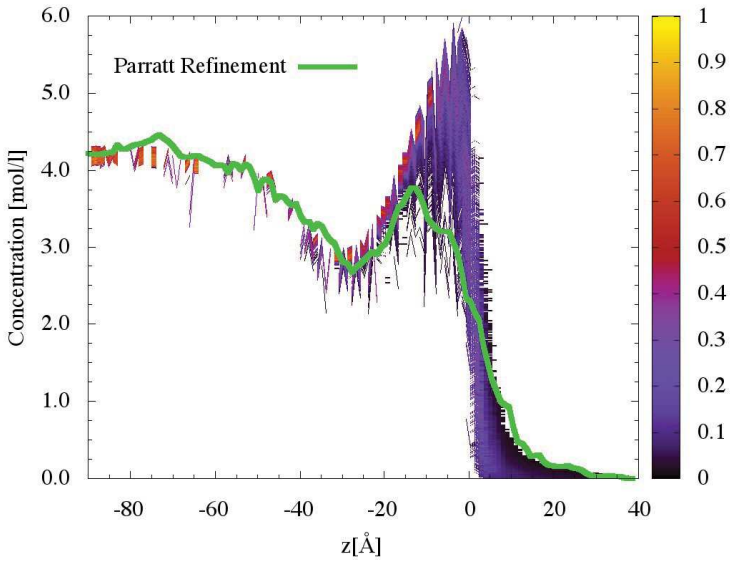

(a) Dodecane

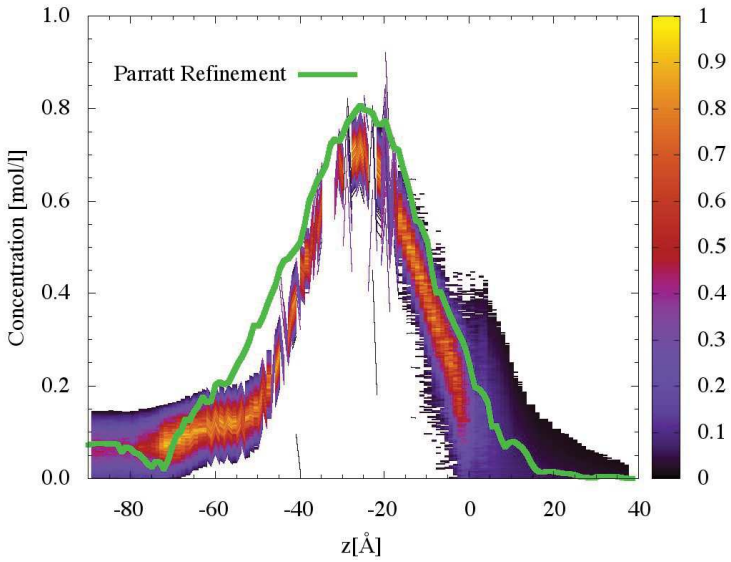

(b) DMDBTDMA

Figure 9.6: Concentration of (a) dodecane and (b) DMDBTDMA (mol/L) versus z-depth. Sample: DMDBTDMA in dodecane (0.2 M) contacted with nitric acid aqueous solution (2 mol/L). The green line represents the result of the Parratt Refinement and the color map the result of the SLD Profile Analysis.

9.1.2 Water and Neodymium Nitrate

As shown in Section 4.2.3 we report the list of samples invesitgated and analyzed with the RMCS code in Table 9.2.

Concentration [mol/l]	X-ray	Neutron
0.02 M	**X**	**X**
0.07 M	**X**	**X**
0.09 M	**X**	**X**
0.1 M	**X**	**X**

Table 9.2: List of samples for DMDBTDMA in dodecane contacted with an aqueous phase at 2 M of $LiNO_3$ and 0.25 M of $Nd(NO_3)_3$ analyzed with the RMCS code. The X means the sample has been measured, the - it has not, and the bold **X** means the data have been analyzed with the RMCS to investigate the liquid/liquid interfacial structure. For neutron experiments an organic phase composed by fully deuterated dodecane, $C_{12}D_{12}$, has been used.

0.02 M of DMDBTDMA in Dodecane

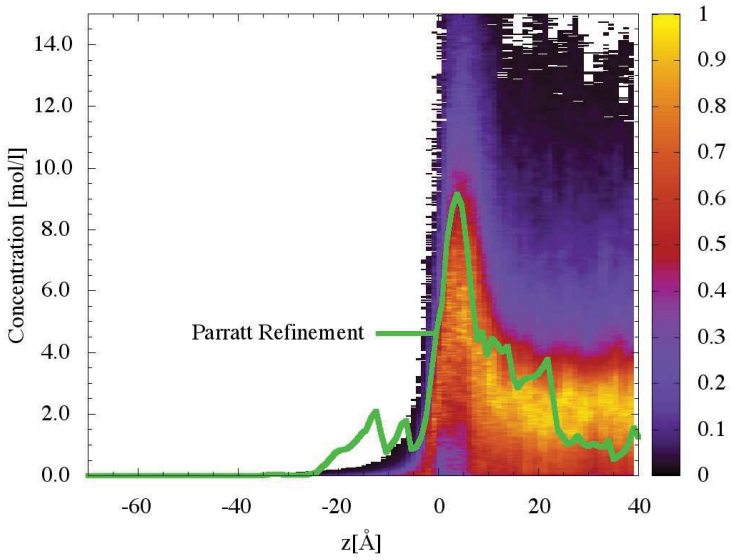

(a) Lithium

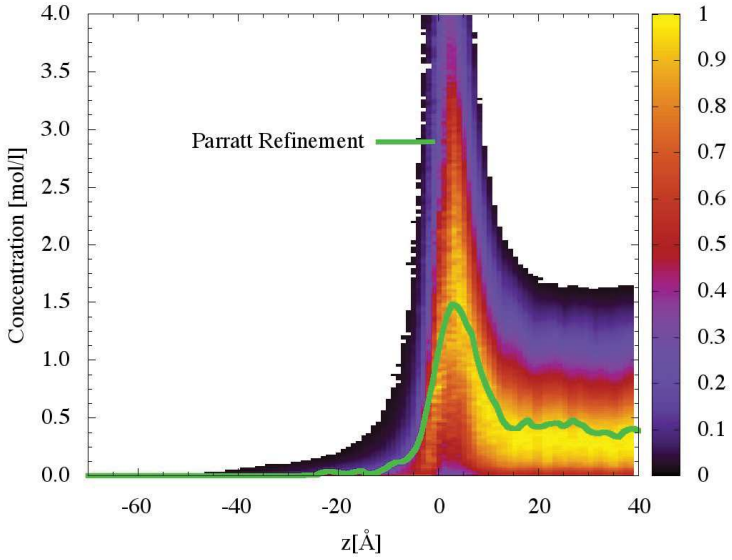

(b) Neodymium

Figure 9.7: Concentration of (a) lithium and (b) neodymium (mol/L) versus z-depth. Sample: DMDBTDMA in dodecane (0.02 M) contacted with neodymium nitrate (0.25 mol/L) and lithium nitrate (2 mol/L) aqueous solution. The green line represents the result of the Parratt Refinement and the color map the result of the SLD Profile Analysis.

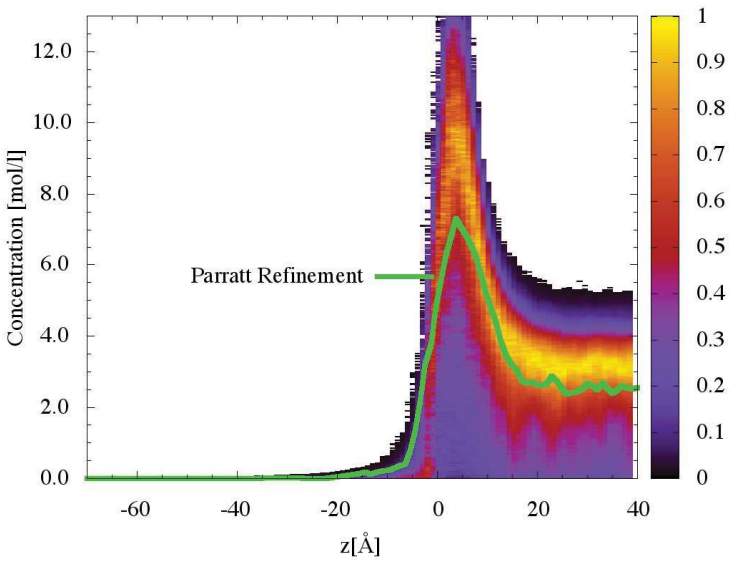

(a) Nitrate

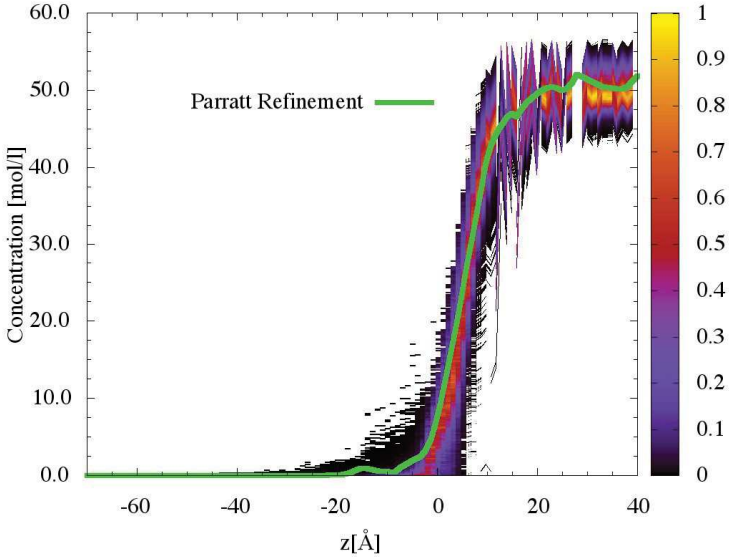

(b) Water

Figure 9.8: Concentration of (a) nitrate and (b) water (mol/L) versus z-depth. Sample: DMDBTDMA in dodecane (0.02 M) contacted with neodymium nitrate (0.25 mol/L) and lithium nitrate (2 mol/L) aqueous solution. The green line represents the result of the Parratt Refinement and the color map the result of the SLD Profile Analysis.

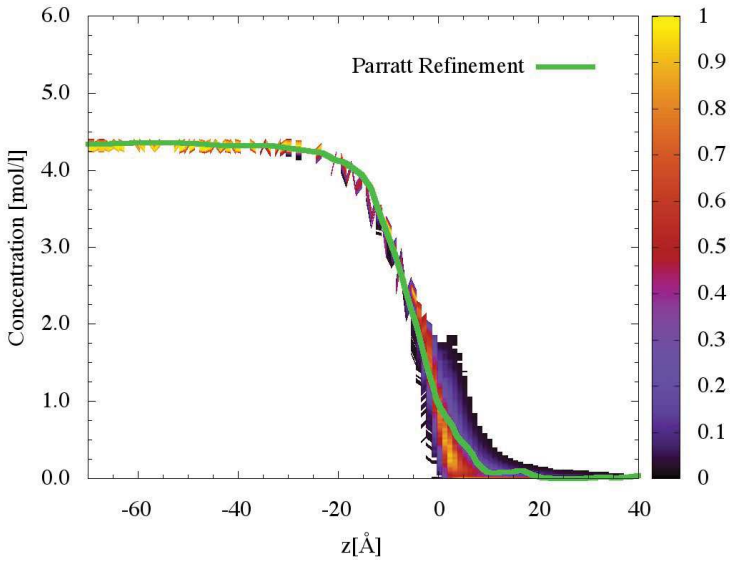

(a) Dodecane

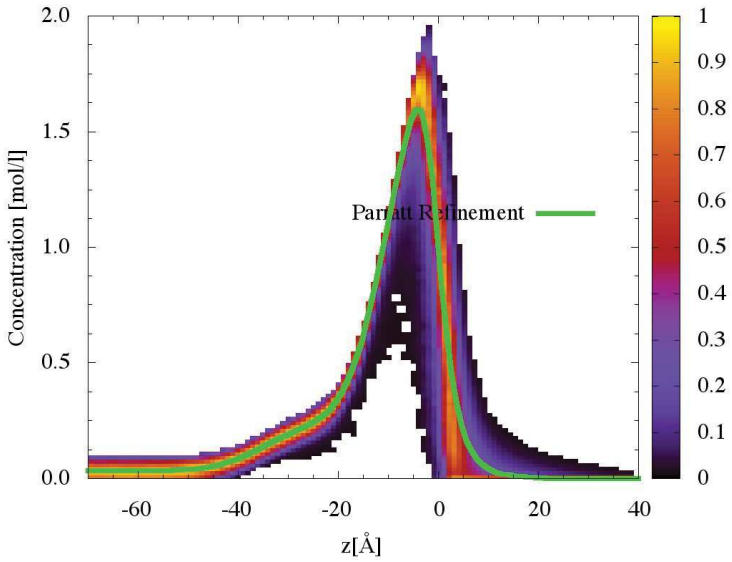

(b) DMDBTDMA

Figure 9.9: Concentration of (a) dodecane and (b) DMDBTDMA (mol/L) versus z-depth. Sample: DMDBTDMA in dodecane (0.02 M) contacted with neodymium nitrate (0.25 mol/L) and lithium nitrate (2 mol/L) aqueous solution. The green line represents the result of the Parratt Refinement and the color map the result of the SLD Profile Analysis.

0.07 M of DMDBTDMA in Dodecane

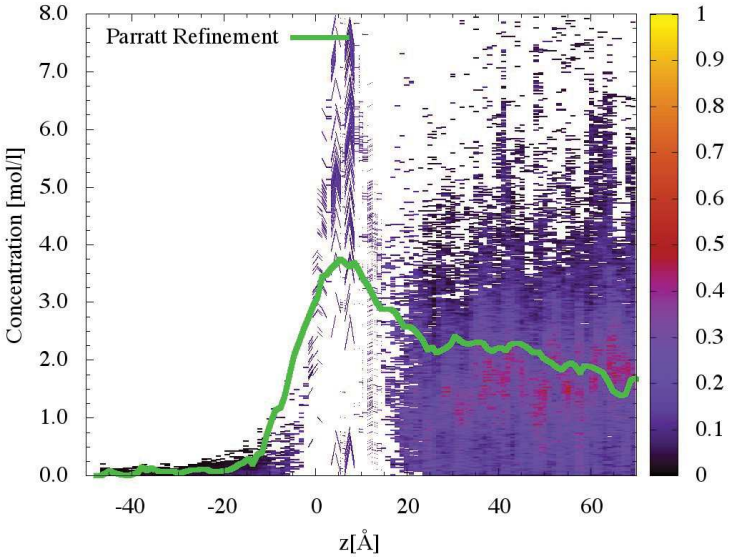

(a) Lithium

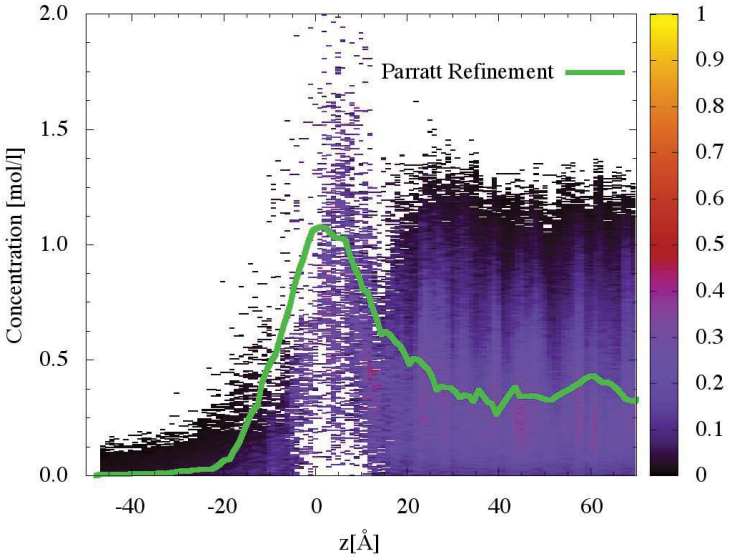

(b) Neodymium

Figure 9.10: Concentration of (a) lithium and (b) neodymium (mol/L) versus z-depth. Sample: DMDBTDMA in dodecane (0.07 M) contacted with neodymium nitrate (0.25 mol/L) and lithium nitrate (2 mol/L) aqueous solution. The green line represents the result of the Parratt Refinement and the color map the result of the SLD Profile Analysis.

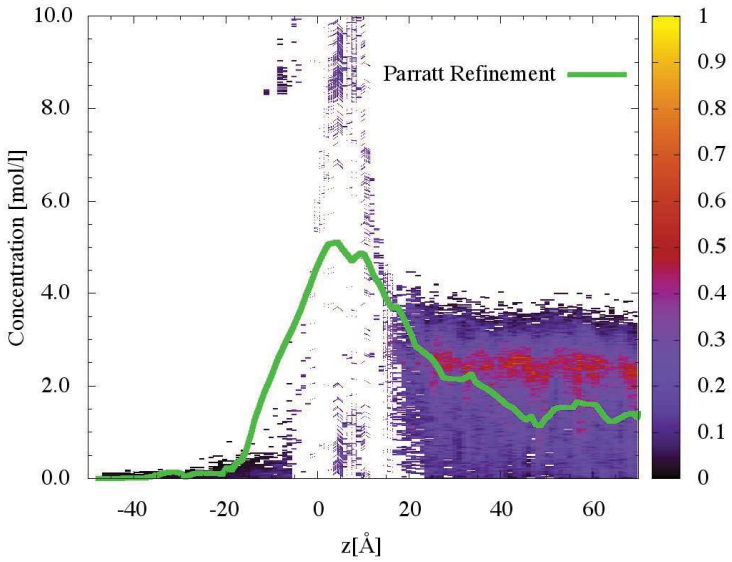

(a) Nitrate

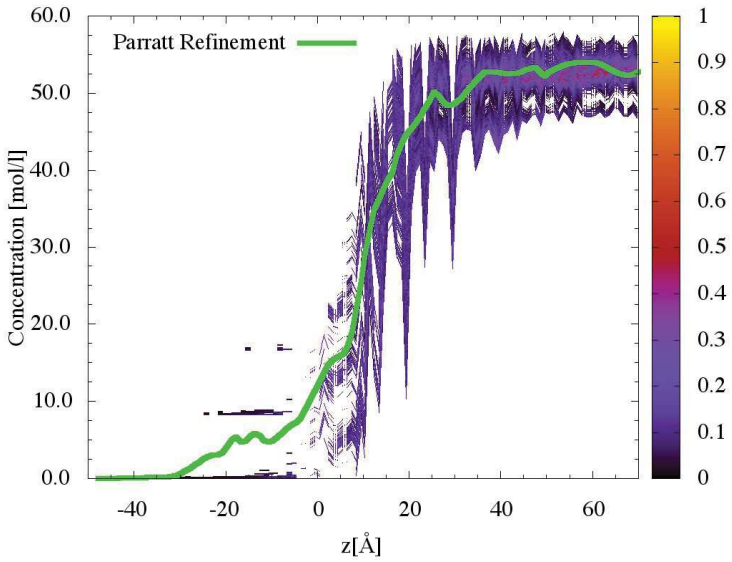

(b) Water

Figure 9.11: Concentration of (a) nitrateand (b) water (mol/L) versus z-depth. Sample: DMDBTDMA in dodecane (0.07 M) contacted with neodymium nitrate (0.25 mol/L) and lithium nitrate (2 mol/L) aqueous solution. The green line represents the result of the Parratt Refinement and the color map the result of the SLD Profile Analysis.

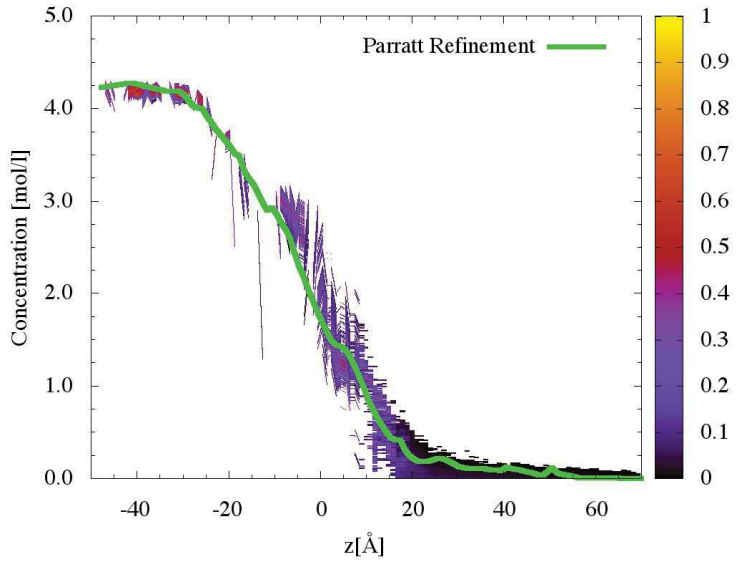

(a) Dodecane

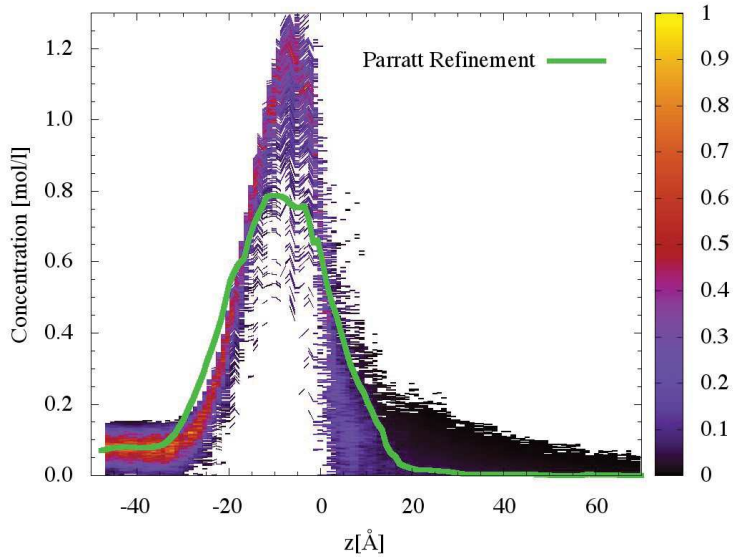

(b) DMDBTDMA

Figure 9.12: Concentration of (a) dodecaneand (b) DMDBTDMA (mol/L) versus z-depth. Sample: DMDBTDMA in dodecane (0.07 M) contacted with neodymium nitrate (0.25 mol/L) and lithium nitrate (2 mol/L) aqueous solution. The green line represents the result of the Parratt Refinement and the color map the result of the SLD Profile Analysis.

0.09 M of DMDBTDMA in Dodecane

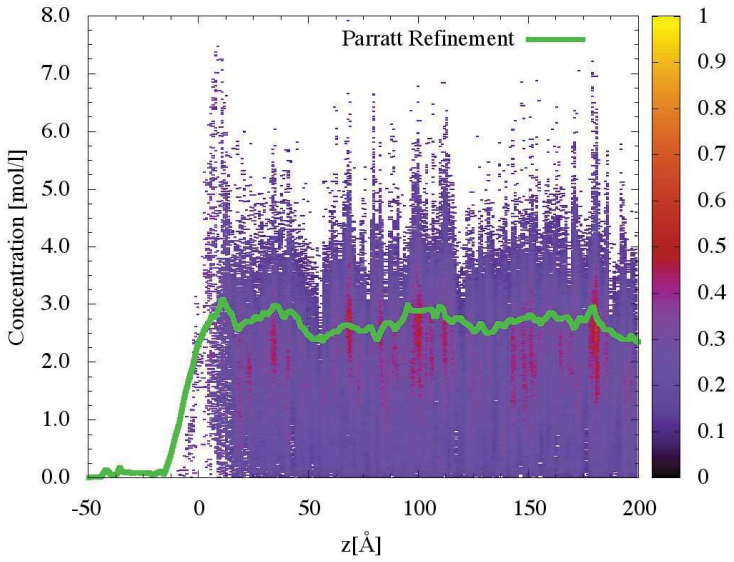

(a) Lithium

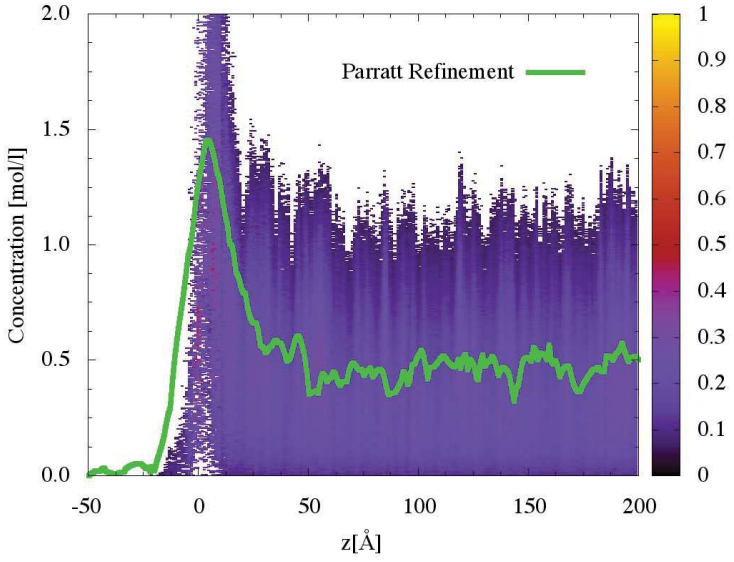

(b) Neodymium

Figure 9.13: Concentration of (a) lithium and (b) neodymium (mol/L) versus z-depth. Sample: DMDBTDMA in dodecane (0.09 M) contacted with neodymium nitrate (0.25 mol/L) and lithium nitrate (2 mol/L) aqueous solution. The green line represents the result of the Parratt Refinement and the color map the result of the SLD Profile Analysis.

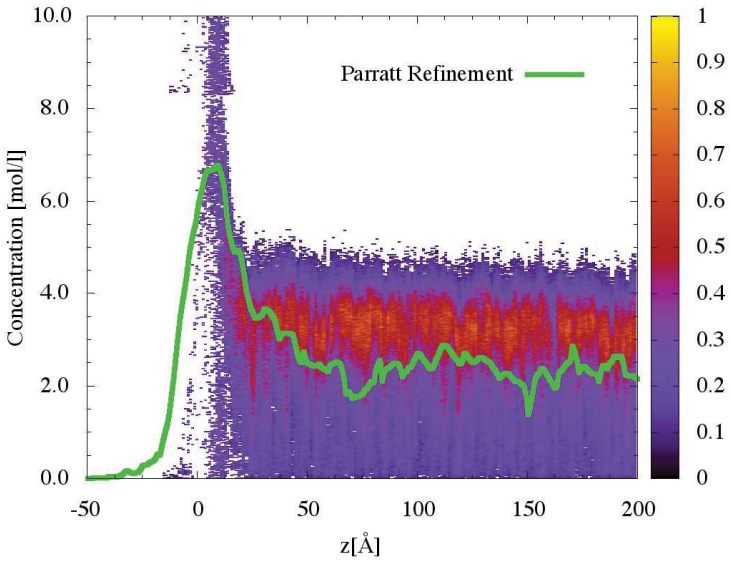

(a) Nitrate

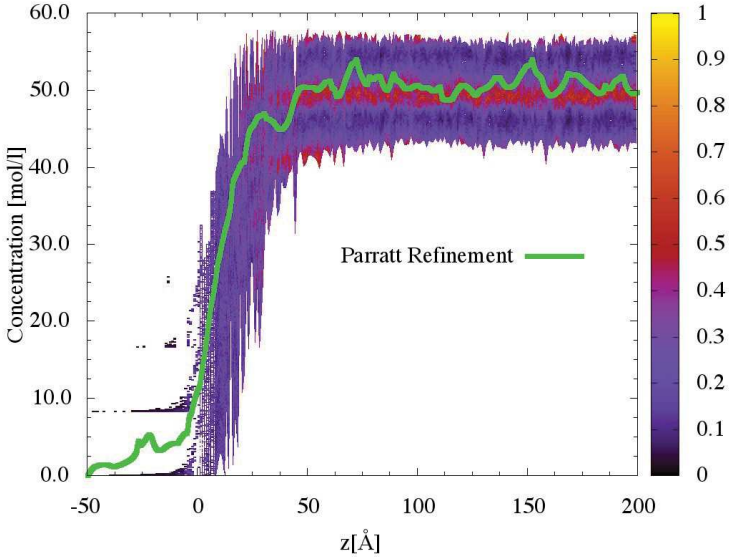

(b) Water

Figure 9.14: Concentration of (a) nitrate and (b) water (mol/L) versus z-depth. Sample: DMDBTDMA in dodecane (0.09 M) contacted with neodymium nitrate (0.25 mol/L) and lithium nitrate (2 mol/L) aqueous solution. The green line represents the result of the Parratt Refinement and the color map the result of the SLD Profile Analysis.

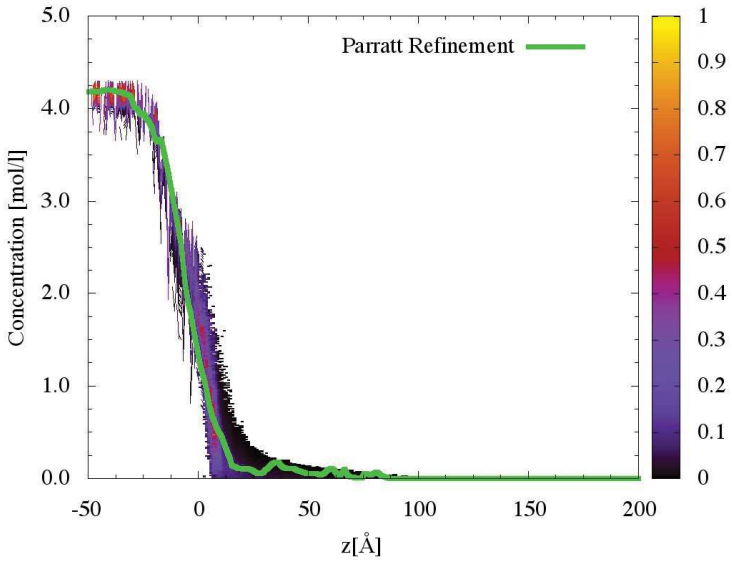

(a) Dodecane

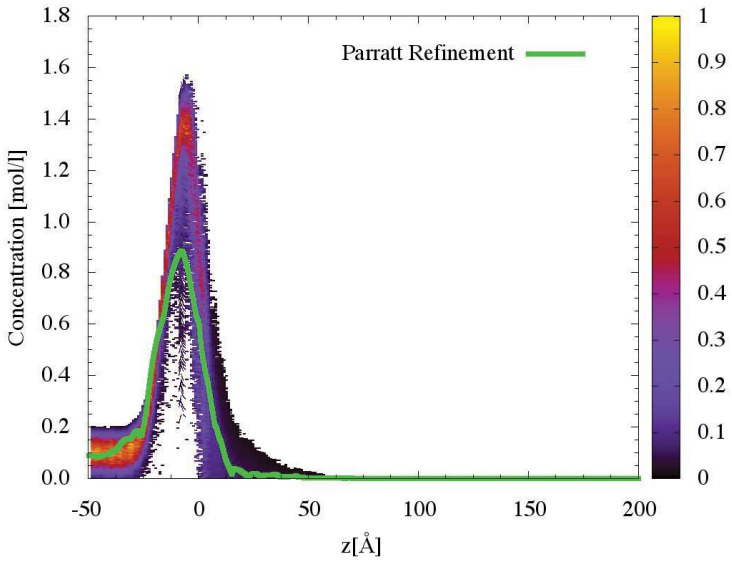

(b) DMDBTDMA

Figure 9.15: Concentration of (a) dodecane and (b) DMDBTDMA (mol/L) versus z-depth. Sample: DMDBTDMA in dodecane (0.09 M) contacted with neodymium nitrate (0.25 mol/L) and lithium nitrate (2 mol/L) aqueous solution. The green line represents the result of the Parratt Refinement and the color map the result of the SLD Profile Analysis.

0.1 M of DMDBTDMA in Dodecane

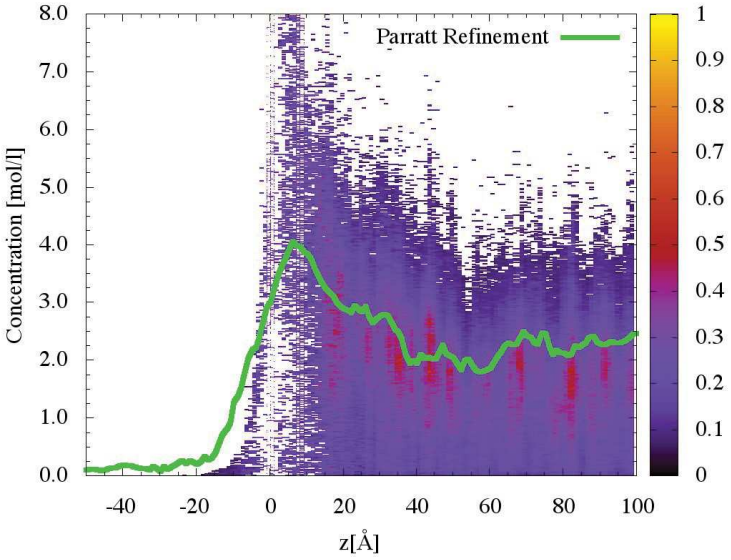

(a) Lithium

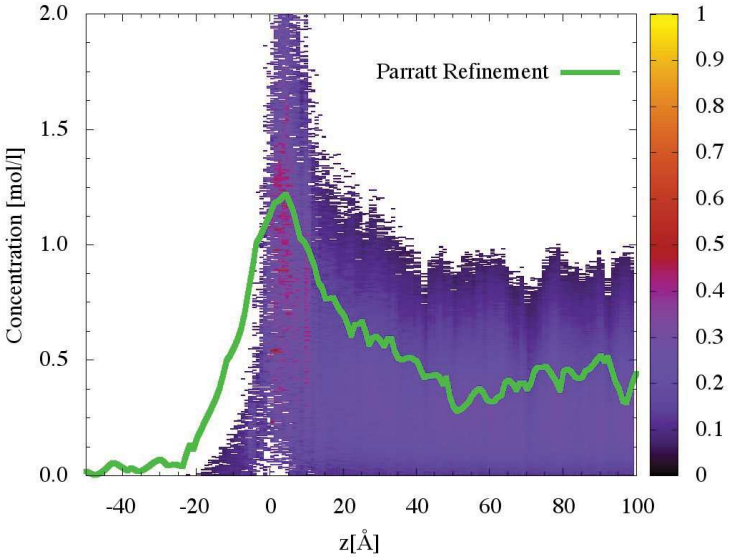

(b) Neodymium

Figure 9.16: Concentration of (a) lithium and (b) neodymium (mol/L) versus z-depth. Sample: DMDBTDMA in dodecane (0.1 M) contacted with neodymium nitrate (0.25 mol/L) and lithium nitrate (2 mol/L) aqueous solution. The green line represents the result of the Parratt Refinement and the color map the result of the SLD Profile Analysis.

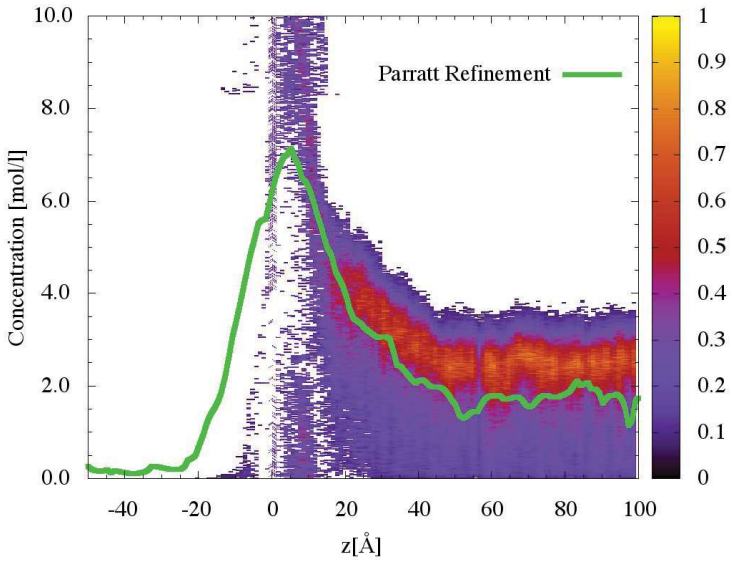

(a) Nitrate

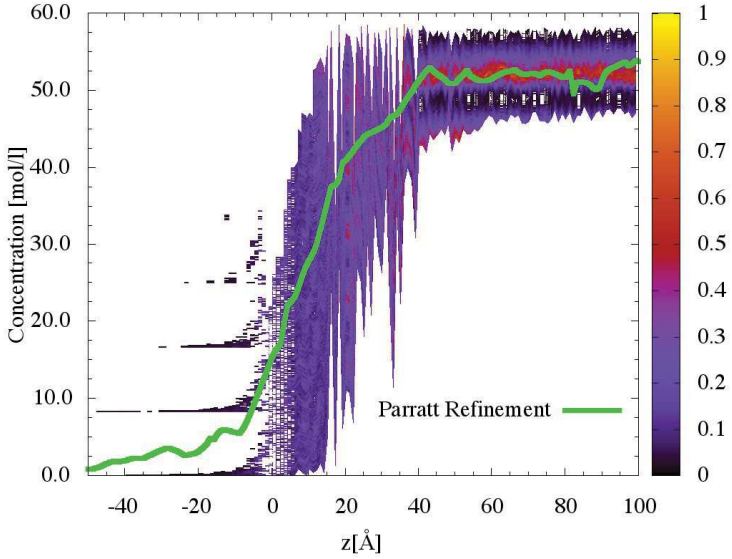

(b) Water

Figure 9.17: Concentration of (a) nitrate and (b) water (mol/L) versus z-depth. Sample: DMDBTDMA in dodecane (0.1 M) contacted with neodymium nitrate (0.25 mol/L) and lithium nitrate (2 mol/L) aqueous solution. The green line represents the result of the Parratt Refinement and the color map the result of the SLD Profile Analysis.

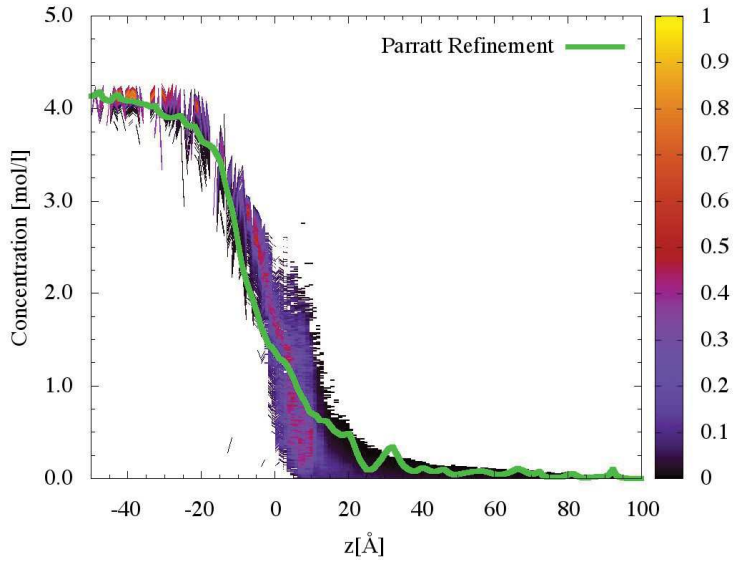

(a) Dodecane

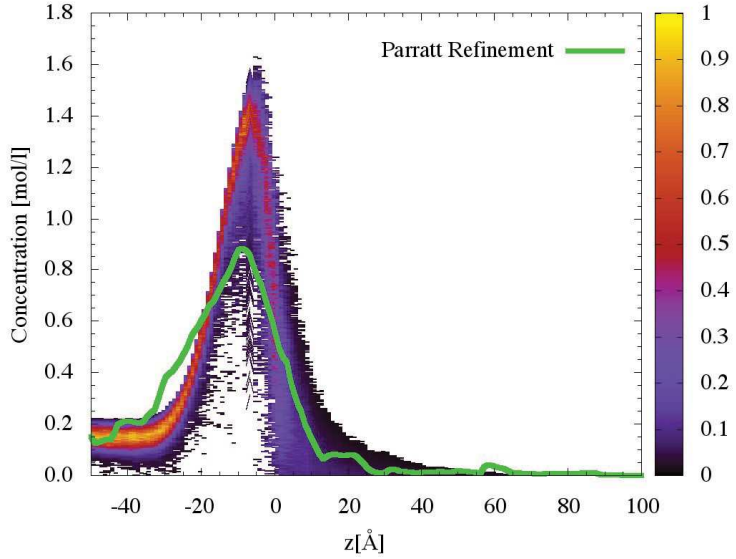

(b) DMDBTDMA

Figure 9.18: Concentration of (a) dodecane and (b) DMDBTDMA (mol/L) versus z-depth. Sample: DMDBTDMA in dodecane (0.1 M) contacted with neodymium nitrate (0.25 mol/L) and lithium nitrate (2 mol/L) aqueous solution. The green line represents the result of the Parratt Refinement and the color map the result of the SLD Profile Analysis.

9.2 DMDOHEMA at Liquid-Liquid interface

9.2.1 Pure Water

As shown in Section 4.3.1 we report the list of samples invesitgated and analyzed with the RMCS code in Table 9.3.

Concentration [mol/l]	**X-ray**	**Neutron** (37.7/62.3)	**Neutron** (0/100)
0.002 M	**X**	**X**	**X**
0.007 M	**X**	**X**	**X**
0.01 M	**X**	**X**	**X**
0.04 M	**X**	**X**	**X**

Table 9.3: List of samples for DMDOHEMA in dodecane contacted with water analyzed with the RMCS code. The X means the sample has been measured, the - it has not, and the bold **X** means the data have been analyzed with the RMCS to investigate the liquid/liquid interfacial structure. (37.7/62.3) and (0/100) is the volume ratio between $C_{12}H_{26}/C_{12}D_{26}$ used to vary the contrast. The (37.7/62.3) column represents the samples measured with D_2O and a mixture of hydrogenated/protonated dodecane to obtain an SLD=$4.0 \cdot 10^{-6}$ Å^{-2}. The (0/100) column represents the samples measured with D_2O and $C_{12}D_{26}$.

0.002 M of DMDOHEMA in Dodecane

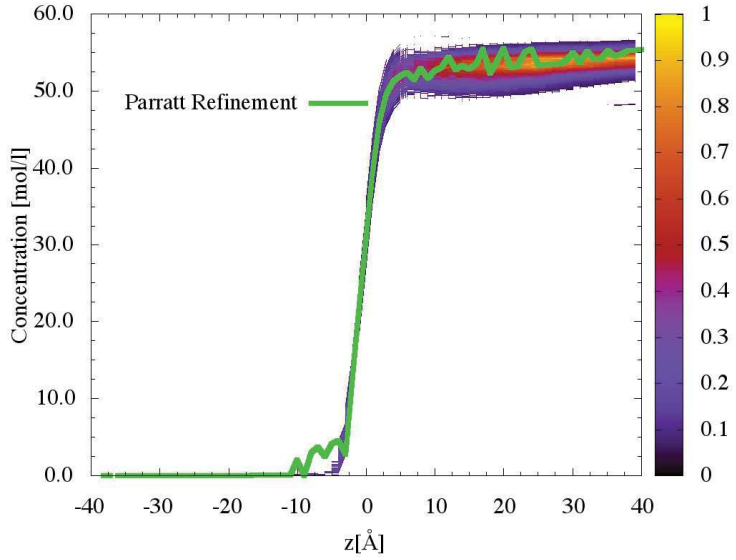

(a) Water

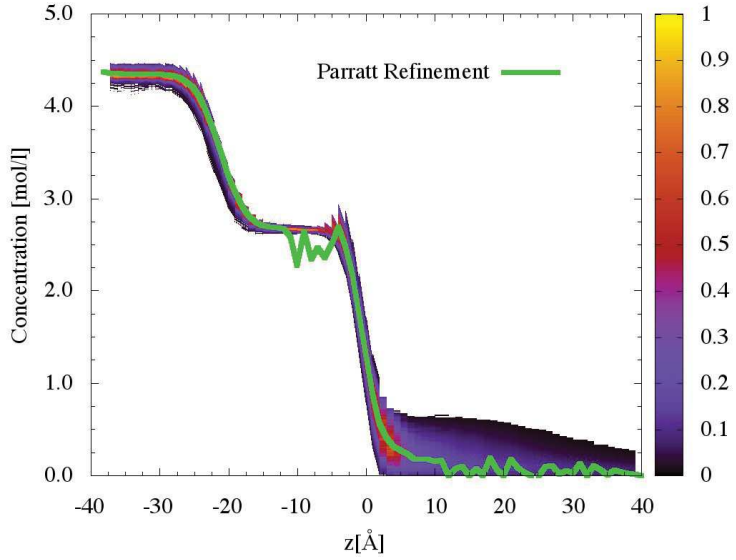

(b) Dodecane

Figure 9.19: Concentration of (a) water and (b) dodecane (mol/L) versus z-depth. Sample: DMDOHEMA in dodecane (0.002 M) contacted with pure water. The green line represents the result of the Parratt Refinement and the color map the result of the SLD Profile Analysis.

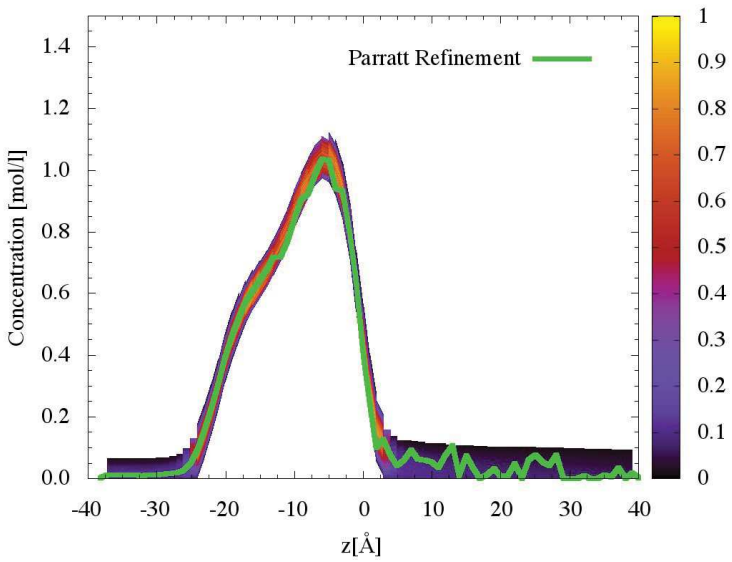

Figure 9.20: Concentration of DMDOHEMA (mol/L) versus z-depth. Sample: DMDOHEMA in dodecane (0.002 M) contacted with pure water. The green line represents the result of the Parratt Refinement and the color map the result of the SLD Profile Analysis.

0.007 M of DMDOHEMA in Dodecane

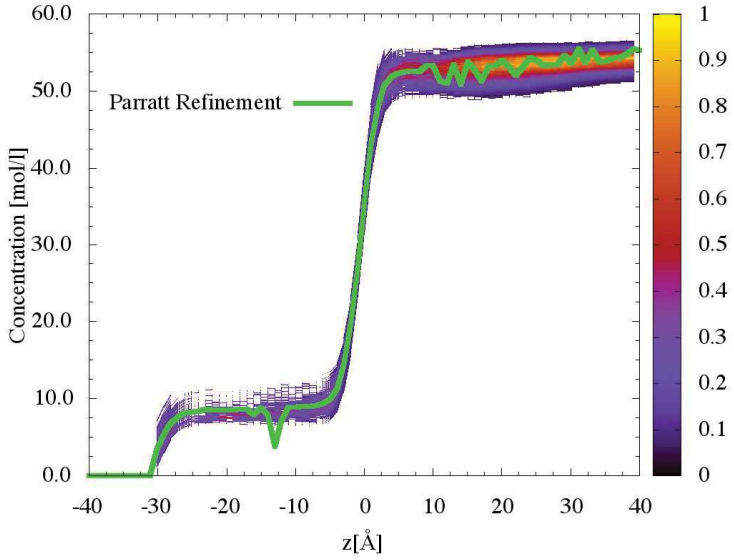

(a) Water

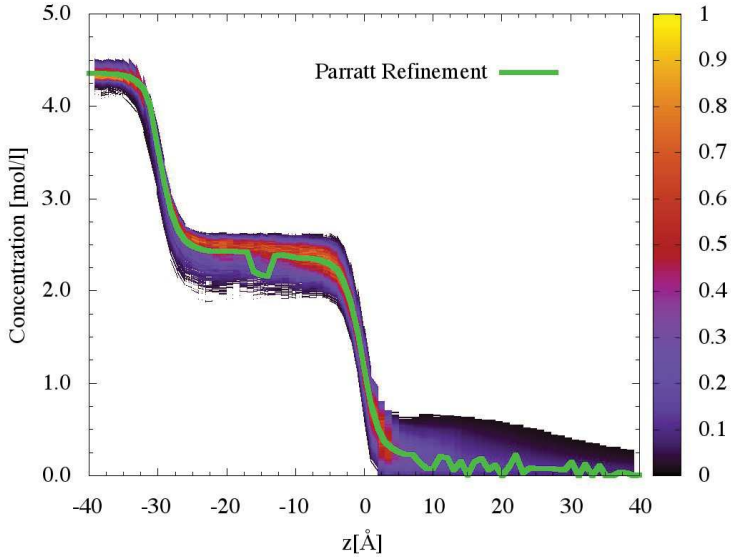

(b) Dodecane

Figure 9.21: Concentration of (a) water and (b) dodecane (mol/L) versus z-depth. Sample: DMDOHEMA in dodecane (0.007 M) contacted with pure water. The green line represents the result of the Parratt Refinement and the color map the result of the SLD Profile Analysis.

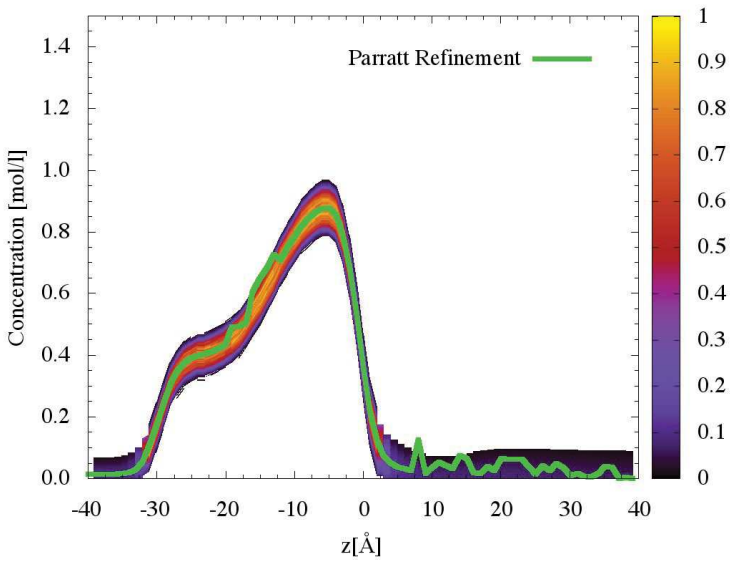

Figure 9.22: Concentration of DMDOHEMA (mol/L) versus z-depth. Sample: DMDOHEMA in dodecane (0.007 M) contacted with pure water. The green line represents the result of the Parratt Refinement and the color map the result of the SLD Profile Analysis.

0.01 M of DMDOHEMA in Dodecane

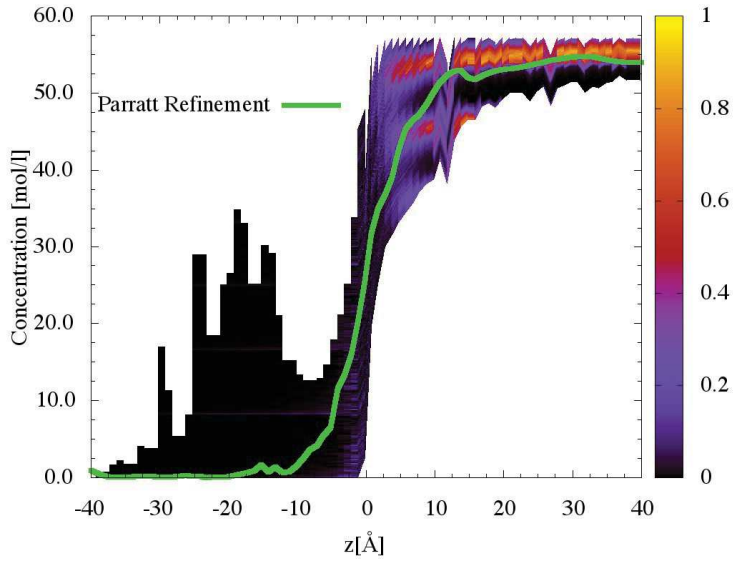

(a) Water

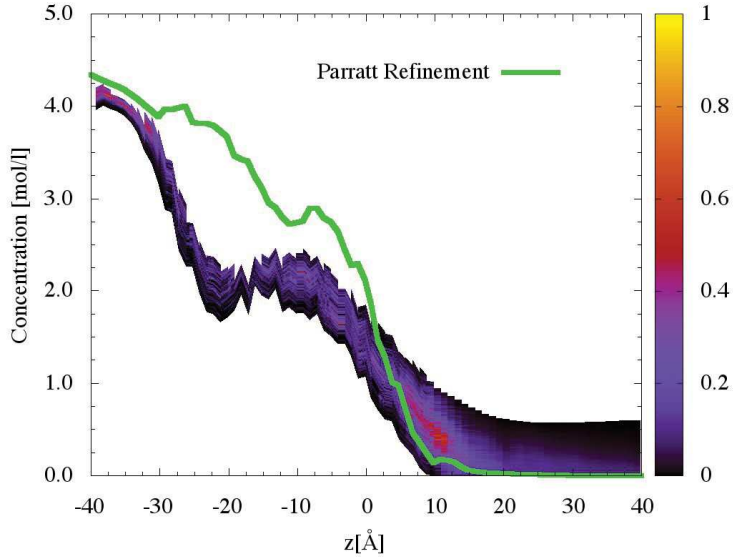

(b) Dodecane

Figure 9.23: Concentration of (a) water and (b) dodecane (mol/L) versus z-depth. Sample: DMDOHEMA in dodecane (0.01 M) contacted with pure water. The green line represents the result of the Parratt Refinement and the color map the result of the SLD Profile Analysis.

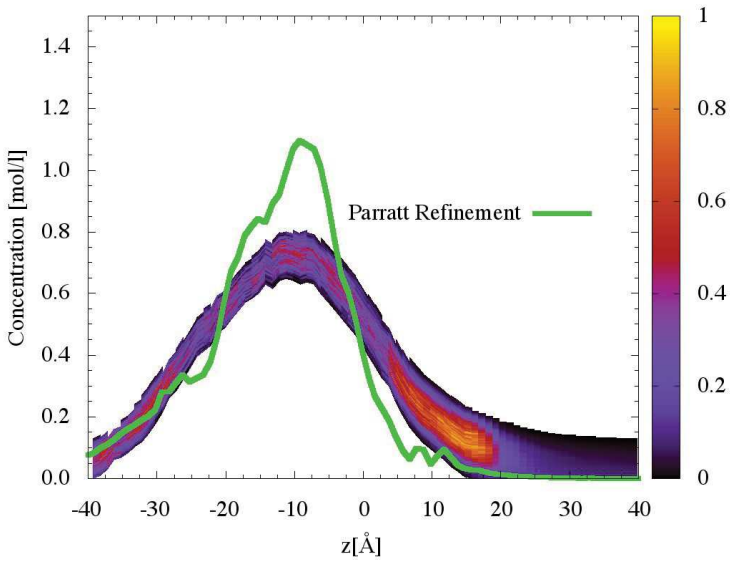

Figure 9.24: Concentration of DMDOHEMA (mol/L) versus z-depth. Sample: DMDOHEMA in dodecane (0.01 M) contacted with pure water. The green line represents the result of the Parratt Refinement and the color map the result of the SLD Profile Analysis.

0.04 M of DMDOHEMA in Dodecane

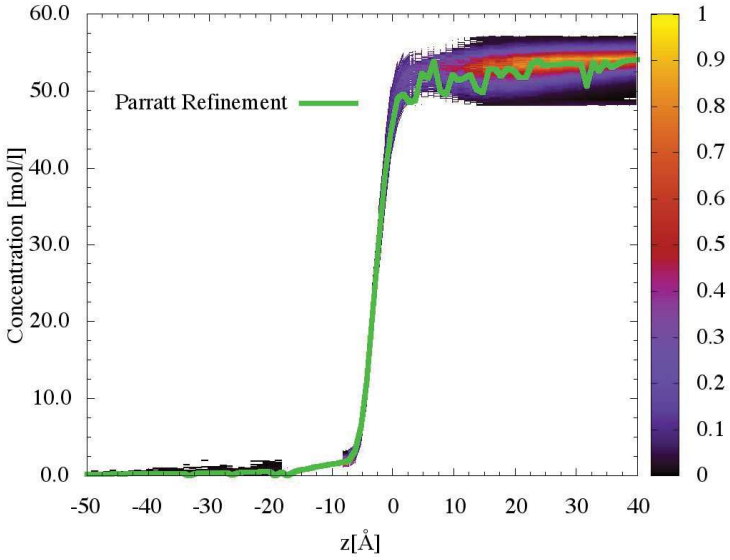

(a) Water

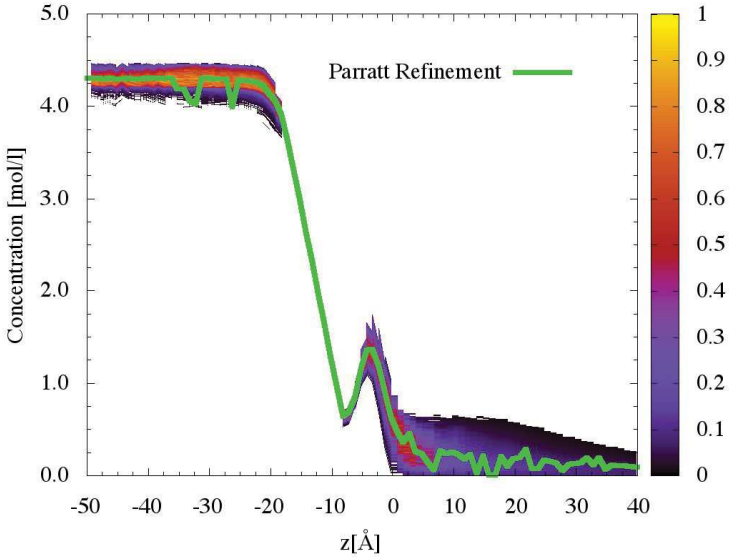

(b) Dodecane

Figure 9.25: Concentration of (a) water and (b) dodecane (mol/L) versus z-depth. Sample: DMDOHEMA in dodecane (0.04 M) contacted with pure water. The green line represents the result of the Parratt Refinement and the color map the result of the SLD Profile Analysis.

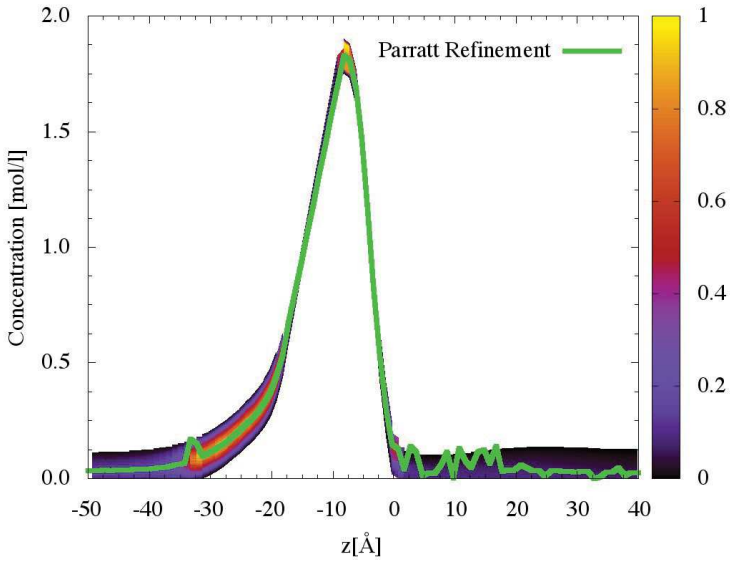

Figure 9.26: Concentration of DMDOHEMA (mol/L) versus z-depth. Sample: DMDOHEMA in dodecane (0.04 M) contacted with pure water. The green line represents the result of the Parratt Refinement and the color map the result of the SLD Profile Analysis.

9.2.2 Water and Nitric Acid

As shown in Section 4.3.2 we report the list of samples invesitgated and analyzed with the RMCS code in Table 9.4.

Concentration [mol/l]	X-ray	Neutron
0.002 M	**X**	**X**
0.007 M	**X**	**X**
0.01 M	**X**	**X**

Table 9.4: List of samples for DMDOHEMA in dodecane contacted with an aqueous phase at 2 M of Nitric Acid analyzed with the RMCS code. For x-ray's experiment the HNO_3 in H_2O has been used, replaced by DNO_3 in D_2O for the neutron's one. The X means the sample has been measured, the - it has not, and the bold **X** means the data have been analyzed with the RMCS to investigate the liquid/liquid interfacial structure.

0.002 M of DMDOHEMA in Dodecane

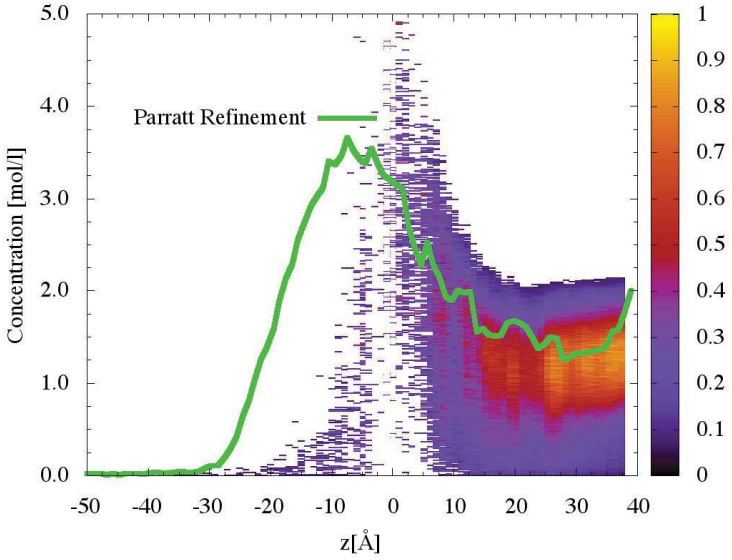

(a) Nitric Acid

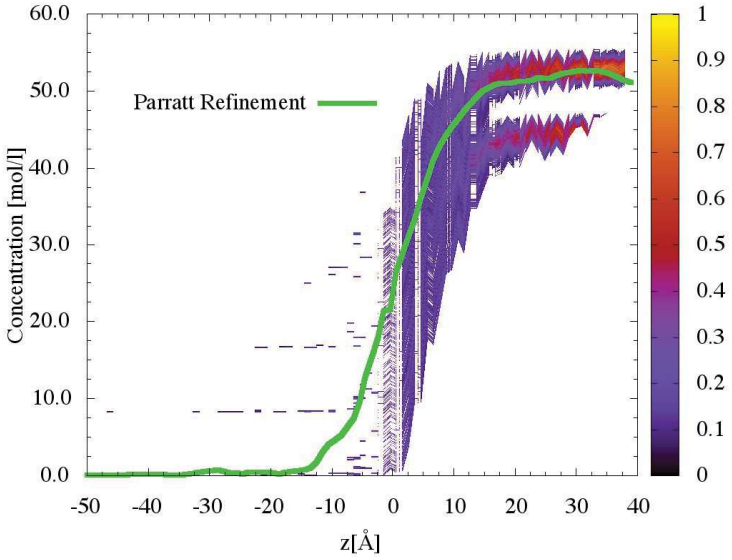

(b) Water

Figure 9.27: Concentration of (a) nitric acid and (b) water (mol/L) versus z-depth. Sample: DMDOHEMA in dodecane (0.002 M) contacted with nitric acid aqueous solution (2 mol/L). The green line represents the result of the Parratt Refinement and the color map the result of the SLD Profile Analysis.

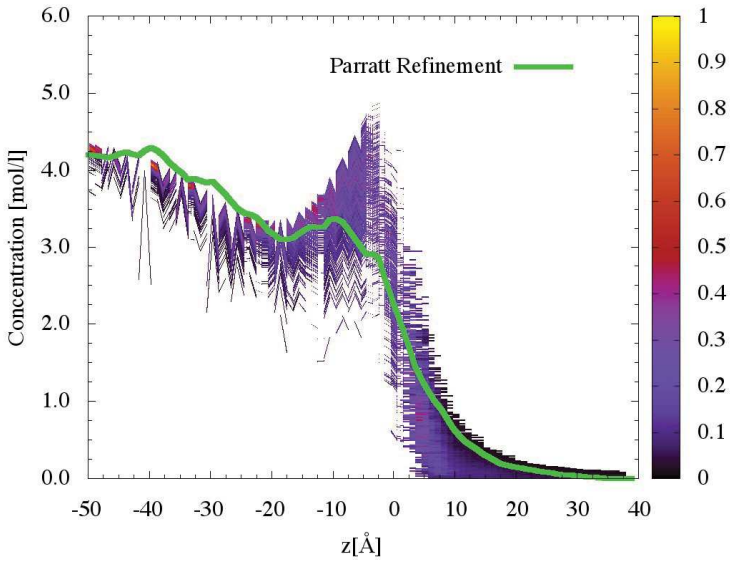

(a) Dodecane

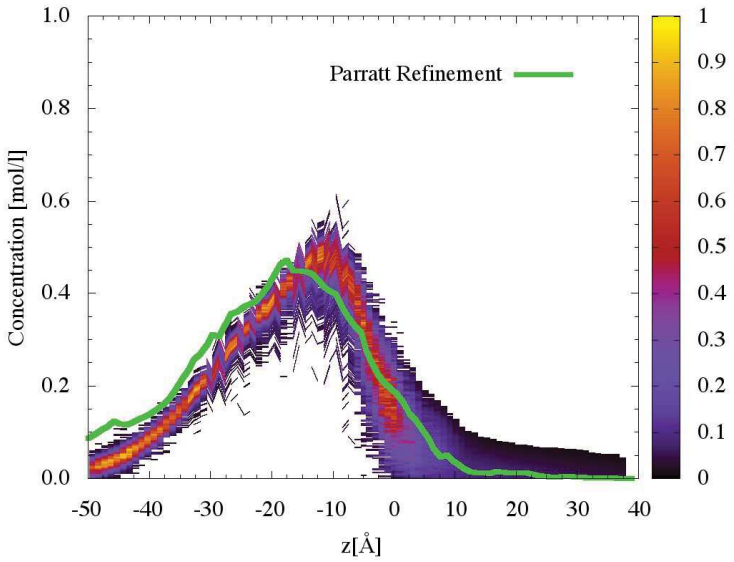

(b) DMDOHEMA

Figure 9.28: Concentration of (a) dodecane and (b) DMDOHEMA (mol/L) versus z-depth. Sample: DMDOHEMA in dodecane (0.002 M) contacted with nitric acid aqueous solution (2 mol/L). The green line represents the result of the Parratt Refinement and the color map the result of the SLD Profile Analysis.

0.007 M of DMDOHEMA in Dodecane

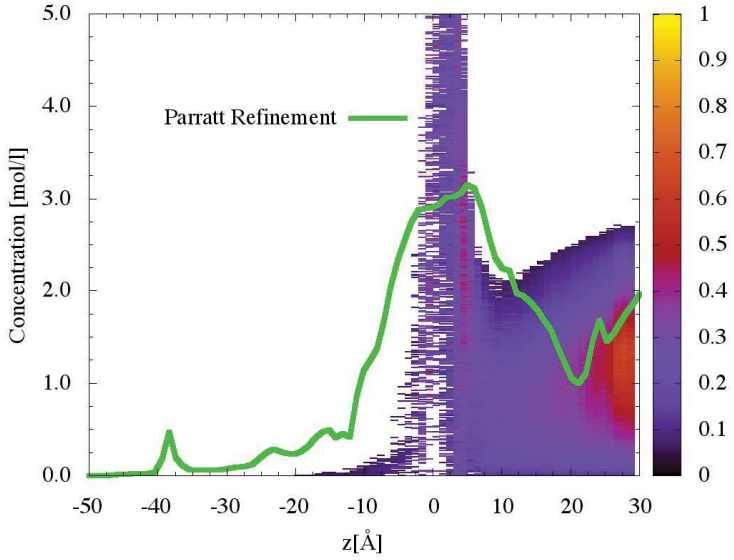

(a) Nitric Acid

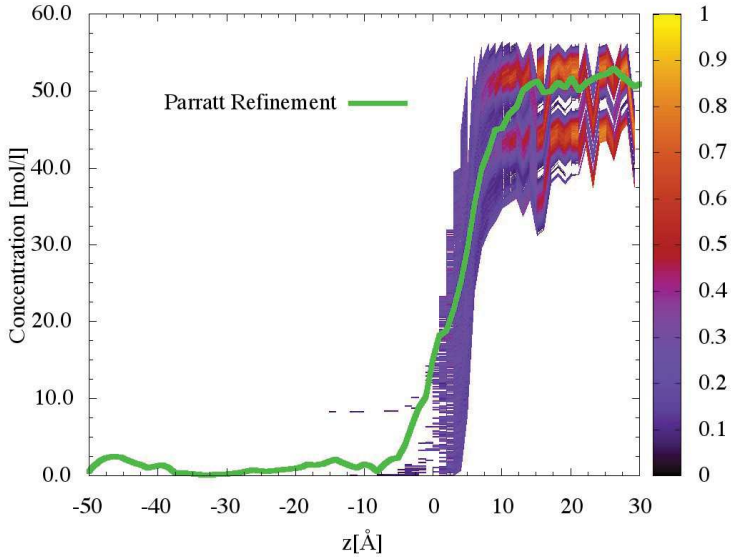

(b) Water

Figure 9.29: Concentration of (a) nitric acid and (b) water (mol/L) versus z-depth. Sample: DMDOHEMA in dodecane (0.007 M) contacted with nitric acid aqueous solution (2 mol/L). The green line represents the result of the Parratt Refinement and the color map the result of the SLD Profile Analysis.

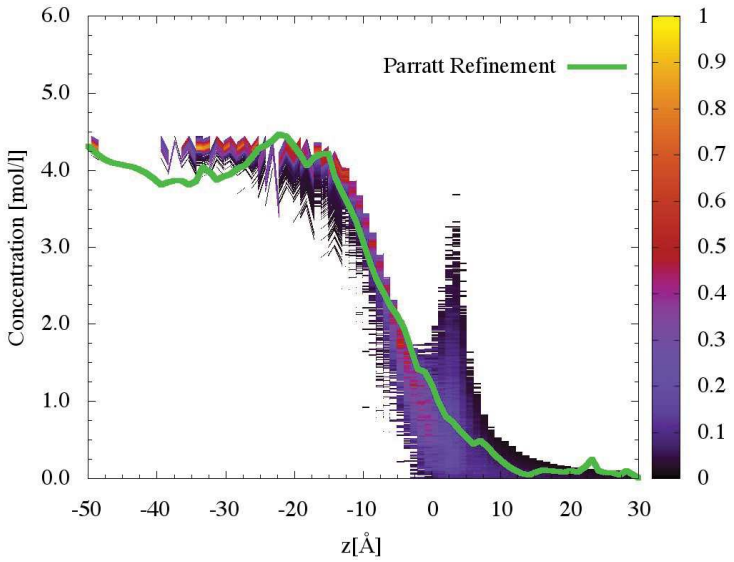

(a) Dodecane

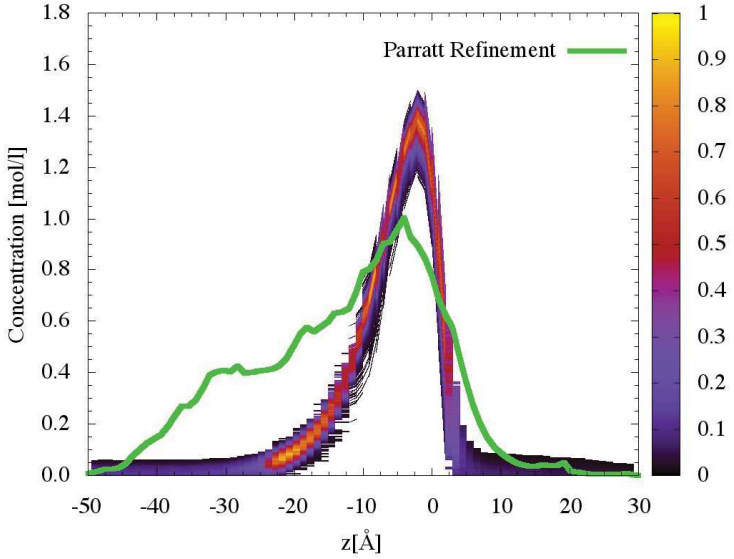

(b) DMDOHEMA

Figure 9.30: Concentration of (a) dodecane and (b) DMDOHEMA (mol/L) versus z-depth. Sample: DMDOHEMA in dodecane (0.007 M) contacted with nitric acid aqueous solution (2 mol/L). The green line represents the result of the Parratt Refinement and the color map the result of the SLD Profile Analysis.

0.01 M of DMDOHEMA in Dodecane

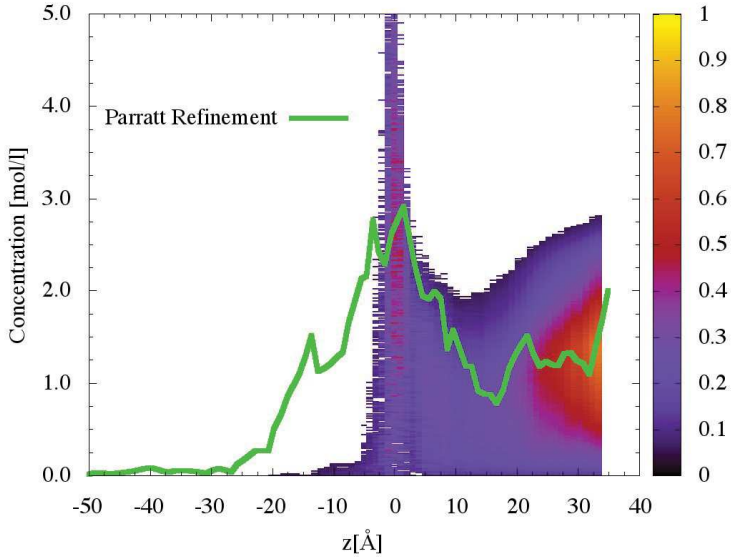

(a) Nitric Acid

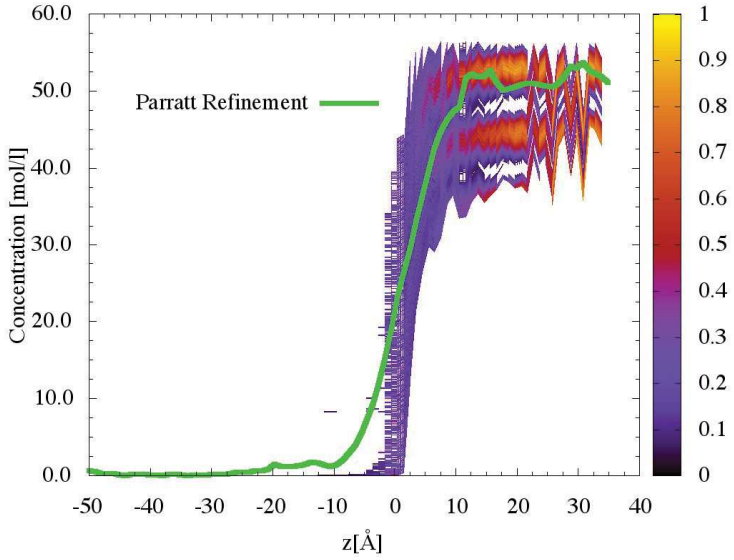

(b) Water

Figure 9.31: Concentration of (a) nitric acid and (b) water (mol/L) versus z-depth. Sample: DMDOHEMA in dodecane (0.01 M) contacted with nitric acid aqueous solution (2 mol/L). The green line represents the result of the Parratt Refinement and the color map the result of the SLD Profile Analysis.

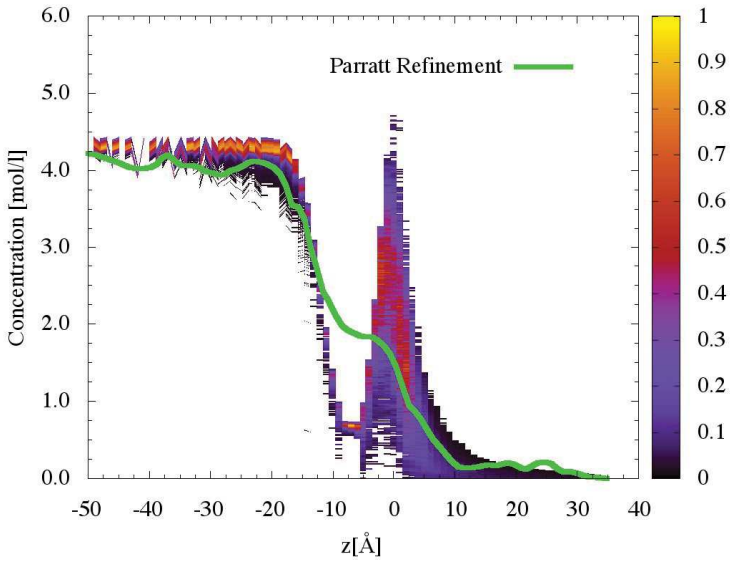

(a) Dodecane

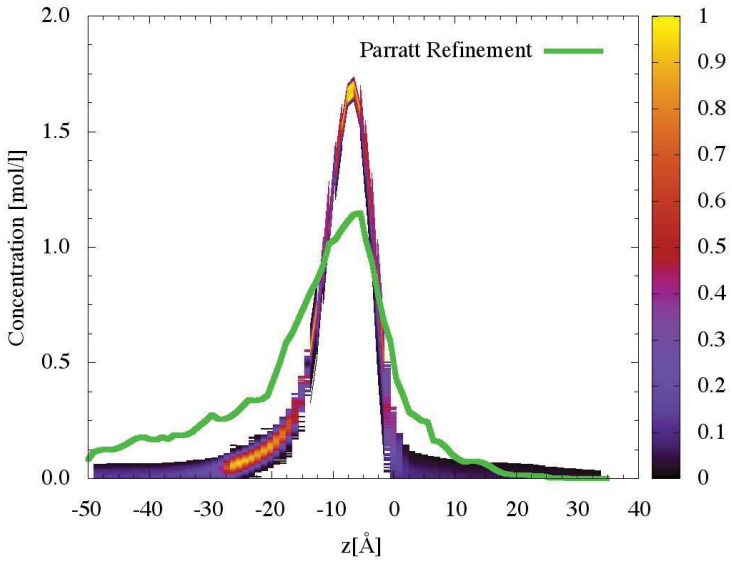

(b) DMDOHEMA

Figure 9.32: Concentration of (a) dodecane and (b) DMDOHEMA (mol/L) versus z-depth. Sample: DMDOHEMA in dodecane (0.01 M) contacted with nitric acid aqueous solution (2 mol/L). The green line represents the result of the Parratt Refinement and the color map the result of the SLD Profile Analysis.

9.2.3 Water and Neodymium Nitrate

As shown in Section 4.3.3 we report the list of samples invesitgated and analyzed with the RMCS code in Table 9.5.

.

Concentration [mol/l]	X-ray	Neutron
0.002 M	**X**	**X**
0.007 M	**X**	**X**
0.01 M	**X**	**X**
0.02 M	**X**	**X**
0.04 M	**X**	**X**
0.07 M	**X**	**X**

Table 9.5: List of samples for DMDOHEMA in dodecane contacted with an aqueous phase at 2 M of $LiNO_3$ and 0.25 M of $Nd(NO_3)_3$ analyzed with the RMCS code. The X means the sample has been measured, the - it has not, and the bold **X** means the data have been analyzed with the RMCS to investigate the liquid/liquid interfacial structure.

0.002 M of DMDOHEMA in Dodecane

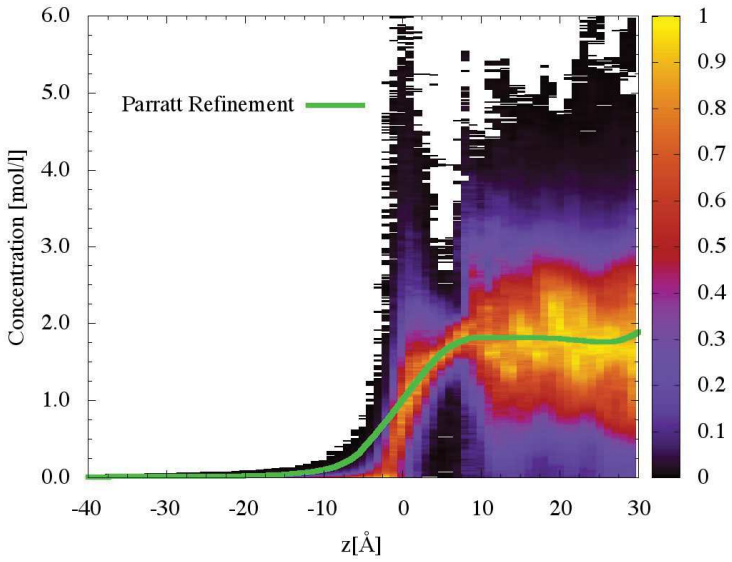

(a) Lithium

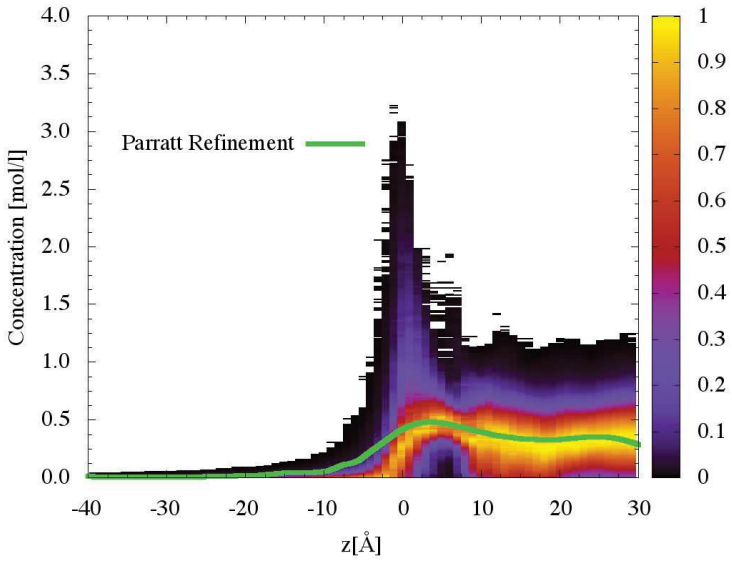

(b) Neodymium

Figure 9.33: Concentration of (a) lithium and (b) neodymium (mol/L) versus z-depth. Sample: DMDOHEMA in dodecane (0.002 M) contacted with neodymium nitrate (0.25 mol/L) and lithium nitrate (2 mol/L) aqueous solution. The green line represents the result of the Parratt Refinement and the color map the result of the SLD Profile Analysis.

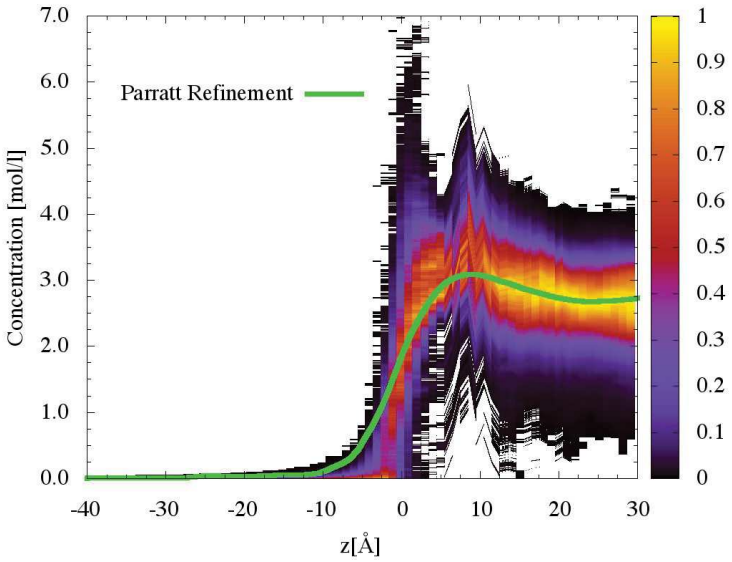

(a) Nitrate

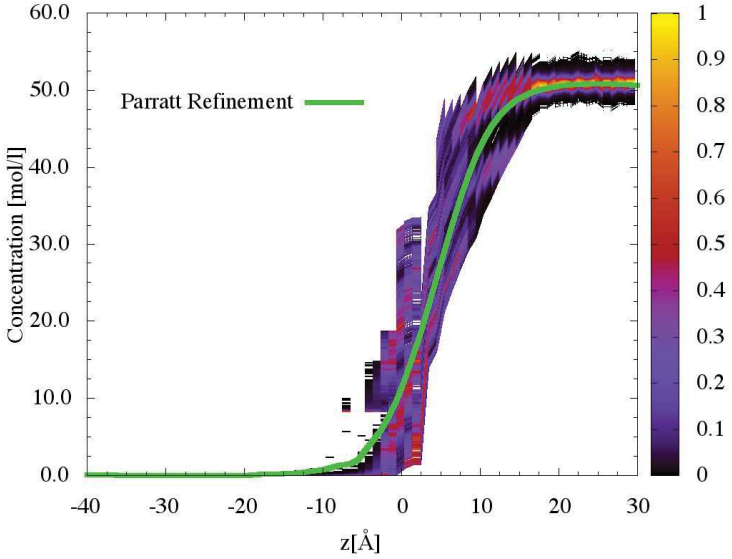

(b) Water

Figure 9.34: Concentration of (a) nitrate and (b) water (mol/L) versus z-depth. Sample: DMDOHEMA in dodecane (0.002 M) contacted with neodymium nitrate (0.25 mol/L) and lithium nitrate (2 mol/L) aqueous solution. The green line represents the result of the Parratt Refinement and the color map the result of the SLD Profile Analysis.

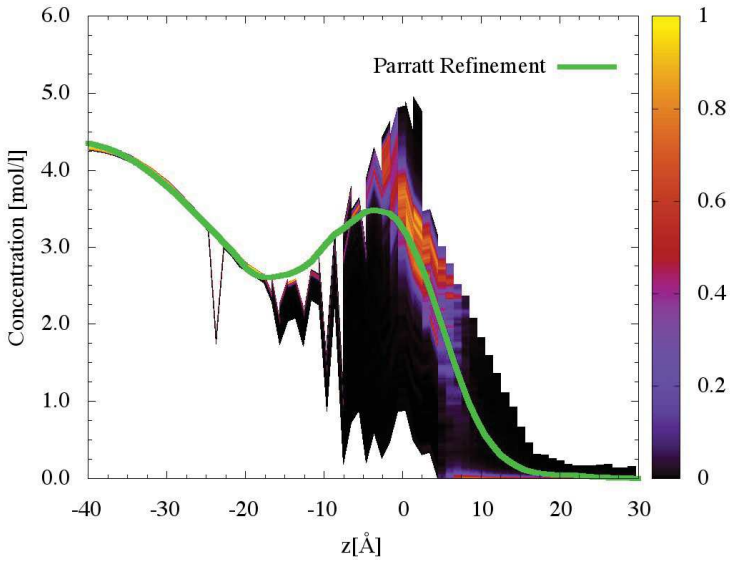

(a) Dodecane

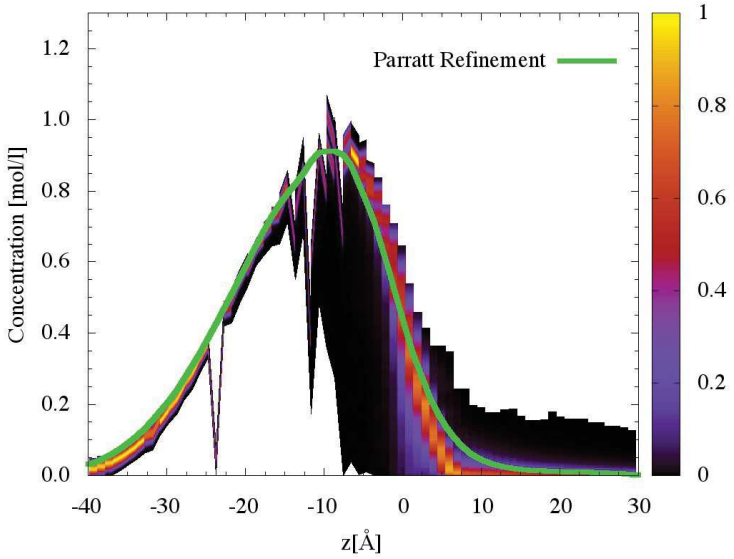

(b) DMDOHEMA

Figure 9.35: Concentration of (a) dodecane and (b) DMDOHEMA (mol/L) versus z-depth. Sample: DMDOHEMA in dodecane (0.002 M) contacted with neodymium nitrate (0.25 mol/L) and lithium nitrate (2 mol/L) aqueous solution. The green line represents the result of the Parratt Refinement and the color map the result of the SLD Profile Analysis.

0.007 M of DMDOHEMA in Dodecane

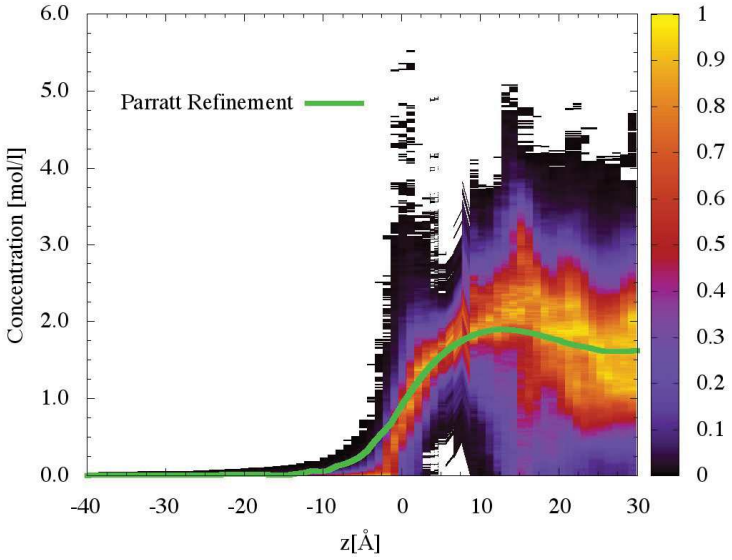

(a) Lithium

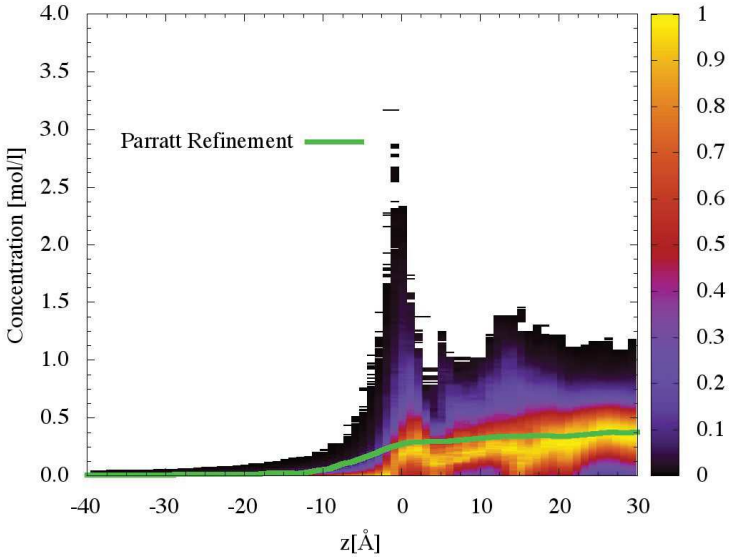

(b) Neodymium

Figure 9.36: Concentration of (a) lithium and (b) neodymium (mol/L) versus z-depth. Sample: DMDOHEMA in dodecane (0.007 M) contacted with neodymium nitrate (0.25 mol/L) and lithium nitrate (2 mol/L) aqueous solution. The green line represents the result of the Parratt Refinement and the color map the result of the SLD Profile Analysis.

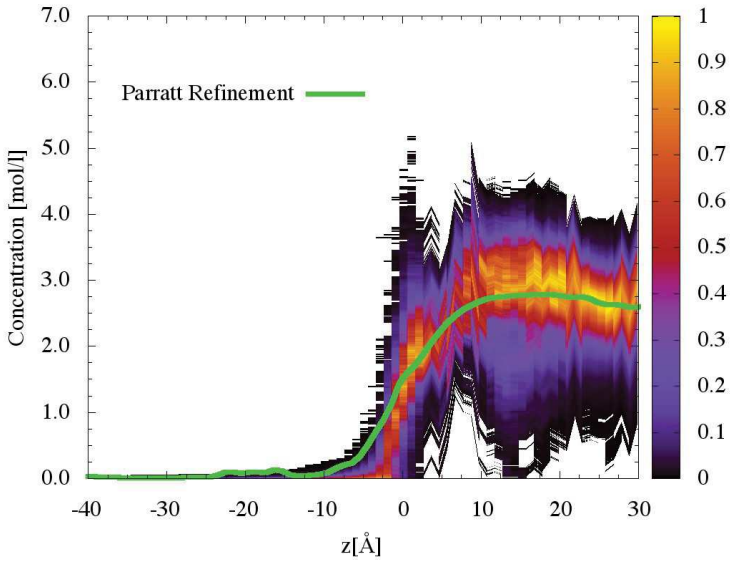

(a) Nitrate

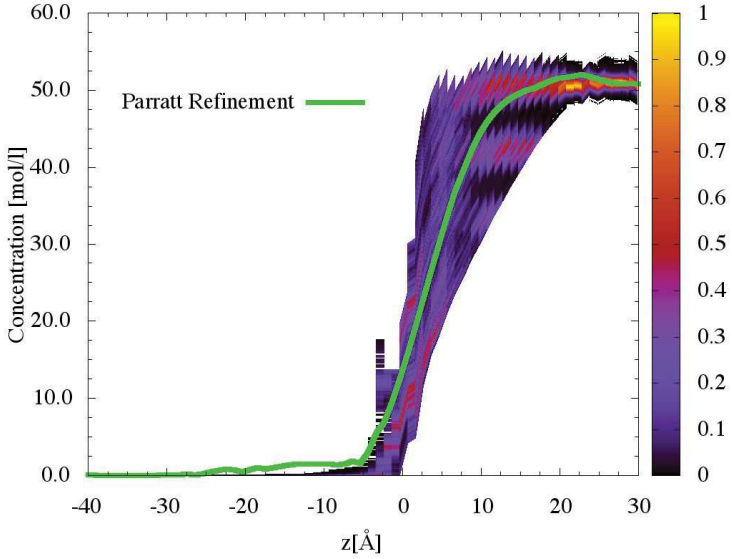

(b) Water

Figure 9.37: Concentration of (a) nitrate and (b) water (mol/L) versus z-depth. Sample: DMDOHEMA in dodecane (0.007 M) contacted with neodymium nitrate (0.25 mol/L) and lithium nitrate (2 mol/L) aqueous solution. The green line represents the result of the Parratt Refinement and the color map the result of the SLD Profile Analysis.

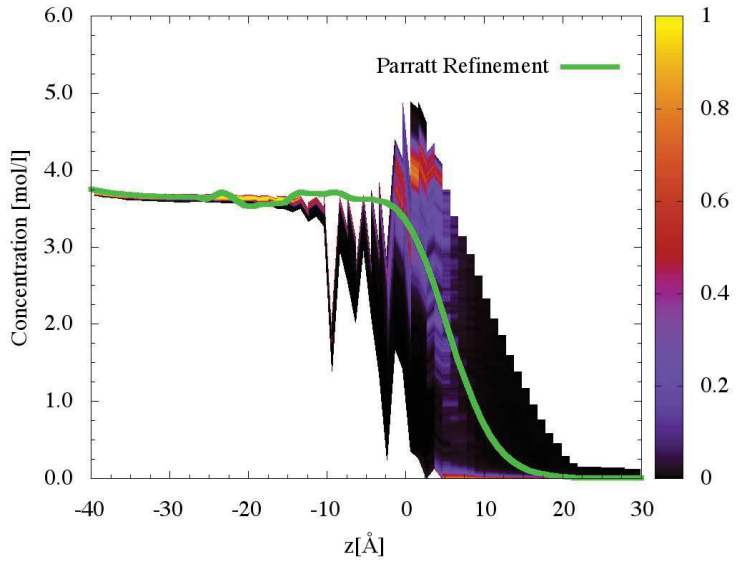

(a) Dodecane

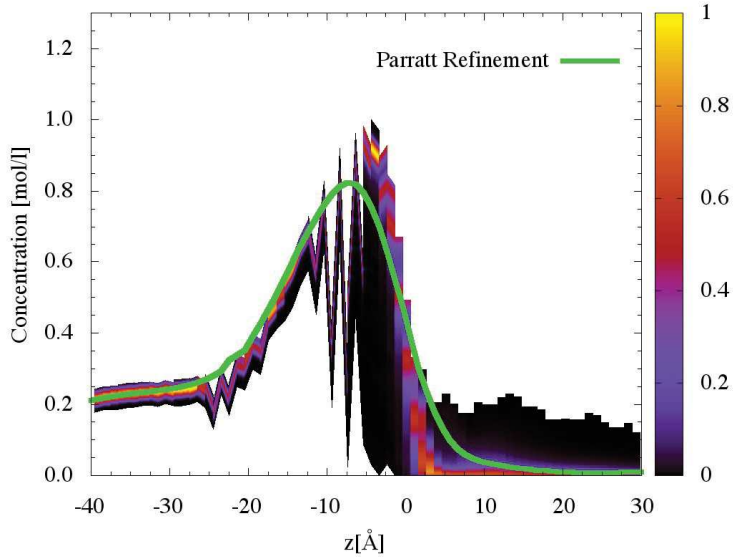

(b) DMDOHEMA

Figure 9.38: Concentration of (a) dodecane and (b) DMDOHEMA (mol/L) versus z-depth. Sample: DMDOHEMA in dodecane (0.007 M) contacted with neodymium nitrate (0.25 mol/L) and lithium nitrate (2 mol/L) aqueous solution. The green line represents the result of the Parratt Refinement and the color map the result of the SLD Profile Analysis.

0.01 M of DMDOHEMA in Dodecane

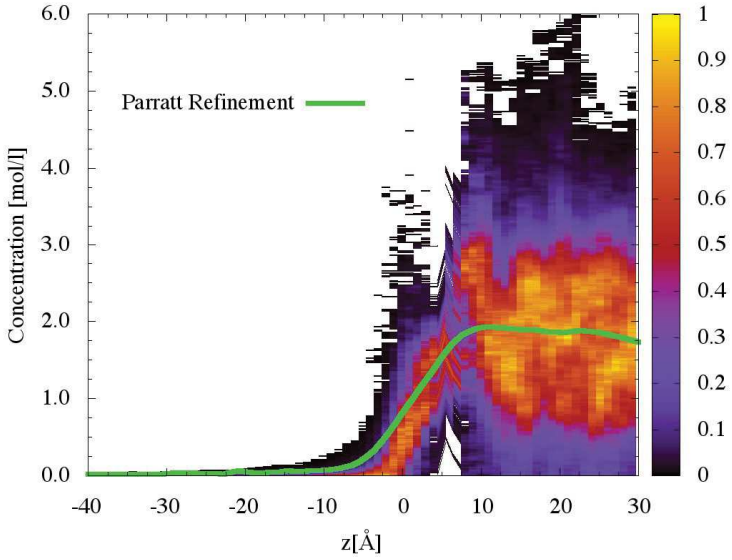

(a) Lithium

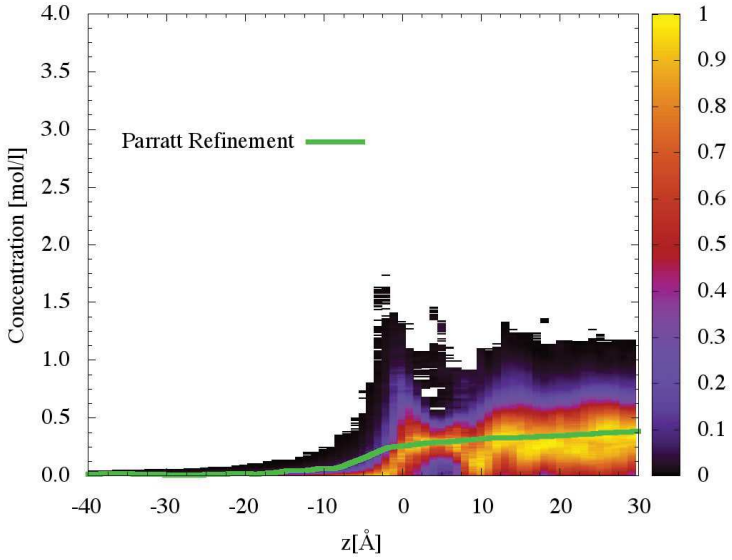

(b) Neodymium

Figure 9.39: Concentration of (a) lithium and (b) neodymium (mol/L) versus z-depth. Sample: DMDOHEMA in dodecane (0.01 M) contacted with neodymium nitrate (0.25 mol/L) and lithium nitrate (2 mol/L) aqueous solution. The green line represents the result of the Parratt Refinement and the color map the result of the SLD Profile Analysis.

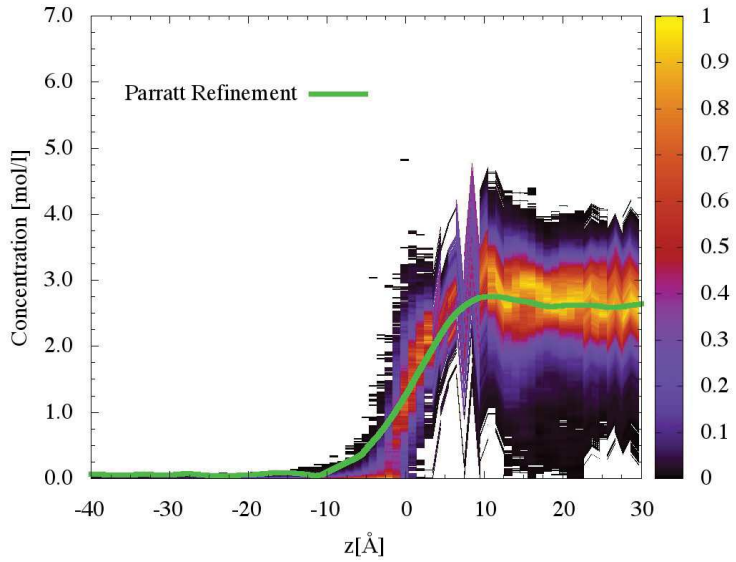

(a) Nitrate

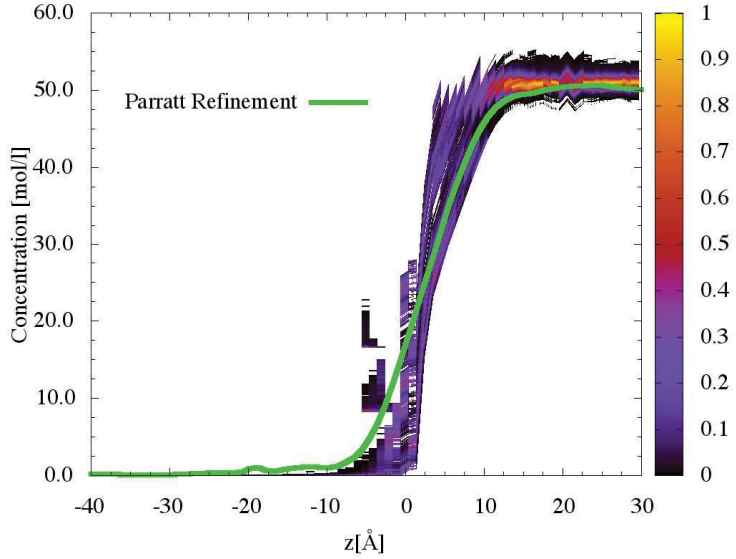

(b) Water

Figure 9.40: Concentration of (a) nitrate and (b) water (mol/L) versus z-depth. Sample: DMDOHEMA in dodecane (0.01 M) contacted with neodymium nitrate (0.25 mol/L) and lithium nitrate (2 mol/L) aqueous solution. The green line represents the result of the Parratt Refinement and the color map the result of the SLD Profile Analysis.

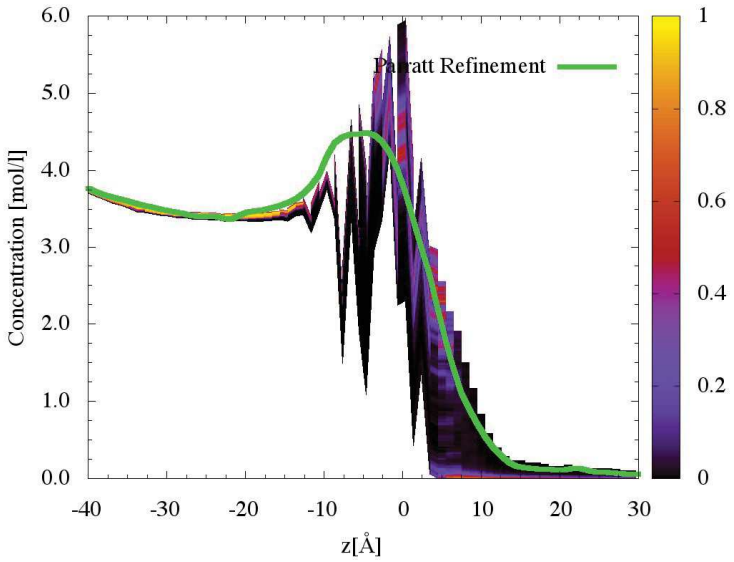

(a) Dodecane

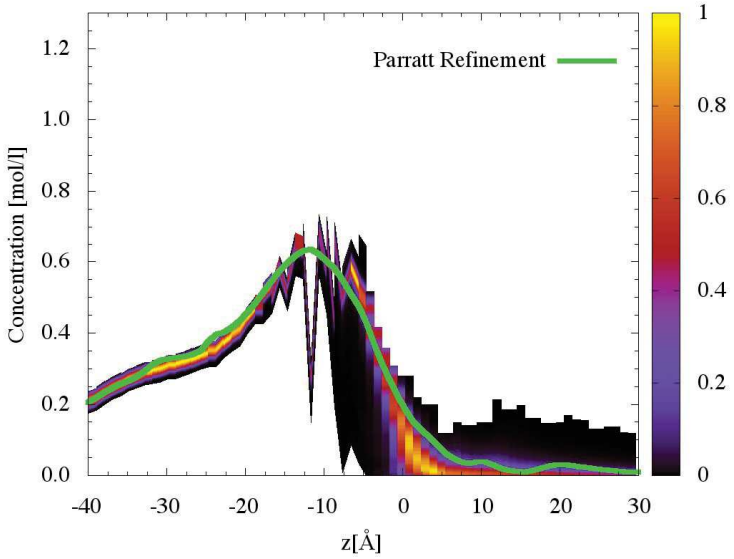

(b) DMDOHEMA

Figure 9.41: Concentration of (a) dodecane and (b) DMDOHEMA (mol/L) versus z-depth. Sample: DMDOHEMA in dodecane (0.01 M) contacted with neodymium nitrate (0.25 mol/L) and lithium nitrate (2 mol/L) aqueous solution. The green line represents the result of the Parratt Refinement and the color map the result of the SLD Profile Analysis.

0.02 M of DMDOHEMA in Dodecane

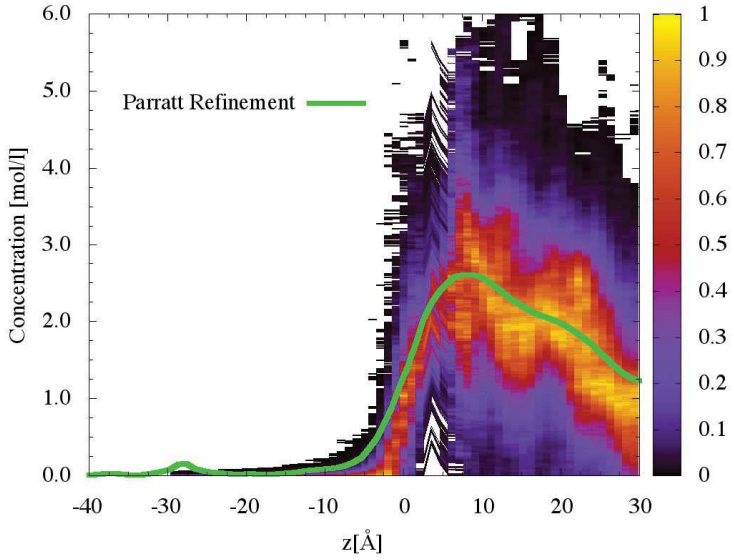

(a) Lithium

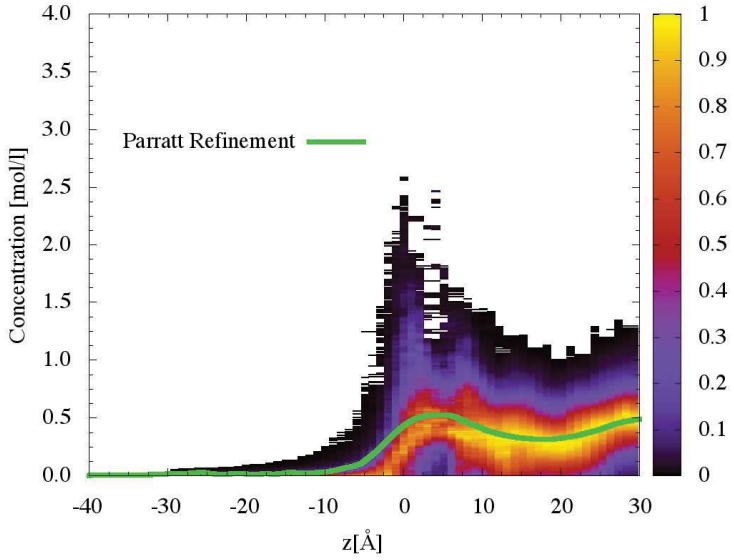

(b) Neodymium

Figure 9.42: Concentration of (a) lithium and (b) neodymium (mol/L) versus z-depth. Sample: DMDOHEMA in dodecane (0.02 M) contacted with neodymium nitrate (0.25 mol/L) and lithium nitrate (2 mol/L) aqueous solution. The green line represents the result of the Parratt Refinement and the color map the result of the SLD Profile Analysis.

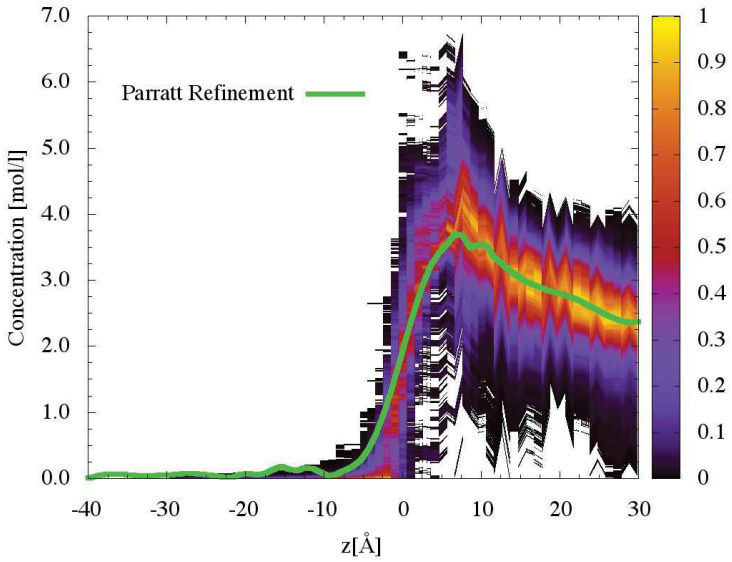

(a) Nitrate

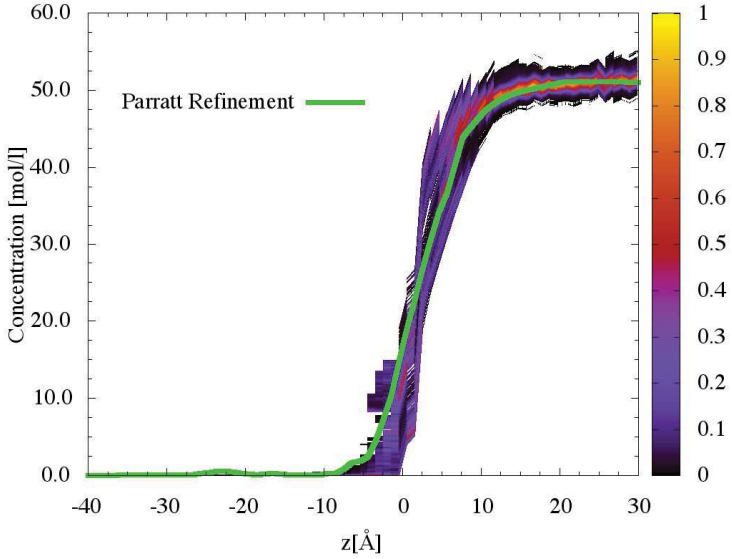

(b) Water

Figure 9.43: Concentration of (a) nitrate and (b) water (mol/L) versus z-depth. Sample: DMDOHEMA in dodecane (0.02 M) contacted with neodymium nitrate (0.25 mol/L) and lithium nitrate (2 mol/L) aqueous solution. The green line represents the result of the Parratt Refinement and the color map the result of the SLD Profile Analysis.

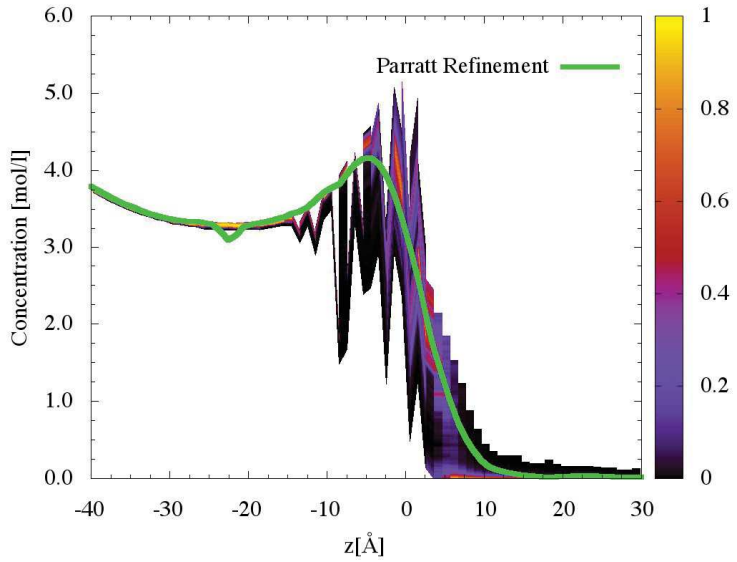

(a) Dodecane

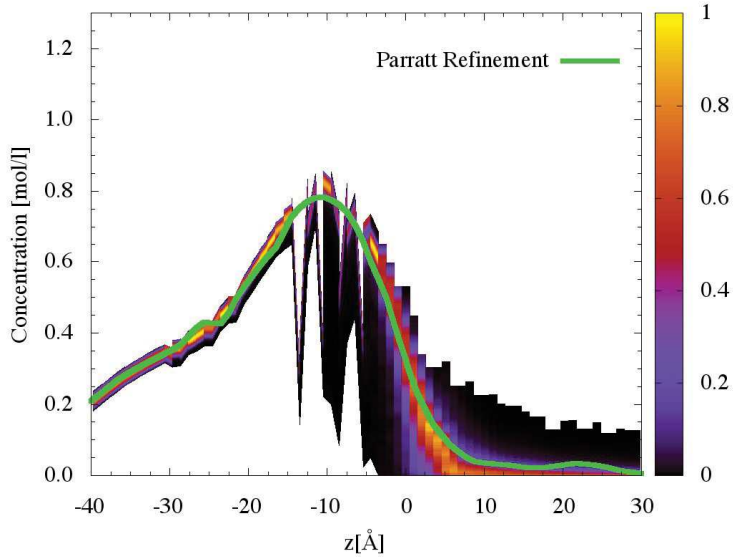

(b) DMDOHEMA

Figure 9.44: Concentration of (a) dodecane and (b) DMDOHEMA (mol/L) versus z-depth. Sample: DMDOHEMA in dodecane (0.02 M) contacted with neodymium nitrate (0.25 mol/L) and lithium nitrate (2 mol/L) aqueous solution. The green line represents the result of the Parratt Refinement and the color map the result of the SLD Profile Analysis.

0.04 M of DMDOHEMA in Dodecane

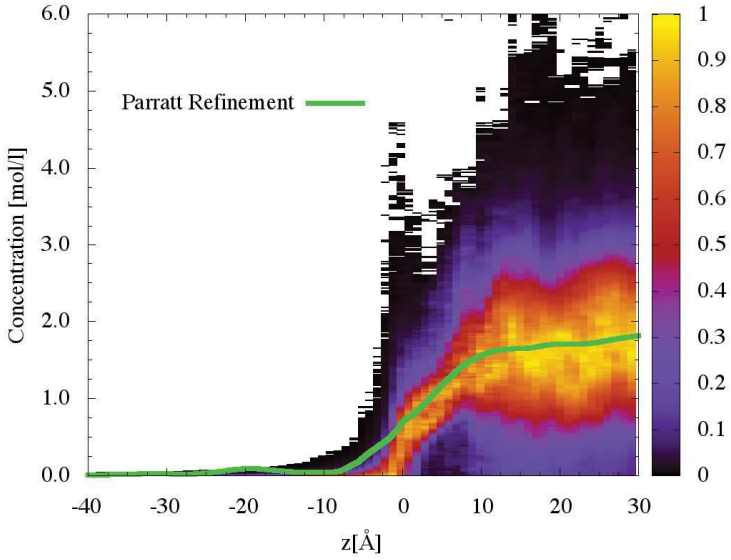

(a) Lithium

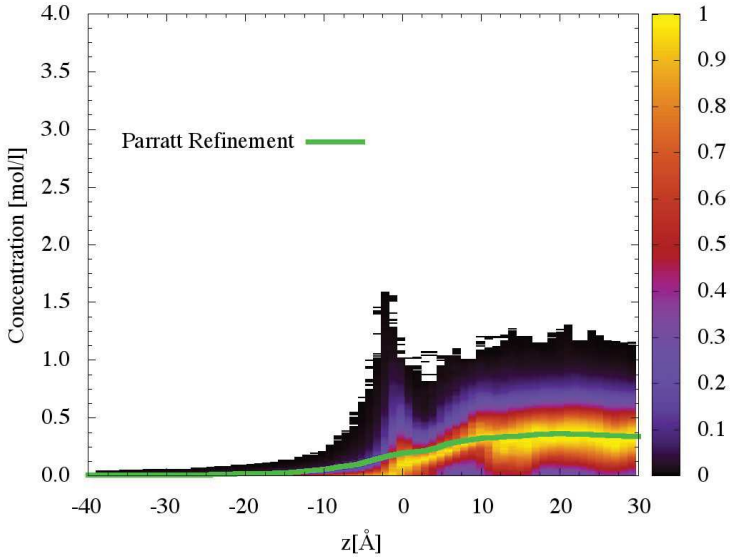

(b) Neodymium

Figure 9.45: Concentration of (a) lithium and (b) neodymium (mol/L) versus z-depth. Sample: DMDOHEMA in dodecane (0.04 M) contacted with neodymium nitrate (0.25 mol/L) and lithium nitrate (2 mol/L) aqueous solution. The green line represents the result of the Parratt Refinement and the color map the result of the SLD Profile Analysis.

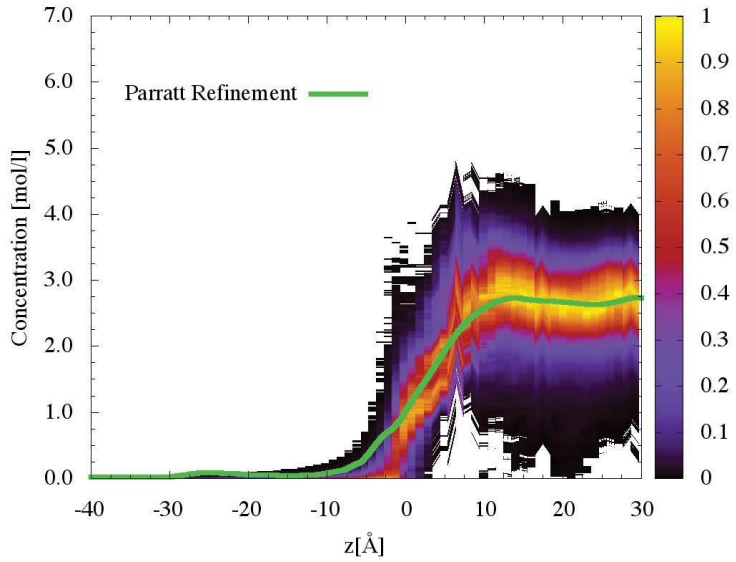

(a) Nitrate

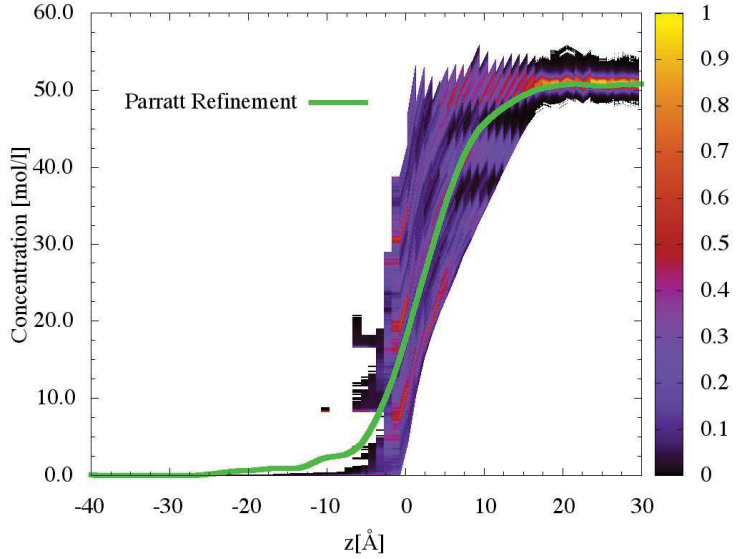

(b) Water

Figure 9.46: Concentration of (a) nitrate and (b) water (mol/L) versus z-depth. Sample: DMDOHEMA in dodecane (0.04 M) contacted with neodymium nitrate (0.25 mol/L) and lithium nitrate (2 mol/L) aqueous solution. The green line represents the result of the Parratt Refinement and the color map the result of the SLD Profile Analysis.

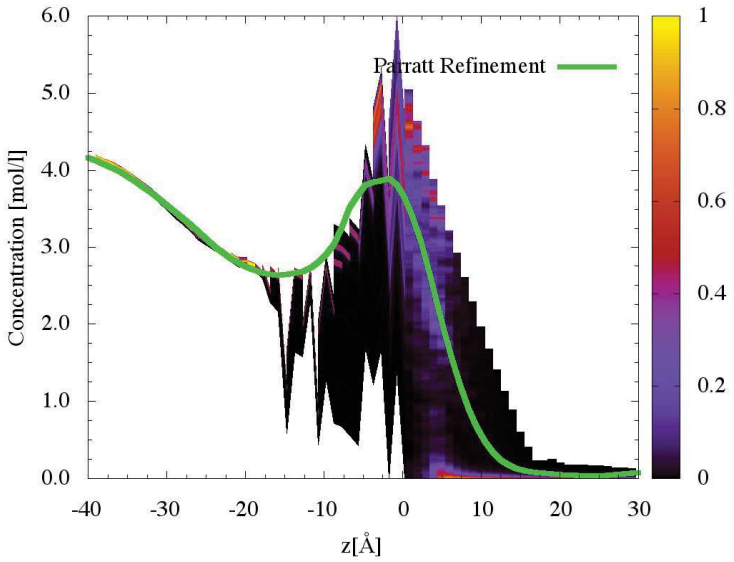

(a) Dodecane

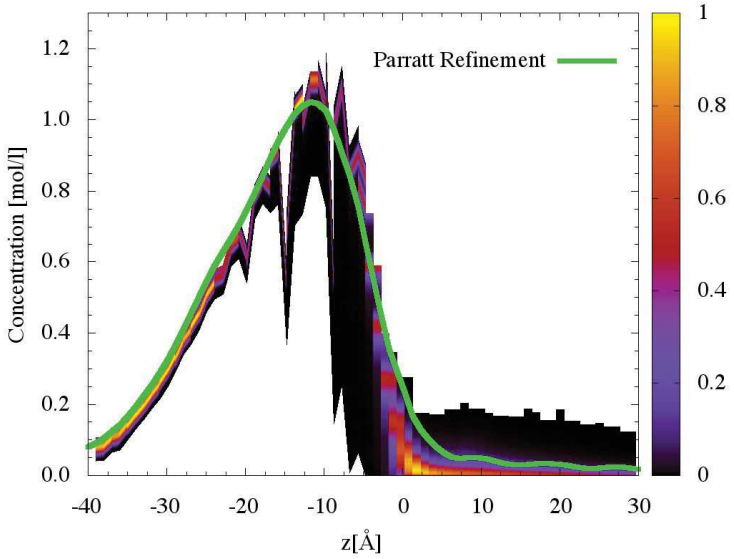

(b) DMDOHEMA

Figure 9.47: Concentration of (a) dodecane and (b) DMDOHEMA (mol/L) versus z-depth. Sample: DMDOHEMA in dodecane (0.04 M) contacted with neodymium nitrate (0.25 mol/L) and lithium nitrate (2 mol/L) aqueous solution. The green line represents the result of the Parratt Refinement and the color map the result of the SLD Profile Analysis.

0.07 M of DMDOHEMA in Dodecane

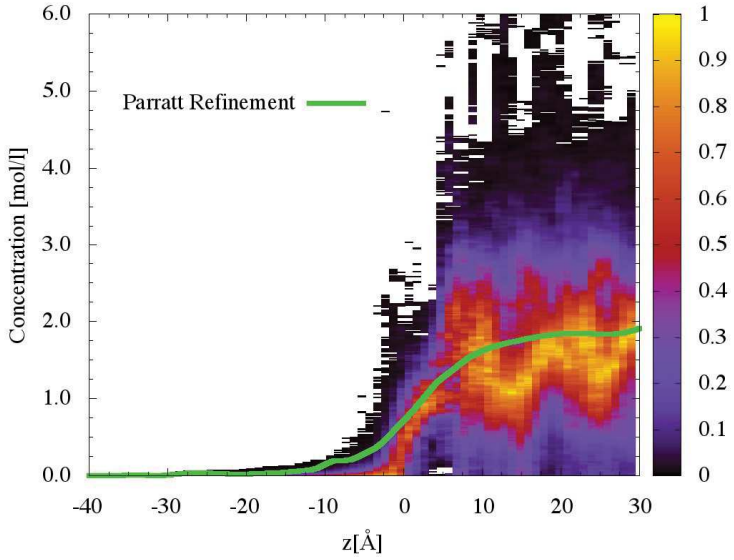

(a) Lithium

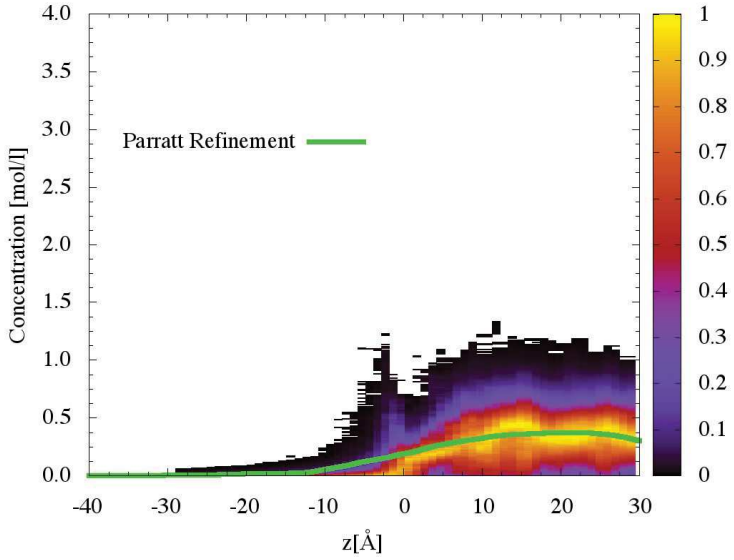

(b) Neodymium

Figure 9.48: Concentration of (a) lithium and (b) neodymium (mol/L) versus z-depth. Sample: DMDOHEMA in dodecane (0.07 M) contacted with neodymium nitrate (0.25 mol/L) and lithium nitrate (2 mol/L) aqueous solution. The green line represents the result of the Parratt Refinement and the color map the result of the SLD Profile Analysis.

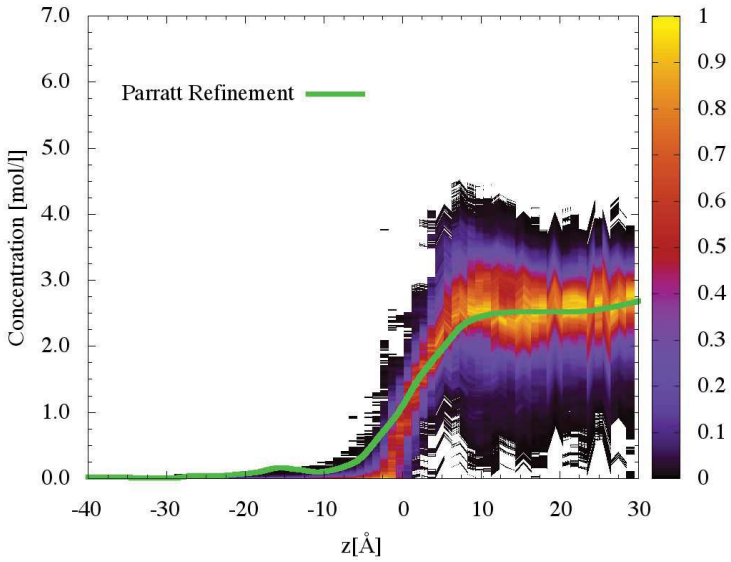

(a) Nitrate

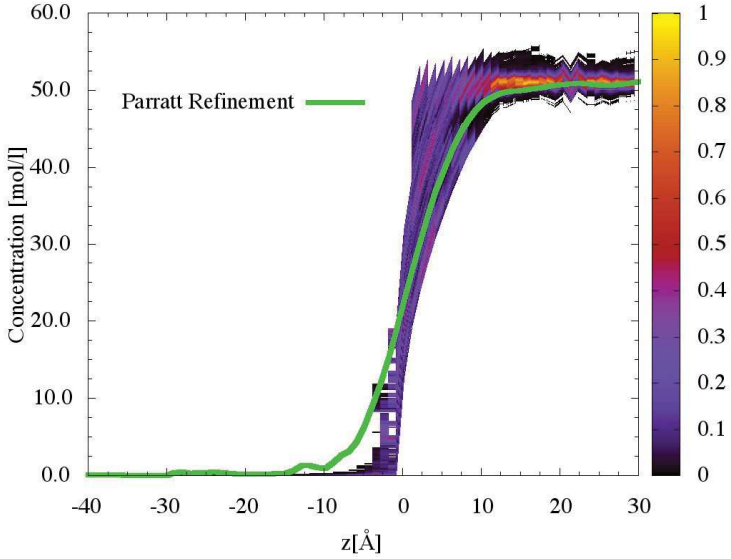

(b) Water

Figure 9.49: Concentration of (a) nitrate and (b) water (mol/L) versus z-depth. Sample: DMDOHEMA in dodecane (0.07 M) contacted with neodymium nitrate (0.25 mol/L) and lithium nitrate (2 mol/L) aqueous solution. The green line represents the result of the Parratt Refinement and the color map the result of the SLD Profile Analysis.

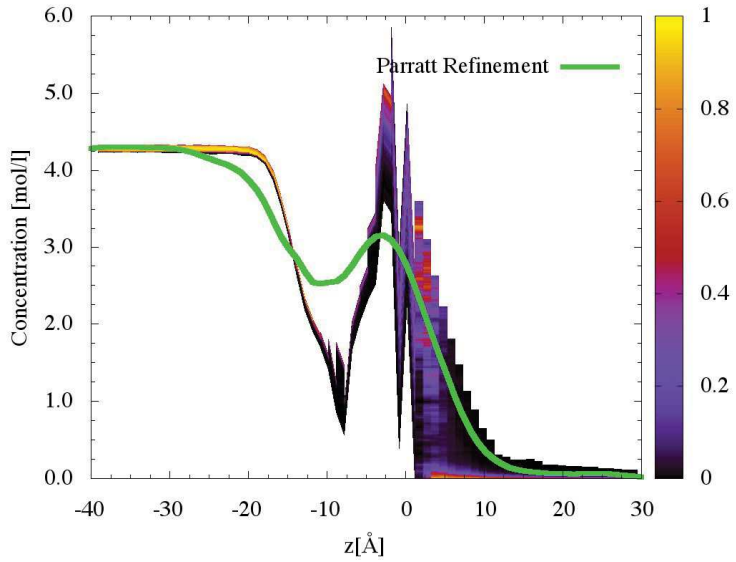

(a) Dodecane

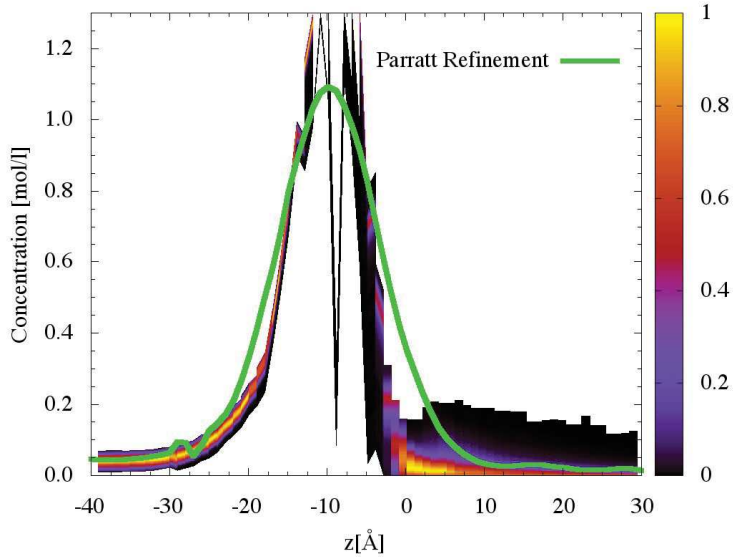

(b) DMDOHEMA

Figure 9.50: Concentration of (a) dodecane and (b) DMDOHEMA (mol/L) versus z-depth. Sample: DMDOHEMA in dodecane (0.07 M) contacted with neodymium nitrate (0.25 mol/L) and lithium nitrate (2 mol/L) aqueous solution. The green line represents the result of the Parratt Refinement and the color map the result of the SLD Profile Analysis.

Neutron Reflectivity Experiments Tables

In this appendix technical details for neutron reflectivity experiments. For each sample measured, analyzed and presented in Chapter 4 we report the counting rates for transmitted and reflected beam and slit settings. The latter are important because they define the footprint (or illumination area).

10.1 Water/Dodecane interface

Concentration [mol/L]	**Transmission [count/sec]**		**Reflection [count/sec]**	
	$\theta = -0.617°$	$\theta = -1.400°$	$\theta = -0.623°$	$\theta = -1.400°$
0/100	5080	3210	15	-
5/95	5080	3210	20	-
25/75	5088	3210	33	-
31/69	5088	3210	36	146
37.7/62.3	5088	3210	29	124
65/35	5088	3210	76	-
100/0	5088	3210	115	176

Table 10.1: Counting rates for transmitted and reflected beams in neutron reflectivity experiments at the buried water/dodecane interface. In the first columen is reported the volume ratio between $C_{12}H_{26}/C_{12}D_{26}$ used for the organic phase.

Slit	$\theta = -0.623°$	$\theta = -1.400°$
S2H	0.998	2.298
S3H	0.058	0.138
S2W	55.998	55.998
S3W	43.998	43.998

Table 10.2: Slit settings for neutron reflectivity experiments with DMDBTDMA in contact with nitric acid aqueous solution (2 mol/L).

10.2 DMDBTDMA at Liquid/Liquid interface

10.2.1 Water and Nitric Acid

Concentration [mol/L]	**Transmission [count/sec]**		**Reflection [count/sec]**	
	$\theta = -0.617°$	$\theta = -1.400°$	$\theta = -0.623°$	$\theta = -1.400°$
0.02	4686	1574	50	132
0.07	4686	1574	53	134
0.20	4686	1574	70	155

Table 10.3: Counting rates for transmitted and reflected beams in neutron reflectivity experiments with DMDBTDMA in contact with nitric acid aqueous solution (2 mol/L).

Slit	$\theta = -0.623°$	$\theta = -1.400°$
S2H	0.998	2.298
S3H	0.058	0.138
S2W	55.998	55.998
S3W	43.998	43.998

Table 10.4: Slit settings for neutron reflectivity experiments with DMDBTDMA in contact with nitric acid aqueous solution (2 mol/L).

10.2.2 Water and Neodymium Nitrate

The structure of DMDBTDMA in dodecane contacted with nedoymium nitrate (0.25 mol/L) and lithium nitrate (2 mol/L) has been investigated at various extractant bulk concentration. The data have been collected during two different experiments, one in July 2014 and one in October 2014. The counting rates and settings for these experiments are reported in Tables 10.5, 10.6 (July 2014) and 10.7, 10.8 (October 2014).

Concentration [mol/L]	**Transmission [count/sec]**		**Reflection [count/sec]**	
	$\theta = -0.617°$	$\theta = -1.400°$	$\theta = -0.623°$	$\theta = -1.400°$
0.02	519	2919	10	37
0.07	519	2919	9	40
0.10	519	2919	9	38

Table 10.5: Counting rates for transmitted and reflected beams in neutron reflectivity experiments with DMDBTDMA in contact with neodymium nitrate (0.25 mol/L) and lithium nitrate (2.0 mol/L) aqueous solution.

Slit	$\theta = -0.623°$	$\theta = -1.400°$
S2H	0.998	2.298
S3H	0.098	0.258
S2W	49.998	49.998
S3W	39.998	39.998

Table 10.6: Slit settings for neutron reflectivity experiments with DMDBTDMA in contact with neodymium nitrate (0.25 mol/L) and lithium nitrate (2.0 mol/L) aqueous solution.

Concentration [mol/L]	**Transmission [count/sec]**		**Reflection [count/sec]**	
	$\theta = -0.617°$	$\theta = -1.400°$	$\theta = -0.623°$	$\theta = -1.400°$
0.04	1388	4190	12	54
0.09	1388	4190	14	58
0.15	1388	4190	10	52

Table 10.7: Counting rates for transmitted and reflected beams in neutron reflectivity experiments with DMDBTDMA in contact with neodymium nitrate (0.25 mol/L) and lithium nitrate (2.0 mol/L) aqueous solution.

Slit	$\theta = -0.617°$	$\theta = -1.400°$
S2H	0.998	2.298
S3H	0.058	0.138
S2W	55.970	55.970
S3W	43.998	43.998

Table 10.8: Slit settings for neutron reflectivity experiments with DMDBTDMA in contact with neodymium nitrate (0.25 mol/L) and lithium nitrate (2.0 mol/L) aqueous solution.

10.3 DMDOHEMA at Liquid/Liquid interface

10.3.1 Pure Water

In Section 4.3.1 we have shown the results obtained for the DMDOHEMA at dodecane/water interface. This is the only one case in this work for which we have colected neutron data at two different contrasts with fully deuterated dodecane or with a $C_{12}H_{26}/C_{12}D_{26}$ mixture to obtain an SLD$= 4.0 \cdot 10^{-6}$ Å^{-2}.
Counting rates for transmitted and reflected beams and slit settings for samples with fully deuterated dodecane and mixture of hydrogenated/deuterated alkane are reported in Tables 10.9, 10.10 and in Tables 10.11, 10.12 respectively.

Concentration [mol/L]	**Transmission [count/sec]**		**Reflection [count/sec]**	
	$\theta = -0.617°$	$\theta = -1.400°$	$\theta = -0.623°$	$\theta = -1.400°$
0.002	5040	3176	22	129
0.007	5040	3176	23	138
0.010	5040	3176	24	138
0.040	5040	3176	24	143

Table 10.9: Counting rates for transmitted and reflected beams in neutron reflectivity experiments with DMDOHEMA in contact pure water. The organic solvent is fully deuterated dodecane.

Slit	$\theta = -0.623°$	$\theta = -1.400°$
S2H	0.998	2.098
S3H	0.058	0.258
S2W	55.998	55.998
S3W	43.998	43.998

Table 10.10: Slit settings for neutron reflectivity experiments with DMDOHEMA in contact with pure water. The organic solvent is fully deuterated dodecane.

Concentration [mol/L]	**Transmission [count/sec]**		**Reflection [count/sec]**	
	$\theta = -0.617°$	$\theta = -1.400°$	$\theta = -0.623°$	$\theta = -1.400°$
0.002	5088	3210	44	155
0.007	5088	3210	43	153
0.010	5088	3210	43	151
0.040	5088	3210	44	157

Table 10.11: Counting rates for transmitted and reflected beams in neutron reflectivity experiments with DMDOHEMA in contact pure water. The organic solvent is a mixture of $C_{12}H_{26}/C_{12}D_{26}$ with a volume ratio 37.7/62.3.

Slit	$\theta = -0.623°$	$\theta = -1.400°$
S2H	0.998	2.098
S3H	0.058	0.258
S2W	55.998	55.998
S3W	43.998	43.998

Table 10.12: Slit settings for neutron reflectivity experiments with DMDOHEMA in contact with pure water. The organic solvent is a mixture of $C_{12}H_{26}/C_{12}D_{26}$ with a volume ratio 37.7/62.3.

10.3.2 Water and Nitric Acid

Concentration [mol/L]	**Transmission [count/sec]**		**Reflection [count/sec]**	
	$\theta = -0.617°$	$\theta = -1.400°$	$\theta = -0.623°$	$\theta = -1.400°$
0.002	4835	3061	38	148
0.007	4835	3061	36	149
0.010	4835	3061	36	149

Table 10.13: Counting rates for transmitted and reflected beams in neutron reflectivity experiments with DMDOHEMA in contact with nitric acid aqueous solution (2 mol/L).

Slit	$\theta = -0.623°$	$\theta = -1.400°$
S2H	0.998	2.098
S3H	0.058	0.258
S2W	55.998	55.998
S3W	43.998	43.998

Table 10.14: Slit settings for neutron reflectivity experiments with DMDOHEMA in contact with nitric acid aqueous solution (2 mol/L).

10.3.3 Water and Neodymium Nitrate

Concentration [mol/L]	**Transmission [count/sec]**		**Reflection [count/sec]**	
	$\theta = -0.617°$	$\theta = -1.400°$	$\theta = -0.623°$	$\theta = -1.400°$
0.002	1180	5923	11	57
0.007	1180	5923	11	57
0.010	1180	5923	10	57
0.020	1180	5923	11	57
0.040	1180	5923	11	57
0.070	1180	5923	10	57

Table 10.15: Counting rates for transmitted and reflected beams in neutron reflectivity experiments with DMDOHEMA in contact with neodymium nitrate (0.25 mol/L) and lithium nitrate (2.0 mol/L) aqueous solution.

Slit	$\theta = -0.617°$	$\theta = -1.400°$
S2H	0.998	2.098
S3H	0.058	0.258
S2W	55.998	55.998
S3W	43.998	43.998

Table 10.16: Slit settings for neutron reflectivity experiments with DMDOHEMA in contact with neodymium nitrate (0.25 mol/L) and lithium nitrate (2.0 mol/L) aqueous solution.

Interfacial Potential

In this appendix we report the results obtained for the study of the interfacial potential for the DMDBTDMA and DMDOHEMA. As shown in Chapter 4 we have been able to determine the distribution of extractant, solvents and aqueous solute at the interface. For the samples in contact with Lithium and Neodymium salts aqueous solution we have been able to determine the interfacial potential for the Neodymium using the Poisson-Boltzmann Equation.

The curvature of the electrostatic potential $\psi(z)$ is defined by the Poisson equation

$$\frac{d^2\psi(z)}{dz^2} = \psi''(z) = -\frac{\rho_{el}(z)}{\epsilon_r\epsilon_0} = -\frac{\sum_i q_i\rho_i(z)}{\epsilon_r\epsilon_0} \tag{11.1}$$

with q_i and $\rho_i(z)$ the charge and charge density vs z for each ions.
It exists also a relationship between the charge density for each electrolytes and both $\psi(z)$ the electrostatic and $V_i(z)$ the interfacial potential the latter being defined by the extractant distribution at the Liquid/Liquid interface and governs by a Boltzmann equation:

$$\rho_i(z) = \rho_i(\infty)e^{[-\beta(V_i(z)+q_i\psi(z))]}. \tag{11.2}$$

With the Boltzmann Equation we can calculate the interfacial potential for the ith species:

$$V_i(z) = -\frac{1}{\beta}ln\left(\frac{\rho_i(z)}{\rho_i(\infty)}\right) - q_i\psi(z). \tag{11.3}$$

The electrostatic potential can be calculated integrating twice the Equation 11.1 and with the knowledge of the density profile distribution of each species we can calculate the corresponding interfacial potential. In particular, for the Neodymium

species for the samples presented in Sections 4.2.3 and 4.3.3, we can calculate the potential $V_{Nd}(z)$ as follow:

$$V_{Nd}(z) = -\frac{1}{\beta} ln \left(\frac{\rho_{Nd}(z)}{\rho_{Nd}(\infty)} \right) - q_{Nd}\psi(z). \tag{11.4}$$

In Figure 11.1 we show the results obtained for $V_{Nd}(z)$ in the cases of Lithium and Neodymium nitrate aqueous solution in contact with an organic phase containing DMDOHEMA (Figure 11.1a) or DMDBTDMA (Figure 11.1b).

The interfacial potential is calculated for all the extractant concentrations in dodecane below or at the CAC. In Figure 11.2 we show the comparison between the interfacial potential of Neodymium at the CAC for DMDOHEMA and DMDBT-DMA.

It is possible to observe that in the case of DMDBTDMA the potential barrier has a maximum value $\approx 2k_BT$ lower than for DMDOHEMA. Moreover, a shift of the barrier towards the organic phase with DMDBTDMA is observed.

These two results (lower energy barrier and shift) could be correlated to the different extraction regime observed for the two extractants [13].

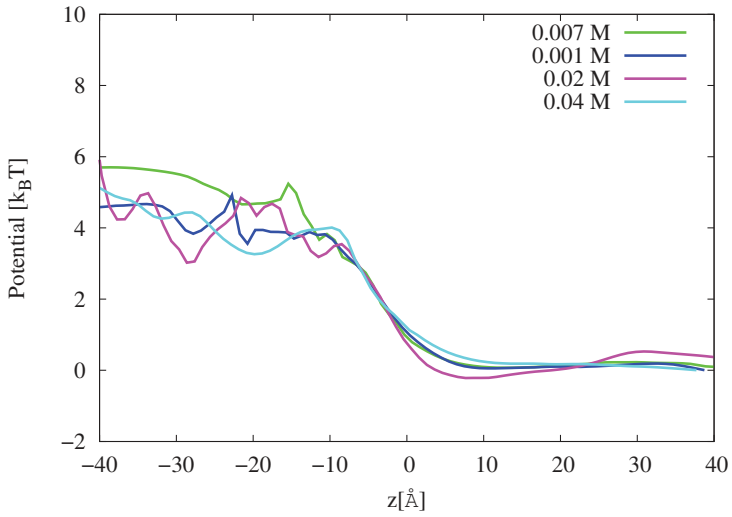

(a) Neodymium Potental when in contact with DMDOHEMA.

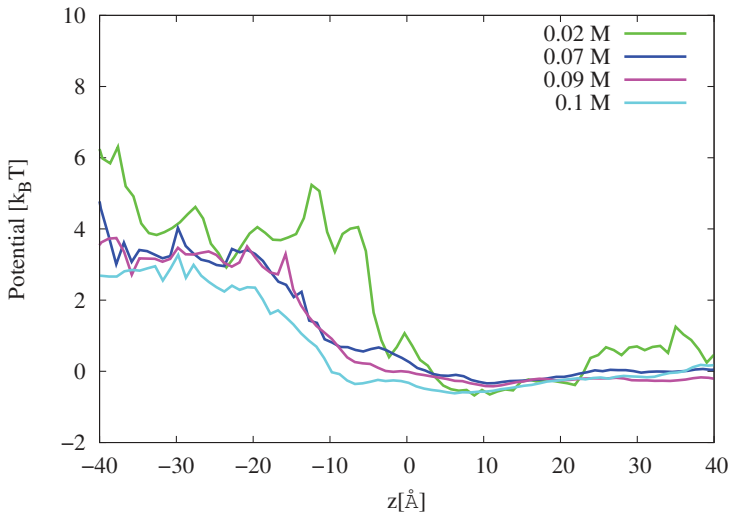

(b) Neodymium Potental when in contact with DMDBTDMA.

Figure 11.1: Interfacial potential for Neodymium when a Lithium and Neodymium nitrate aqueous solution is contacted with and organic solution containing (a) DMDOHEMA or (b) DMDBTDMA. In the legend we report the extractant concentration in organic phase. We report the results obtained using the Poisson-Boltzmann Equation for the concentration of extractant below the CAC.

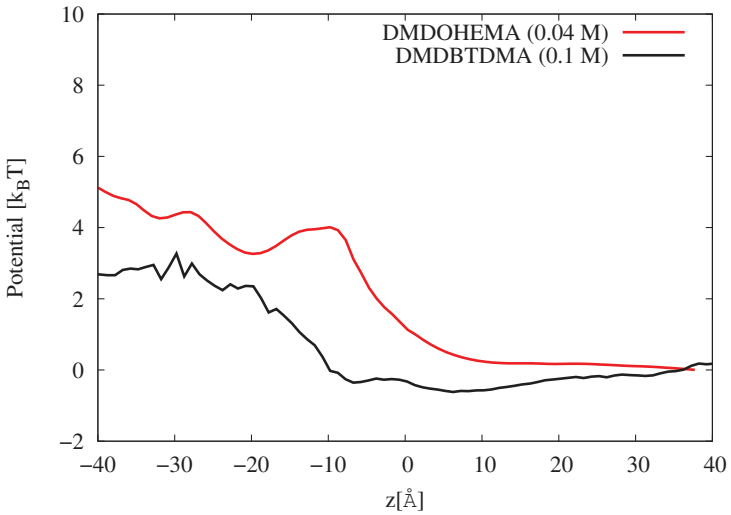

Figure 11.2: Interfacial potential for Neodymium when a Lithium and Neodymium nitrate aqueous solution is contacted with and organic solution containing (red) DMDOHEMA or (black) DMDBTDMA at the CAC.